On the Morphology and Kinematics of the Ionised Gas in Brightest Cluster Galaxies

HALSON, MARCUS,DAVID

On the Morphology and Kinematics of the Ionised Gas in Brightest Cluster Galaxies

Marcus Halson

A Thesis presented for the degree of
Doctor of Philosophy

Department of Physics
Durham University
United Kingdom
August 2025

Abstract

Brightest Cluster Galaxies (BCGs) occupy a distinct position in the galaxy population, residing at the centres of galaxy clusters where they are embedded within dense intracluster media and subject to complex baryonic processes. This thesis presents a detailed investigation of the morphology, kinematics, and excitation mechanisms of the warm ionised gas in a representative sample of X-ray–selected BCGs from the Kaleidoscope survey, observed with the Multi Unit Spectroscopic Explorer (MUSE) on the Very Large Telescope. The high spatial and spectral resolution of MUSE enables spatially resolved mapping of the ionised gas, revealing a striking diversity of filamentary and clumpy structures, coherent velocity fields, and disturbed kinematics indicative of feedback-driven outflows and gas accretion. Emission-line diagnostics are employed to disentangle the relative contributions of active galactic nucleus (AGN) photoionisation, shocks, and star formation, thereby constraining the interplay between cooling flows and feedback in cluster cores.

Following the introduction to the field (Chapter 1), I present the properties of the *Kaleidoscope* survey—the largest census of X-ray–selected BCGs observed with MUSE—and describe the custom pipeline developed for data analysis (Chapter 2). A robust framework is then established for separating the sample according to the presence of optical line emission, yielding a line-emitting fraction of 35.6%, in good agreement with previous studies (Chapter 3). Building on the work of Hamer et al. [2016] based on VIMOS data, I apply morphological classifications to the *Kaleidoscope* sample (Chapter 4). The enhanced sensitivity and resolution of MUSE reveal a markedly different distribution of morphologies, motivating the development of a new algorithm designed to exploit the full capabilities of MUSE.

The most remarkable result is the identification of a systematic offset of $\sim 100\,\mathrm{km\,s^{-1}}$ between the mean velocity of the ionised gas and the systemic stellar velocity (Chapter 5). I examine the finely tuned combinations of geometry, obscuration, and line-of-sight motions required to reproduce such an offset, and then probe the line-of-sight velocity distributions of the ionised gas in each system using the velocity structure function (Chapter 6). This analysis enables a systematic

classification of kinematic profiles across the sample.

I investigate the ionisation mechanisms powering the observed line emission using standard diagnostic diagrams, including BPT line ratios (Chapter 7). The majority of systems lie along the LINER/Composite boundary, underscoring the complex interplay of star formation, AGN photoionisation, and shocks in BCGs. Finally, I examine the underlying stellar populations, placing constraints on star formation histories and evolutionary pathways of the BCGs in our sample (Chapter 8).

Declaration

The work in this thesis is based on research carried out at the Department of Physics, Durham University, United Kingdom. No part of this thesis has been submitted elsewhere for any other degree or qualification and it is all my own work unless referenced to the contrary in the text.

Acknowledgements

The most valuable outcome of my PhD has been the people I have met, all of whom have shaped its final form. I wish to acknowledge a few of them here.

To my supervisor, *Alastair Edge*: your introduction to—and guidance through—a vibrant and dynamic corner of astrophysics led to a stimulating and exciting PhD. More broadly, your patience, generosity, and unwavering support have made my time in Durham what it was. Thank you.

To *David Lagattuta*, for your detailed explainers and the endless time you devoted to solving technical problems. To *Leah Morabito* and *Mathilde Jauzac*, for welcoming me into your respective groups at different stages, and for your valuable feedback during review meetings.

To *Zoe, Sarah, Ciera, and Sutti*: your constant efforts shaped the department more than most seemed to see. Of the many things I will miss, our lunchtime chats rank highly. To *Victor, Duncan, Nency, and Emmy*: a happy office makes for a happy PhD, and your company made that a constant throughout my time here.

To *the British taxpayer*: most people are not funded to pursue their hobby, and for this opportunity I am deeply grateful.

To *John Bell*, my senior school physics teacher, for setting this journey in motion many years ago with incredible passion, inspiration, and support.

To my family, especially *my parents*: I cannot conceive of a more charmed, idyllic and loving path to this point in my life. Through your work and sacrifice, I was granted time and opportunities unavailable to you. Any positive outcomes that follow are attributable in their entirety to this foundation.

Contents

List of Figures

List of Tables

CHAPTER 1

Introduction

With the expectation that my non-scientific family will represent a significant fraction of the readership I will start the introduction assuming no extraordinary knowledge on the topic of galaxy clusters. The subject sometimes resists a straightforward, linear exposition and some terms will appear before they're formally defined; persistence is rewarded.

In this chapter we will zoom in from the scale of the Universe to the very centre of a galaxy cluster in § 1.1, pausing at relevant intermediate spatial scales, before covering the formation and evolution of the large galaxy at the centre of a cluster in § 1.2 and § 1.3 respectively. The observational signatures of these galaxies are covered in § 1.4. Finally, § 1.5 will justify this work and set out the questions we aim to answer, or partially answer, in the subsequent chapters.

1.1 Background

1.1.1 Forces and Ingredients

There are, we think, four fundamental forces in the Universe and on large scales only one is generally relevant: gravity. Newton proposed that gravity is an attractive force

between any two objects with mass. Einstein later showed this was only true in a low gravity regime, but the environments considered in this work are sufficiently distant from the central supermassive black hole that Newton's formulation will suffice—and will be far from the most liberal assumption made in the analysis. The attractive force, F, increases with the product of the respective masses, and decreases with the square of the separation:

$$F = G\frac{m_1 m_2}{r^2} \tag{1.1}$$

where G is Newton's gravitational constant, m_1 and m_2 are the respective masses, and r is the separation distance. This simple equation governs the past, present, and future of the large-scale dynamics of galaxies, both internally and in their interactions with the surrounding Universe.

The energy in the Universe is split between four key ingredients, the relative (and changing) ratios of which determine its evolution. These are: ordinary ('baryonic') matter (the atoms and molecules we know), radiation (the energy carried by photons and relativistic particles), dark matter (an unseen form of mass), and dark energy (a force driving the accelerated expansion of space). Following the Big Bang, the expansion of the Universe initially proceeded as predicted for a matter–radiation dominated cosmos, with gravitational attraction slightly slowing the expansion. However, observations of distant supernovae and nearby galaxies reveal that a few billion years ago the expansion began to accelerate again [Riess et al., 1998], an effect attributed to dark energy. Current observations indicate that roughly 30% of the cosmic energy density is in matter (baryonic and dark) and 70% in dark energy [Aghanim et al., 2020], with radiation now negligible.

A key observational pillar for these proportions comes from the cosmic microwave background (CMB), relic radiation from the hot, dense early Universe, now cooled to just under 3 K. Its blackbody spectrum constrains the photon energy budget to $\sim 5\times10^{-5}$ of the critical density [1], and its minute temperature anisotropies reveal the

[1] The critical density ρ_c is the energy density that separates different possible geometries of the Universe. It is defined as $\rho_c = 3H_0^2/(8\pi G)$, where H_0 is the Hubble constant and G is Newton's gravitational constant. If the total density $\rho > \rho_c$, the Universe is closed, meaning it has positive

matter distribution in the young Universe. Study of these fluctuations shows that only $\sim 1/6$ of the matter is baryonic [Aghanim et al., 2020, Hinshaw et al., 2013], with the rest in the form of dark matter—detected only via gravitational effects [Rubin and Ford, 1970, Zwicky, 1937]. In density parameter terms, $\Omega_m \approx 0.31$ consists of $\Omega_b \approx 0.05$ in baryons and $\Omega_c \approx 0.26$ in cold dark matter, consistent with large-scale structure surveys [Alam et al., 2017].

Taken together, these measurements underpin what is now the standard model of cosmology: the Λ cold dark matter (ΛCDM) framework. In this model, the matter and dark matter fractions inferred from the CMB and galaxy surveys are combined with a dominant dark energy component to describe the geometry, contents, and evolution of the Universe [Navarro et al., 1997, Riess et al., 1998]. The 'Λ' denotes the cosmological constant—Einstein's term for a uniform energy density permeating space—now associated with dark energy and responsible for the observed late-time acceleration of cosmic expansion. The 'CDM' component refers to 'cold dark matter', a form of non-relativistic, non-baryonic matter that interacts primarily through gravity and serves as the gravitational web for cosmic structure formation.

Although the CMB is remarkably uniform, its tiny anisotropies pinpoint where matter was slightly over- or under-dense. Over cosmic time, overdense regions decelerated more than average, eventually halting expansion locally and collapsing under their own gravity. Dark matter provided the gravitational scaffolding for this collapse, while baryons cooled radiatively to form stars within nascent protogalaxies. Hierarchical growth ensued: small systems merged into larger galaxies and, eventually, galaxy clusters.

After a few billion years of structure growth, star formation and galaxy assembly peaked, a point termed 'cosmic noon', and the accelerated expansion driven by dark energy began to dominate. This cosmic 'push' slowed down the rate at which new structures form, as distant regions of space are pulled apart more rapidly. While overdense regions that had already collapsed continue to grow in mass by attracting

spatial curvature and would eventually recollapse. If $\rho < \rho_c$, the Universe is open, with negative spatial curvature and it would expand forever. The special case $\rho = \rho_c$ corresponds to a flat Universe with zero spatial curvature. The density parameters Ω used in cosmology are defined relative to this reference value, $\Omega = \rho/\rho_c$.

more matter, the accelerating expansion effectively isolates these structures from one another on the largest scales.

1.1.2 Observational History

Faint 'nebulae' (Latin: 'clouds') were catalogued by observers such as Charles Messier in the 18th century, who sought to distinguish these diffuse patches from comets [Messier, 1781]. Thomas Wright, William Herschel and Immanuel Kant in the late 18th century speculated that some nebulae might be 'island universes', or distant star systems like our own Milky Way [Herschel, 1786, Kant, 1755, Wright, 1750], but this remained controversial. The debate culminated in the 1920 'Great Debate' between Harlow Shapley and Heber Curtis over the scale of the Universe [Shapley and Curtis, 1921]. This question was settled by Edwin Hubble just a few years later. He used Cepheid Stars - a type of variable star with strong correlation between period and luminosity - to measure the distance to the Andromeda nebula. These famous measurements conclusively demonstrated that it, and other spiral nebulae, were in fact entirely separate systems beyond our own Milky Way. [Hubble, 1923]. These 'island universes' - systems of millions or billions of stars, together with gas and dust, bound within a gravitational potential well dominated by dark matter - are now known as galaxies.

1.1.3 Galaxy Clusters

Studies of large-scale structure indicate that a significant fraction—typically 20–30% depending on the sample's luminosity limit—of galaxies are relatively isolated, while the majority reside within gravitationally bound systems of other galaxies [Coil, 2013]. A galaxy is generally considered isolated, or a 'field galaxy', if it lacks a neighbour within a defined search radius and line-of-sight velocity. Gravitationally bound systems of galaxies are broadly categorised as groups and clusters. While a simple membership count is often used as a first-pass distinction—with 'groups' containing up to approximately 50 members and 'clusters' containing hundreds to thousands—the more physically meaningful dividing line is based on total system

mass. Systems with a total mass below approximately 10^{14} solar masses ($M_\odot$) are typically classified as groups, whereas more massive structures are considered clusters. This mass threshold also corresponds to differences in dynamical state and the presence of a hot, X-ray emitting intracluster medium (ICM) [Kravtsov and Borgani, 2012]. Galaxy clusters are the largest gravitationally bound structures in the Universe [2]. They provide unique laboratories for studying many aspects of galaxy formation and evolution. These theories contains many, sometimes contradictory, postulates which are being explored with both observation and simulation.

The immense gravitational potential well of a galaxy cluster, shaped predominantly by its dark matter halo, creates a deep, centrally concentrated environment in which gas, galaxies, and dark matter subhalos sink toward the core. As infalling galaxies merge and dynamical friction drags them inward, their stars and gas coalesce to build up the central galaxy's mass. Cooling of the hot ICM, discussed in § 1.1.4, can funnel additional material onto the core, further fuelling the growth of the galaxy at the cluster's centre. Together, these processes produce a central galaxy of extraordinary size and luminosity known as the Brightest Cluster Galaxy (BCG) - § 1.1.5.

1.1.4 Intra Cluster Medium

The ICM is the diffuse, X-ray–emitting plasma that fills the space between the galaxies in a cluster; it constitutes the cluster's largest baryonic component and typically accounts for 10–15% of the cluster's total mass [Sarazin, 1986, Voit, 2005]. This proportion, when combined with the smaller mass of stars, makes the baryon fraction of clusters a powerful probe of the cosmic mean baryon density, Ω_b/Ω_m, providing results consistent with those from the cosmic microwave background [Allen et al., 2011]. Composed primarily of ionised hydrogen and helium with trace metals injected by supernovae and galactic winds, the ICM reaches temperatures of $T \sim 10^7$–$10^8\,\mathrm{K}$ and particle densities of $n \sim 10^{-4}$–$10^{-2}\,\mathrm{cm}^{-3}$ [Peterson and Fabian, 2006]. Its thermal bremsstrahlung continuum and line emission—particularly from

[2] I have been told many times that this sentence is obligatory in any discussion on the subject

iron—make it bright in X-rays, allowing detailed mapping of temperature, density, and metallicity gradients [Allen et al., 2011]. These profiles reveal the cluster's dynamical state (e.g. shocks and cold fronts from recent mergers) as well as cooling cores where density is highest and radiative losses are greatest [Fabian, 1994].

1.1.5 Brightest Cluster Galaxies

BCGs are frequently classified as giant ellipticals or cD galaxies. This class exhibits distinct properties when compared to typical field ellipticals. Many BCGs have extended, diffuse stellar envelopes beyond their main body, sometimes referred to as the 'cD halo' [Matthews et al., 1964]. These low-surface-brightness regions are signatures of multiple past mergers, including "dry mergers" where little gas is present. BCGs can be embedded in diffuse intracluster light (ICL) that was stripped from infalling satellite galaxies. Studying the spatial distribution and metallicity of the ICL around BCGs helps constrain cluster assembly history and the role of merging [Montes, 2019, Rudick et al., 2007, Zibetti et al., 2005]. BCGs commonly host super massive black holes (SMBHs) at their centres, making them critical for investigating the correlation between SMBH growth and galaxy evolution [Lauer et al., 2007]. Energetic feedback from these black holes can regulate star formation not only in the BCG itself but also, through large-scale jets, in the wider cluster environment [Fabian, 2012]. These phenomena will be explored in § 1.1.6 .

A pillar of the modern cosmological model is hierarchical structure formation, whereby small dark matter halos merge to form increasingly larger systems. Clusters of galaxies, and their central BCGs, are the endpoint of this process. To achieve their size BCGs have undergone repeated mergers across cosmic time and so provide a record of the cluster assembly history [Lidman et al., 2012]. Spectroscopic and photometric studies of BCGs can reveal stellar population ages, merger remnants, and metallicity gradients that link to the underlying dark matter merger tree and star formation history. By observing BCGs at different redshifts (i.e., at various epochs), one can piece together how massive elliptical galaxies evolve in high-density environments. It has been shown that BCG stellar masses grow over time, often through a combination of minor and major mergers [Burke et al., 2015, Lidman

et al., 2012]. [3] The fate of a BCG is closely tied to the evolution of its host cluster, including heating and cooling of the ICM, cluster mergers, and large-scale accretion of surrounding material. This interplay offers insights into how changes on the cluster scale impact the central galaxy, and vice versa.

The cluster core environment is fundamentally different from the field. High temperatures in the ICM, frequent gravitational interactions, and the presence of numerous satellite galaxies shape the properties of the central galaxy. Optical IFU instruments, covered in § 2.1.1, are the perfect instrument to explore these regions as they provide spatially resolved spectroscopy, enabling detailed mapping of the kinematics, ionisation structure, and stellar populations across the galaxy and its surroundings. BCGs often exhibit old, metal-rich stellar populations [Edwards et al., 2019]. Repeated mergers can build up these populations over time, while cluster-specific processes may quench star formation more effectively than in less dense environments. The stars we see today were typically formed in much smaller galaxies, a very different environment, long before the galaxy achieved its current mass. The merging history imprints itself on the velocity dispersion profile and kinematic structure of the BCG, producing anisotropic velocity distributions, kinematically decoupled cores, or extended halos with distinct, transitory rotational properties [Loubser et al., 2020]. Satellite accretion, high-speed encounters, and stripping of material from other galaxies in the cluster environment can transform the inner regions of a galaxy, producing faint shells, tidal streams, and other features that give detailed clues about the merger history [Hernquist and Quinn, 1988, Martínez-Delgado et al., 2010]. These are all phenomena arising from the galaxies central location within a cluster and are not mirrored in isolated field galaxies.

BCGs are evidently enormously useful testing-grounds for observational astronomy. Their brightness makes them easier to detect and study, even at moderate to high redshifts, providing a direct window into galaxy evolution across a large portion of cosmic time. The structural signatures of past mergers—such as shells,

[3] A common convention is to distinguish mergers by their stellar mass ratios. Major mergers involve progenitors with mass ratios larger than 1:4, while minor mergers have smaller companions with mass ratios below this threshold.

tidal tails, and diffuse outer envelopes—are accessible with sensitive imaging, especially in deep surveys. Since galaxy clusters can be identified through multiple means including: X-ray emission, Sunyaev–Zel'dovich effect, galaxy overdensities, BCGs often serve as markers for cluster centres, enabling the study of large cosmological samples of galaxies in well-characterised environments. This enables cluster selection independent of the constituent galaxy population.

1.1.6 Active Galactic Nuclei

Zooming in from the cluster scale to the centre of its potential well reveals the BCG, and at its very core lies a SMBH — the singularity marking the deepest point of the well. This SMBH is most readily observed when the accretion of surrounding matter creates a luminous Active Galactic Nucleus (AGN) [Heckman and Best, 2014]. However even when quiescent its properties can be probed indirectly. This can be done by observing the high-velocity orbits of nearby stars through stellar dynamics [Kormendy and Ho, 2013], or by using the SMBH's mass contribution to a strong gravitational lens system, as was done to detect the ultramassive black hole in the galaxy cluster Abell 1201 [Nightingale et al., 2023].

While actively accreting, the gravitational potential energy liberated is released either as emission across many bands of the electromagnetic spectrum or as strong bipolar outflows centred on the black hole, and sometimes both [Königl, 1999]. While in this state the black hole, and the surrounding region, is known as an AGN. [4]

AGN are now some of the most studied objects in the sky following two discoveries made at the end of the last century. Firstly, that there appears to be a consistent correlation between the properties of the AGN and the stars, even beyond the region where the AGN dominates the galaxy's dynamics. The central velocity dispersion of the galaxy's stars and the total stellar mass of its bulge both correlate with the black hole mass [Ferrarese and Merritt, 2000, Gebhardt et al., 2000, Magorrian et al., 1998]. Secondly, the AGN are also observed to drive outflows with kinetic power almost identical to the radiative losses from gas surrounding the galaxy. The corre-

[4] In honour of Prof Morabito we will leave the reader to determine whether AGN is plural or singular and not sink to the level of using 'AGNs'

lation may appear coincidental, but simulations that omit AGN feedback produce unrealistic galaxies, manifesting as galaxies with excessive stellar mass. The model allows far too much gas to cool and turn into stars, creating central galaxies that are significantly more massive and dense than any observed in the real Universe [Balogh et al., 2001, Benson, 2010, Borgani et al., 2004, Somerville and Davé, 2015]. The relationships found between supermassive black holes and their host galaxies imply a causal origin resulting from AGN feedback, an umbrella term for all mechanisms related to this interplay [Fabian, 2012]. The phrase is generally used, without qualification, to refer to *negative* feedback, where energetic outflows heat or expel gas, thereby quenching or suppressing the rate of star formation within the galaxy. However, AGN feedback can also be *positive*, acting to trigger or enhance star formation. In this scenario, the same powerful jets and winds that might quench a galaxy globally can, on a local scale, have the opposite effect. As an outflow expands, it can compress dense clouds of gas in the surrounding interstellar medium, increasing their density beyond the critical point for gravitational collapse and thus inducing a new burst of star formation [Gaibler et al., 2012]. There is growing observational evidence for this 'jet-induced star formation', including the discovery of young stars forming directly within a galactic outflow, far from the main stellar disc of the galaxy [Maiolino et al., 2017]. While the large-scale quenching effects of negative feedback are considered essential for explaining the observed properties of massive galaxies, the role of positive feedback highlights the complex and multifaceted nature of the relationship between a supermassive black hole and its host.

1.2 Building a BCG

BCG formation is intertwined with the hierarchical assembly of their host clusters: they grow within the deepest potential wells, accreting stars and dark matter through a sequence of mergers and interactions embedded in the evolving cluster environment. While the bulk of their stellar mass forms early ($z \gtrsim 2$) in intense starbursts hosted by massive progenitors, subsequent growth is dominated by the accretion of satellite galaxies, with the ICM and tidal field shaping the nature of

these events [Oser et al., 2010]. Understanding the relative roles of early in-situ star formation, ex-situ accretion, and cluster-scale processes is key to explaining the structural, kinematic, and stellar-population properties of present-day BCGs.

1.2.1 Context in ΛCDM: Progenitors and Assembly Sites

In the ΛCDM paradigm, the most massive dark-matter haloes at any epoch are the natural assembly sites for BCGs [Blumenthal et al., 1984, Dubinski, 1994, White and Rees, 1978]. The early Universe rapidly forms compact, quenched progenitors by $z \gtrsim 2$, which later assemble into the central galaxies of rich [5] clusters through hierarchical growth [Naab et al., 2009, Oser et al., 2010]. Semi-analytic models embedded in the ΛCDM framework predict that BCGs build a significant fraction of their final stellar mass at late times via the accretion of already-quenched satellites [De Lucia and Blaizot, 2007, Guo et al., 2011]. Cosmological hydrodynamical simulations further show that the deep cluster potential funnels massive satellites to the centre, while tidal interactions and stripping disperse stars into both the bound galaxy and the surrounding stellar halo [Martizzi et al., 2012, Ragagnin et al., 2022, Ragone-Figueroa et al., 2013].

1.2.2 Merger-Driven Assembly: Dynamical Friction and Orbital Decay

The efficiency of satellite sinking is governed by dynamical friction [Chandrasekhar, 1943], which transfers orbital energy and angular momentum from the satellite to the background halo and stellar distribution. The characteristic decay time decreases with increasing mass ratio and depends on orbital eccentricity and halo structure [Boylan-Kolchin et al., 2008, Jiang et al., 2015]. In rich clusters, repeated infall of quenched, massive satellites leads to an accretion history dominated by dry (gas-poor) mergers, with minor mergers — involving mass ratios of roughly 1:4 or smaller

[5] A rich galaxy cluster contains hundreds to thousands of member galaxies bound within a massive ($\sim 10^{14}$–$10^{15}\,M_{\odot}$) dark matter halo. Richness refers to the number of galaxies above a given luminosity threshold within a defined radius, and correlates with properties such as high galaxy density, a hot X-ray–emitting ICM, and strong gravitational lensing potential

— frequent, and occasional major mergers — with more comparable galaxy masses — still possible. These collisions rearrange pre-existing stars, often visible in the kinematics, rather than trigger significant in-situ star formation. This is the reason BCGs are often (though sometimes incorrectly – Chapter 8) referred to as 'red and dead'[6] [Bernardi et al., 2003, Laporte et al., 2013, Martizzi et al., 2012].

1.2.3 Dry vs Wet Channels and Structural Consequences

The ICM and tidal field efficiently deplete and strip cold gas from infalling galaxies [Boselli and Gavazzi, 2006, Gunn and Gott, 1972], a phenomena observed most spectacularly in 'jellyfish' galaxies. Here asymmetric, one-sided tails of stripped gas and star-forming knots trace ongoing ram-pressure interactions as they travel through the cluster [e.g. Owers et al., 2012, Poggianti et al., 2017]. As a result, the late-time growth of BCGs is principally dissipationless, meaning driven by gravitational dynamics without significant radiative cooling or star formation. Dry mergers swell galaxies: the effective radius increases faster than stellar mass for a sequence of minor mergers, producing extended cD-like envelopes and shallow outer surface-brightness profiles, while leaving central stellar ages largely unchanged [Bernardi, 2009, Laporte et al., 2013, van Dokkum et al., 2010]. By contrast, genuinely gas-rich ('wet') events are significantly rarer in cluster cores at low redshift and contribute little to integral star formation histories of BCGs, consistent with their red colours and weak nebular emission in most systems [Bell et al., 2006, Liu et al., 2009].

1.2.4 The Role of Intracluster Light: Partitioning Accreted Stars

A central diagnostic of BCG assembly is the partition of accreted stellar mass between the bound BCG and the diffuse ICL. Tidal stripping and satellite disruption feed a luminous, low surface-brightness component extending to hundreds of kilopar-

[6]The phrase red and dead refers to galaxies whose stellar populations are dominated by old, metal-rich stars, giving them a red optical colour, and which exhibit little or no ongoing star formation.

secs [Contini, 2021, DeMaio et al., 2015, 2017, Gonzalez et al., 2005]. Observational evidence from $z \sim 1$ to $z \sim 0$ suggest substantial co-evolution of BCGs and ICL: while the total central stellar content (BCG+ICL) grows steadily, a non-negligible fraction of newly accreted stars are deposited directly into the ICL, helping reconcile modest BCG mass growth with vigorous cluster accretion [Burke et al., 2015, DeMaio et al., 2020, Golden-Marx et al., 2023]. Simulations support this picture and highlight that operational definitions of the BCG/ICL boundary (e.g. surface-brightness cuts vs. kinematic separation) can bias inferred growth rates [Contini, 2021, Contreras-Santos et al., 2024, Pillepich et al., 2018].

1.2.5 Observational constraints on assembly since $z \sim 1$

Empirical estimates of BCG stellar mass growth since $z \sim 1$ span a broad range. Early work found little evolution [Collins et al., 2009, Whiley et al., 2008], whereas later analyses reported factors of ~ 1.5–2 increase in stellar mass, driven by mergers within the maturing cluster environment [Lidman et al., 2012, 2013, Lin et al., 2025]. Counts of close companions, tidal features, and ongoing interactions at low redshift directly support continued assembly via dry mergers [Burke and Collins, 2013, Edwards and Patton, 2012, Liu et al., 2015]. Analyses of large cluster samples show that BCGs exhibit distinctive properties compared to typical central galaxies, including alignment between their stellar light and the cluster's major axis, large luminosity gaps to the next brightest member, and minimal offsets from the cluster centre. These trends reflect their unique assembly histories and their position deep within the cluster's gravitational potential well [Dalal et al., 2021, De Propris et al., 2020]. Studies extending to $z \sim 1.8$ indicate that many present-day properties are already in place at these early times, with subsequent evolution dominated by accretion and structural growth rather than any widespread 'rejuvenation' [Chu et al., 2021, 2022].

1.2.6 Simulation Insights and Data-Theory Tension

State-of-the-art simulations broadly reproduce qualitative trends—old stellar populations, size growth via dry mergers, and the emergence of extended envelopes—but often struggle to match the absolute stellar masses and the detailed BCG/ICL partition at the highest halo masses [Puchwein et al., 2010, Ragagnin et al., 2022, Ragone-Figueroa et al., 2013]. These tensions point to sensitivities in some, or all, of: AGN feedback implementations, numerical resolution of tidal stripping, or the criteria used to separate bound and unbound stars. However, the general hierarchical picture is robust: BCGs assemble late, mostly ex-situ, within the largest haloes [De Lucia and Blaizot, 2007, Martizzi et al., 2012].

1.2.7 The Complete Lifecycle

Combining the previous sections a coherent formation pathway emerges. (i) Massive, compact progenitors form early and quench by $z \gtrsim 2$; (ii) subsequent growth is dominated by ex-situ, dissipationless accretion governed by dynamical friction, producing rapid size evolution and extended stellar halos; (iii) a substantial and environment-dependent share of accreted stars populates the ICL rather than remaining bound, so that the BCG+ICL budget grows more strongly than the BCG alone [Contreras-Santos et al., 2024, DeMaio et al., 2020, Golden-Marx et al., 2023]. This narrative naturally explains old central stellar populations, cD-like envelopes, and the tight coupling between BCG assembly and cluster growth.

With the bulk of stellar mass assembled largely through dry accretion, the subsequent evolution of BCGs is governed less by star formation and more by the regulation of baryons and energy in the cluster core. In particular, the thermodynamic balance between radiative cooling of the ICM and mechanical heating from AGN—and the associated growth of central supermassive black holes that underpin the Magorrian-type scaling relations [Magorrian et al., 1998]—sets the pace of any residual star formation and shapes the observable multiphase gas, X-ray cavities, radio jets, and emission-line diagnostics that we turn to next. Exploring this Mpc scale connection between the central AGN and the properties of the BCG as a whole

is a primary focus of this work. The underlying physical mechanisms and theories are covered in the next section.

1.3 Evolution of a BCG

The evolution of BCGs is intimately linked to the baryon cycle operating in the cores of galaxy clusters, where hot, warm, and cold phases of gas continually exchange mass and energy. In the absence of heating, the hot ICM should cool radiatively, condensing into molecular clouds and fuelling star formation at rates far exceeding those observed—the classical 'cooling-flow problem' [Fabian, 1994]. Instead, energy input from AGN hosted by the BCG offsets much of this cooling, driving jets, bubbles, and shocks that heat the surrounding gas and uplift low-entropy material [Canning et al., 2013, Gaspari and Churazov, 2013a, McNamara and Nulsen, 2007, Voit et al., 2015]. This feedback-regulated cycle allows some gas to precipitate out of the hot phase through thermal instabilities, forming dusty, cold filaments that can be ionised and, occasionally, converted into new stars, while the remainder may be reaccreted onto the black hole in a process of 'chaotic cold accretion' [Gaspari et al., 2018]. Over cosmic time, this interplay between cooling, precipitation, feedback, and star formation governs the gas content, star-formation activity, and structural evolution of the BCG, coupling its fate to the thermodynamic state of the cluster core.

1.3.1 The Classical Cooling-Flow Problem

In the cores of relaxed, X-ray luminous clusters, the ICM has short radiative cooling times, sometimes $\lesssim 10^8$–10^9 yr within the central $\sim$ 10–50 kpc [Fabian, 1994, Peterson and Fabian, 2006]. Classical cooling-flow models predicted prodigious mass-deposition rates ($\dot{M} \sim$ 100–1000 $M_\odot$ yr^{-1}) and correspondingly high star-formation rates (SFRs) in BCGs [Fabian, 1994]. High-resolution X-ray spectroscopy (e.g. XMM-Newton/RGS) revealed a deficit of gas cooling below $\sim \frac{1}{3}$ of the virial temperature, dramatically smaller than classical expectations [Peterson and Fabian, 2006]. At the same time, multiwavelength observations showed that BCGs in cool-

core clusters do host some star formation and cold gas, but at levels far below the classical $\dot{M}$, implying that a heating process offsets most radiative losses while permitting residual cooling [Edge, 2001, McDonald et al., 2012a, 2019, O'Dea et al., 2008, Salomé and Combes, 2003]. Empirically, line-emitting and star-forming BCGs are confined to systems with central entropy $K_0 \lesssim 30$ keV cm^2 and $t_{\rm cool} \lesssim 1$ Gyr, the so-called entropy/cooling-time thresholds [Cavagnolo et al., 2008, 2009, Rafferty et al., 2006, Voit et al., 2015].

1.3.2 Feedback-Regulated Cooling: Precipitation and Thermal Instability

The picture that forms is a self-regulated feedback loop in which instabilities in the ICM cause condensation out of the hot phase when the local ratio of cooling to free-fall times, $t_{\rm cool}/t_{\rm ff}$, falls below a critical range $\sim$ 10–20; condensed clouds feed the SMBH, powering AGN outflows that reheat the core and raise $t_{\rm cool}/t_{\rm ff}$ back above threshold [Li and Bryan, 2014, McCourt et al., 2012, Sharma et al., 2012, Voit et al., 2015]. The cooling time is the characteristic timescale for the gas to radiatively lose its thermal energy,

$$t_{\rm cool} \equiv \frac{\frac{3}{2} n k_{\rm B} T}{n_{\rm e} n_{\rm i} \Lambda(T, Z)}, \tag{1.2}$$

where n is the total particle number density, $n_{\rm e}$ and $n_{\rm i}$ are the electron and ion densities respectively, T is the gas temperature, $k_{\rm B}$ is Boltzmann's constant, and $\Lambda(T, Z)$ is the cooling function for gas of temperature T and metallicity Z. The free-fall time is the timescale for a parcel of gas to collapse under gravity in the absence of pressure support,

$$t_{\rm ff} \equiv \sqrt{\frac{2r}{g(r)}} = \sqrt{\frac{2r^3}{GM(<r)}}, \tag{1.3}$$

where r is the radial distance from the cluster centre, $g(r)$ is the local gravitational acceleration, $M(<r)$ is the enclosed mass within radius r, and G is the gravitational constant. Physically, $t_{\rm cool}$ quantifies how quickly the gas can lose energy, while $t_{\rm ff}$ describes how rapidly it would fall inward if unsupported; their ratio indi-

cates whether cooling is fast enough to overcome gravitational stability and trigger multiphase condensation. The empirically determined threshold of $t_{\rm cool}/t_{\rm ff} \sim 10$–$20$ arises from both simulations and X-ray/optical observations of cluster cores, and reflects the balance point where thermal instabilities can grow before being suppressed by buoyancy or turbulent mixing [Voit, 2018]. X-ray images reveal mechanical heating via radio bubbles, cavities, weak shocks and sound waves, with cavity enthalpies and jet powers sufficient on average to offset cooling [Blanton et al., 2011, Fabian, 2012, Forman et al., 2007, McNamara and Nulsen, 2007, McNamara et al., 2004]. Systems with the shortest cooling times and strongest cavity power show the richest multiphase media (molecular, neutral, and ionised gas), consistent with ongoing condensation [McNamara et al., 2014, Rose et al., 2019, Russell et al., 2019, Werner et al., 2014].

1.3.3 Filamentary Structures

Filamentary structures in the ionised gas of BCGs exhibit striking morphologies, with high-resolution narrowband imaging revealing thin, elongated filaments extending tens of kiloparsecs from the galaxy centre [Crawford et al., 2005, Fabian et al., 2003]. These features are often associated with the activity of AGN in the form of buoyant bubbles, which are believed to entrain cooler gas and lift it from the central regions [Churazov et al., 2001, Ruszkowski et al., 2007]. Observations indicate that the filaments display complex kinematics and signs of turbulent motion, suggesting that they are both dynamic and transient in nature [Mathews and Brighenti, 2008, Revaz et al., 2007].

The persistence of these filaments in the hot ICM poses a theoretical challenge, as they should rapidly evaporate without some form of stabilisation. Magnetic fields are thought to play a critical role in this context by suppressing thermal conduction and thereby preventing the evaporation of the cool gas [Fabian et al., 2001]. Even relatively modest magnetic field strengths can significantly reduce the effective conductivity, allowing these structures to persist for timescales that exceed the local cooling time of the surrounding gas [Nipoti and Binney, 2004]. In addition, the geometry of the magnetic field may further influence the morphology of the filaments;

aligned magnetic fields can channel the gas into narrow, coherent strands, while more tangled fields might lead to broader and more diffuse structures [Carilli and Taylor, 2002, Govoni et al., 2004]. High-resolution Hubble Space Telescope (HST) imaging of Perseus filaments by Fabian et al. [Fabian et al., 2008] reveals remarkably fine substructure—knotted strands and braided threads—that underscores the interplay between magnetic tension and thermal instability.

The filaments also offer insights into the interplay between cooling flows and AGN feedback in cluster cores. While the intracluster gas in cool-core clusters would otherwise be expected to cool and condense at high rates, the uplift of gas by AGN activity appears to provide a counteracting mechanism, redistributing the cool gas and possibly triggering localised star formation [Edge, 2001, Fabian, 2012, McNamara et al., 2004, O'Dea et al., 2008]. Furthermore, the mechanical energy injected by the AGN, as traced by the filaments, contributes to the overall thermal balance of the cluster core and affects the mixing and transport of metals within the ICM [Brüggen and Scannapieco, 2010, Fabian, 2012, McNamara and Nulsen, 2007]. Recent observations with the Atacama Large Millimetre Array (ALMA) have further advanced our understanding by detecting cold molecular gas traced by CO emission co-spatial with the optical filaments, reservoir masses of 10^9–$10^{10}\,M_\odot$ uplifted alongside the ionised gas [Russell et al., 2019]. The ALMA data show that this CO-emitting gas forms kinematically coherent structures aligned with the buoyant radio bubbles, highlighting the multimodal nature of AGN-driven uplift and its dual role in fuelling both star formation and SMBH accretion [Tremblay et al., 2018].

1.3.4 Chaotic Cold Accretion (CCA)

Within the precipitation framework, chaotic cold accretion (CCA) provides a dynamical route for fueling the SMBH and sustaining self-regulation [Gaspari and Churazov, 2013a, Gaspari and Sądowski, 2017, Gaspari et al., 2015, 2018]. In CCA, turbulence, uplift and thermal instability promote the condensation of cold clouds and filaments out of the hot ICM. These multiphase structures 'rain' toward the nucleus, undergo frequent inelastic collisions that cancel angular momentum, and

accrete at rates far exceeding the hot Bondi prescription[7]. The ensuing AGN outflows (jets, bubbles) isotropically distribute heat, partly via turbulent mixing and $p\,dV$ work, closing the loop [Gaspari et al., 2015]. Observations support CCA ingredients: extended, filamentary CO and Hα networks correlated with X-ray cavities and radio jets; kpc-scale velocity dispersions comparable to the inferred ICM turbulence; and cold gas uplifted along bubble wakes that later precipitates and rains back [Canning et al., 2012, Fabian et al., 2003, Hamer et al., 2016, McNamara et al., 2014, Rose et al., 2019, Russell et al., 2019, Tremblay et al., 2016a, Werner et al., 2014].

1.3.5 Kinematics of the Ionised Gas

Optical integral-field spectroscopy (IFS) of cool-core BCGs reveals diverse ionised-gas morphologies (filaments, disks, and clumps) and kinematics. Extended Hα filaments often span tens of kpc with modest line-of-sight velocities ($\sim$ 100–300 $\mathrm{km\,s^{-1}}$) and relatively low dispersions, suggestive of gently stirred, pressure-confined structures rather than violently shocked outflows [Hamer et al., 2016, Hatch et al., 2006, McDonald et al., 2012b]. In some BCGs, ordered rotation appears in inner few-kpc disks (likely formed from cooled gas), while outer filaments show signs of uplift along cavity axes and partial infall [Hamer et al., 2016, McDonald et al., 2012b, Olivares et al., 2019]. Multi-phase comparisons show rough kinematic alignment between Hα/[NII] gas and CO, reinforcing a condensation origin for both phases [Edge, 2001, Russell et al., 2019, Salomé and Combes, 2003]. Velocity fields sometimes display shear, twists, or counter-rotating components, seemingly reflecting a mix of uplift, turbulence, cloud–cloud interactions, and weak gravitational torques consistent with CCA [Hamer et al., 2016, Olivares et al., 2019, Tremblay et al., 2016a].

[7] *Bondi accretion* [Bondi, 1952] describes the steady, spherically symmetric inflow of gas onto a compact object from a uniform medium, with the accretion rate depending on the gas density, sound speed, and the mass of the accretor. In contrast, cold chaotic accretion can yield rates orders of magnitude higher due to angular momentum cancellation. The $p\,dV$ term refers to the mechanical work done by expanding AGN-inflated bubbles on the surrounding ICM, where p is the thermal pressure of the ICM and dV is the change in bubble volume. This $p\,dV$ work transfers energy from the bubble to the ICM, contributing to its heating.

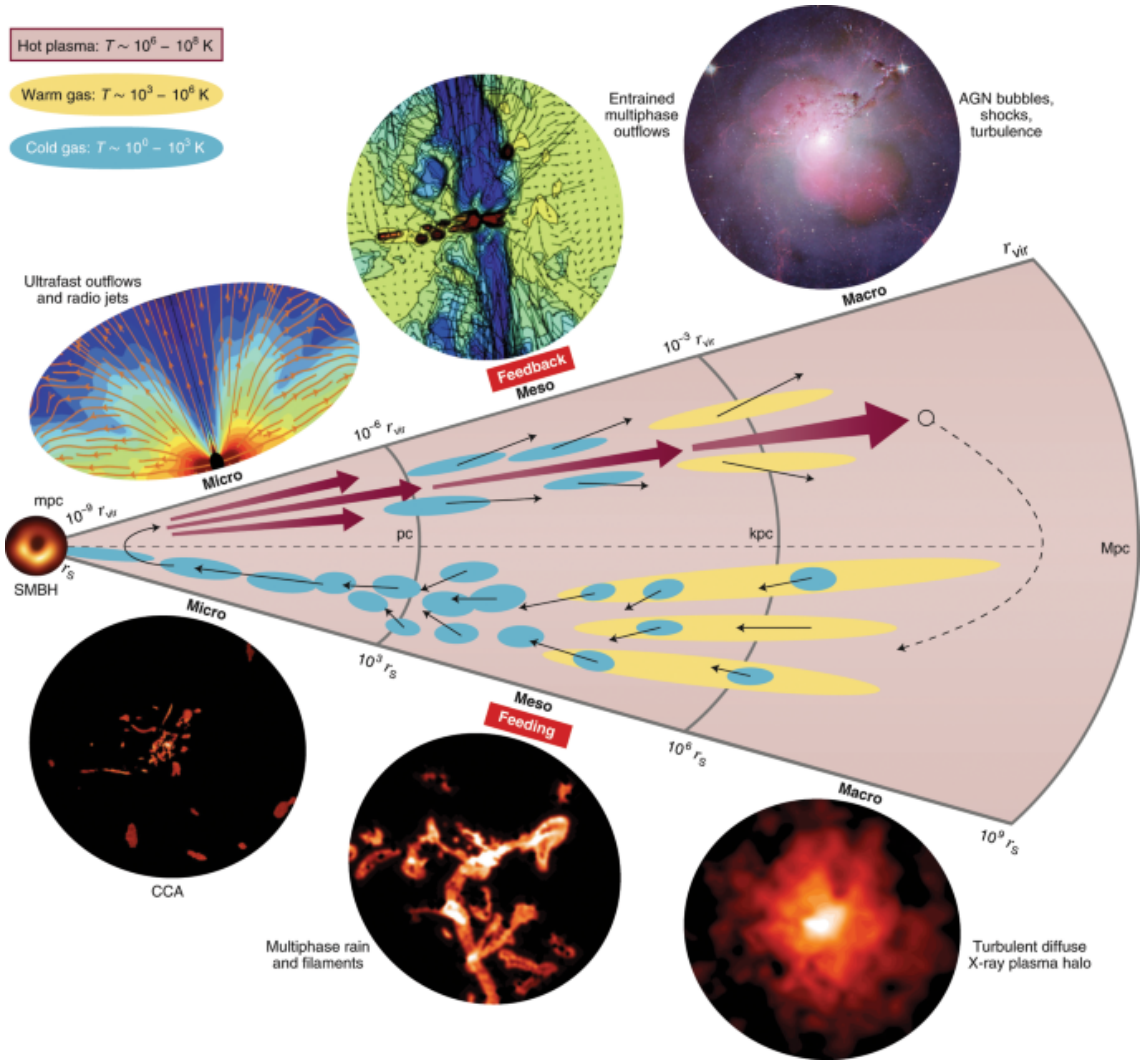

Figure 1.1: This schematic illustrates the interplay between a supermassive black hole and its host galaxy across nine orders of magnitude in spatial scale. The top hemisphere depicts AGN feedback, showing ultrafast outflows and radio jets at the micro-scale (r_s to pc), entrained multiphase outflows at the meso-scale (pc to kpc), and large-scale bubbles and shocks in the macro-environment (kpc to Mpc). The bottom hemisphere illustrates AGN feeding via chaotic cold accretion, where multiphase rain and filaments condense out of the turbulent X-ray halo and precipitate toward the central engine. Colours represent gas temperature phases: hot plasma (10^6–10^8 K; red), warm gas (10^3–10^6 K; yellow), and cold gas (10^0–10^3 K; blue). Figure taken from Gaspari et al. [2020].

1.3.6 Excitation Mechanisms of the Warm Ionised Phase

BCG nebulae show LINER-like (Low-Ionisation Nuclear Emission-line Region) optical line ratios, characterised by elevated [NII]/Hα, [SII]/Hα, and [OI]/Hα. These line ratios place them in distinct regions of the parameter space in certain optical emission-line diagnostic plots (see § 1.4.3 for a full description of BPT diagrams). Such spectra indicate that low-ionisation forbidden lines are unusually strong compared to Balmer recombination lines, a signature typically inconsistent with pure H II-region photoionisation alone and often attributed to a mix of excitation mechanisms including weak AGN activity, shocks, or cooling-flow related processes [Heckman, 1980, McDonald et al., 2012b]. There are multiple potential ionisation sources:

1. **Photoionisation by young stars:** contributes where UV continua and far-IR dust emission indicate ongoing star formation, particularly in extreme systems like Phoenix [McDonald et al., 2012a, O'Dea et al., 2008].

2. **AGN photoionisation:** can dominate in compact nuclear regions but generally under-explains extended filaments [Hatch et al., 2006, McDonald et al., 2012b].

3. **Shocks and turbulent dissipation:** slow shocks ($\sim$ 100–300 $\mathrm{km\,s^{-1}}$) and turbulence can reproduce LINER-like ratios and broadened lines in parts of the filaments [Dopita and Sutherland, 1996, McDonald et al., 2012b].

4. **Particle heating / cosmic-ray and mixing-layer models:** collisional heating by suprathermal particles and turbulent mixing of hot/cold phases reproduce key optical and UV line ratios and the observed correlation with X-ray structures [Begelman and Fabian, 1990, Ferland et al., 2009, Polles et al., 2021, Slavin et al., 1993].

5. **Conduction and magneto-thermal effects:** saturated conduction across hot–cold interfaces can supplement heating locally, though global energy budgets likely require AGN input [Sparks et al., 2009, Voit et al., 2015].

Spatially resolved BPT maps typically reveal composite excitation: star-formation-like ratios near dust lanes or inner disks, and LINER/shock-like ratios along ex-

tended, jet-aligned filaments [Hamer et al., 2016, McDonald et al., 2012b, Werner et al., 2014].

1.3.7 From Cooling to Fuelling: The Cycle

Combining the above it appears that cool-core BCGs appear to follow a precipitation–accretion–feedback cycle. When $t_{\rm cool}/t_{\rm ff}$ dips below $\sim$ 10–20, multiphase gas condenses (molecular + ionised), a fraction migrates inward via CCA to feed the SMBH, and the resulting jets inflate cavities that heat and stir the core, lifting low-entropy gas and promoting further in-situ condensation along bubble rims and wakes [Gaspari et al., 2015, McNamara et al., 2004, Voit et al., 2015, Werner et al., 2014]. This cycle naturally explains the co-spatial alignment of cold filaments with radio/X-ray structures, the modest line widths of extended gas, the entropy/cooling-time thresholds for nebular emission, and the partial (not complete) suppression of star formation [Cavagnolo et al., 2008, McDonald et al., 2012b, Werner et al., 2014].

These processes are inherently multi-phase and multi-scale and therefore demand multiwavelength diagnostics: X-ray (cooling times, cavities, shocks), radio (jets, lobes), millimetre (CO kinematics), and optical/UV IFS (Hα/[NII] velocity fields and BPT line-ratio maps). In the next section, we outline the observational techniques—velocity–dispersion fields, BPT diagnostics, photometric decompositions, and survey strategies—that translate this physical cycle into measurable constraints on BCG evolution.

1.4 Observing BCGs: Techniques and Diagnostics

The emission from BCGs spans the full electromagnetic spectrum, reflecting their inherently multiphase nature and the diverse physical processes operating in cluster cores. In the X-ray, high-resolution imaging and spectroscopy from Chandra and XMM-Newton trace the hot ICM at $T \sim 10^{7-8}\,\mathrm{K}$, mapping thermodynamic quantities such as density, temperature, and entropy, and revealing cavities, shocks, and

cold fronts driven by AGN feedback [Fabian et al., 2003, McNamara and Nulsen, 2007, Werner et al., 2014]. The optical and near-UV capture warm ionised gas at $T \sim 10^4\,\mathrm{K}$ via recombination and forbidden lines, as well as the stellar continuum from both old and young populations. In this regime, IFS provides spatially resolved kinematics and excitation diagnostics [Hamer et al., 2016, Olivares et al., 2022]. Infrared observations from facilities such as Spitzer, Herschel, and JWST reveal thermal emission from dust grains, molecular hydrogen lines, and polycyclic aromatic hydrocarbons (PAHs), probing both star formation and the dusty components of cold filaments [Edge et al., 2010, O'Dea et al., 2008, Rawle et al., 2012]. In the millimetre and sub-millimetre, rotational transitions of CO and other molecules, mapped by ALMA and IRAM, measure the cold molecular reservoirs ($T \sim 10$–$50\,\mathrm{K}$) that dominate the cold gas mass [Edge, 2001, Salomé and Combes, 2003]. At radio wavelengths, continuum emission traces relativistic jets and lobes, which interact with the surrounding medium and often align with the morphology of multiphase filaments [Fabian, 2012]. Together, these complementary windows assemble a coherent view of the gas from hot to cold phases, quantify mass and energy flows, and directly link the feedback processes that regulate BCG and cluster-core evolution.

1.4.1 Optical/UV spectroscopy and integral-field mapping

A modern view of BCG cores is built on optical/UV IFS combined with narrowband imaging. Instruments such as MUSE (VLT) and KCWI (Keck) deliver contiguous 2D maps of emission-line fluxes, radial velocities, and velocity dispersions for Hα, [NII], [SII], and, where available, [OIII] and [OI] [Bacon et al., 2010, 2014, Morrissey et al., 2018]. Data reduction pipelines such as pPXF [Cappellari, 2017] fit multiple Gaussian components to blended doublets (e.g. [NII]$\lambda\lambda 6548, 6583$ with Hα), recover line centroids and widths, and propagate uncertainties. Stellar continua are modelled and subtracted to isolate nebular kinematics and line ratios. These products constrain the dynamical state of the gas — including rotation, uplift, inflow, and turbulence — and, when paired with line-ratio diagnostics (§ 1.4.3), allow a detailed assessment of excitation mechanisms.

1.4.2 Velocity structure function diagnostics

Velocity structure function (VSF) plots, pairing line-of-sight velocity fields with velocity-dispersion maps (σ), separate ordered motions from random motions and reveal how gas couples to AGN feedback and the cluster potential. Rotating disks appear as smooth, bi-lobal velocity gradients with centrally peaked σ that declines with radius, whereas extended filaments display patchy velocities, moderate dispersions ($\sim$50–200 $\mathrm{km\,s^{-1}}$), and kinks aligned with cavity axes [Hamer et al., 2016, McDonald et al., 2012b]. Uplifted gas along radio bubbles often shows coherent velocity streaks with modest σ, transitioning to slow infall at larger radii [Russell et al., 2019, Tremblay et al., 2016a, Werner et al., 2014]. Widespread elevated σ without strong shear suggests turbulent stirring, consistent with chaotic cold accretion [Gaspari et al., 2018, Hamer et al., 2016], while localised σ enhancements at jet–cloud interfaces trace mechanical interaction. Projected velocity reversals across the nucleus, asymmetric σ ridges, and dust lane alignments help distinguish slow inflow from weak outflows, with multi-phase comparisons to CO offering further constraints [Olivares et al., 2019]. VSF profiles such as azimuthally averaged $\sigma(r)$ or $|v|/\sigma$ as a function of radius quantify the balance of ordered and random motions, while kinemetry describes higher-order deviations from circular flows [Krajnović et al., 2006]. Interpretation must account for instrumental resolution, spectral blending, and beam smearing, often via forward modelling with synthetic data cubes [Davies et al., 2011]. The connection between kinematic patterns and excitation mechanisms becomes clear when VSF is analysed alongside spatially resolved line-ratio diagnostics.

1.4.3 Emission-line diagnostics: BPT and beyond

IFS enables spatially resolved optical line-ratio classification using Baldwin–Phillips–Terlevich (BPT) diagrams [Baldwin et al., 1981, Kauffmann et al., 2003, Kewley et al., 2001, 2006], which compare ratios of strong nebular lines to distinguish ionisation mechanisms. The [NII], [SII], and [OI] variants are especially sensitive to low-ionisation emission. BCG nebulae commonly occupy the LINER/LIER region — characterised

by elevated [NII]/Hα, [SII]/Hα, and [OI]/Hα — indicating that low-ionisation forbidden lines are unusually strong relative to Balmer lines. This is inconsistent with pure H II-region photoionisation and instead points to a mixture of excitation processes.

Several channels likely contribute, often co-spatially: young-star photoionisation in rotating inner disks or dusty knots (low σ), dominant in some cooling-flow starbursts [McDonald et al., 2012a, O'Dea et al., 2008]; AGN photoionisation within the central kiloparsec [Hatch et al., 2006, McDonald et al., 2012b]; shocks and shear heating producing elevated [SII]/Hα and [OI]/Hα where VSF shows high dispersion or shear [Allen et al., 2008, Dopita and Sutherland, 1996, Hamer et al., 2016]; turbulent mixing layers at hot–cold interfaces [Begelman and Fabian, 1990, Slavin et al., 1993]; particle or cosmic-ray heating, which can yield strong low-ionisation lines and excite H_2 emission [Ferland et al., 2009, Polles et al., 2021]; and localised heating from thermal conduction or magneto-thermal instabilities [Sparks et al., 2009, Voit et al., 2015]. Combining BPT maps with VSF kinematics links dynamical state to excitation channel: low-σ H II-like regions co-located with UV knots trace star formation, high-σ ridges aligned with cavities favour shocks or mixing, and extended LINER-like regions with weak shear are consistent with particle heating [Hamer et al., 2016, McDonald et al., 2012b, Werner et al., 2014].

1.4.4 Multiwavelength connection

A complete view emerges when ionised-gas diagnostics are connected to other phases. In the X-ray, cavity locations, shocks, and thermodynamic maps show where filaments condense and how jets impart work [Blanton et al., 2011, Forman et al., 2007, McNamara et al., 2004]. At millimetre wavelengths, CO velocity fields and dispersions often mirror ionised-gas kinematics, revealing rotating molecular disks plus radially extended filaments [Edge, 2001, Olivares et al., 2019, Salomé and Combes, 2003]. Radio jets and lobes are frequently co-aligned with ionised and molecular filaments, with spectral age gradients relating to cavity power and stirring history [Fabian, 2012, Russell et al., 2019]. Infrared and UV data provide star formation rates and dust geometry, helping to interpret H II-like regions in BPT maps; UV

knots often coincide with low-σ pockets in rotating disks [Kennicutt and Evans, 2012, O'Dea et al., 2008].

1.4.5 Surveys and data resources

Large homogeneous datasets enable population studies, from SDSS fibre spectroscopy to HSC/DES photometry of extended halos. MUSE GTO programs have targeted cool cores, ALMA has mapped CO in representative BCGs, and catalogues compile X-ray cavity powers and cooling times [Cavagnolo et al., 2008, McDonald et al., 2019, Russell et al., 2019]. For individual case studies, deep MUSE+ALMA+Chandra observations of systems such as Perseus, Abell 1795, and Hydra A provide benchmarks [Fabian et al., 2003, McDonald et al., 2012b]. VSF analysis, when combined with the line-ratio framework of § 1.4.3 and multiwavelength context, offers a powerful route to quantifying the cooling, precipitation, and feedback processes that regulate BCG evolution.

1.5 Known Unknowns

When reviewing what we do know with reference to the current body of literature, it is easy to give the impression that the field is understood in its entirety. This is far from the truth. While decades of observations and modelling have clarified many aspects of BCGs and their role in the baryon cycle, fundamental questions remain unanswered.

This thesis aims to address several of these open issues by exploiting the statistical power and spatially resolved detail afforded by the Kaleidoscope survey, the largest homogeneous sample of X-ray–selected BCGs observed with MUSE. Such a survey is uniquely positioned to disentangle the links between the thermodynamic state of the ICM, the behaviour of multiphase gas, and the impact of feedback.

We first establish the incidence of optical line emission among X-ray–selected BCGs (Chapter 3), quantifying the fraction of systems that host extended warm ionised gas. This census constrains the prevalence of residual cooling and distinguishes BCGs that are actively engaged in baryon cycling from those that are qui-

escent.

In Chapter 4, we construct a new morphological catalogue of ionised-gas structures, examining the spatial correspondence between Hα emission, X-ray peaks, and stellar continua. These comparisons probe the dynamical coupling between the cold, hot, and stellar components, clarifying whether gas condensation proceeds in situ or is displaced by dynamical disturbances.

The question of whether gas and stars share a common dynamical history is then explored in Chapter 5, where we test for coupling between their kinematics and discover a persistent velocity offsets between phases. Chapter 6 extends this by employing velocity structure functions to characterise turbulence and energy-injection scales, placing constraints on whether the observed gas motions are compatible with chaotic cold accretion or shaped primarily by other feedback mechanisms.

In Chapter 7, we turn to the excitation mechanisms of the ionised gas, using BPT diagnostics and related line ratios to disentangle the relative roles of star formation, AGN photoionisation, and shocks. This analysis addresses how the intracluster environment regulates ionisation and explores the connection to cluster thermodynamic state. The same data provide constraints on gas attenuation, from which the dust content in BCG cores can be inferred.

Finally, in Chapter 8, we investigate the stellar populations of BCGs, probing whether signatures of recent star formation are imprinted on their composite spectra and how these populations compare across systems with and without line-emitting gas.

CHAPTER 2

Sample Selection and Reduction

This chapter covers the observational data and analysis procedures. We begin in § 2.1 with a summary of the various instrument types used. § 2.2 presents the scope and selection methodology of the Kaleidoscope Survey, the main dataset for our study. The pipeline developed for the processing and analysis of the data is detailed in § 2.3. Finally, the various archival datasets used to supplement our observations are outlined in § 2.4.

2.1 Instrumentation

The centres of galaxy clusters are information dense environments. The ideal instrument to explore this would have: a large field of view (FOV) to observe the most extended filaments, high angular resolution to resolve to complex morphologies and a high spectral resolution to reconstruct the kinematics. These criteria are, to varying extents, satisfied by Integral Field Units (IFUs).

2.1.1 Integral Field Units

IFUs enable simultaneous spatial and spectral observations resulting in a three-dimensional data cube - two spatial dimensions plus one spectral dimension - in a single exposure. This is achieved by subdividing the telescope's field of view into many small spatial elements, commonly known as spaxels. Each spaxel's light is dispersed into its spectrum and recorded, producing a data cube where every pixel contains complete spectral information. There are several ways this can be achieved including lenslet arrays (small lenses sample the focal plane, each feeding light into a spectrograph), fibre bundles (optical fibres transmit light from different positions in the field to the spectrograph) and image slicers (the field is optically sliced into strips, which are then rearranged along the entrance slit of the spectrograph).

VIMOS

Table 2.1: Instrument and Observational Properties of VIMOS (VLT, IFU Mode)

Parameter	**VIMOS (IFU Mode)**
Telescope	VLT UT3 (8.2 m, Melipal), Paranal, Chile (24°S)
Field of View	$27'' \times 27''$ (high spatial resolution)
Spatial Sampling	$0.67''$ per spatial element
Typical Seeing	$0.6''$ to $1.0''$
Spectral Resolution	$R \sim 200$–2500 (depending on grism)
Wavelength Coverage	370–1000 nm (with multiple grisms)
Physical Resolution at $z = 0.3$	~ 11 kpc
Sky Visibility	Optimal for $\delta < +20°$

The Visible Multi-Object Spectrograph (VIMOS) was a versatile optical instrument mounted on Unit Telescope 3 (Melipal) of the Very Large Telescope (VLT) at Paranal Observatory, operational from 2003 to 2018 [Le Fèvre et al., 2003]. Designed for both multi-object spectroscopy and integral field spectroscopy (IFS), VIMOS consisted of four identical optical channels, each equipped with its own CCD, enabling simultaneous coverage of a large field of view. In its integral field unit (IFU) mode, VIMOS could obtain contiguous spatially resolved spectra over a moderate field, making it well-suited to studies of nearby galaxies, galaxy clusters, and extended emission-line regions.

Although not used for the observations presented here, this instrument was employed in the more directly comparable work of Hamer et al. [2016], against which we will benchmark many of the results presented.

MUSE

Table 2.2: Instrument and Observational Properties of MUSE (VLT)

Parameter	**MUSE (Wide Field Mode)**
Telescope	VLT UT4 (8.2 m, Yepun), Paranal, Chile (24°S)
Field of View	$60'' \times 60''$
Spatial Sampling	$0.2''$ per pixel
Typical Seeing	$0.6''$ to $1.0''$
Spectral Resolution	$R \sim 3000$
Wavelength Coverage	465–930 nm
Physical Resolution at $z = 0.3$	~ 4.4 kpc (e.g. Kaleidoscope survey)
Sky Visibility	Optimal for $\delta < +20°$

The Multi Unit Spectroscopic Explorer (MUSE) is one of the most advanced IFU instruments currently available. Installed on Unit Telescope 4 (Yepun) of the European Southern Observatory's (ESO's) 8.2-m Very Large Telescope (VLT), MUSE combines a wide $1' \times 1'$ field of view with a fine spatial sampling of $0.2''$ per pixel and broad wavelength coverage from $\sim$ 4800Å to 9300Å. This performance is achieved through a modular design comprising 24 individual integral field units, each using an image slicer to partition the field for spectral dispersion.

The spectral range of MUSE is particularly well suited for studies of BCGs, as it enables detection of prominent diagnostic lines such as Hα (rest-frame 656.3,nm) and [O II]$\lambda\lambda 3726, 3729$,Å over a wide redshift interval. At least one of these lines remains accessible in the range $0 < z \lesssim 1.5$, covering all objects in our sample. At higher redshifts, Lyα becomes visible in the MUSE bandpass for $z \gtrsim 3$.

Since Period 101[1], MUSE has offered a Wide Field Mode with ground-layer adaptive optics (WFM-AO) using the GALACSI module of the VLT Adaptive Optics

[1]ESO observing periods are labelled sequentially. Period 101 covered April 1, 2018 to September 30, 2018. Until 2025, observing periods have typically been six months in duration, but beginning in 2026 ESO will move to year-long observing periods.

Facility (AOF), delivering AO correction over the full $1' \times 1'$ field with $0.2''$ sampling. Beginning with Period 103, MUSE has also provided a Narrow Field Mode (NFM) with laser-tomography adaptive optics (LTAO), giving a $7.5'' \times 7.5''$ field of view and a finer spatial sampling of $0.025''$ per pixel. All observations in our sample were conducted in Wide Field Mode in order to capture the full extent of the ionised gas.

The Differential Image Motion Monitor (DIMM) seeing for an observation with MUSE is a quantitative measure of the atmospheric turbulence, expressed as a full width at half maximum (FWHM) in arcseconds, during the data acquisition. It is measured by a separate, dedicated monitor that continuously characterises the site's optical seeing. The DIMM instrument operates by using a small telescope with a two-aperture mask placed over its entrance pupil. When observing a single bright star, this mask creates two distinct images on a detector. As the star's light passes through turbulent atmospheric cells, the wavefront becomes distorted, causing the two stellar images to move randomly and independently. The DIMM precisely measures the variance of the differential motion between these two images, both parallel and perpendicular to the aperture separation axis. This differential technique cancels out local errors such as telescope vibrations or tracking drift, isolating only the motion caused by the atmosphere. This measured variance is then used to directly calculate the Fried parameter, r_0, which is the characteristic coherence length of the atmospheric turbulence. The seeing FWHM, ϵ_{FWHM}, is then derived from the Fried parameter using the relation $\epsilon_{\mathrm{FWHM}} \approx 0.98\lambda/r_0$, where λ is the wavelength of light, typically standardised to 500 nm for comparison. Physically the DIMM seeing represents the effective angular diameter of a stellar point source after being blurred by atmospheric turbulence. Any intrinsic celestial features or separations with an angular size smaller than this value are smeared out by the atmosphere, and their observed size becomes dominated by this seeing disk. Therefore, this seeing value ϵ_{FWHM} directly sets the practical limit for the minimal resolvable scale of an observation, as any two features separated by a smaller angle will be blended and individually unresolved. There is dedicated and powerful MUSE Python Data Analysis Framework (MPDAF) [Bacon et al., 2016]. This package is specifically designed to handle the data-cubes produced by the instrument, providing a com-

prehensive suite of tools for visualisation, manipulation, and analysis of the data. It contains built-in methods for source detection, such as the emission-line finding algorithm MUSELET [Herenz et al., 2017], which enables the creation of extensive line emitter catalogues directly from the reduced data.

2.1.2 X-Ray Telescopes

The space between galaxies in a cluster is filled with a hot, diffuse ICM (§ 1.1.4). With temperatures of $10^7 - 10^8$ K, the ICM radiates primarily via thermal Bremsstrahlung, with its emission peaking in the X-ray band.

The Earth's atmosphere is opaque to X-ray photons at energies $\gtrsim 0.1\,\mathrm{keV}$ so observations of the hot ICM must be carried out from space-based platforms. As X-rays cannot be efficiently refracted or reflected at normal incidence, X-ray telescopes require specialised grazing-incidence optics to achieve imaging capability. In such designs, incoming photons strike the mirror surfaces at very shallow angles (typically $< 1°$), where the reflectivity of high-Z materials such as gold, iridium, or nickel remains high. The most widely adopted configuration is the Wolter type I geometry [Wolter, 1952], which uses nested coaxial shells with a paraboloidal primary mirror segment followed by a hyperboloidal secondary. This arrangement brings the converging rays to a common focus while minimising aberrations over a modest field of view. The use of multiple concentric shells maximises the effective collecting area, essential for detecting the low surface-brightness X-ray emission from the diffuse ICM. Such optical assemblies are employed in major X-ray observatories, including Chandra, enabling spatially resolved spectroscopy of hot cluster gas at sub-arcsecond to arcsecond resolution.

The Chandra X-ray Observatory

Launched by NASA in 1999, the Chandra X-ray Observatory [Weisskopf et al., 2002] is one of the flagship missions of modern astrophysics. It has a resolution of $\sim$0.5 arcseconds and remains the highest resolution instrument of its type enabling the detailed study of structures like AGN jets, supernova remnants, and the complex 'cold fronts' and shock waves within the ICM of galaxy clusters.

The observatory operates in a highly elliptical orbit that takes it far above the Earth's radiation belts, enabling long, uninterrupted observations of celestial targets. Its primary instrument is the Advanced CCD Imaging Spectrometer [ACIS; Garmire et al., 2003], which provides both high-resolution imaging and spatially-resolved spectroscopy over a broad energy range. This dual capability allows us to not only to see the structure of the hot gas but also to measure its temperature and elemental composition.

Table 2.3: Key Properties of the Chandra X-ray Observatory.

Property	**Value / Description**
Launch Date	July 23, 1999
Orbit	Highly Elliptical (16,000 km × 139,000 km)
Angular Resolution	∼0.5 arcseconds (on-axis)
Energy Range	0.2 – 10.0 keV
Primary Instrument	ACIS (Advanced CCD Imaging Spectrometer)
Optics	High-Resolution Mirror Assembly (HRMA)

The analysis of Chandra data is supported by the dedicated software package Chandra Interactive Analysis of Observations [CIAO; Fruscione et al., 2006]. CIAO provides a comprehensive environment for all stages of processing, from initial reduction and calibration with the Chandra Calibration Database (CALDB) through to the production of final scientific outputs.

2.2 Kaleidoscope Sample

2.2.1 Sample Selection

MUSE, for the reasons described in § 2.1.1, is one of the most popular ESO astronomical instruments with an over-subscription factor averaging close to ten in the the period 2020-2025. The Kaleidoscope Survey (PI: A. Edge) was proposed as a filler survey comprising a large and flexible target list making use of sub-optimal seeing conditions or transparency.

Time was awarded to observe X-ray selected clusters from the ROSAT All-Sky Survey [Voges et al., 1999] in ESO observation periods P100, P102, P103, P104,

P109, P111, P113 and P114. The primary sample during the first three periods focused on the MACS [2] sample ($z > 0.3$) with $L_x > 4.5 \times 10^{44}$ erg/s, which has extensive follow-up observations, including HST Snapshot coverage in up to four bands, Chandra/XMM-Newton data, and complementary radio, FIR, and MIR observations [Ebeling et al., 2001]. Beginning with P104 the selection criteria were extended to include $0.15 < z < 0.3$ and $L_x > 3 \times 10^{44}$ erg/s, greatly expanding the volume from which clusters were selected.

Constraint	**Value**
Declination	$< +31°$
Galactic Latitude ($\|b\|$)	$> 20°$
X-ray Flux (f_x)	$> 10^{-12}$ erg cm^{-2}s^{-1} (0.1 − 2.4 keV)
X-ray Luminosity (L_x)	$> 3 \times 10^{44}$ erg s^{-1} (0.1 − 2.4 keV)

Table 2.4: Constraints on the Kaleidoscope Survey. No consideration is given to the properties of the BCG.

2.2.2 Observation

The MUSE instrument on VLT's UT4 was used for all observations in the sample. The IFU has a field of view of 60"×60" enabling the entire line emitting region to be mapped in even the most extended systems. As of today, in excess of 220 MUSE observations have been collected for the project, this is supplemented additional data from other archival MUSE projects. The sky positions of these objects are shown in Fig. 2.1

The formal constraints, summarised in Table 2.4, on the selection are as follows: the declination (Dec) must be less than +31°, the galactic latitude ($|b|$) must be greater than 20°, the X-ray flux (f_x) must be $f_x > 10^{-12}$ erg cm^{-2} s^{-1} (0.1-2.4 keV), and the X-ray luminosity (L_x) must be $L_x > 3 \times 10^{44}$ erg s^{-1} (0.1-2.4 keV). No other consideration is given to the properties of the BCG. The observation generally is centred on the BCG though was shifted if doing so enabled additional objects of interest to be captured in the window. These included gravitationally lensed arcs

[2] The MAssive Cluster Survey (MACS) was specifically designed to find the most X-ray luminous, and therefore most massive, galaxy clusters at redshifts $z > 0.3$.

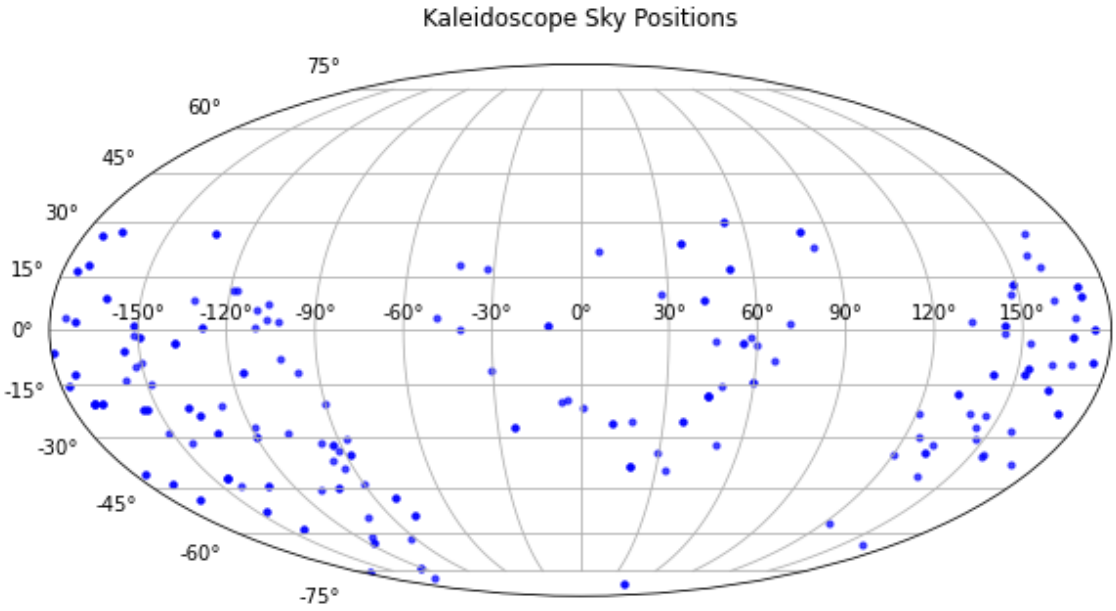

Figure 2.1: Distribution of sky positions for all observations in the Kaleidoscope sample.

and 'jellyfish' cluster members.

Objects were allocated one hour observation blocks (OBs) which, accounting for overheads, meant approximately 45 min exposure per target. Objects which satisfied the Kaleidoscope selection criteria and had already been observed via Guaranteed Time Observing (GTO) programs were taken directly from the ESO archive. GTO refers to the MUSE consortium's large-scale, long-term observational projects. The complete list of objects and observing parameters are listed in their entirety in Appendix A.

A summary plot of all spectra extracted for the central $1'' \times 1''$ region across the Kaleidoscope survey is shown in Fig. 2.2. The vertical axis encodes redshift, so rest-frame features migrate upward as z increases: any emission line with rest wavelength λ_0 follows $x = \lambda_0(1+z)$ horizontally, while the vertical offset records z. Coherent diagonal ridges—where many spectra show peaks aligned with a dashed track—thus identify prominent transitions across the sample. Key emission lines [O II] $\lambda\lambda 3726, 3729$, H$\beta$, [O III] $\lambda 5007$, and Hα are marked in red. Sky features appear as vertical overdensities, most notably the strong telluric O_2 A-band at $\sim$7600Å, which can overlap with redshifted astrophysical lines (e.g. Hα at $z \approx 0.16$, [O III] at $z \approx 0.52$). Features falling in or near this band are susceptible to

continuum depressions and subtraction residuals. These features can be modelled during reduction but their effects cannot be entirely eliminated (§ 2.3.1).

In Fig. 2.3 we show the rest–frame spectral heat map for the Kaleidoscope survey. Each horizontal strip corresponds to one BCG (sorted by redshift from bottom to top) and shows the central $1'' \times 1''$ aperture–averaged spectrum, rebinned into equal–width wavelength bins; colours encode the mean normalised flux in each bin. Because the observed MUSE bandpass is fixed, shifting to the rest frame ($\lambda_{\rm rest} = \lambda_{\rm obs}/(1+z)$) produces the sloping envelope that limits the accessible wavelength range at higher redshift. Dashed vertical guides mark the principal diagnostic features—[O II] $\lambda\lambda 3726, 3729$ and Hα $\lambda 6563$. This visual summary highlights the prevalence and diversity of emission across the sample and provides a basis for selecting the emission–line subsample for subsequent analysis of gas kinematics and excitation via the two lines highlighted.

2.3 Data Reduction

2.3.1 Cleaning and Sky Subtraction

Before carrying out any scientific analysis, the raw MUSE datacubes must be carefully cleaned to mitigate residual artefacts introduced by the atmosphere and the instrument. As illustrated in the preceding figures, strong sky emission features and telluric absorption bands (such as the O_2 A-band around 7600,Å) imprint vertical structures in the stacked spectra and can overlap with astrophysical lines of interest. In addition, continuum depressions and imperfect sky subtraction can leave residuals that vary with wavelength and position in the field. This is essential to ensure that the emission-line diagnostics discussed in subsequent sections reflect the intrinsic properties of the galaxies rather than artefacts of the observing conditions. The raw MUSE datacubes were all cleaned via a pipeline created by David Lagatutta. An outline of the process is provided here with a more complete description detailed in Section 2.22 of Lagattuta et al. [2022]

The general reduction procedure begins with the application of calibration frames to characterise and correct for systematic effects. This includes bias and flat–field

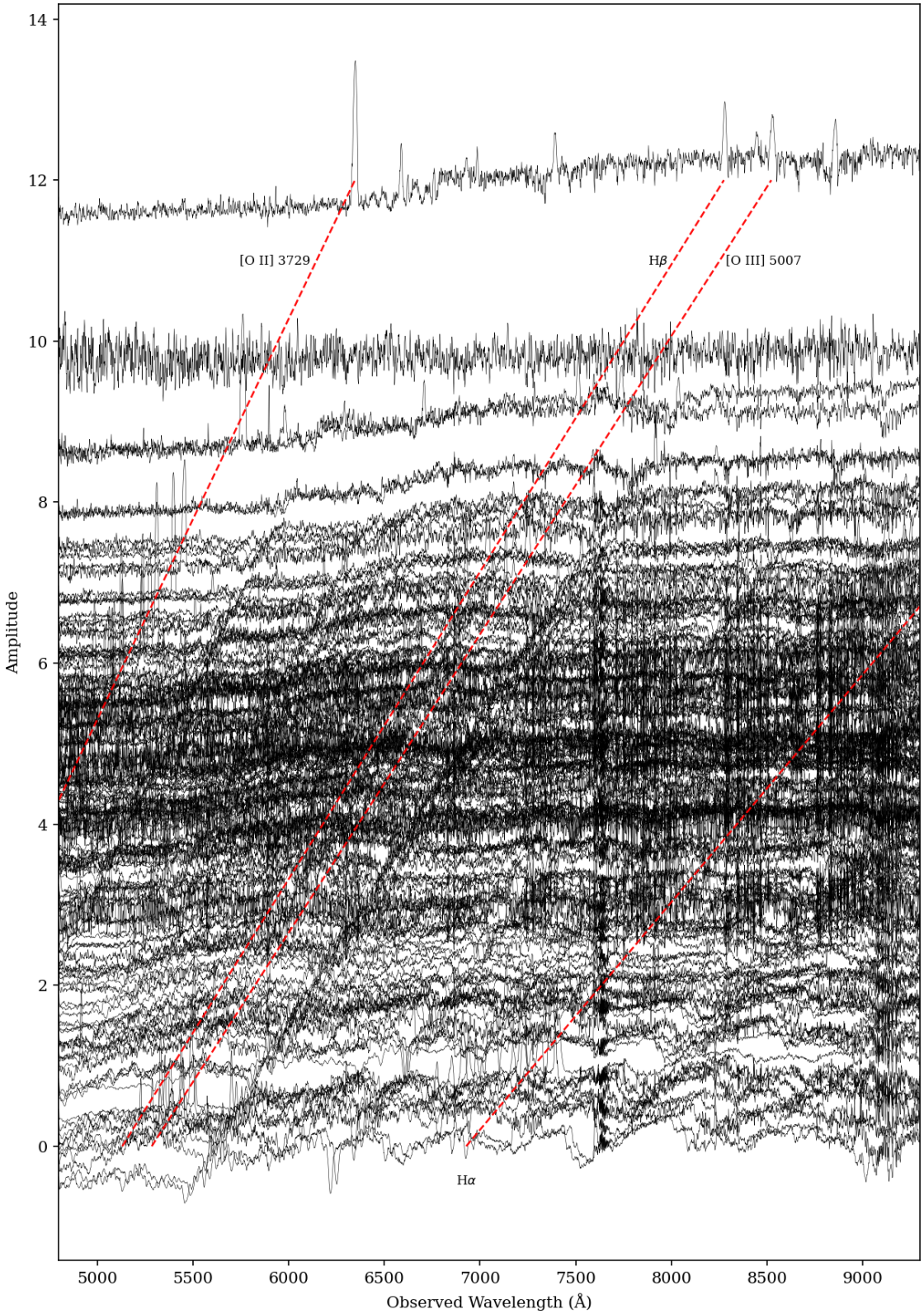

Figure 2.2: Stacked 1D spectra (black) are vertically offset in proportion to redshift. Red dashed curves explicitly label the loci $\lambda_{\rm obs} = \lambda_0(1+z)$ traced by the emission lines: [O II] $\lambda\lambda 3726, 3729$, H$\beta$, [O III] $\lambda 5007$, and Hα. Non-astrophysical features, for example the $\sim$7590–7690 Å telluric O_2 A-band, appear as vertical features.

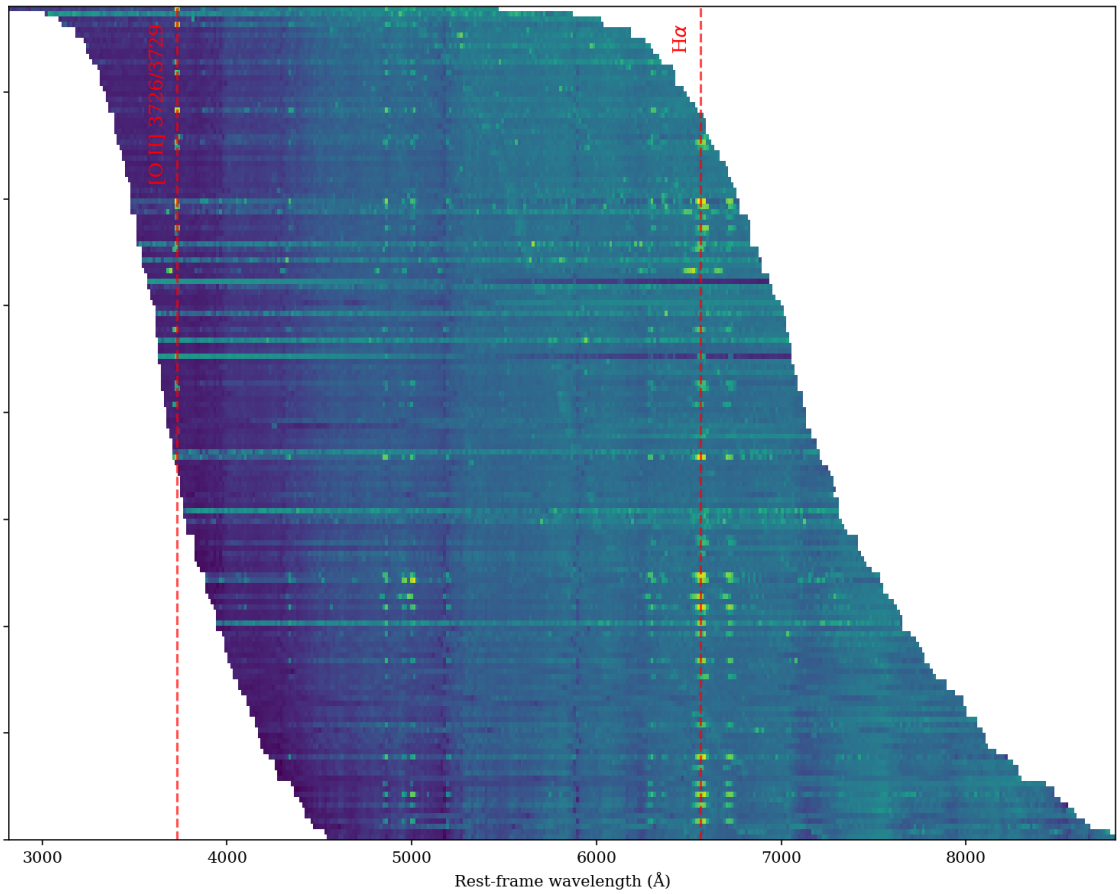

Figure 2.3: Rest-frame spectral heat map for the Kaleidoscope survey. Each horizontal strip shows the central $1'' \times 1''$ aperture-averaged spectrum of one BCG, sorted by redshift (from 0.06 at the bottom to 0.7 at the top). Colours encode the mean normalised flux in equal-width wavelength bins; the curved envelope reflects varying rest-frame coverage from the fixed MUSE bandpass. Dashed vertical lines indicate [O II] $\lambda\lambda 3726, 3729$ and Hα $\lambda 6563$

corrections, determination of the wavelength solution and line–spread function, creation of illumination corrections, and tracing of the detector geometry. The data are then reformatted into non–interpolated pixel tables, which are computationally efficient to process. In this form, they are flux–calibrated using standard–star observations, corrected for telluric absorption and atmospheric dispersion, transformed into the barycentric reference frame, and cleaned of any instrument–specific artefacts.

Astrometric alignment is achieved by cross–matching the spectroscopic data with high–resolution imaging that has been resampled to match the spatial scale and point–spread function of the IFU observations. This step also serves as a secondary flux–calibration check by comparing the spectroscopic and photometric fluxes in overlapping broadband filters. Following calibration, the pixel tables are reconstructed into data cubes, incorporating self–calibration stages to remove residual flat–field structures and using customised masks to prevent bright sources from contaminating the background estimation.

Individual exposures are then scaled according to their flux–normalisation factors and combined into master data cubes using a resampling scheme that also rejects cosmic rays. These master cubes, containing both the reduced data and associated variances, are further cleaned with sky–residual suppression techniques applied consistently with the masking used in earlier steps.

2.3.2 Pipeline

The methodology and logic of the scientific analysis broadly follows that of Hamer et al. [2016], who used optical integral-field spectroscopy with VIMOS to map the morphology, kinematics, and ionisation structure of extended ionised gas in BCGs within optically selected clusters, with the aim of linking nebular properties to AGN feedback and thermodynamics of the ICM. His work emphasised the use of spatially resolved velocity–σ fields and emission-line diagnostics to distinguish between ordered rotation, filamentary inflows, and AGN-driven outflows, as well as to identify likely excitation mechanisms (e.g. star formation, shocks, particle heating). In the present study, we adopt a similar analytical framework but adapt it for the ca-

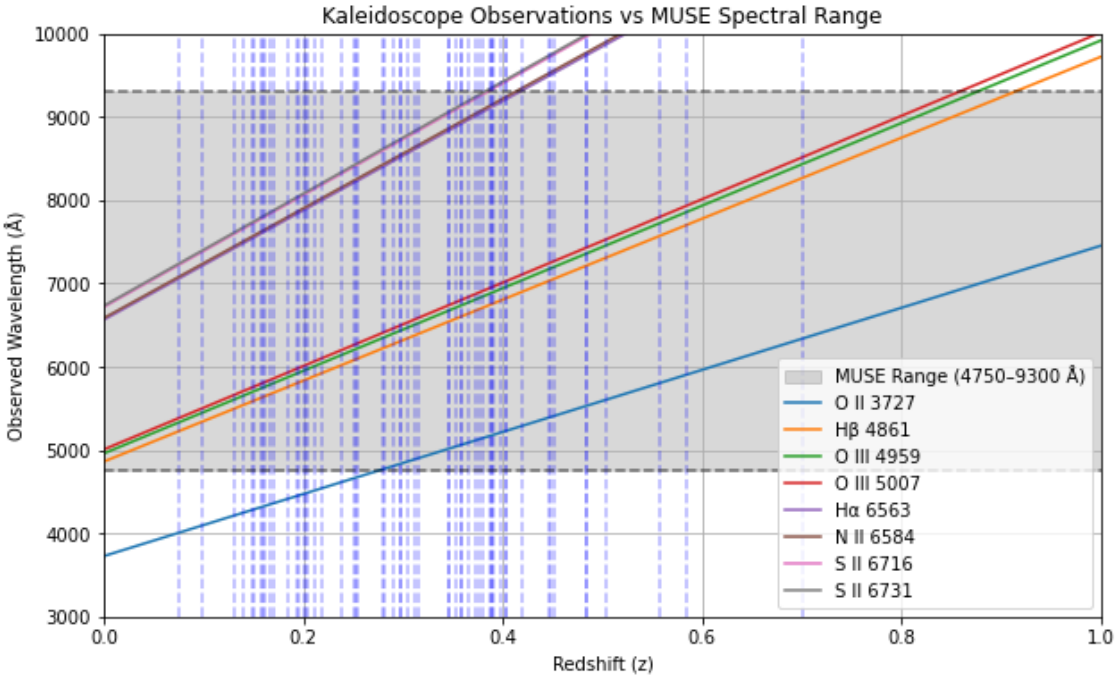

Figure 2.4: Here we show the visibility of lines at across different redshift for the MUSE spectral range. The dashed blue lines show observations in the Kaleidoscope survey, the grey region shows the MUSE spectral range and the coloured lines a sample of the lines of interest.

pabilities of modern integral-field spectrographs and improved reduction pipelines, capitalising on advances in both software and hardware over the past decade.

Stellar Fit

The cleaned MUSE cubes were reduced spatially to a region of 100×100 pixels ($20'' \times 20''$) centred on the BCG. This field of view was chosen because it encompassed the full spatial extent of the ionised gas filaments associated with the BCG, ensuring that all relevant emission-line structures were captured in the analysis. Expanding the field of view beyond this region generally added no additional emission but did increase the volume of data to process, extending computation times unnecessarily. Minor adjustments to the extraction region were made in cases where the BCG lay near the edge of the original MUSE pointing or where the ionised gas was unusually extended and asymmetric. The full spectral range (4800–9300 Å) was preserved for all subcubes to retain coverage of the principal diagnostic emission lines.

The nearest and brightest objects had sufficient signal-to-noise (SNR) to perform

a pixel-wise fit of the stellar continuum. However most objects required some spatial binning of the spectral data, via Voronoi tessellation, to achieve the target signal-to-noise ratio (SNR) of 20. This process involves first computing the median signal across the spectra and estimates the noise as the square root of the signal. The Voronoi binning algorithm [Cappellari and Emsellem, 2004] is then applied which uses the spatial coordinates, signal, noise, and target S/N to produce bin assignments, centres, achieved S/N, and other bin properties; the resulting tessellation and underlying pixel SNR values are shown for Abell S780 in Fig. 2.5.

We iterate over each Voronoi bin, summing the spectra within each to form a composite galaxy spectrum. The set of pixels to be used in the spectral fit is refined by iteratively clipping outliers based on their deviation from the best-fit model. In each iteration, a scale factor is computed to match the best-fitting template to the galaxy spectrum over the current good pixels using

$$\text{scale} = \frac{\sum_{i \in \text{goodpixels}} \text{galaxy}[i] \times \text{bestfit}[i]}{\sum_{i \in \text{goodpixels}} \text{bestfit}[i]^2},$$

and the residuals are calculated as

$$\text{resid}[i] = \text{scale} \times \text{bestfit}[i] - \text{galaxy}[i].$$

A robust error estimate is obtained and the set of good pixels is updated to include only those indices for which

$$|\text{bestfit}[i] - \text{galaxy}[i]| < 3 \times \text{err}.$$

This process is repeated until the set of good pixels remains unchanged and we begin a two-step pPXF fitting procedure.

We use stellar population synthesis (SPS) models from [Vazdekis et al., 2016], which provide high-resolution model spectra for single stellar populations (SSPs) spanning a broad range of ages and metallicities. These templates are constructed by combining empirical stellar libraries with updated Padova isochrones and an assumed initial mass function (IMF) [Chabrier, 2003], producing theoretical spectra

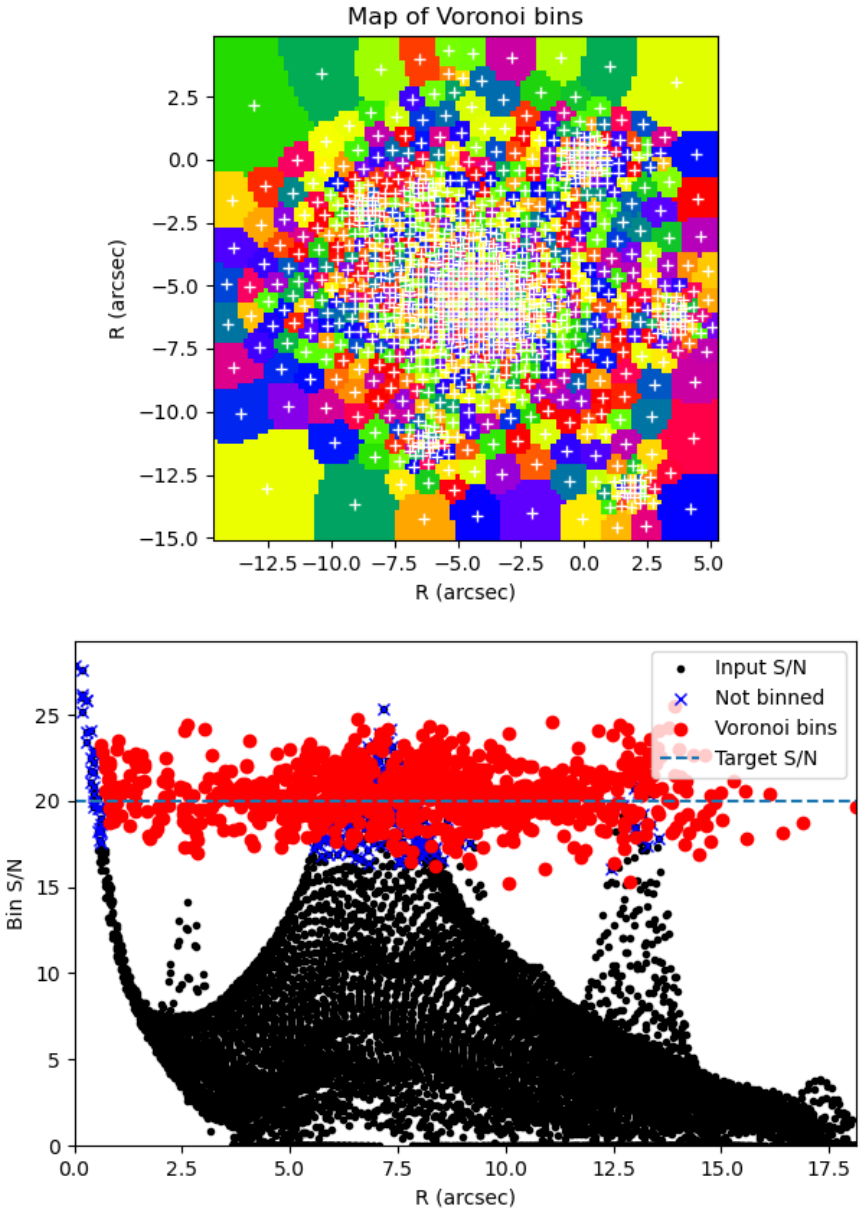

Figure 2.5: **Top panel:** Voronoi bins from the tessellation of Abell S780 with a target SNR of 20. **Lower panel:** Distribution of the individual spaxel SNRs are shown as black circles. The SNR of the Voronoi bins, constructed from the spaxels, are shown as blue crosses or red circles according to whether they contain one or multiple spaxels respectively. It should be noted that S780 is an exceptionally high SNR object and it is rare for an object to have this many, if any, single spaxel bins. The dashed horizontal line represents the target SNR.

that reproduce the integrated light of a stellar population in the absence of nebular emission. The models used here employ the MILES stellar library [Vazdekis et al., 2016] and cover ages from 0.03 to 14 Gyr and metallicities from [M/H] = −2.27 to +0.40. They serve as the basis for modelling and subtracting the stellar continuum from our observed spectra, enabling accurate measurement of emission-line fluxes, kinematics, and diagnostic ratios. Prior to fitting, the templates are normalised by their median flux to avoid introducing continuum slope biases, and a mask of 'good' pixels is determined to exclude spectral regions where strong emission lines are expected, thereby ensuring that the continuum fit is not contaminated by nebular features. pPXF is called with these input stellar templates, the galaxy spectrum, noise estimates, a velocity scale, and the following initial guess for the kinematics, with upper and lower bounds shown in brackets: velocity = 0km/s (-1500, 1500) and velocity dispersion = 150km/s (20, 750). After this first fit, the resulting best-fit model is cleaned to remove spectral bins deviating by more than 3σ. The refined set of good pixels is intersected with the original mask, and a second pPXF fit is performed using the updated pixel set. The optimal stellar template is then computed as a linear combination of the input templates modulated by the derived weights.

The light-weighted stellar age and metallicity are estimated directly from the distribution of template weights obtained during the spectral fitting. Each SPS template corresponds to a single stellar population with a specific age and metallicity; the fitting algorithm assigns weights to these templates to best reproduce the observed continuum. To recover a physically plausible star formation history (SFH) rather than a noisy, over-fitted set of discrete weights, we impose a regularisation penalty that enforces smooth variation of the weights in age–metallicity space [e.g. Cappellari, 2017]. This approach mitigates the degeneracy between neighbouring templates and prevents unphysical oscillations in the SFH caused by noise in the data. The mean stellar age is then defined as the luminosity-weighted average of the ages associated with the best-fit template weights, and likewise for the mean metallicity. This methodology has been widely applied to integral-field spectroscopy datasets from surveys such as SAURON [Bacon et al., 2001], ATLAS^{3D} [Cappellari

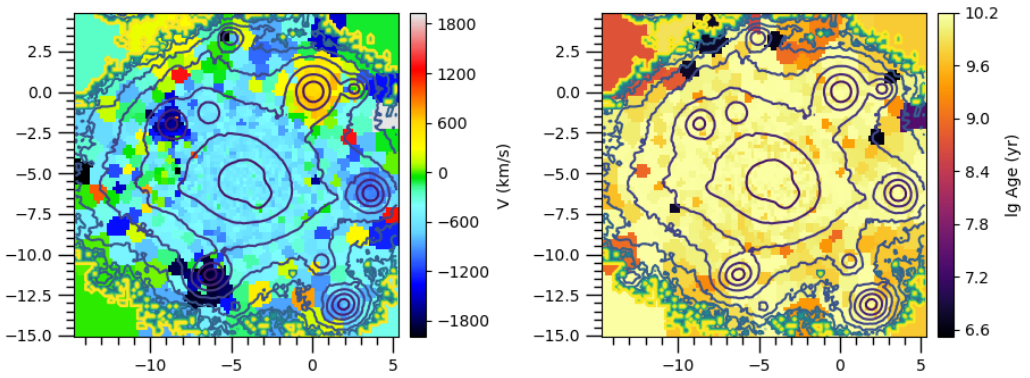

Figure 2.6: **Left panel:** Raw output of the stellar velocity for each Voronoi bin, shown relative to the initial redshift estimate. The overlaid black contours in both panels represent the stellar surface brightness isophotes. **Right panel:** Stellar age estimate

et al., 2011], CALIFA [Sánchez et al., 2016], and MaNGA [Bundy et al., 2015] to map stellar population parameters across galaxies. The stellar ages we calculate for Abell S780 are shown in the right-hand panel of Fig. 2.6.

In addition to population parameters, pPXF simultaneously derives the stellar kinematics for each Voronoi bin by fitting the absorption line profiles with the broadened template spectra. The best-fit line-of-sight velocity corresponds to the shift applied to the templates, while the velocity dispersion is determined from the Gaussian broadening required to match the observed line widths. We adopt the median velocity of all bins with centroids within 5 kpc of the BCG as the systemic reference, and report subsequent velocities relative to this zero-point. Average values of the stellar velocity for varying radii are shown in Fig. 2.7 for Abell S780, demonstrating minimal scatter and no systematic trend with increasing radius. This behaviour is consistent across all objects in the sample, confirming that our choice of a 5kpc radius aperture to define zero-velocity does not introduce a systematic bias.

We update the initial redshift guess by first estimating the peculiar redshift

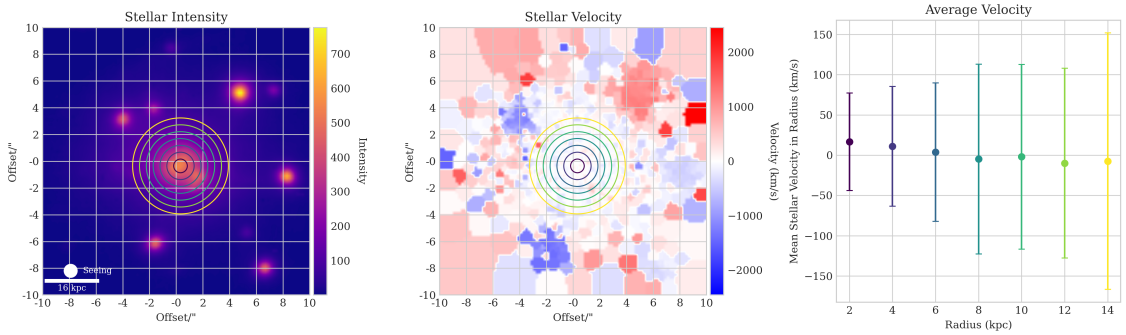

Figure 2.7: An overview of the stellar kinematics for the galaxy Abell S780. **Left panel:** The stellar continuum intensity map. **Middle panel:** The corresponding line-of-sight stellar velocity map. The concentric circles overlaid on both maps represent the circular apertures used to calculate the zero velocity. **Right panel:** The mean stellar velocity as a function of radius, calculated within each aperture. The error bars represent the 1σ velocity dispersion within each annulus. The plot clearly demonstrates that there is minimal variation in the mean stellar velocity as a function of radius.

associated with the median stellar velocity:

$$z_{\text{pec}} = \sqrt{\frac{1+\frac{v}{c}}{1-\frac{v}{c}}} - 1,$$

where v is the median stellar velocity and c is the speed of light. We then remove this peculiar component from the observed redshift z_{obs} to obtain the corrected cosmological redshift:

$$z_{\text{cos}} = \frac{1+z_{\text{obs}}}{1+z_{\text{pec}}} - 1.$$

This value is taken to be the redshift of the BCG. All line-of-sight gas velocities will be quoted relative to the stellar average within the 5kpc radius circle used for this calculation.

Emission Lines

The emission-line templates in pPXF are constructed as narrow Gaussians centred at the rest wavelengths of the transitions of interest, redshifted according to the gas line-of-sight velocity distribution (LOSVD), and scaled to match the observed fluxes. For doublets or multiplets, pPXF allows physically motivated constraints to

Emission Line	Wavelength (Å)
[OII]	3726.03, 3728.82
Hδ	4101.76
Hγ	4340.47
Hβ	4861.33
[OIII]	4958.92, 5006.84
[OI]	6300.30
[NII]	6548.03, 6583.41
Hα	6562.80
[SII]	6716.47, 6730.85
Ca	7291.47

Table 2.5: Fitted emission lines with their corresponding rest-frame wavelengths.

be imposed on the relative amplitudes of the lines. In our analysis, we adopt the following constraints:

- **[O II] λ3727/λ3729 doublet** — The intensity ratio of this density-sensitive doublet is physically restricted to the range 0.28–1.47 [e.g., Osterbrock and Ferland, 2006]. To enforce this, we model the observed [O II] feature as a linear combination of two synthetic doublets: one constructed with the minimum allowed ratio and one with the maximum allowed ratio. pPXF then fits for the optimal combination of these two, which by construction yields a ratio within the permitted range. This method is both numerically stable and physically motivated, as it ensures the resulting line ratio corresponds to a valid electron density state (n_e) between the low- and high-density limits.

- **[S II] λ6717/λ6731 doublet** — The [S II] ratio is likewise constrained by atomic physics to lie between 0.44 and 1.43 [e.g., Osterbrock and Ferland, 2006]. We apply the same linear-combination-of-extremes method as for [O II], ensuring the fitted ratio remains within the allowed range.

- **[O III], [O I], and [N II] doublets** — For these transitions, the relative intensities are set by well-established transition probabilities and are effectively fixed in the low-density limit [e.g., Storey and Zeippen, 2000]. In each case, pPXF fits a single amplitude for the brighter component and scales the fainter one accordingly. The fixed flux ratios adopted in this work are:

O III $\lambda5007/\lambda4959$: 2.98 [Storey and Zeippen, 2000]

O I $\lambda6300/\lambda6364$: 3.05 [Storey and Zeippen, 2000]

N II $\lambda6583/\lambda6548$: 2.96 [Storey and Zeippen, 2000]

- **Balmer lines** — Although the intrinsic ratios of the Balmer series are fixed by atomic physics (under Case B recombination; Osterbrock and Ferland 2006), we allow their relative fluxes to vary freely. This accounts for the large wavelength separation of the Balmer lines, which makes them susceptible to differential dust extinction. Departures from the intrinsic ratios therefore provide a direct probe of the dust content along the line of sight (see § 7.4). This is particularly important in brightest cluster galaxies, where dust lanes and patchy obscuration are frequently observed [e.g., Tremblay et al., 2018].

The best-fitting continuum, calculated as described in § 2.3.2, is subtracted from the observed spectrum to isolate the residual emission-line spectrum. The gas templates are then fit to these residuals while simultaneously refitting the continuum to account for any template mismatch or overlapping absorption features (particularly important for Balmer lines where stellar absorption can bias flux measurements). This iterative approach ensures that the derived emission-line kinematics and fluxes are minimally biased by an imperfect continuum model, and vice versa. However, for very nearby, bright targets with high S/N, we find that the specific pPXF setup used for stellar-continuum fitting can, in some cases, over-fit narrow absorption complexes (e.g. Balmer and metal-line blends). Our baseline configuration fits the galaxy spectrum in log-wavelength space using the stellar template grid described above with no additive polynomial and a low-order multiplicative polynomial to absorb large-scale calibration mismatches. We solve for the first two stellar kinematic moments (velocity and dispersion) with a modest penalization (bias) together with the iteratively refined goodpixels mask (§ 2.3.2). Despite masking nebular wavelengths in the initial pass, when a deep stellar absorption trough lies beneath an expected emission feature the combination of high S/N, flexible template weights, and polynomial freedom can drive a local over-subtraction of the continuum. The resulting residuals may appear as narrow, positive 'emission' peaks precisely at the

locations where line emission would be expected (thereby producing spurious detections). It is typically diagnosed by (1) excessive pixel-to-pixel scatter in the residuals relative to the propagated variance, (2) non-contiguous regions flagged as emission in the resulting line-flux maps, (3) residuals concentrated at the centres of strong stellar absorption features, and (4) unphysical behaviour in basic diagnostics (e.g. inconsistent Balmer decrements or incoherent BPT-classification patches). We adopt conservative polynomial orders (degree= 0, mdegree$\lesssim$ 6–8), increase the pPXF bias to suppress overfitting of higher-order moments (or fix $h_3 = h_4 = 0$), and, when feasible, use light regularization of the template weights.

We define the primary diagnostic line to be Hα for objects at $z < 0.42$ and [OII]$\lambda\lambda 3726, 3729$ for objects at higher redshift. Unqualified references to gas should be interpreted as referring to the primary diagnostic line. We analyse the kinematic properties of the stars and gas on a spaxel-by-spaxel basis, applying no spatial binning to preserve the original resolution of the data. For each spaxel, we use the Penalised Pixel-Fitting routine [pPXF; Cappellari, 2017, Cappellari and Emsellem, 2004] to model the observed spectrum. The model is a linear combination of two main components: high-resolution stellar population templates to represent the stellar continuum, and a set of Gaussian templates to model the gas emission lines. This simultaneous fitting allows for a robust de-blending of the stellar and gas contributions, enabling an independent measurement of the kinematics for each component.

The kinematics of the ionised gas are determined by fitting simple Gaussian profiles at the expected wavelength of each emission line. These emission line templates are included in the fit alongside the stellar templates. By optimising the stellar continuum and gas emission simultaneously, pPXF correctly models and subtracts the underlying stellar absorption features (e.g., the Balmer absorption lines), which is essential for obtaining an unbiased measurement of the true flux and kinematics of the superimposed gas emission. The velocity, dispersion, and amplitude of each gas component are treated as free parameters, providing a direct measurement of the gas kinematics.

The initial detection of emission is based on an F-test, a statistical method for

comparing nested models. For each potential emission line, we test the null hypothesis (H0), that the spectrum within a $\pm 1000\,\mathrm{km\,s^{-1}}$ window is adequately described by a stellar continuum, against the alternative hypothesis (H1), that the model requires the addition of a single Gaussian component. The F-statistic quantifies the significance of the improvement in the fit—as measured by the reduction in the residual sum of squares—when the additional parameters of the Gaussian are included. The null hypothesis is rejected, and a spaxel is subsequently flagged as containing significant line emission, if its p-value falls below our adopted significance threshold corresponding to a 5σ confidence level.

A purely statistical threshold can produce a mask contaminated by isolated, noisy spaxels that pass the significance test by chance. To ensure the physical coherence of the detected structures, we apply a spatial connectivity analysis to this initial statistical mask. A labelling algorithm identifies contiguous, multi-pixel regions, and we retain only the most spatially extended of these for the final emission line mask. This morphological filtering step is crucial for isolating genuine, large-scale kinematic structures from pixel-level noise events. We show the pixels flagged as line emitting by this process, for all lines in the MUSE spectral window, for Abell S780 in Fig. 2.8

For each spaxel within the robustly defined emission mask, we seek to determine the optimal kinematic model that best describes the observed line profile. The hierarchy of models tested for each emission line consists of three physically motivated scenarios. The simplest model is a single Gaussian profile, representing a single, dynamically relaxed gas component. We then test two distinct two-component models. The first is a cospatial double Gaussian, where two components share a common central velocity but are allowed to have different velocity dispersions (one narrow, one broad). This model is designed to identify phenomena such as a quiescent gas disc coexisting with a more turbulent outflow. The second two-component model consists of two offset Gaussians of the same width, where the components share a common velocity dispersion but are allowed to have different central velocities. This model is effective at identifying kinematically distinct merging clouds or bipolar outflows with similar turbulence. This hierarchical process ensures that the final

kinematic maps are derived from the most statistically appropriate model for each spaxel. For each competing model, we evaluate the chi-squared (χ^2) value and its associated degrees of freedom to calculate a p-value. The model that yields the highest p-value is adopted as signifying the most probable description of the data.

This approach enables a detailed, spatially resolved kinematic analysis of individual galaxies, providing insight into localised dynamical processes such as turbulence, rotation, and feedback-driven outflows. However, since the focus of this thesis is on the global properties of the sample rather than the full complexity of any single system, we adopt the single Gaussian fit as the fiducial model for all objects (unless explicitly stated otherwise). This uniform treatment allows us to compare kinematic quantities across the full sample in a consistent manner, while still retaining the capacity to revisit more complex models for individual cases of particular interest.

Morphology

Once a robust emission mask has been established, we can construct a two-dimensional map of the line-emitting pixels, which provides the foundation for studying the morphology of the ionised gas. Such maps not only reveal the overall extent of the emission, but also allow us to quantify structural features such as elongation, asymmetries, or clumpiness in the distribution of ionised material. The overall shape of the ionised gas is captured by two numbers: the major and minor axes measured from the Hα (or [OIII]) intensity map.

The overall shape of the ionised gas can be approximated by two numbers: the major and minor axes measured from the Hα (or [OIII]) intensity map. We begin by smoothing the raw image $I(x, y)$ with a 3×3 pixel median filter to suppress pixel-scale noise, and we define the peak position $P_p = (x_p, y_p)$ as the coordinates of the brightest pixel in this filtered map $I_{\rm filt}$. Only the contiguous mask region that contains this peak is considered in what follows. Within that region, we examine every pair of pixels and select the two whose straight-line segment is longest while still intersecting the peak; the Euclidean distance between these pixels is taken to be the major-axis length $L_{\rm maj}$. A vector perpendicular to this major axis is then constructed through the peak, and we trace it in both directions until we exit the

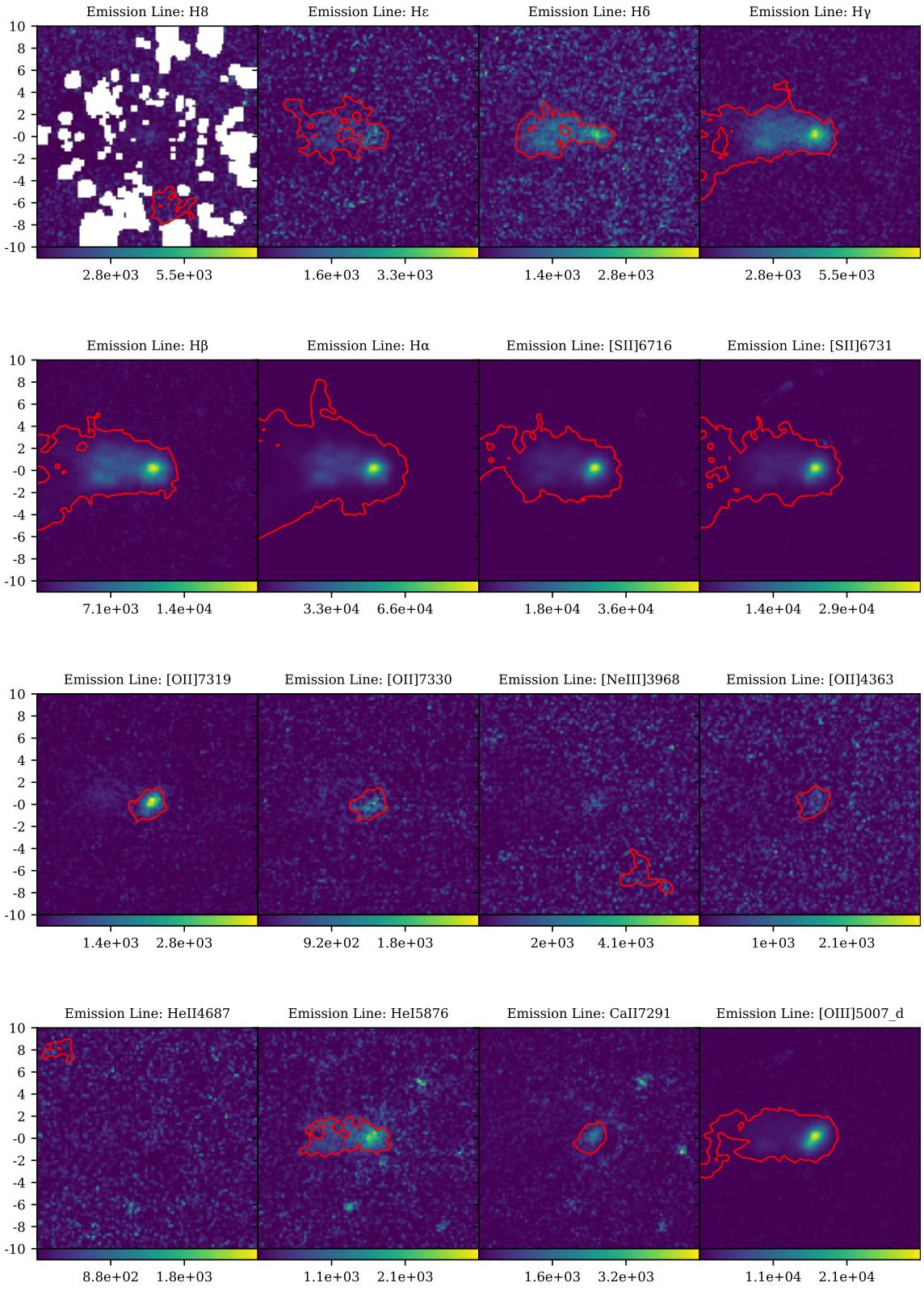

Figure 2.8: Intensity maps for all target lines within the spectral range for Abell S780. The red contours highlight regions defined as line emitting by the process described in § 2.3.2. The map scales are illustrative and require a scaling factor to be converted into physical values; however, they are directly comparable between lines and are chosen to illustrate the spatial extent of the emission.

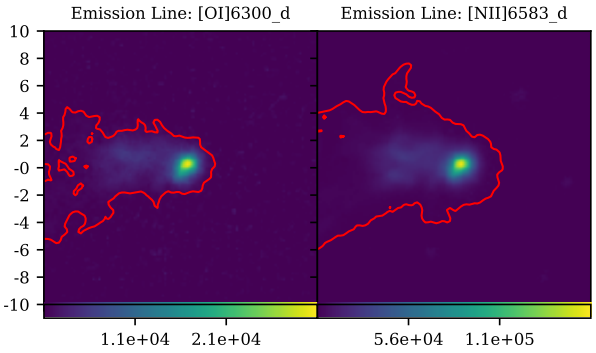
Emission Line: [OI]6300_d
Emission Line: [NII]6583_d
10
8
6
4
2
-0
-2
-4
-6
-8
-10
1.1e+04
2.1e+04
5.6e+04
1.1e+05

Continued

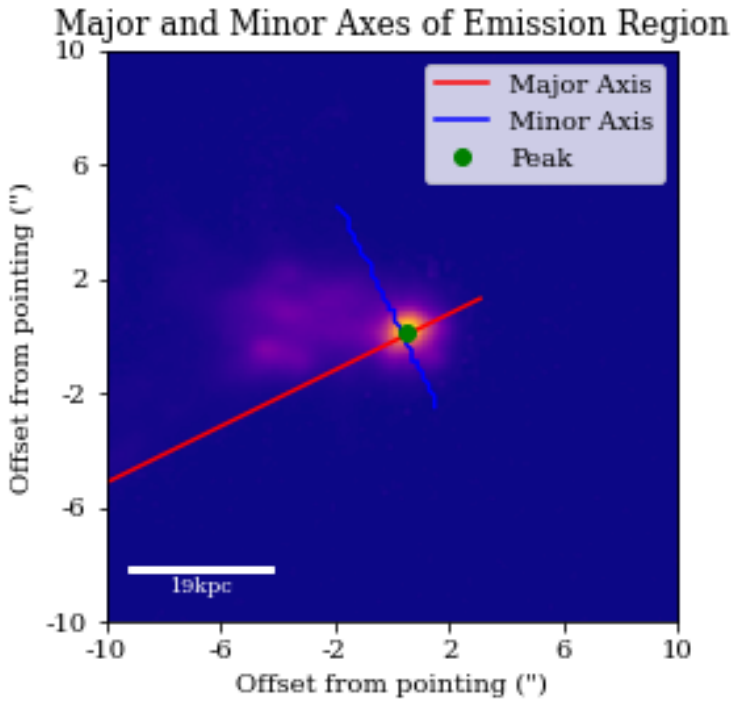

Figure 2.9: The major (red) and minor (blue) axes of emission for Hα in Abell S780.

emission region; the length of this perpendicular segment defines the minor-axis length $L_{\rm min}$. Finally, the pixel-based measurements are converted to angular size via the instrument plate scale and subsequently into physical kiloparsecs using the galaxy's redshift. The pair ($L_{\rm maj}$, $L_{\rm min}$) provides a basic description of the extent and elongation of the line-emitting gas surrounding each BCG, shown in Fig. 2.9 for Abell S780. We will use these values to classify the morphology in Chapter 4. T

Kinematics

Gas velocity structure can reveal disturbances and may be more reliable than surface brightness for detecting motion, especially in low surface brightness regions. Mean line-of-sight velocity maps were created to study this. Many cluster cores show a clear velocity gradient across the line emission peak, suggestive of rotation or inclined outflow/inflow.

Peak-to-peak velocity is defined as the maximum velocity difference across the line-emission peak. To calculate this, velocity maps were median-smoothed within a 3×3 pixel region. From the emission peak, we rotated a line in 10° increments

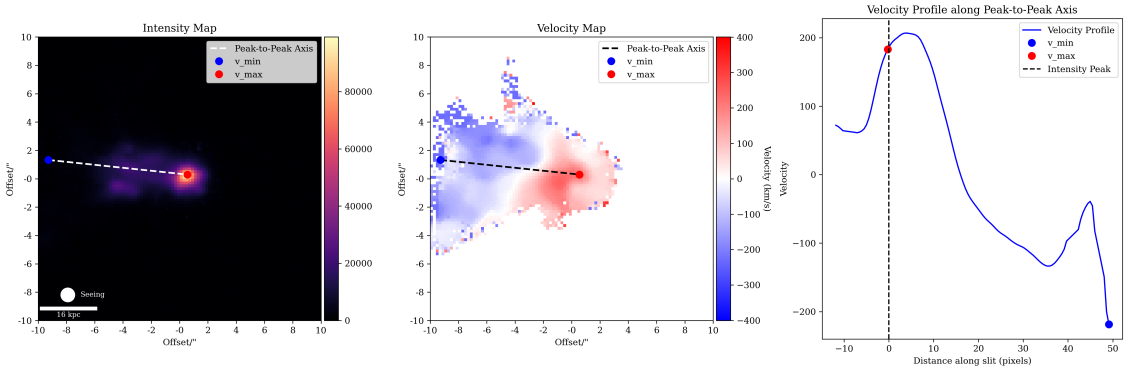

Figure 2.10: **Left:** Emission-line intensity map. **Centre:** Line-of-sight velocity field derived from Gaussian fitting, with the axis used for velocity extraction indicated. **Right:** Velocity profile extracted along the longest line of contiguous emitting pixels passing through the emission peak, showing the maximum blueshift–redshift separation used to define the peak-to-peak velocity.

and extracted a velocity profile along the longest contiguous set of emitting pixels intersected by that line. For each orientation, the peak-to-peak velocity was taken as the difference between the most blueshifted and most redshifted points relative to the average stellar velocity (see § 2.3.2), with the requirement that these extrema lie on opposite sides of the emission peak. In disturbed velocity fields where no clear opposing peaks were present, the extrema were instead defined as the pair of points that maximized the velocity difference across the central emission. We show this, in addition to the 2D LOS velocity map, for Abell S780 in Fig. 2.10.

Excitation Mechanism

We extract the following line ratios used in the three classic diagnostic plots of excitation mechanism (covered in § 7.2.2): [O III]λ5007/Hβ, [NII]λ6584/Hα, [SII]$\lambda\lambda$6717, 6731/Hα, and [OI]λ6300/Hα. Values are calculated for the regions corresponding to the intersection of the relevant emission maps for both lines. This region is typically dictated by the non-Balmer line.

We also extract ratio maps of the Balmer lines, which can be used to trace dust, via the same process.

2.4 Ancillary Data

2.4.1 ACCEPT Survey

The Archive of Chandra Cluster Entropy Profile Tables (ACCEPT) [Cavagnolo et al., 2009] was a project that utilised the Chandra archive to study the thermodynamic properties of the ICM in a large sample of galaxy clusters. The primary goal of the survey was to measure the radial profiles of gas entropy.

The ACCEPT survey was based on publicly available data from the Chandra Data Archive. The sample is not selected based on a single set of observational criteria; it comprises a large collection of galaxy clusters that have been observed by Chandra for a range of scientific purposes. The instrument used for these observations is the Advanced CCD Imaging Spectrometer (ACIS), which provided both imaging and spectral information with high angular resolution.

The data reduction for the ACCEPT survey followed a standardised pipeline primarily using the Chandra Interactive Analysis of Observations (CIAO) software package, along with the most current Chandra Calibration Database (CALDB) available at the time of processing. Raw (Level 1) event files for each observation were reprocessed to ensure that the latest calibration files are applied, accounting for time-dependent changes in the instrument's performance, such as the gain and charge transfer inefficiency corrections. This step generates a new, calibrated (Level 2) event file.

The high angular resolution of Chandra allowed for the detection and removal of X-ray point sources, such as foreground stars and background AGN, that were superimposed on the extended cluster emission. These sources were masked out from subsequent analysis. Background spectra are extracted from blank-sky background files and subtracted during the spectral fitting process.

The core of the ACCEPT survey's analysis was the extraction and fitting of X-ray spectra in concentric annuli centred on the peak of the cluster's X-ray emission. For each cluster, a series of concentric annuli were defined, and spectra are extracted from each annulus. The width of the annuli is chosen to ensure a sufficient number of counts in each spectrum for a robust spectral fit. The spectra from each annulus

were fitted with an absorbed thermal plasma model (the APEC model in XSPEC). This model accounts for the emission from the hot gas and the absorption by Galactic neutral hydrogen. The projected temperature and emission measure profiles obtained from the spectral fitting were deprojected to infer the three-dimensional radial profiles of the gas properties. This was done using a non-parametric deprojection technique, which assumes spherical symmetry. This process yields the radial profiles of the electron temperature (T_e) and electron density (n_e).

The deprojected radial profiles of electron temperature and density are used to calculate the gas entropy profile. The entropy is typically defined as:

$$K(r) = k_B T_e(r) n_e(r)^{-2/3}$$

These derived entropy profiles were the primary data product of the ACCEPT survey and enabled calculation of the cooling time, t_{ff}. The profiles were fitted with a model of the form:

$$K(r) = K_0 + K_{100} \left(\frac{r}{100\,\mathrm{kpc}} \right)^{\alpha}$$

where K_0 represents the central entropy floor, K_{100} is the entropy at a fiducial radius of 100 kpc, and α is the power-law slope at larger radii.

The ACCEPT survey is an enormously rigorous, detailed, and accessible resource for finding key values related to the X-ray properties of galaxy clusters. The sample is sufficiently large, standardised and object-agnostic to enable to derive population-wide statistics. It has been an incredibly useful tool, and I am extremely grateful to the authors for their analysis and maintenance of this resource. An aim of this work was to establish the foundations of an optical counterpart: a large, unbiased reference sample spanning a broad range of properties of interest across a representative set of BCGs.

2.4.2 Archival Chandra Data

For each Kaleidoscope object we searched the Chandra archive for ACIS-I observations and selected the single pointing with the longest effective exposure time. We retrieved the corresponding level-2 event files and extracted the events within

a region co-spatial with the MUSE FOV. The event distributions were binned into two-dimensional histograms and smoothed with a Gaussian kernel to suppress noise and highlight the extended X-ray morphology. From the smoothed maps we measured the centroid of the X-ray emission and converted positional offsets to physical units using the target redshift and a flat ΛCDM cosmology. These reduced products provide a uniform X-ray dataset for the subset of line-emitting systems with archival coverage, enabling direct comparison between the hot ICM and the ionised gas observed with MUSE, while noting that only a partial overlap of 20 objects exists between the line-emitting objects in the Kaleidoscope sample and available Chandra data.

CHAPTER 3

Line Emission Properties in Kaleidoscope

Observationally, the presence of gas emission lines—such as Hα or [O II]—in BCGs serves as an indicator of cooling activity, potential star formation and/or AGN feedback. Crawford et al. (1999), studying 177 central galaxies in the ROSAT Brightest Cluster Sample, found that 27% exhibit emission-line spectra typical of cooling-flow nebulae, with a further 6% showing only [N II] emission above the stellar continuum. Similarly, Edwards et al. (2007) reported that, across the NOAO Fundamental Plane Survey, only $\sim 15\%$ of BCGs show detectable line emission overall; however, in clusters hosting cooling flows [Cavagnolo et al., 2009], this fraction rises to $71^{+9}_{-14}\%$ and approaches $100^{+0}_{-15}, \%$ for BCGs within 50 kpc of the X-ray peak.

Together, these surveys demonstrate that line emission in BCGs is tightly linked to the presence of cool cores, consistent with a scenario in which cooling X-ray gas condenses and fuels either star formation or low-ionisation nuclear emission-line regions (LINERs). By contrast, BCGs in non–cool-core clusters show only a few percent incidence of emission, comparable to field or control samples [Crawford et al., 1999, Edwards et al., 2007].

In this chapter, we extend these studies by quantifying emission-line prevalence in the purely X-ray–selected Kaleidoscope sample using MUSE data (§ 2.2). Our

analysis covers not only Hα but a broad suite of optical emission lines, enabling a systematic census of nebular activity. This motivates a clear division of the sample into emission-line and quiescent BCGs. The emission-line subset will then serve as the focus for detailed investigations into the morphology (Chapter 4), kinematics (Chapter 5 and Chapter 6), and excitation mechanism (Chapter 7) of the ionised gas.

3.1 Defining Line Emission

The presence of an emission line is assessed for each spaxel using the pipeline described in § 2.3.2. At the object level, we define a BCG to exhibit line emission if there exists a contiguous set of emitting spaxels (spaxels flagged as line emitting by the pipeline) in either Hα or [O II] whose projected area is $\geq 1'' \times 1''$. Contiguity is evaluated on the native sampling with 8–connected neighbourhoods. This area threshold filters out unresolved or marginal nuclear detections and ensures that the 'line–emitting' class traces extended nebulae amenable to spatially resolved kinematic and excitation analysis. Galaxies that do not meet this contiguity and area criterion in either line are assigned to the non–line–emitting set. This dichotomy defines the line–emitting subsample referenced throughout the subsequent chapters. The results of this process are summarised in Fig. 3.1, Fig. 3.2 and Table 3.1.

It should be emphasised that some degree of ambiguity is inherent in defining the boundary between line–emitting and non–line–emitting systems. Spaxels near the detection threshold may be flagged differently under modest changes in the adopted criteria, and consequently the assignment of a given BCG to one class or the other is not always unique. Within the line–emitting subset itself there exists an additional distinction: while the statistics presented here refer to all systems meeting the emission criterion, only the subset with spatially extended emission provide the basis for constructing line–of–sight velocity maps and undertaking detailed kinematic and excitation analyses.

Fig. 3.1 summarises the incidence of optical emission across our X-ray–selected BCG sample in the form of a binary heat map in which each row corresponds to

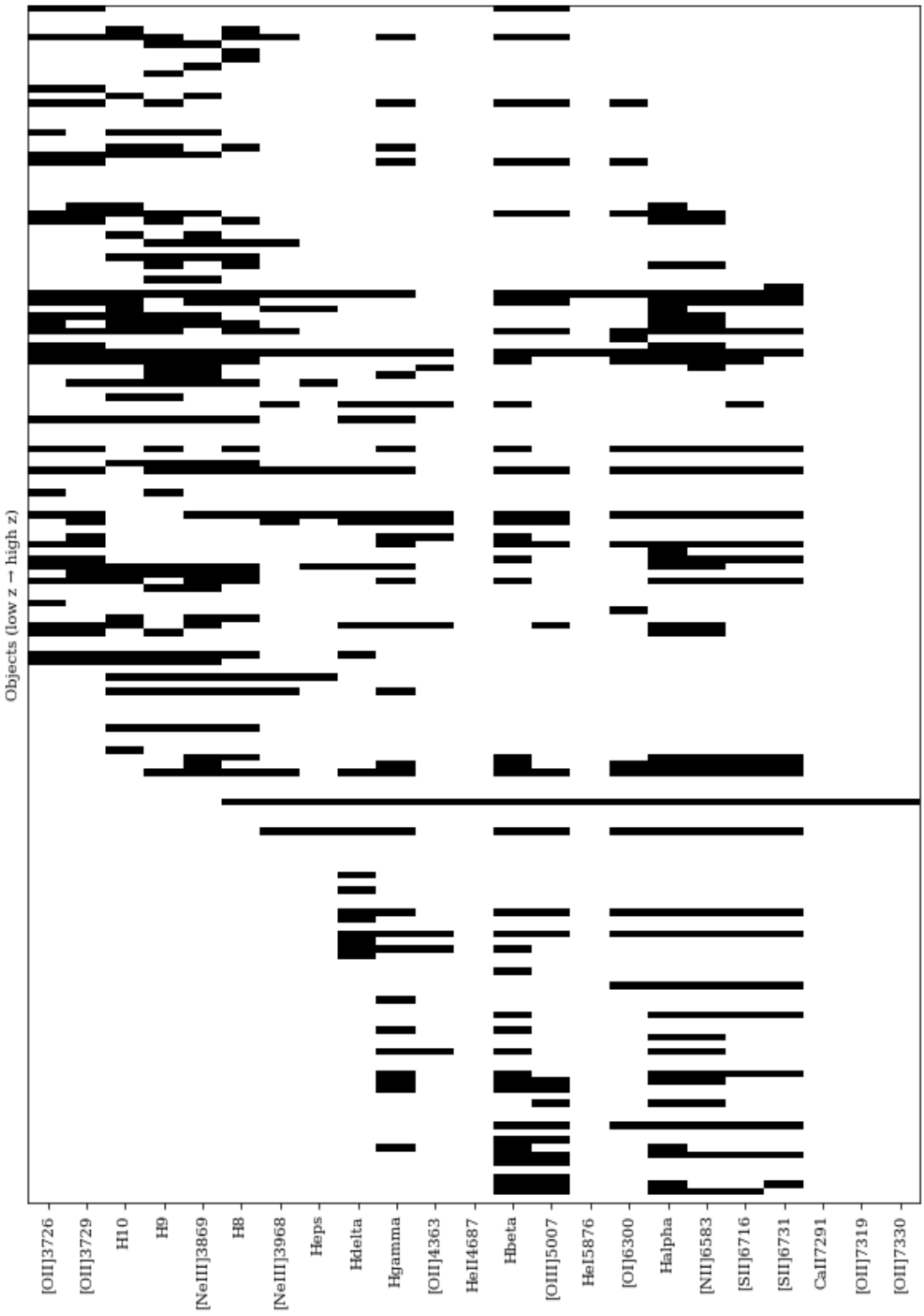

Figure 3.1: Binary heatmap of emission line detections across the BCG sample. Each row corresponds to one galaxy, ordered by redshift (lowest at the bottom, increasing upwards). Each column represents an emission line; black indicates emission above the threshold, white indicates no detection. This plot is the result of applying our line emssion threshold to the continuous map shown in Fig. 2.3

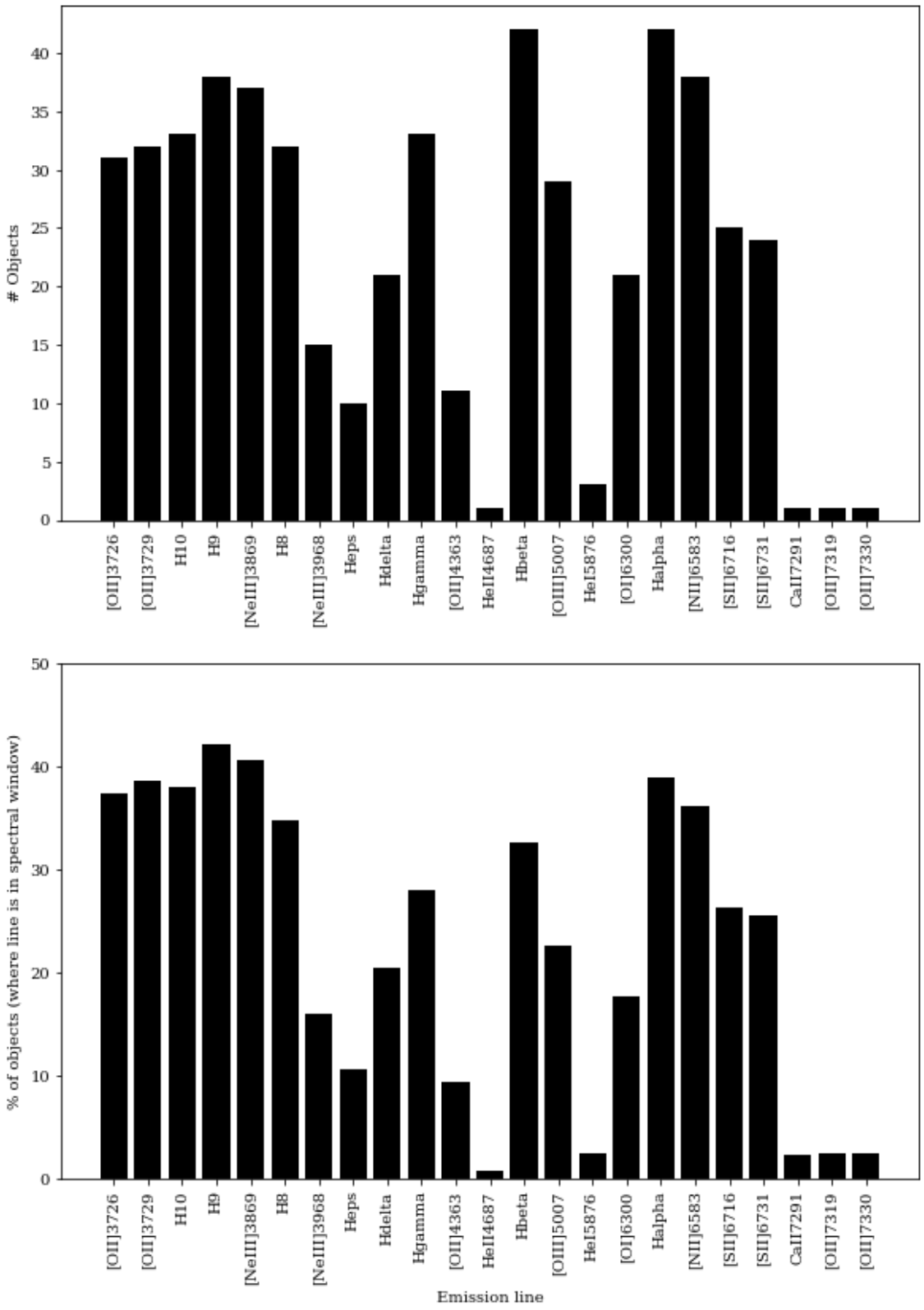

Figure 3.2: Histogram summaries of emission line detections across the BCG sample. **Top:** Absolute number of galaxies showing emission above the adopted threshold for each line. **Bottom:** Percentage of galaxies with detected emission relative to the number of galaxies where the given line is within the observed spectral window (i.e. excluding missing values).

Table 3.1: Emission-line detection statistics for the Kaleidoscope MUSE BCG sample for each line of interest. The wavelength of the line and the raw number of detections are shown in the second and third columns respectively. The final row reports the fraction of objects classed as exhibiting emission for each line. In this table we do not normalise for the redshift dependence of line visibility and percentages are provided with reference to the entire sample.

Line	λ [Å]	$N_{\rm det}$	Fraction
[O II]3726/3729	3726	34	19.5%
H10	3799	34	19.5%
H9	3835	40	23.0%
[Ne III]3869	3869	39	22.4%
H8	3889	34	19.5%
[Ne III]3968	3968	18	10.3%
Hϵ	3970	12	6.9%
Hδ	4102	24	13.8%
Hγ	4340	36	20.7%
[O II]4363	4363	12	6.9%
He II4687	4687	2	1.1%
Hβ	4861	47	27.0%
[O III]5007	5007	33	19.0%
He I5876	5876	5	2.9%
[O I]6300	6300	24	13.8%
Hα	6563	46	26.4%
[NII]6583	6583	43	24.7%
[S II]6716	6716	28	16.1%
[S II]6731	6731	27	15.5%
CaII7291	7291	1	0.6%
[O II]7319	7319	1	0.6%
[O II]7330	7330	2	1.1%
Total objects			174
Line-emitting objects (Hα/[O II])			62 (35.6%)

a BCG (sorted by increasing redshift from bottom to top) and each column is an emission line ordered by rest wavelength. Black cells indicate a detection above our adopted threshold, while white cells denote non-detections. The charts in Fig. 3.2 report the number of detections per line, both in absolute terms (upper panel) and as a percentage of possible detections (lower), providing an overview of prevalent lines in the sample. MUSE covers ∼4800–9300 Å in the observed frame so the visibility of a rest-frame feature depends on redshift. For example, Hα ($\lambda_{\rm rest} = 6563$ Å) lies within the MUSE bandpass for $z \lesssim 0.42$, whereas the [O II] doublet ($\lambda\lambda 3726, 3729$) enters the band at $z \gtrsim 0.29$ and remains visible beyond the highest redshift objects in our sample. These windows imprint themselves on the heat map as horizontal swaths of availability, and the natural modulation they impose is important to remember in discussions of absolute detection count. Hα (and its neighbouring low-ionisation lines ([N II]) are preferentially sampled at lower redshift, while [O II] becomes the principal tracer at higher redshift where Hα redshifts beyond the instrumental cut-off. The dominance of the strongest cool-core diagnostics—Hα, [N II] λ6583, and Hβ is evident in both figures. We find fewer detections in intrinsically weaker and/or more extinction-sensitive lines (e.g. He I λ5876, [O I] λ6300, [O II] $\lambda\lambda$7319, 7330), consistent with expectations for metal-rich, low-ionisation nebulae in BCGs. Taken together with the spatially extended morphologies seen in our maps these statistics are in line with classic results from the literature.

In Fig. 3.3 we summarise the emission averaged across the line-emitting objects in the sample. The graph shows the probability of detecting Line 2 (x-axis), given that Line 1 (y-axis) is detected in the sample (P(Line 2 observed | Line 1 observed)). High Line 2 probability values, appearing as vertical streaks in the plot, are indicative of the dominant lines in the sample. Examples include [OII] $\lambda\lambda 3726, 3729$, [NII] λ6583 and Hα

3.2 Comparison to the Literature

We measure a line–emitting fraction of $f_{\rm LE} = 36\%$ (62/174), using the object–level criterion defined in this work (a contiguous region of Hα or [OII] emission with

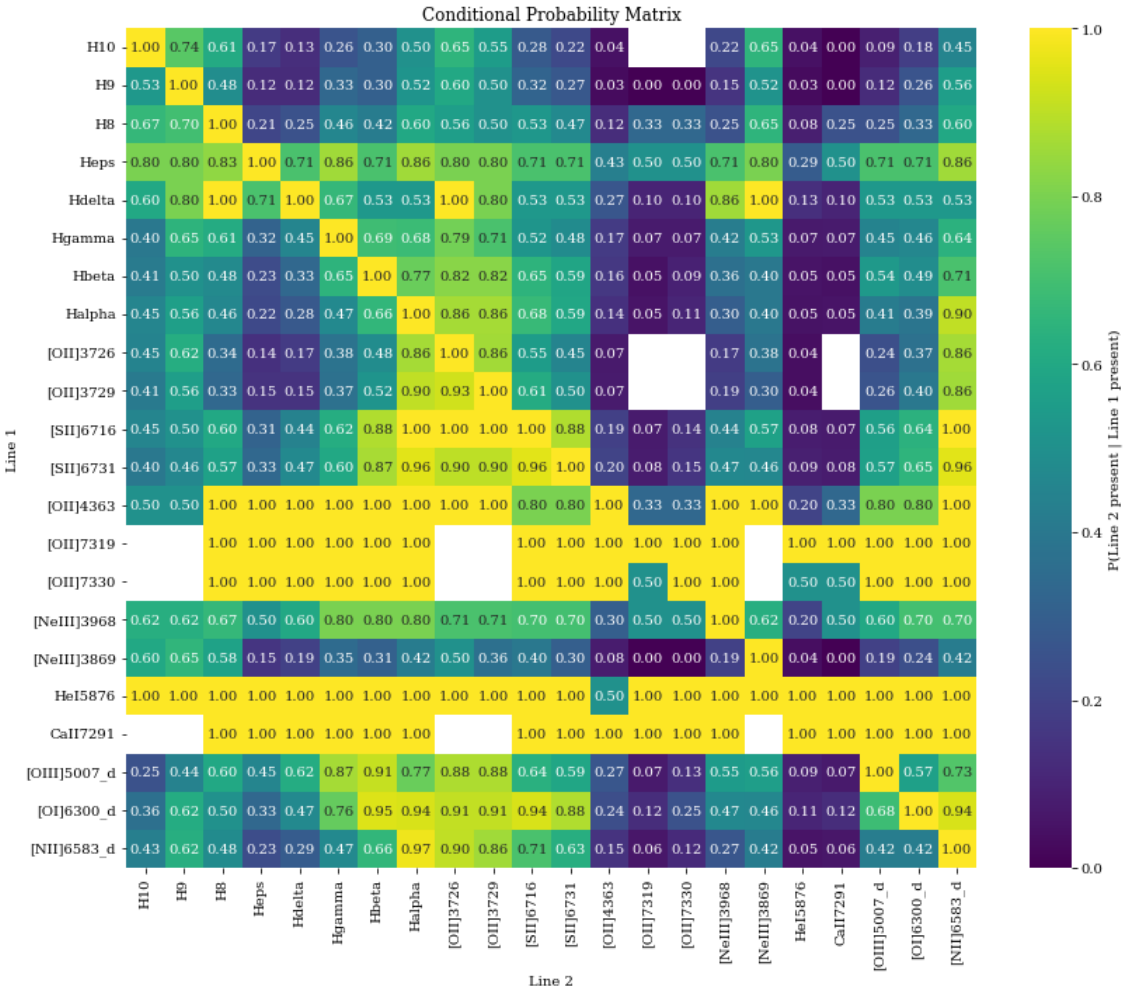

Figure 3.3: Summary of the conditional likelihood of observing a target emission line given the presence of another. The values show the probability of observing Line 2 in the object given that Line 1 was observed averaged across the entire line-emitting subset of the sample. Blank regions are a product of the finite spectral window of MUSE.

projected area $\geq 1'' \times 1''$). The corresponding Wilson 95% confidence interval is 36^{+7}_{-7}% (29–43%). Excluding detections in six nearby objects [1] with extremely deep stellar absorption features—where emission flagged by the pipeline is difficult to separate from the deep stellar absorption feature and therefore considered uncertain, as discussed in § 2.3.2—the incidence drops to 56/174 = 32%, with a Wilson interval of 32^{+7}_{-7}% (26–39%).

Classic X–ray–selected samples at low redshift reported similar fractions: the ROSAT Brightest Cluster Sample found 27% of central galaxies with emission–line spectra, with a further 6% showing [NII] only (effectively ~ 33% if counted as emitters) [Crawford et al., 1999]. The REXCESS sample reported Hα (or forbidden–line) emission in 7/32 = 22% of BCGs overall, rising to ~ 70% among cool–core clusters [Donahue et al., 2010a]. In mixed optical/X–ray selections, Edwards et al. [2007] measured a modest overall incidence of ~ 15% but showed that the fraction climbs steeply in cooling–flow systems: 71^{+9}_{-14}% for BCGs in cooling–flow clusters and effectively 100^{+0}_{-15}% for those within 50 kpc of the X–ray centre. More recent work using large optical catalogues finds little evolution in the total fraction over $0.3 \lesssim z \lesssim 0.6$, with hints of an upturn in strongly emitting systems at $z \gtrsim 0.3$ [McDonald, 2011]. Finally, IFU–based surveys targeting line–emitting BCGs reinforce the tight connection between extended optical nebulae and rapidly cooling intracluster gas [e.g. Hamer et al., 2012].

Taken together, our incidence (36^{+7}_{-7}%, or 32^{+7}_{-7}% excluding questionable detections) is consistent with BCS/REXCESS all–cluster means and within the range expected once one accounts for (i) our spatially resolved, area–based definition (which recovers low–surface–brightness, extended emission), (ii) X–ray selection (which enhances the cool–core fraction relative to optical cluster catalogues), and (iii) sensitivity differences between long–slit/fibre spectroscopy and modern IFU data. These comparisons are also consistent with the well–established entropy (cool–core) threshold for multiphase gas and Hα emission in BCGs at $K_0 \lesssim 30$ keV cm^2 [Cavagnolo et al., 2008].

[1] Abell 2420, Abell 3266, Abell 3667, Abell 2426, Abell 2496, Abell 2580

These results demonstrate that our end-to-end pipeline is effective. The conservative, spatially extended area criterion and uniform processing across all targets enable recovery of low–surface–brightness nebulae while suppressing spurious detections. Because each object is evaluated against the same object-level rule, the resulting set of 62 emitters constitutes a clean, reproducible line–emitting subset with a transparent selection function. This subset provides the foundation for the analysis that follows on morphology (Chapter 4), kinematics (Chapter 5 and Chapter 6), and excitation mechanism (Chapter 7)

CHAPTER 4

Morphology

Having identified a well-defined, line-emitting sub-sample and the validation of our selection pipeline, we now turn from whether systems emit to how that emission is distributed on the sky. The advantages of an IFU are extremely apparent here: by delivering a datacube (x, y, λ), MUSE enables us to separate continuum and line emission cleanly, to construct narrow-band maps around specific transitions, and to compare those maps directly to X-ray morphology. Crucially, the IFU view avoids slit/aperture biases and allows us to trace low–surface–brightness structures while preserving spatial context. In this chapter we therefore focus deliberately on the spatial parameter space of the ionised gas—centroids, extents, shapes, and relative alignments—with a full analysis of kinematics (velocity fields, dispersions, structure functions and ordered vs. disturbed motions) in the subsequent chapters.

We begin in § 4.1 with an obvious but essential point: morphology depends on wavelength. Differences in extinction, ionisation structure, and PSF sampling mean that Hα and [OII] need not trace identical structures. We quantify the consequences of anchoring our spatial metrics to a fiducial line (Hα where available, otherwise [OII]) and document how line choice influences apparent sizes and concentrations. In § 4.2 we measure the projected separations between the stellar continuum peak,

the ionised-gas peak, and the X-ray centre, reporting offsets both in kpc and in units of the MUSE PSF. These offsets serve as zeroth-order diagnostics of dynamical coupling between the BCG, its nebula, and the hot atmosphere.

Next, § 4.3 surveys morphology taxonomies from the literature (e.g. compact cores, filamentary networks, disc-like structures, and clumpy/irregular systems) and motivates a streamlined, IFU-oriented scheme that can be applied reproducibly to MUSE maps. To provide simple, quantitative anchors for those classes, § 4.4 fits ellipses to isophotal contours of the line-emitting regions, yielding ellipticity and position angle measures that are robust to modest S/N variations. We then extend the spatial view beyond the primary tracers in § 4.5, mapping less common transitions (e.g. [OI], [SII], He I, [OIII]) where available to highlight ionisation gradients and to test whether the inferred structures persist across diagnostics.

Finally, § 4.6 places these results within the broader context of BCG cooling–flow studies, emphasising how our IFU–based, area–driven approach refines—or, where appropriate, revises—conclusions drawn from long–slit and fibre surveys. We have assembled a spatially resolved catalogue of line–emitting BCGs and characterised their morphology, which we can use to probe correlations between this morphology and kinematic signatures in subsequent chapters.

4.1 Morphological Dependence on Wavelength

The apparent morphology of the BCG and its surrounding ICM is strongly wavelength dependent—both within narrow-band optical diagnostics (see § 4.5) and, more obviously, across the full electromagnetic spectrum.

At X-ray wavelengths, the dominant emission arises from the hot, diffuse plasma of the ICM, with temperatures in the range of $10^7 - 10^8$ K. Embedded within this we may see AGN-inflated cavities as depressions or voids in the X-ray surface brightness distribution [McNamara and Nulsen, 2007]. These features signify regions where the relativistic plasma expelled by the AGN has displaced the dense, X-ray emitting gas. The interaction of the expanding radio lobes with the ICM can also lead to the formation of shock fronts, observable as bright rims of compressed, heated

gas surrounding these cavities. The overall X-ray morphology can thus appear disturbed, often showing asymmetries and filamentary structures of cooler gas that may have been uplifted from the cluster core by the buoyant rise of these bubbles [Fabian, 2012].

The same region observed in the radio would instead isolate the energetic AGN jets and the synchrotron-emitting relativistic plasma that fills the X-ray cavities. These are the radio bubbles and lobes respectively. The morphology at radio frequencies range from highly collimated jets emanating from the core of the BCG to more diffuse, extended lobe structures that coincide with the X-ray decrements [Bîrzan et al., 2004]. The age and power of the AGN outburst, as well as the density of the surrounding ICM, influence the observed radio morphology. In some instances, 'ghost cavities' are observed in X-rays, which lack the expected radio emission, implying that the radio-emitting particles have aged and faded at GHz frequencies over time.

In the optical and ultraviolet (UV) bands, the morphology is primarily characterised by the stellar component of the BCG, which is typically a massive elliptical galaxy with an older stellar population. However, the impact of AGN feedback can be observed through associated phenomena. Filaments of young, blue stars and emission-line nebulae are frequently detected along the peripheries of X-ray cavities and radio lobes [Tremblay et al., 2018]. This indicates that the energetic outflows can compress gas, triggering star formation, or that gas uplifted by the buoyant bubbles cools and subsequently forms stars. Dust lanes, associated with cooler gas components, can also be prominent, obscuring parts of the BCG at these wavelengths.

Observations in the infrared (IR) and sub-millimetre regimes trace cooler gas phases and dust. Significant reservoirs of molecular gas (e.g., CO) have been found in filamentary structures spatially correlated with X-ray cavities and radio bubbles in a growing number of systems [Russell et al., 2019]. This cold gas represents the fuel for ongoing or future star formation and can also be involved in the AGN feeding cycle. The morphology of this cold gas often mirrors the structures observed at other wavelengths, highlighting the multi-phase nature of the gas influenced by

AGN feedback.

While the examples above highlight the most dramatic end of the spectrum, the broader BCG population is markedly heterogeneous: gas content, spatial extent, clumpiness, alignment with the stellar and X-ray components, and levels of star formation or AGN activity vary widely from system to system. Some galaxies host compact nuclear nebulae; others show extended filaments or disc-like structures; many exhibit only weak signatures—or none at all—of these phenomena.

4.2 Peak Offsets

The degree of spatial (and kinematic) coincidence between the peaks of the stellar continuum, the hot X-ray emitting ICM, and the ionised gas provides a diagnostic of the dynamical state of a galaxy cluster and the physics of the baryon cycle. In a fully relaxed, dynamically old cluster, the BCG is expected to sit at the bottom of the cluster's gravitational potential well. In this idealised scenario these three components should be co-spatial and at the same velocity. The stellar continuum peak marks the centre of the galaxy's mass, which should align with the minimum of the potential. The hot ICM, in hydrostatic equilibrium, will also exhibit a centrally-peaked, symmetric surface brightness distribution, with its peak coincident with the BCG. If a cooling flow is present, gas from the ICM cools and condenses, leading to nebular emission (e.g., from Hα or [OII]) and potential star formation that is also expected to be centrally located, feeding directly onto the BCG [Fabian, 1994]. This alignment is the hallmark of a quiescent, cool-core cluster.

Deviations from this are indicative of recent or ongoing dynamical processes. A significant offset between the BCG's stellar continuum peak and the centroid of the large-scale X-ray emission may be an indicator of a recent cluster-cluster merger [Hamer et al., 2012, Sanderson and Ponman, 2010]. During a merger, the collisionless galaxies and the collisional ICM respond differently to the gravitational perturbation. The ICM clouds from the two subclusters collide, shock, and coalesce, with their combined X-ray peak marking the new centre of the merged potential well. The BCG, however, being a collisionless system of stars, can be displaced from this

new minimum and will oscillate within the potential, eventually sinking back to the centre via dynamical friction over several hundred million years [Lauer et al., 2014]. The magnitude of this offset is therefore correlated with the dynamical youth of the cluster, providing a 'clock' for the time elapsed since a major merger event [Rossetti et al., 2016].

Offsets involving ionised gas reveal more localised physics related to gas accretion and AGN feedback. The morphology of this gas is often filamentary and clumpy, extending for tens of kiloparsecs. An offset between the peak of the ionised gas emission and the stellar continuum can signify that star formation is being triggered externally, for instance in a plume of gas stripped from the BCG by ram pressure. In many cool-core clusters, the AGN at the centre of the BCG inflates relativistic jets that push aside the hot ICM, creating X-ray-dim bubbles or 'cavities'. Observations have repeatedly shown that the bright Hα filaments are not located at the X-ray peak, but are often wrapped around the rims of these AGN-driven cavities [Hogan et al., 2015]. This spatial anti-correlation represents some of the strongest observational evidence for the AGN feedback loop, where the mechanical energy from the central black hole prevents catastrophic cooling of the ICM by displacing the gas that would otherwise cool, or by uplifting already-cooled gas from the very centre [McNamara and Nulsen, 2007]. The relative locations of these components allow us to directly witness the complex interplay between gravity, cluster dynamics, and galaxy feedback.

Fig. 4.1 summarises the diversity in the morphology of the ionised gas in the Kaleidoscope sample. We show four panels for each line-emitting object: the 2D continuum and ionised gas maps overlaid with contours highlighting the X Ray emission in addition to the velocity and velocity dispersion maps of the ionised gas.

Fig. 4.2 shows the offset of the stellar continuum peak and the gas peak relative to the X-ray centroid for each line-emitting BCG in our sample with Chandra data. By construction, the stellar offsets are always positive, while gas offsets are signed according to whether they lie on the same side of the X-ray peak as the stellar centroid. The 'sides' are separated by the line which passes through the X-Ray centroid and is perpendicular to that connecting this point with the stellar peak.

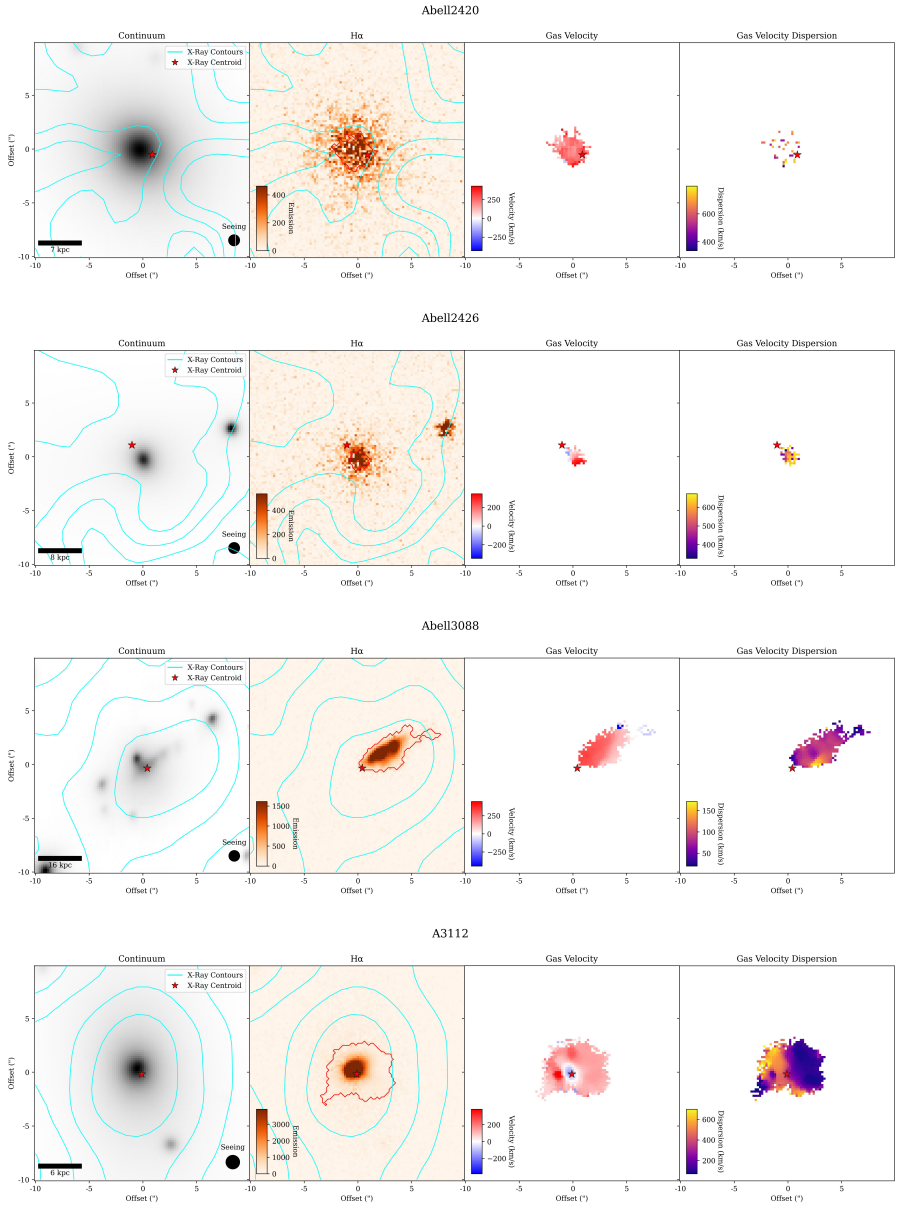

Figure 4.1: Summary of ionised line emission and X-Ray properties of the sample. The left hand panel shows the stellar continuum from MUSE observations, with cyan contours representing X-ray emission. The red star indicates the X-ray centroid. The second panel shows the distribution map of the primary ionised gas emission, typically Hα or [OII]. The red contour outlines the region of emission used for kinematic analysis. The third panel shows the line-of-sight velocity field of the ionised gas, showing its motion relative to the observer. The final panel shows the velocity dispersion map of the gas, which indicates the degree of turbulent or random motion.

A3266

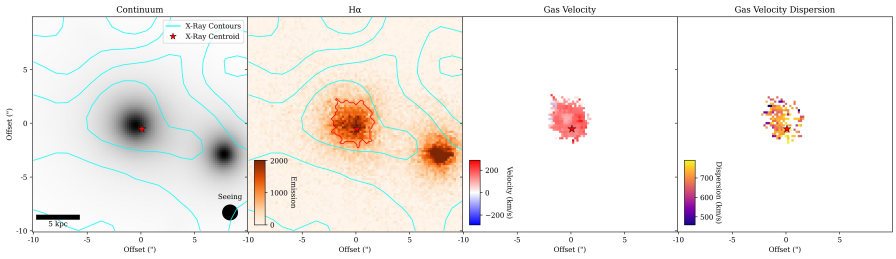

A383

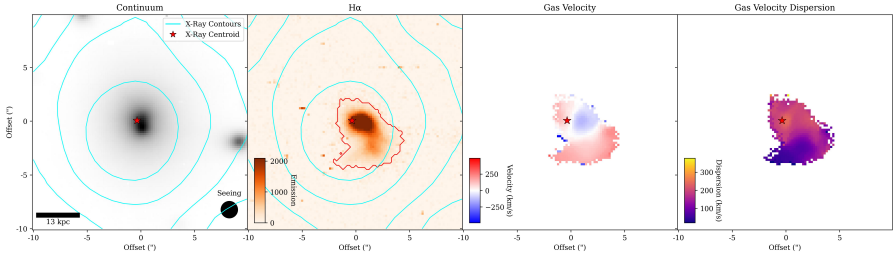

A3866

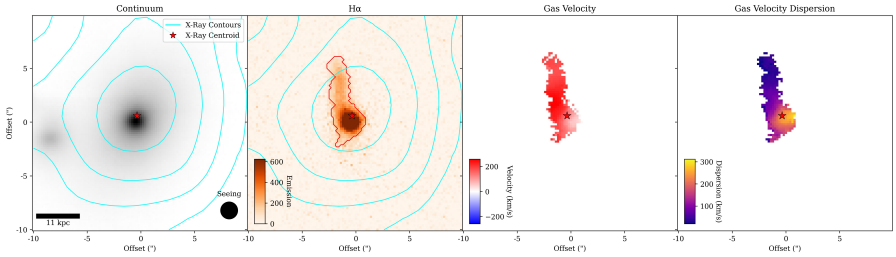

A3017

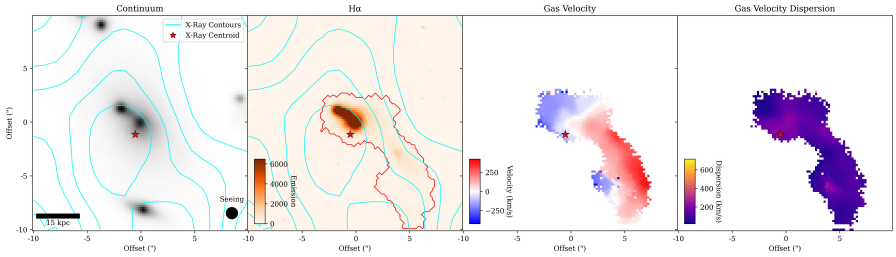

Continued

A3378

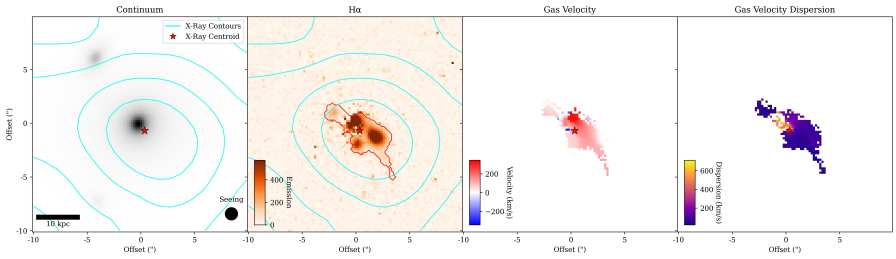

MACS0150.3-1005

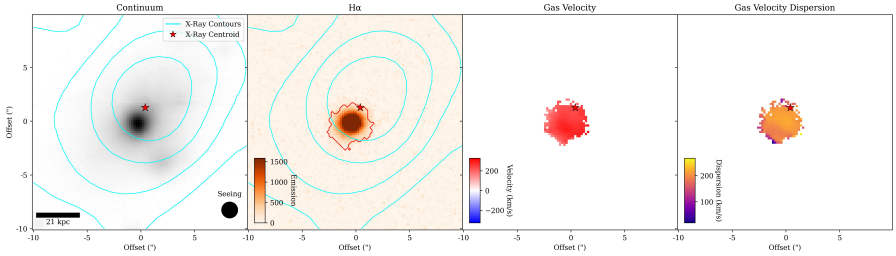

MACS0159.8-0849

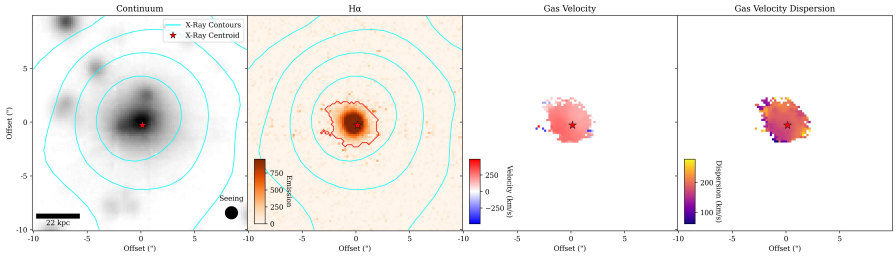

MACS1423.8+2404

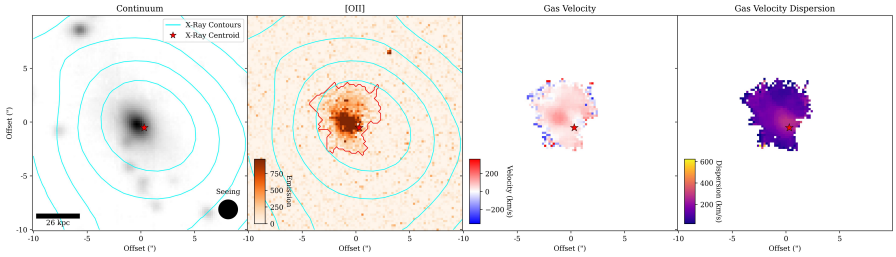

Continued

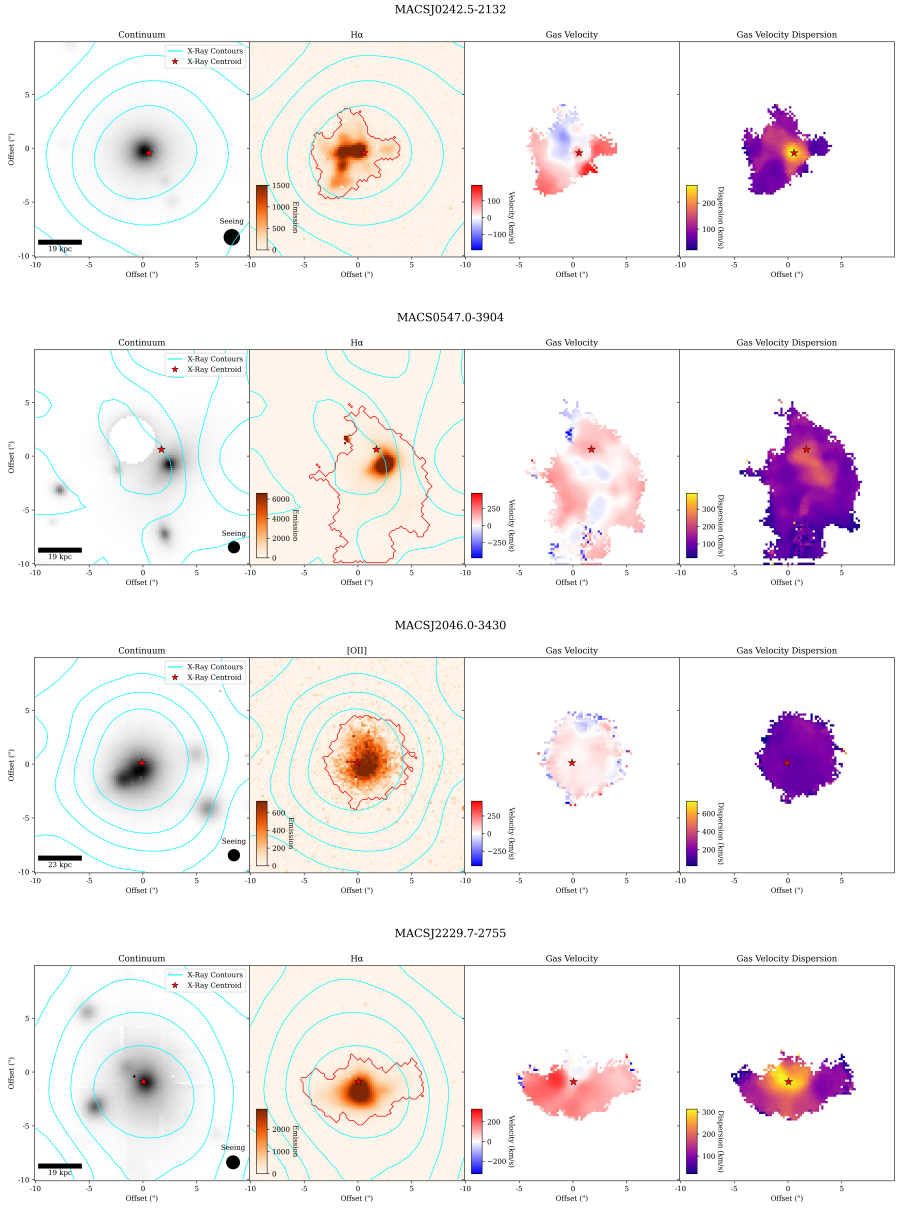
MACSJ0242.5-2132
Continuum
Hα
Gas Velocity
Gas Velocity Dispersion
X-Ray Contours
X-Ray Centroid
Seeing
19 kpc
Emission
Velocity (km/s)
Dispersion (km/s)
Offset (")
MACS0547.0-3904
Continuum
Hα
Gas Velocity
Gas Velocity Dispersion
X-Ray Contours
X-Ray Centroid
Seeing
19 kpc
Emission
Velocity (km/s)
Dispersion (km/s)
Offset (")
MACSJ2046.0-3430
Continuum
[OII]
Gas Velocity
Gas Velocity Dispersion
X-Ray Contours
X-Ray Centroid
Seeing
23 kpc
Emission
Velocity (km/s)
Dispersion (km/s)
Offset (")
MACSJ2229.7-2755
Continuum
Hα
Gas Velocity
Gas Velocity Dispersion
X-Ray Contours
X-Ray Centroid
Seeing
19 kpc
Emission
Velocity (km/s)
Dispersion (km/s)
Offset (")

Continued

MACSJ1115.8+0129

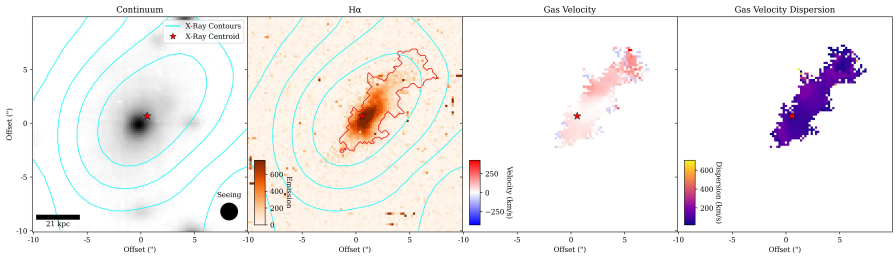

MACSJ1427.6-2521

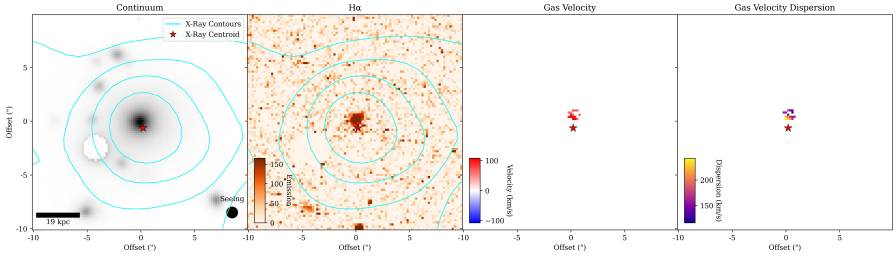

Zw2089

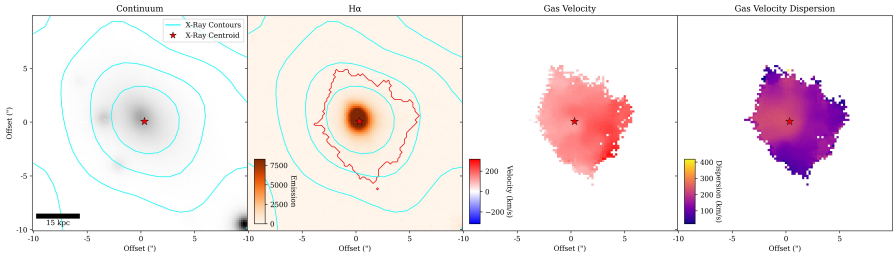

Zw3146

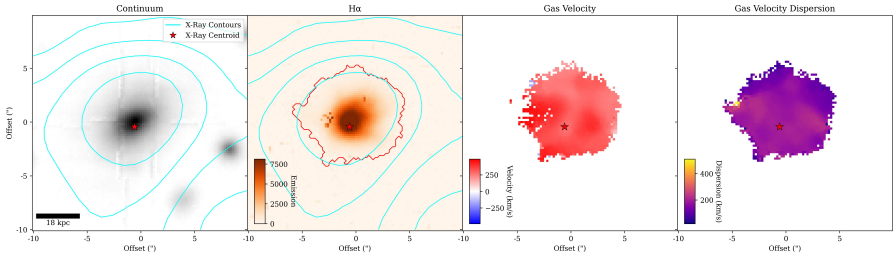

Continued

Sanderson et al. (2009) measure the two-dimensional separation between the X-ray surface-brightness centroid and the optical position of the brightest cluster galaxy (BCG) for a sample of 65 LoCuSS clusters at $0.15 \leq z \leq 0.3$ (median $z = 0.23$). The distribution of these offsets is approximately log–normal, with a median of

$$\Delta_{\mathrm{X–BCG}} \simeq 13 \text{ kpc} \quad (\sim 1.0\% \, r_{500})$$

and an interquartile range corresponding to 0.0035–0.04 r_{500}. When normalised by r_{500}, 80 per cent of the clusters lie within $0.02\,r_{500}$ of the BCG, demonstrating that in the majority of systems the stars sit tightly at the bottom of the potential well.

Splitting the sample by the presence of Hα line emission in the BCG reveals a dichotomy: all 23 of the line-emitting BCGs have $\Delta_{\mathrm{X–BCG}} \leq 15\,\mathrm{kpc}$ (or $\leq 0.02\,r_{500}$), whereas non–line emitters show a much broader offset distribution (median $\sim 35\,\mathrm{kpc}$; $\sim 0.028\,r_{500}$). As an aside; they find a similar trend holds for radio-active BCGs, although a secondary peak of radio emitters at intermediate offsets (0.03–0.08 r_{500}) suggests that some AGN may be triggered by recent dynamical disturbances even when the galaxy is not coincident with the cool core.

Our data, summarised in Fig. 4.2, support the conclusion that Hα-bright BCGs lie exclusively within 15 kpc of the X-ray centroid, providing further evidence that star formation in cluster cores requires not only a deep potential and low central entropy ($K < 30\,\mathrm{keV\,cm^2}$) but also close spatial alignment of the cold gas with the X-ray peak (the 'cool core'). We note that only $N = 17$ systems are shown, reflecting the partial overlap between the line-emitting Kaleidoscope sub-sample and available Chandra coverage (drawn primarily from the ACCEPT compilation and supplemented by additional archival observations); nevertheless, the same trend is evident. Offsets larger than $\sim$ 10–15 kpc likely reflect gas sloshing induced by minor mergers or AGN outbursts, displacing the coolest gas (and associated line emission) from the bottom of the potential well.

Fig. 4.3 reveals a positive correlation between the absolute offset from the X–ray peak and redshift for both the stellar continuum and the ionised gas. The best–fit slopes are 8.82 ± 3.57 and 10.00 ± 4.99 kpc per unit redshift for the continuum and gas, respectively, implying detections at $\sim 2.5\sigma$ (continuum) and $\sim 2.0\sigma$ (gas).

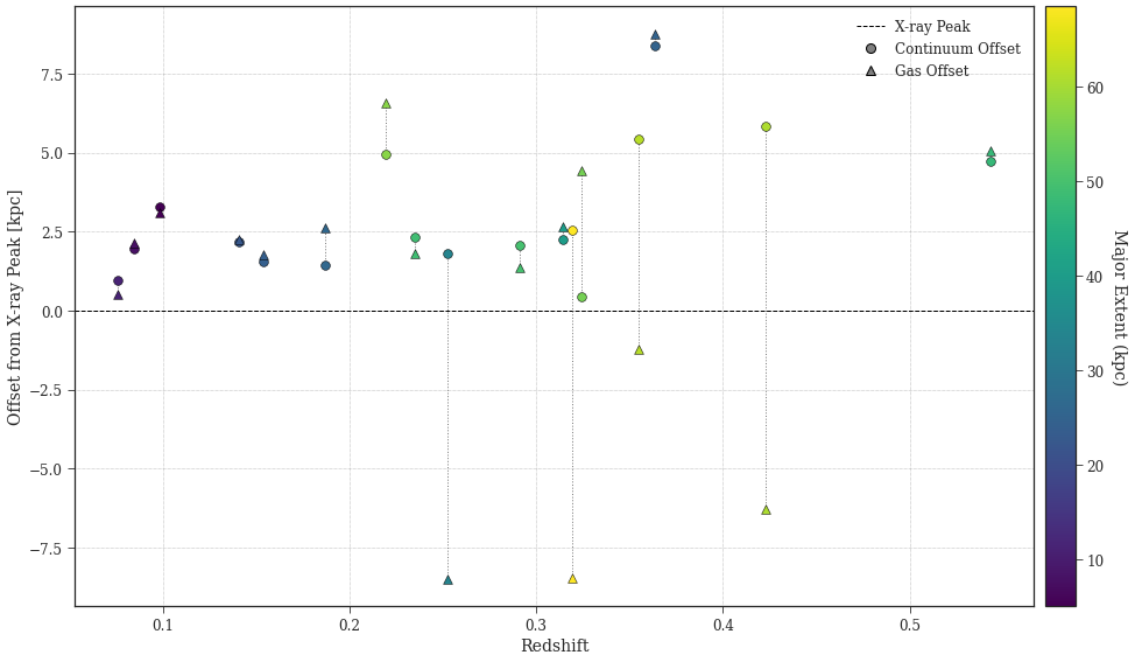

Figure 4.2: Spatial offset of the stellar continuum (circles) and ionised gas (triangles) from the central X-ray peak as a function of redshift. The horizontal dashed line at 0 kpc marks the X-ray peak. For each galaxy, the stellar offset is plotted as positive by construction, while the gas offset is signed to indicate whether it lies on the same (positive y) or opposite (negative y) side of the X-ray peak. Point colour encodes the galaxy's major physical extent (kpc), as shown by the colourbar. Only $N = 17$ systems are shown because only a subset of the line-emitting Kaleidoscope sample has suitable Chandra coverage—drawn primarily from the ACCEPT compilation and supplemented by additional archival observations—so the overlap between the IFU sample and available X-ray data is partial.

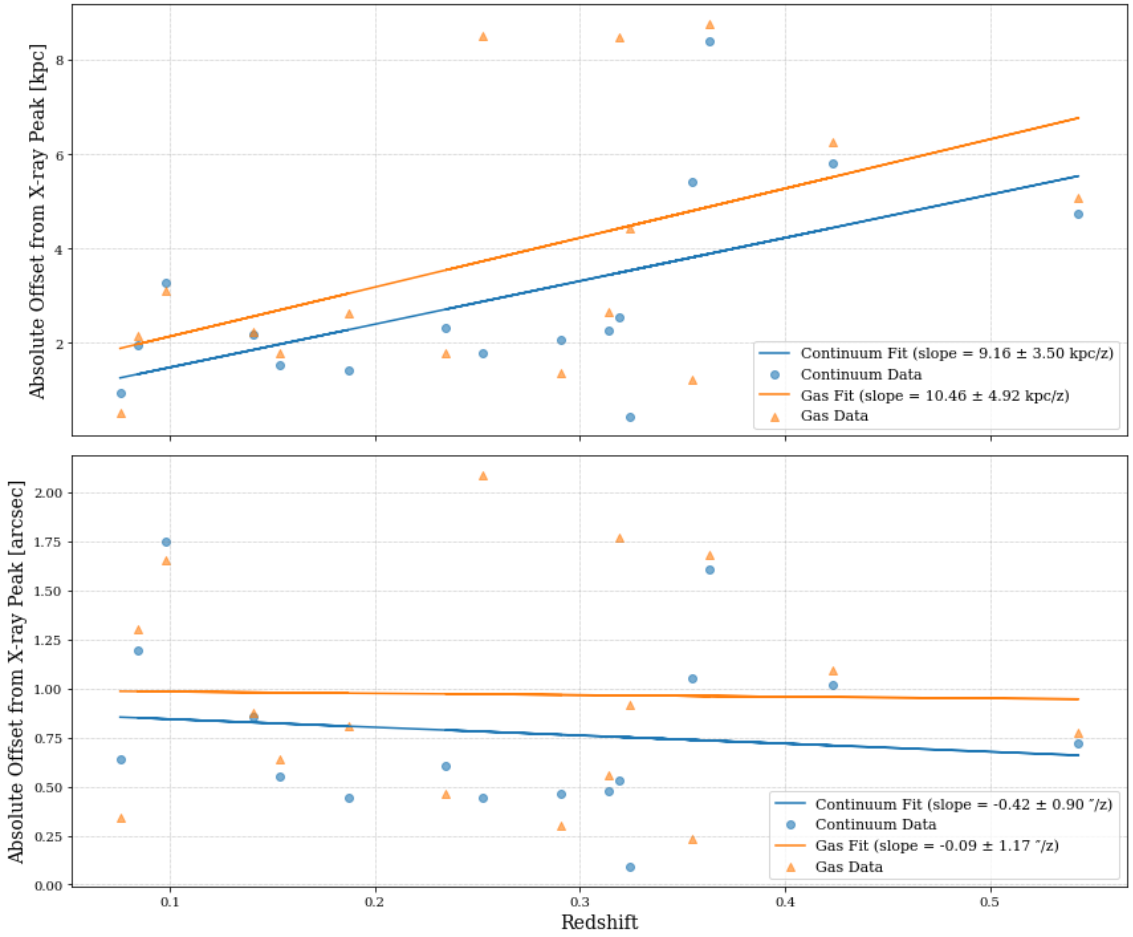

Figure 4.3: Absolute offset between the X–ray peak and the peaks of the stellar continuum (blue circles) and ionised gas (orange triangles) as a function of redshift, shown in two units. **Top:** Offsets in physical units (kpc). Linear fits yield slopes of 9.16 ± 3.50 kpc per unit redshift for the continuum and 10.46 ± 4.92 kpc per unit redshift for the gas, indicating a positive trend of physical separation with redshift. **Bottom:** The same offsets in angular units (arcsec). The best–fitting slopes, -0.42 ± 0.90 arcsec/z (continuum) and -0.09 ± 1.17 arcsec/z (gas), are consistent with no redshift dependence. Together, the panels show that while the physical separations increase with redshift the angular separations remain roughly constant and, importantly, at separations typically less than the seeing. Solid lines in each panel denote the least-squares fits; uncertainties are 1σ.

At fixed redshift the gas points frequently lie above the continuum, and the gas shows visibly larger scatter, suggesting that non–gravitational processes (e.g. AGN feedback, ram pressure, sloshing) displace or stir the ionised phase more efficiently than the stars. Quantitatively, across the observed baseline ($z \sim 0.1$–0.5) the fits imply a typical increase of a few kiloparsecs in the characteristic offset for both tracers—non–negligible compared to the median separations in the sample. While the trend is suggestive there is significant scatter within what is a small sample of obejcts, and the absolute offsets are still small.

4.3 Classification

4.3.1 Ionised Gas

We will now restrict our attention to just the morphology of the ionised gas. While this is diverse, as seen in Fig. 4.1, it is possible to split the sample into several broad categories. The region of emission, that is the set of pixels whose shape we are categorising, is defined following the process described in § 2.3.2 and shown in Figure Fig. 4.4. We also use the following derived properties to aid in the classification: the major axis, defined as the maximum straight length of continuous emission which passes through the Hα peak, and the minor axis, the length of continuous emission perpendicular to the major axis also coincident with the peak of Hα emission. These values were calculated as described in § 2.3.2. We will first apply the morphology classification outlined in [Hamer et al., 2016], which were based on a large BCG survey with the VIMOS instrument on the VLT. This X-ray–selected IFU sample comprises BCGs drawn from the ROSAT Brightest Cluster Survey (BCS; 201 systems) and the ESO EXCESS survey (446 systems). Long-slit spectroscopy in EXCESS identified optical line emitters (Hα in $\sim$30%, consistent with BCS), after which we required an integrated Hα flux $> 10^{-15}\,\mathrm{erg\,cm^{-2}\,s^{-1}}$ and an extent $> 2''$, yielding 78 candidates (73 observed) with VIMOS/VLT targeting Hα to $z \leq 0.25$. Although the total number of observations is significantly smaller than in the Kaleidoscope survey, this sample was explicitly selected for optical line emission and therefore contained a larger number of line-emitting systems. The classification

algorithm is as follows.

1. **Compact:** The minor extent of emission is less than twice the average DIMM seeing during the observation of that object. DIMM seeing values varied between 1.005 and 2.114 in the observation comprising the sample and redshift ranged from 0.0556 to 0.702 and as such this classification will cover a broad range of physical extents.

2. **Plume:** A plume describes a morphology in which the extent of Hα emission is not symmetric about the peak. The location of the peak along the major axis is parameterised on a 0-1 scale with a plume defined as when this value is below 0.33 or greater than 0.66.

3. **Offset:** An object is offset if the peak of Hα emission is offset from the peak in the continuum emission by more than twice the DIMM seeing.

4. **Quiescent:** Quiescent objects have Hα emission extending beyond twice the seeing with an elliptical, centrally concentrated morphology.

5. **Disturbed:** The final classification has no strict selection criteria and instead includes all objects which do not fit into one of the four morphologies above. To be classed as disturbed an object must necessarily have an extended, non-uniform morphology.

Applying this methodology to the Kaleidoscope sample results in the breakdown shown in Table 4.1

The morphology distributions for the line–emitting subsamples differ markedly between Kaleidoscope (MUSE) and the VIMOS survey of Hamer et al. [2016]. In Kaleidoscope, plumes dominate (27/46; 58.7%), with compact, quiescent, and disturbed systems each contributing 13.0% (6/46) and truly offset systems being rare (1/46; 2.2%). By contrast, the VIMOS sample is predominantly quiescent (45/73; 61.6%), with disturbed 17.8%, plumes 13.7%, offsets 5.5%, and compact 1.4%. Despite such a contrast the differences are largely explained by instrumental and selection differences rather than intrinsic population changes.

Table 4.1: Morphology distribution for the line–emitting Kaleidoscope subsample compared to the VIMOS BCG sample of Hamer et al. [2016].

	Kaleidoscope		Hamer+16 (VIMOS)	
Morphology	Count	%	Count	%
Compact	6	13.0	1	1.4
Plume	27	58.7	10	13.7
Offset	1	2.2	4	5.5
Quiescent	6	13.0	45	61.6
Disturbed	6	13.0	13	17.8
Total	46	100.0	73	100.0

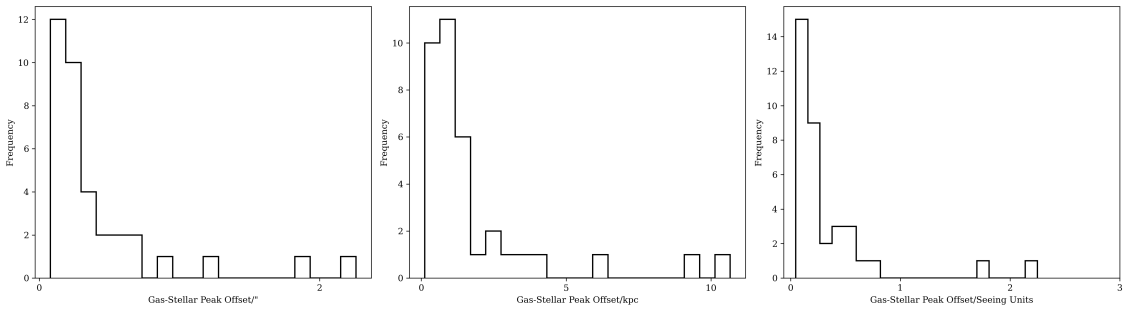

Figure 4.4: Distribution of the separation between the the peak in the continuum and the peak in the intensity of the diagnostic line in units of arcsec (left), kpc (centre), and seeing (right)

The finer spatial sampling of MUSE (0.2″ spaxels) enable robust resolution of narrow, low–surface–brightness filamentary extensions that would be smoothed into centrally concentrated emission at the coarser sampling and seeing that characterised VIMOS observations. Because the decision boundaries are explicitly tied to the PSF (e.g., "extent $> 2\times$ seeing," offsets within or beyond the seeing disk), a larger PSF and coarser sampling systematically push borderline cases toward the *quiescent* bin, whereas MUSE resolves the same systems as *plumes* or *disturbed*. We therefore reclassify a substantial fraction of objects that would appear *quiescent* at VIMOS resolution into *plume* or *disturbed* categories, consistent with the operational, PSF–anchored definitions.

It should be noted that a given gas morphology will frequently satisfy more than one of these criteria therefore placing importance on the somewhat arbitrary ordering of the decision tree. The result of the classification, shown in Table 4.1

and Fig. 4.5, should be interpreted with this in mind. Later analysis focussing on a morphological subset of the sample will use this classification scheme flexibly.

A significant amount of time was spent trying to produce statistics demonstrating the diversity in morphology contained in this sample. This will be discussed, though no quantisation illustrates this spread as effectively as the tile plot Fig. 4.4. The white contour outlines the region of line emission as defined in § 2.3.2. The diversity of orientation, extent and morphology is evident, as are the limitations of the classification algorithm.

We propose an update to this classification algorithm to take advantage of the significant hardware improvements afforded by MUSE. This morphology scheme is physically motivated to separate centrally concentrated cooling from anisotropic, mechanically driven flows, and it is designed to exploit the strengths of MUSE relative to VIMOS. The decision boundaries are tied to the instantaneous PSF (e.g. the 1.5× DIMM thresholds and the requirement that true "offsets" exceed the seeing disk), so a well–sampled, stable PSF is crucial. With MUSE's 0.2″ spaxels and higher surface–brightness sensitivity over a contiguous IFU field, we can (i) resolve the minor axis to distinguish *Extended Core* from *Diffuse Core*, (ii) measure small but astrophysically meaningful centroid separations to identify *Offset* systems, (iii) recover low–contrast, one–sided extensions that signify *Plumes*, and (iv) quantify light–distribution asymmetry for *Disturbed* cases. These measurements are the ones most susceptible to PSF under–sampling, slit/fibre losses, and coarse spatial sampling; at VIMOS resolution many such features blend into apparently quiescent, centrally peaked morphologies.

This provides a classification algorithm which maps directly onto physical scenarios: unresolved emission is consistent with compact nuclear or beam–smeared structure; clear offsets point to displaced or infalling gas; plumes trace directed transport (e.g. uplift or sloshing) rather than isotropic cooling; extended or diffuse cores indicate round, centrally concentrated emission with different levels of beam–limited resolution; and disturbed systems capture non–uniform structures symptomatic of ongoing feedback or accretion. In short, the same quantitative cuts that were conservative at VIMOS become discriminating with MUSE, allowing us to

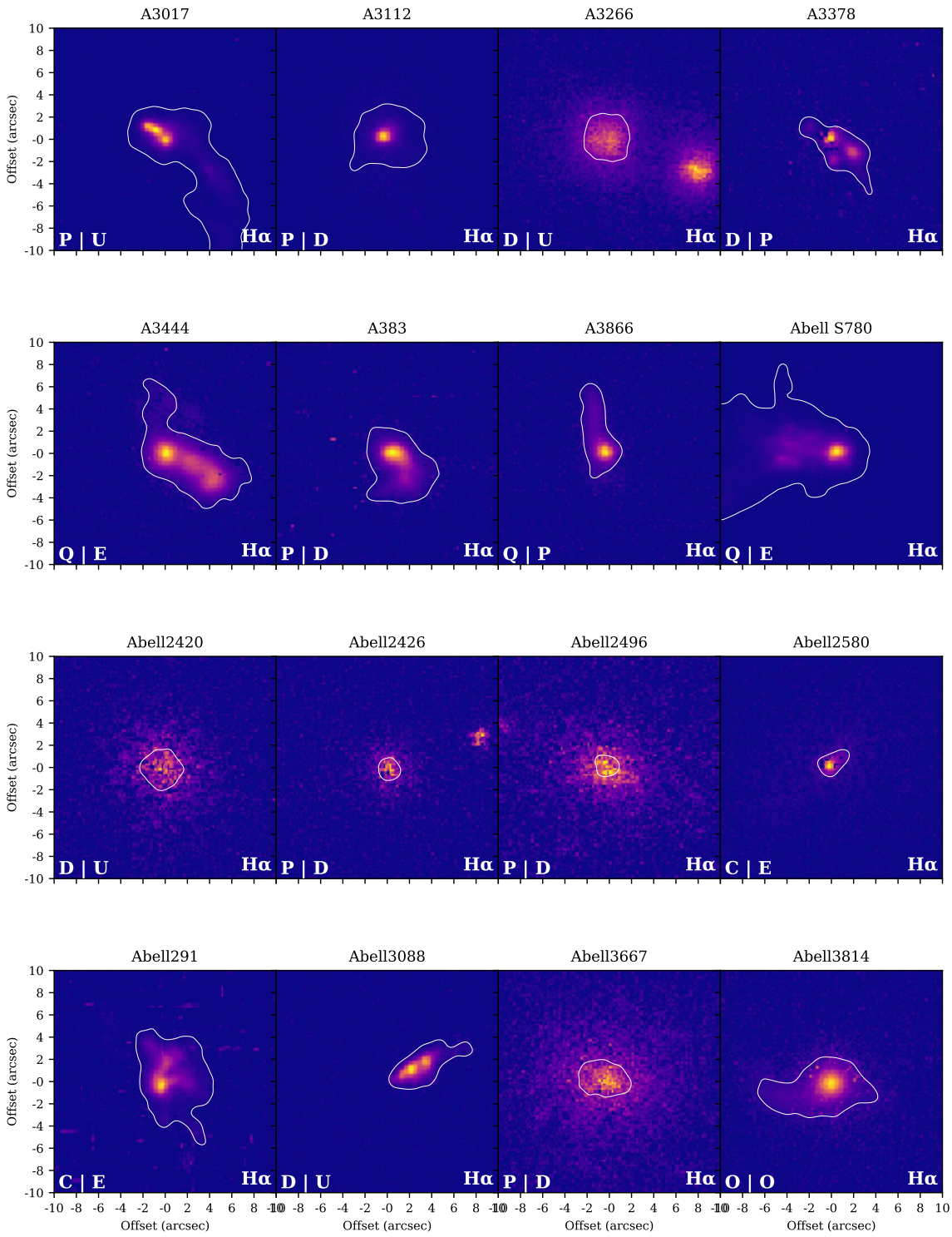

Figure 4.5: Tiled view of ionised–gas intensity maps for the Kaleidoscope line–emitting BCGs. Each panel is centred on the stellar–continuum peak of the BCG and annotated with the morphology codes in the format Old — New, where the first letter denotes the original scheme (**C**ompact, **Q**uiescent, **P**lume, **D**isturbed, **O**ffset), the second letter the revised scheme (**U**nresolved, **E**xtended core, **C** diffuse core, **P**lume, **D**isturbed, **O**ffset), and the trailing tag indicates the diagnostic line used (Hα or [OII]).

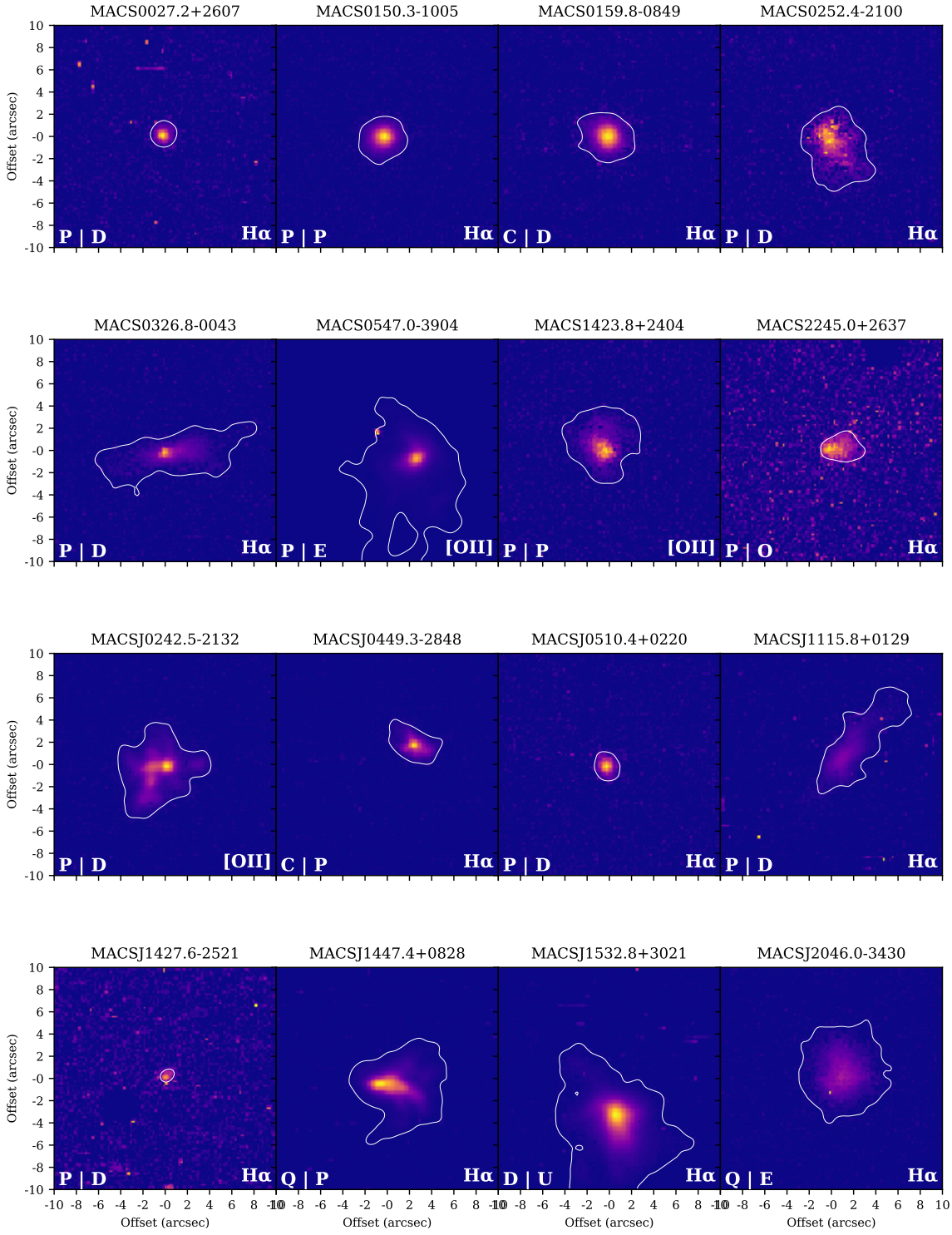
MACS0027.2+2607
MACS0150.3-1005
MACS0159.8-0849
MACS0252.4-2100
P | D Hα
P | P Hα
C | D Hα
P | D Hα
MACS0326.8-0043
MACS0547.0-3904
MACS1423.8+2404
MACS2245.0+2637
P | D Hα
P | E [OII]
P | P [OII]
P | O Hα
MACSJ0242.5-2132
MACSJ0449.3-2848
MACSJ0510.4+0220
MACSJ1115.8+0129
P | D [OII]
C | P Hα
P | D Hα
P | D Hα
MACSJ1427.6-2521
MACSJ1447.4+0828
MACSJ1532.8+3021
MACSJ2046.0-3430
P | D Hα
Q | P Hα
D | U Hα
Q | E Hα
Offset (arcsec)
Offset (arcsec)

Continued

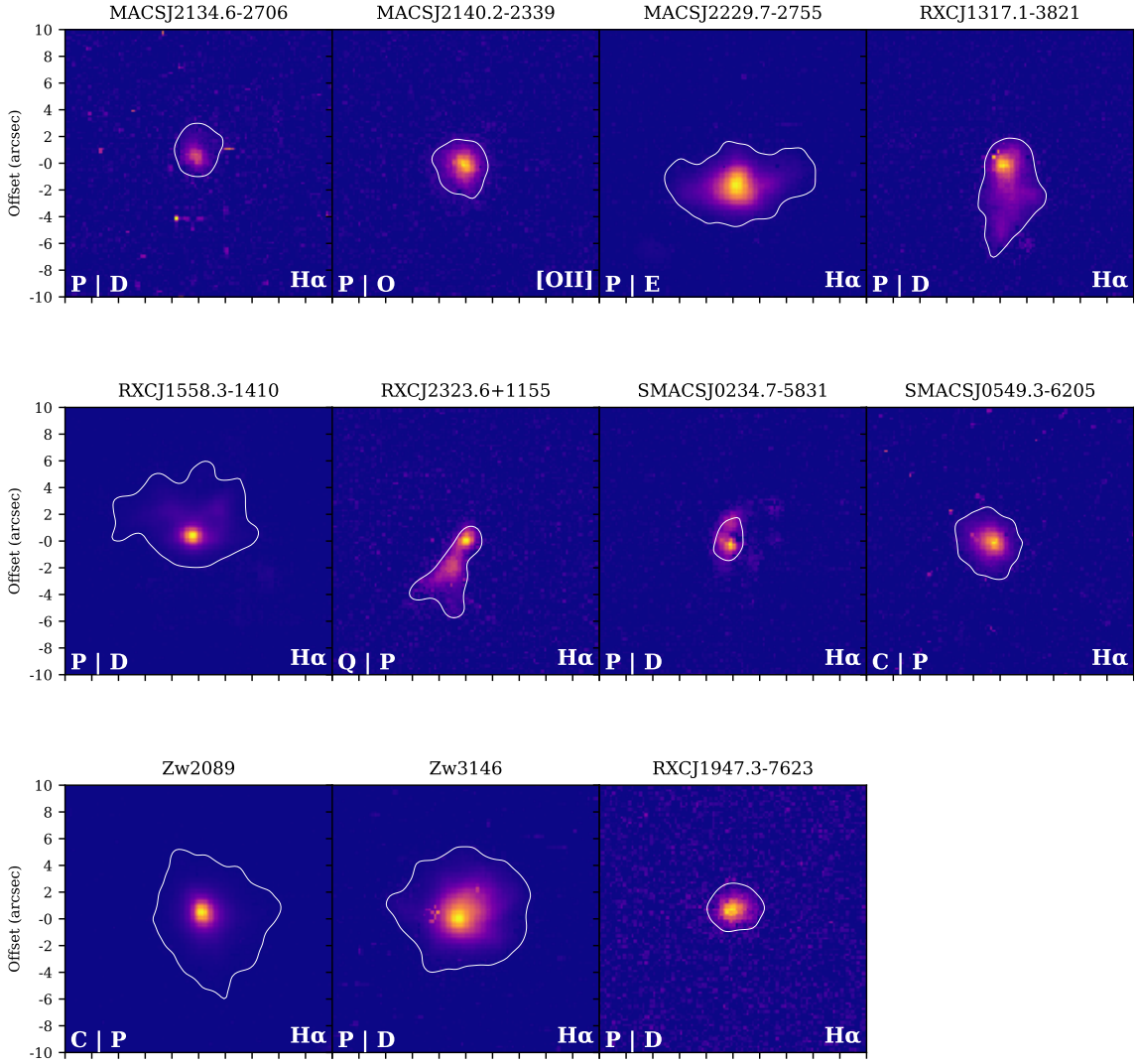
MACSJ2134.6-2706
MACSJ2140.2-2339
MACSJ2229.7-2755
RXCJ1317.1-3821
RXCJ1558.3-1410
RXCJ2323.6+1155
SMACSJ0234.7-5831
SMACSJ0549.3-6205
Zw2089
Zw3146
RXCJ1947.3-7623
Offset (arcsec)
P | D
P | O
[OII]
P | E
Q | P
C | P
Hα

Continued

separate genuinely anisotropic or displaced gas from apparently quiescent emission that was previously blurred by instrumental limitations.

1. **Unresolved:** The object's emission is classified as unresolved if its major axis extent is less than or equal to 1.5× the DIMM seeing value. This is the initial check for all objects.

2. **Offset:** An object is classified as offset if it is resolved (major axis > 1.5× DIMM seeing), but the peak of its gas emission is separated from the stellar continuum peak by a distance greater than the DIMM seeing value. This classification takes precedence over shape-based categories.

3. **Plume:** This describes a resolved, centered object that is distinctly elongated. The classification is applied when the ratio of the object's minor axis extent to its major axis extent is less than 0.5.

4. **Extended Core:** This classification is for objects that are 'roundish' (axis ratio ≥ 0.5) and symmetric (asymmetry parameter between 0.3 and 0.7). Crucially, the object must be well-resolved along both axes, with its minor axis extent also being greater than 1.5× the DIMM seeing.

5. **Diffuse Core:** This describes an object that is also roundish and symmetric, similar to an 'Extended Core'. However, while its major axis is resolved, its minor axis is not, being less than or equal to 1.5× the DIMM seeing.

6. **Disturbed:** This classification is applied to a resolved, centered object that is roundish in shape (axis ratio ≥ 0.5) but is asymmetric in its light distribution (asymmetry parameter is ≤ 0.3 or ≥ 0.7).

4.4 Ellipticity

Fig. 4.6 displays the relationship between the major and minor axes of ionised gas nebulae in the sub-sample of line-emitting BCGs. The nebulae are observed to be predominantly non-circular, with most data points lying significantly below the 1:1 circularity line (shown as the grey, dashed line). The sample spans a wide range of

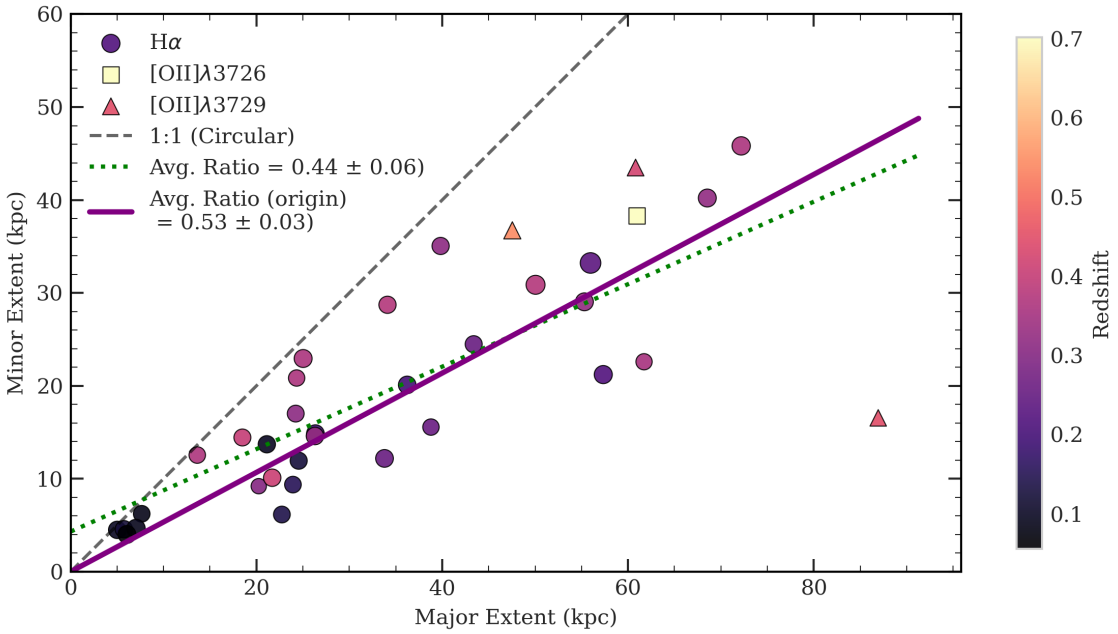

Figure 4.6: The relationship between the major and minor axes of ionised gas nebulae in our BCG sample. Data points are colour-coded by the redshift of the object while the shape indicates the diagnostic line used for measurement: Hα (red), [OII]λ3726 (blue), or [OII]λ3729 (green). The grey, dashed line shows the 1:1 locus, where objects would be perfectly circular. The green, dashed line represents a linear fit to the data, which has a slope of 0.44, indicating a strong tendency for the nebulae to be elongated rather than spherical. The slope increases to 0.53 when forcing a fit through the origin (solid purple)

sizes, with some nebulae extending to major axes of approximately 90 kpc. This visual trend is quantified by a linear fit to the data, which reveals an average axis ratio of $\langle b/a \rangle = 0.44$. While this first-order analysis does not consider projection effects, the sample size is large enough that some systems should be observed face-on. The notable lack of extended objects near the 1:1 line therefore strongly implies that the ionised gas does not typically settle into a quiescent, circular disc around the BCG.

This pronounced elongation points towards physical processes that are inherently anisotropic, rather than a simple, relaxed spherical distribution of gas. This follows from the theory of how the gas cools in § 1.3.4. Gas that cools and condenses from the ICM is not expected to do so perfectly isotropically and can form extensive filamentary networks. In this 'cold feedback' scenario, AGN jets can then provide the energy to prevent runaway cooling, either by directly pushing gas outwards

along a preferred axis or by inflating bubbles that stretch and disrupt the cooling gas, potentially causing or enhancing its elongated appearance.

This analysis does not account in any way for projection effects. It is possible to perform a very simple calculation with many simplifications to account for this. Calculating the expected mean axis ratio (purple line in Fig. 4.6) for a large population of intrinsically circular, thin discs that are oriented randomly in three dimensions with the obvious assumption that the gas surrounding a BCG can be modelled as an infinitesimally thin, circular disc of radius R. When observed, our line of sight makes an inclination angle, i, with the axis normal to the disc. An inclination of $i = 0°$ corresponds to a face-on view, while $i = 90°$ is an edge-on view. In projection, the disc appears as an ellipse. Its major axis, a, remains equal to the intrinsic radius R. The minor axis, b, is foreshortened by the projection and is given by $b = R\cos(i)$. The measured axis ratio, q, is therefore a direct function of the inclination angle:

$$q = \frac{b}{a} = \frac{R\cos(i)}{R} = \cos(i) \tag{4.1}$$

For a sample of objects with random spatial orientations, the probability of observing a system with an inclination between i and $i + di$ is proportional to the solid angle element, $dP \propto \sin(i)di$. Integrating $q(i)$ over all possible orientations (from $i = 0$ to $i = \pi/2$) and normalising by the integrated probability yields the expected value of the axis ratio

$$\langle q \rangle = \frac{\int_0^{\pi/2} q(i)\sin(i)di}{\int_0^{\pi/2} \sin(i)di} = \frac{\int_0^{\pi/2} \cos(i)\sin(i)di}{\int_0^{\pi/2} \sin(i)di} \tag{4.2}$$

Solving we find the expected mean axis ratio is:

$$\langle q \rangle = \frac{1/2}{1} = 0.5 \tag{4.3}$$

The average axis ratio observed in our sample is 0.44 ± 0.06 for an unconstrained linear fit to the data. This becomes 0.53 ± 0.03 when forcing a fit through the origin. These values are remarkably close to the theoretical expectation for randomly oriented, infinitely thin circular discs. This agreement is not evidence for such a

distribution of gas. The aim is to illustrate a fundamental bias inherent in morphological summary statistics: since observing a 3D structure in projection can only ever shorten an axis, never lengthen it, any statistical analysis will be systematically skewed toward smaller, more circular shapes. It is crucial to remain aware of this non-uniform effect of projection when interpreting such results.

4.5 Other Lines

§ 4.5 shows two–dimensional maps of several optical emission lines for a representative subset of the sample. In addition to Hα, which we used as our primary tracer in earlier sections, we now include other commonly used diagnostics such as [N,II]λ6583, [S,II]$\lambda\lambda$6716, 6731, [O,I]λ6300, [O,III]λ5007, and [O,II]$\lambda\lambda$3727, 7325. Each panel is centred on the BCG nucleus, with offsets shown in arcseconds and physical scales indicated in kiloparsecs.

These maps allow a direct comparison of the morphology and extent of different emission lines within the same galaxy. The most consistent result is that Hα and [N,II] are nearly always co-spatial, tracing the same filamentary structures and extended regions. The other low-ionisation lines show broadly similar distributions, though we can see the relative line strengths visualised as decreasing concentric areas.

This approach also provides a cross-check on our use of Hα as the preferred diagnostic at low redshift, and [O,II] at higher redshift when Hα is shifted out of the spectral window. The overall consistency between these tracers supports their largely interchangeable use in measuring the morphology of the ionised gas.

A striking feature of our sample is the near-universal cospatiality of the [N II] and Hα emission. Across essentially all systems, the two lines trace identical structures on both small and large scales, with no significant offsets between their spatial distributions. This remarkable alignment suggests that the warm ionised gas is chemically well-mixed and that both lines arise from the same physical component of the interstellar medium. Similar results have been reported in previous IFU studies of BCGs and cluster cores [e.g. Hatch et al., 2006, McDonald et al., 2012b,

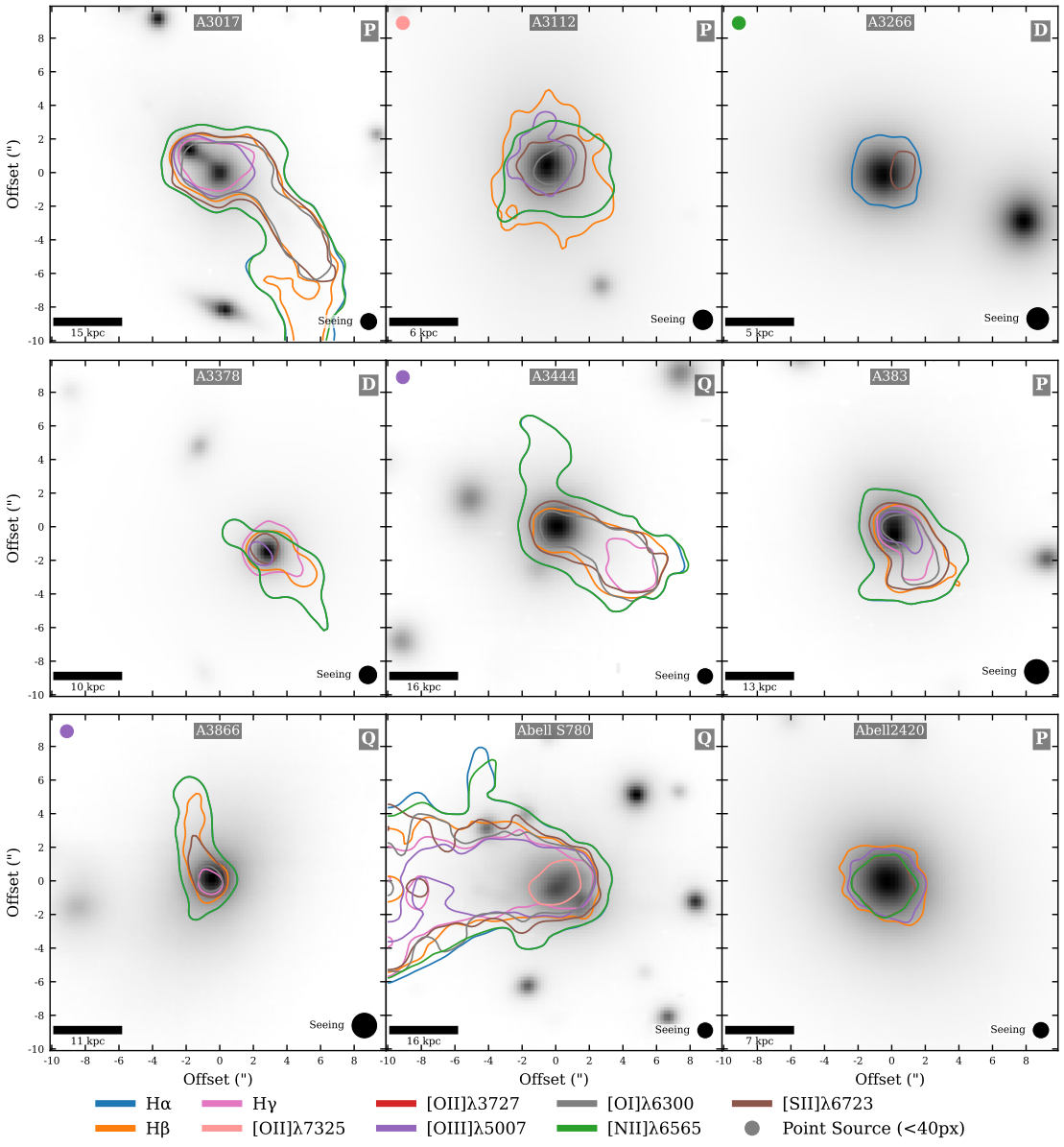

Figure 4.7: The spatial distribution of ionised gas for the line emitting galaxies in the Kaleidoscope sample. Each plot displays the stellar continuum emission in greyscale, with overlaid contours tracing the morphology of various ionised gas emission lines. The colour-coding for the emission line contours is defined in the legend at the bottom of each page, including key lines such as Hα (blue), [NII]$\lambda\lambda$6548, 6583 (green), and [OII]$\lambda\lambda$3726, 3729 (red). For emission line doublets, only the contour of the line with the larger total area is shown (these are typically very similar). Small coloured circles at the top of a panel indicate unresolved point-source emission (area $<$ 40 pixels) for the corresponding line. The letter in the top-right corner indicates the visual morphology classification: 'P' for plume, 'D' for disturbed, 'Q' for quiescent, and 'C' for compact based on the primary diagnostic line (Hα or [OII]$\lambda\lambda$3726, 3729. Small coloured circles at the top of a panel indicate unresolved, central, point-source emission ($area < 40pix$) for the corresponding line

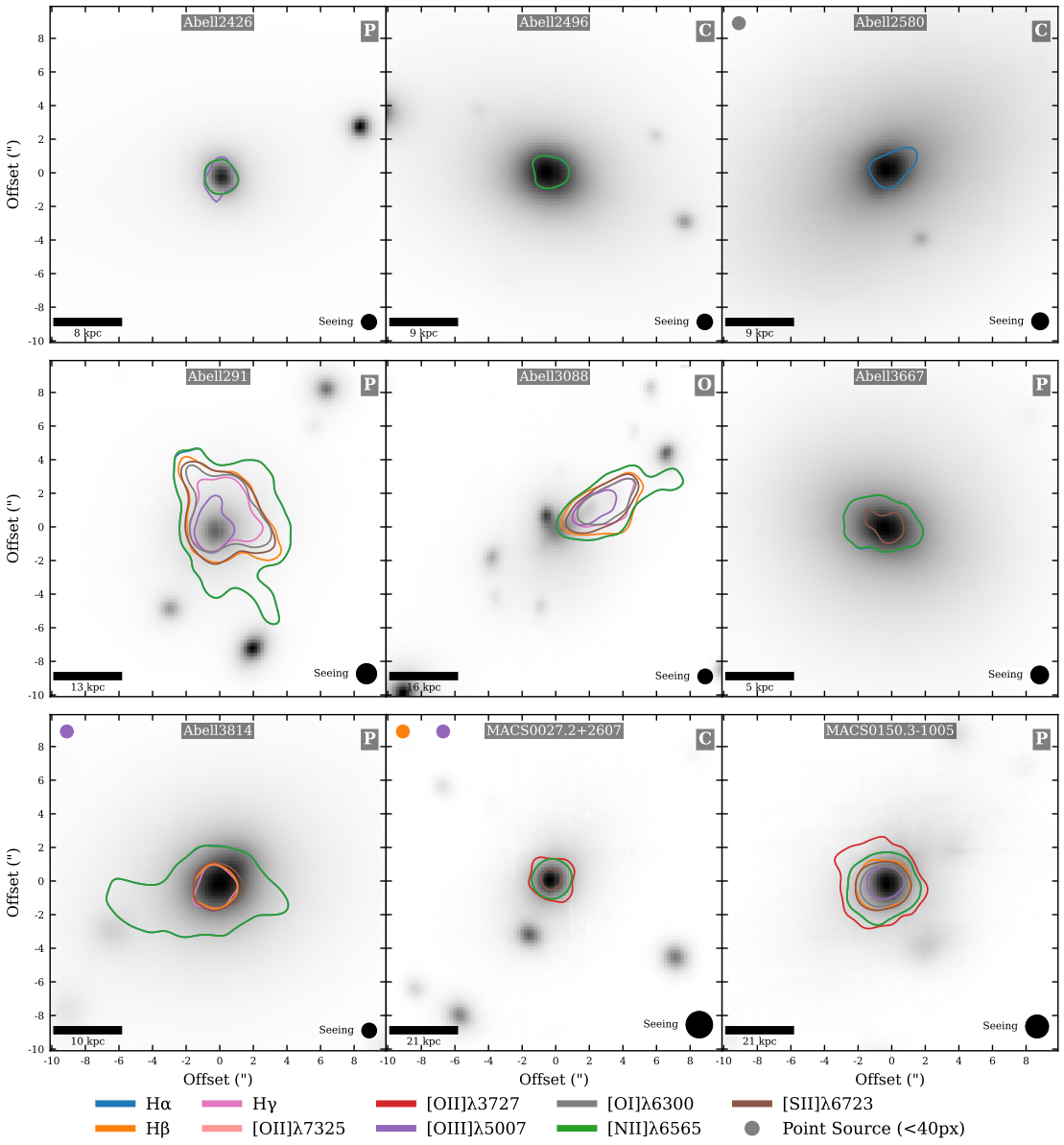
Abell2426
P
Abell2496
C
Abell2580
C
Abell291
P
Abell3088
O
Abell3667
P
Abell3814
P
MACS0027.2+2607
C
MACS0150.3-1005
P
Offset (")
Seeing
8 kpc
9 kpc
13 kpc
16 kpc
5 kpc
10 kpc
21 kpc
Hα
Hβ
Hγ
[OII]λ7325
[OII]λ3727
[OIII]λ5007
[OI]λ6300
[NII]λ6565
[SII]λ6723
Point Source (<40px)

Continued

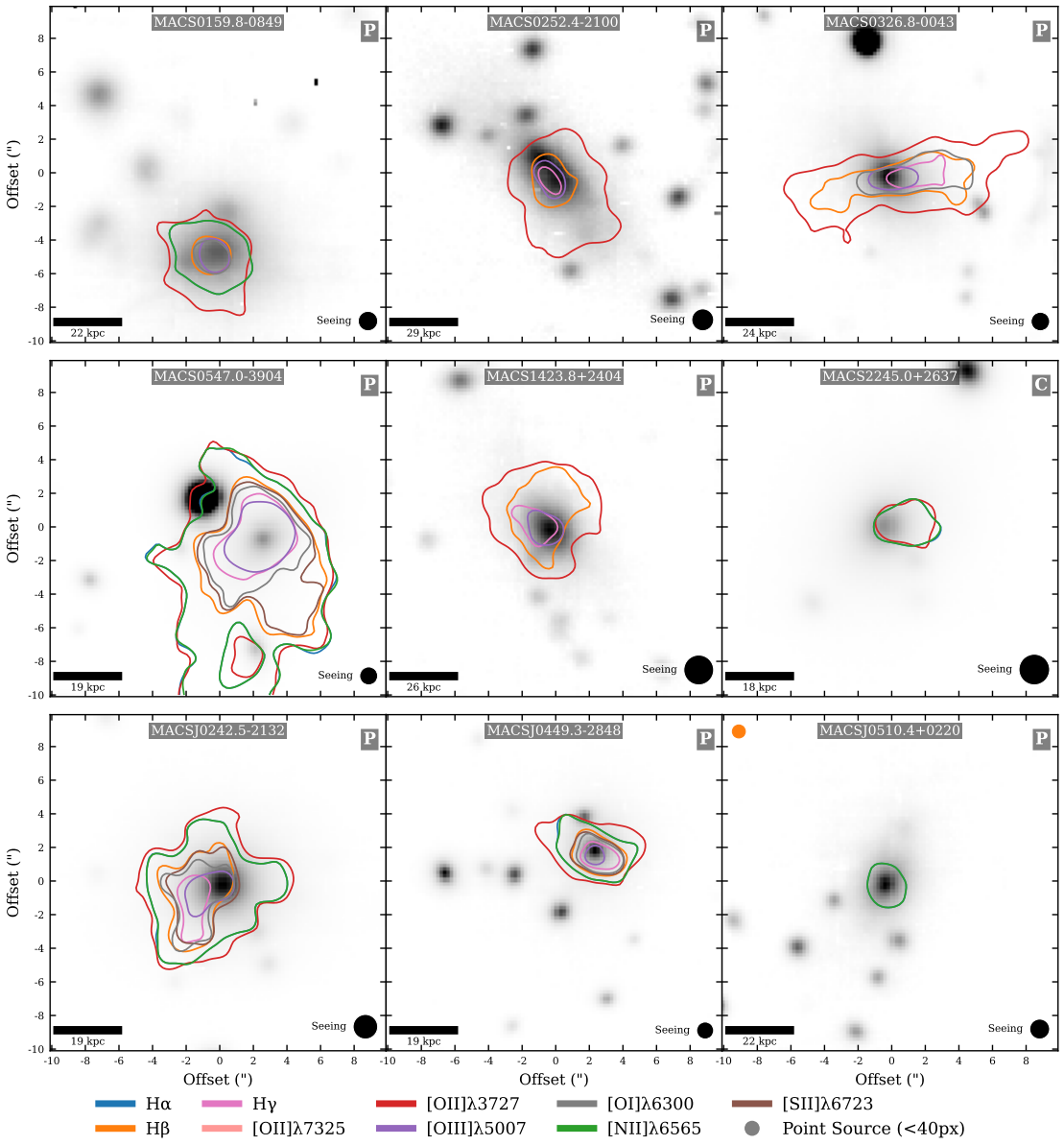
MACS0159.8-0849
MACS0252.4-2100
MACS0326.8-0043
MACS0547.0-3904
MACS1423.8+2404
MACS2245.0+2637
MACSJ0242.5-2132
MACSJ0449.3-2848
MACSJ0510.4+0220
P
C
Seeing
22 kpc
29 kpc
24 kpc
19 kpc
26 kpc
18 kpc
19 kpc
19 kpc
22 kpc
Offset (")
Hα
Hβ
Hγ
[OII]λ7325
[OII]λ3727
[OIII]λ5007
[OI]λ6300
[NII]λ6565
[SII]λ6723
Point Source (<40px)

Continued

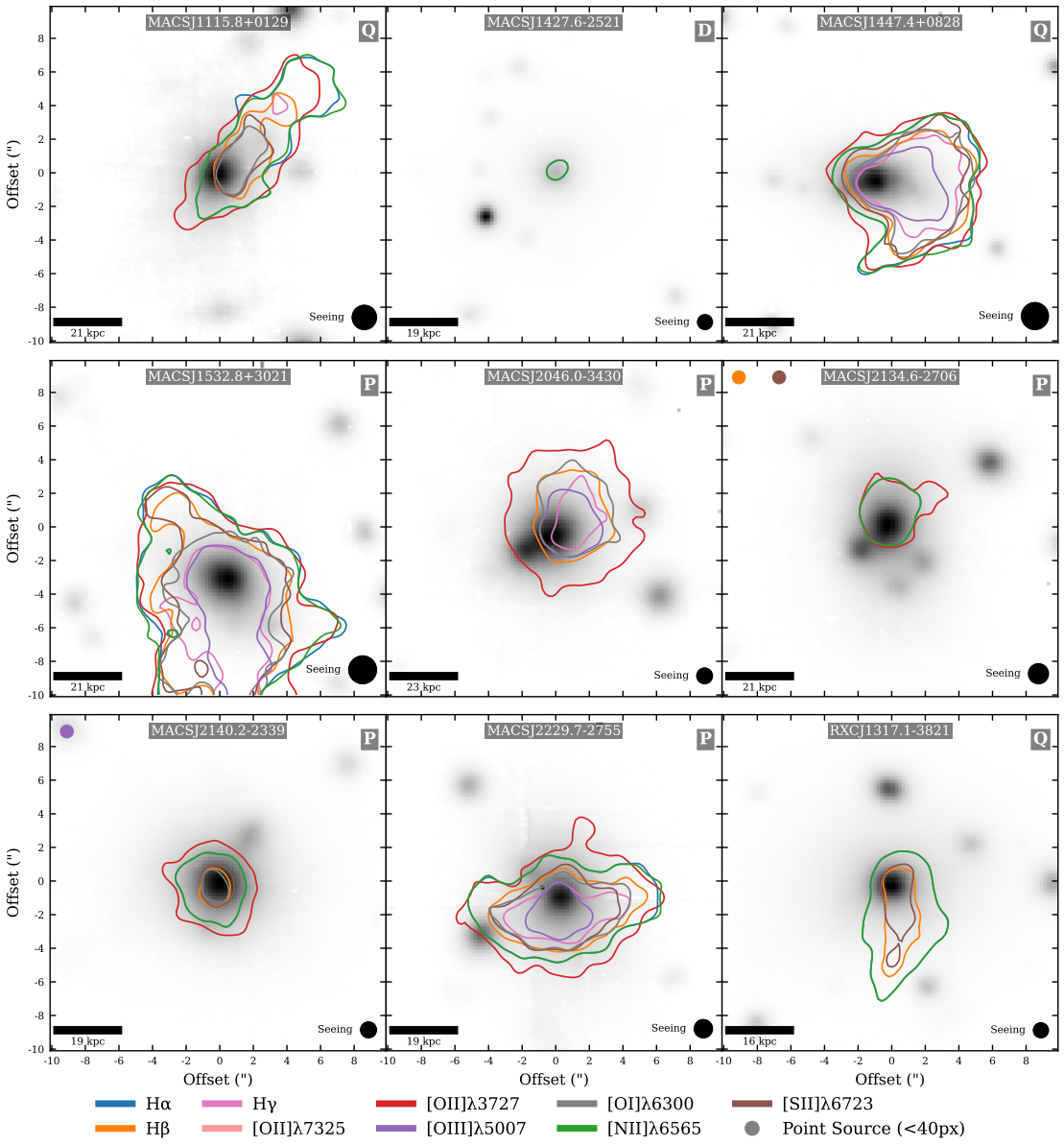
MACSJ1115.8+0129
Q
MACSJ1427.6-2521
D
MACSJ1447.4+0828
Q
MACSJ1532.8+3021
P
MACSJ2046.0-3430
P
MACSJ2134.6-2706
P
MACSJ2140.2-2339
P
MACSJ2229.7-2755
P
RXCJ1317.1-3821
Q
Seeing
21 kpc
19 kpc
23 kpc
16 kpc
Offset (")
Hα
Hβ
Hγ
[OII]λ7325
[OII]λ3727
[OIII]λ5007
[OI]λ6300
[NII]λ6565
[SII]λ6723
Point Source (<40px)

Continued

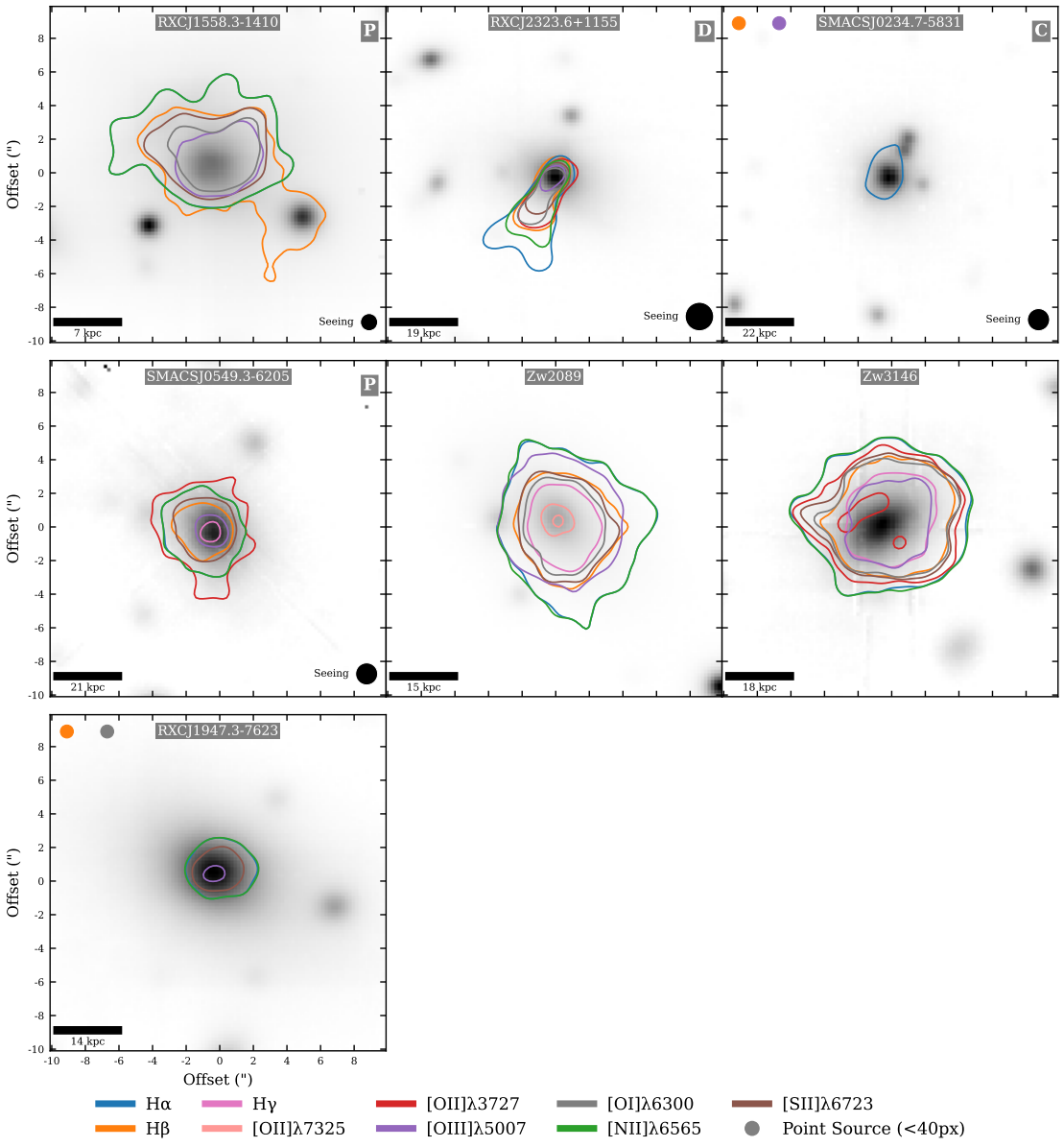
RXCJ1558.3-1410
P
RXCJ2323.6+1155
D
SMACSJ0234.7-5831
C
SMACSJ0549.3-6205
P
Zw2089
Zw3146
RXCJ1947.3-7623
Offset (")
Seeing
7 kpc
19 kpc
22 kpc
21 kpc
15 kpc
18 kpc
14 kpc
Hα
Hβ
Hγ
[OII]λ7325
[OII]λ3727
[OIII]λ5007
[OI]λ6300
[NII]λ6565
[SII]λ6723
Point Source (<40px)

Continued

Tremblay et al., 2018], where Hα and low-ionisation forbidden lines were found to be co-spatial and to trace extended filamentary structures. The consistency observed here reinforces our use of Hα (or [O II] at higher redshift) as a robust tracer of ionised gas morphology in BCGs.

4.5.1 [O II] vs. $H\alpha$

In § 2.3.2 we stated that any unqualified reference to 'gas' should be interpreted as referring to Hα if it is within the spectral window at the object redshift ($\approx z < 0.42$). At higher redshifts this would be taken to mean the [O II]λ3727 doublet. This logic covers all objects in our sample.

This definitional change introduces a potential systematic in any line-agnostic measurements of 'gas' properties, observed as a step-function at $z \approx 0.42$. We explore this in Fig. 4.8 by focussing on the subset of objects for which both lines are simultaneously visible. The comparison between Hα and [O,II] emission areas shows a tight correlation, with a best-fit slope of 0.91 ± 0.04 that lies close to unity. This indicates that both lines trace the ionised gas to very similar spatial extents. Since Hα is our preferred diagnostic, but is shifted out of the observed spectral window at higher redshift, this result validates the use of [O,II] as a substitute in those cases. The near-unity slope demonstrates that no major systematic bias is introduced by switching between the two tracers, and that our measurements of ionised gas extent are robust across the full redshift range of the sample.

Expanding the sample size to all objects we find that, on average, the [O II] emission region is ≈28% larger than that of Hα. However, significant object-to-object scatter in this ratio precludes the application of a simple, global correction factor. Furthermore, the measured extents are subject to observational effects, such as astronomical seeing and signal-to-noise limitations, which contribute to the measurement uncertainty. The sample size is too small to immediately attribute the redshift-extent correlation we see in Fig. 4.6 to this effect (and there is no obvious discontinuity at z = 0.42) but the possible bias should be noted.

4.6 Summary

In this chapter we have transitioned from establishing the incidence of optical line emission to quantifying how that emission is arranged on the sky. Leveraging the strengths of IFU data, we constructed continuum-subtracted, line-specific maps and derived spatial metrics that are uniform across the line-emitting sub-sample. We discussed the wavelength dependence of morphology (§ 4.1), validated a fiducial approach that prioritises Hα (or [OII] when Hα is inaccessible), and quantified projected offsets among the stellar continuum, ionised gas, and the X-ray centre (§ 4.2). A morphology scheme was introduced and simple, reproducible shape descriptors (ellipticity, characteristic radii; §§ 4.3 and 4.4) were extracted. Mapping additional, less common lines (§ 4.5) showed that low-ionisation tracers are typically co-spatial with Hα, supporting the use of interchangeable diagnostics for spatial characterisation. The overarching result is a heterogeneous portrait of BCGs: some systems host compact nuclear nebulae, others extended filaments or disc-like structures, and many exhibit weak or negligible line emission—diversity that is now captured by a consistent set of IFU-based spatial measurements.

These spatial diagnostics reinforce the cool-core picture while clarifying its limits. Hα-bright BCGs are found very close to the X-ray peak, consistent with the requirement of low central entropy for multiphase gas, whereas larger offsets likely trace dynamical disturbance (sloshing, AGN outbursts) that displaces the coolest material from the potential minimum. The statistics for X-ray alignment are somewhat limited by the limited overlap of our line-emitting Kaleidoscope sub-sample with available Chandra coverage, however we explore the $N = 17$ systems which do have data for the offset analysis. The observed trends are consistent with previous work and with the physical expectation that close spatial coincidence promotes condensation. The morphology–environment connections established here provide a controlled, spatially resolved context in which to interpret subsequent kinematic measurements.

The next chapter (Chapter 5) turns to the two-dimensional line-of-sight (LOS) velocity and velocity-dispersion fields derived from the same data.

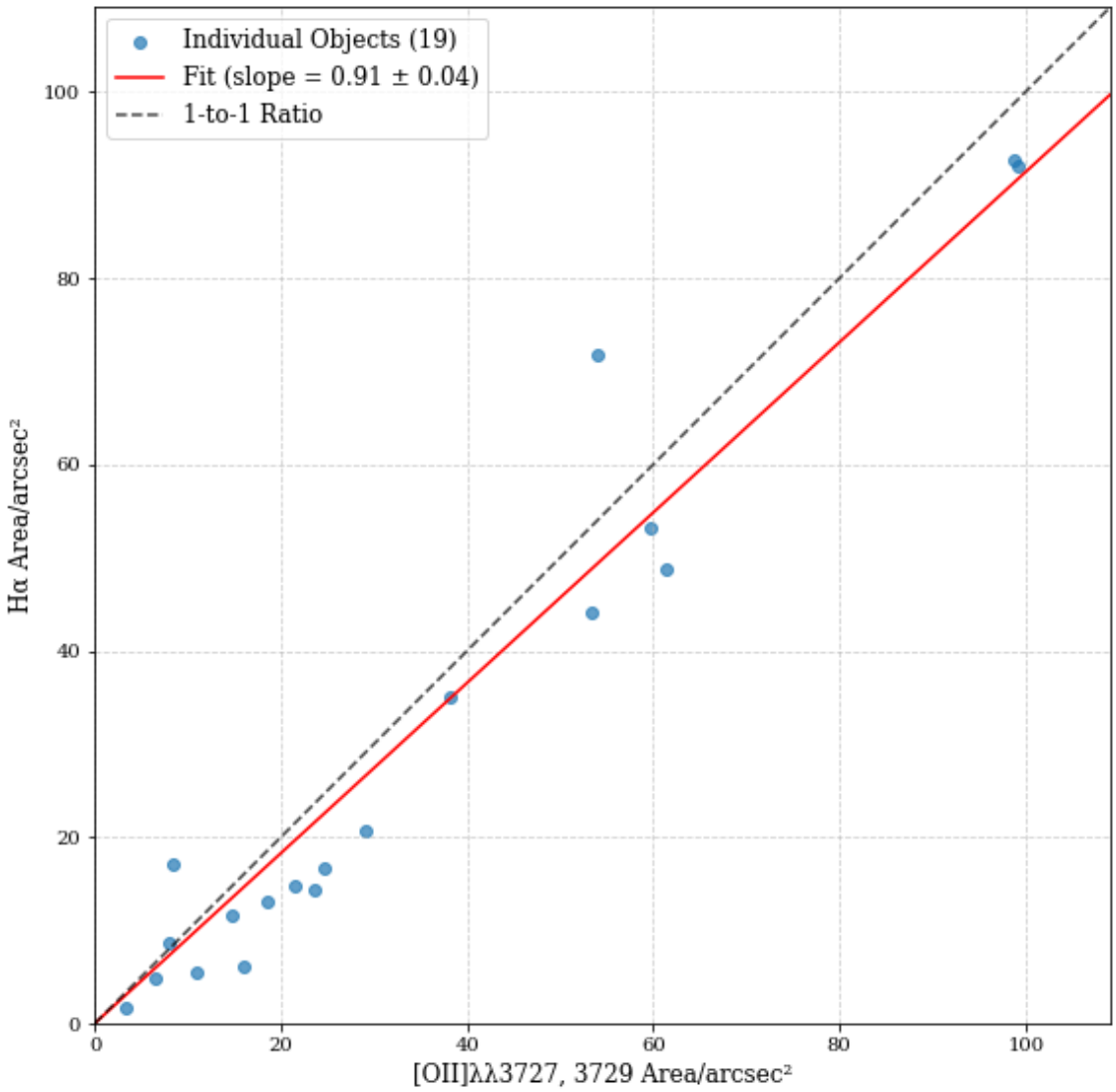

Figure 4.8: Comparison of ionised gas extent measured from Hα and [O II]$\lambda\lambda$3727,3729. We use Hα as the primary tracer of ionised gas in BCGs, but for higher-redshift systems where Hα is redshifted out of the spectral window we instead use [O II]. The figure shows the emission areas derived from both lines for objects where they are simultaneously visible. Blue points denote individual BCGs, the red line indicates a best-fit relation (slope 0.91 ± 0.04), and the dashed black line shows the 1-to-1 ratio. The close-to-unity slope demonstrates that the two tracers yield consistent spatial extents, with no major systematic difference in emission area.

CHAPTER 5

Kinematics

Having established a uniform description of the spatial properties of the ionised gas in Chapter 4, we now turn to its dynamics by mapping the two–dimensional LOS velocity and velocity dispersion fields of the same line–emitting sub–sample. Using the fiducial tracer defined previously (Hα where available, otherwise [OII]), we construct kinematic maps from spaxel–by–spaxel emission–line fits.

A key quantity in what follows is its velocity offset, defined as the mean LOS velocity of the ionised gas within the region of emission, measured relative to the stellar systemic velocity of the BCG. When considered alongside the characteristic gas velocity dispersion, this offset provides a compact, model–agnostic diagnostic of the dynamical state of the cold phase and its coupling to the host galaxy. Motivated by theoretical expectations for multiphase condensation, we examine the plane spanned by velocity offset (mean gas–minus–stellar velocity) and dispersion ($\sigma_{\rm gas}$). In constructing this diagnostic, we uncovered a systematic, positive mean gas velocity relative to the stars that persists across many systems. This empirical feature motivates § 5.1, where we quantify the magnitude and significance of the offset, build a toy model of possible geometries which may cause such an effect and finally explore potential physical origins.

We then place these measurements in the context of chaotic cold accretion (CCA) in § 5.2. There we assess whether the observed combinations of velocity offset and dispersion, together with their spatial patterns in the 2D maps, are consistent with condensation from the hot phase and subsequent gravitational settling, or whether they instead favour sustained bulk motions driven by feedback and cluster weather.

5.1 Stellar-Gas Velocity Offset

In an idealised, dynamically relaxed galaxy cluster, the BCG resides at lowest point of a cluster's gravitational potential well. In this state, the gas and stellar components are expected to be in kinematic equilibrium and co-moving with the galaxy. The resulting distribution of gas–star velocity offsets ($\bar{v}_{\rm gas}$) would be Gaussian and centred on zero. We show the raw distribution for our sample in Fig. 5.1. The significant observed systematic shift toward positive velocities demonstrates that this simple model needs refinement.

A positive velocity offset is most naturally explained by large-scale spherical inflow combined with 'far-side' obscuration. Such an offset indicates that, on average, the ionised gas is receding relative to the stars, consistent with near-side material falling toward the galaxy centre. In cluster environments, the ICM can cool and condense, producing clouds of cold gas that precipitate onto the BCG (§ 5.2). Additional inflow could in principle arise from gas stripped from orbiting satellites or brought in by minor mergers; however, in cluster cores most satellites are gas-poor due to environmental processes (e.g. ram-pressure stripping), so such channels are typically negligible compared to cooling of the ICM [Boselli and Gavazzi, 2006]. It should be noted that while all these mechanisms induce gas motion relative to the systemic stellar velocity they do so symmetrically, and therefore there must be a second stage which preferentially obscures far-side gas. Blueshifted far-side inflow may be suppressed in the observed spectrum if it is shocked or kinematically disturbed upon interaction with the interstellar medium, while the near-side inflow remains coherent and luminous. In merging UltraLuminous Infra-Red Galaxies (ULIRGs), apparent velocity–offset asymmetries are often created by differential dust extinc-

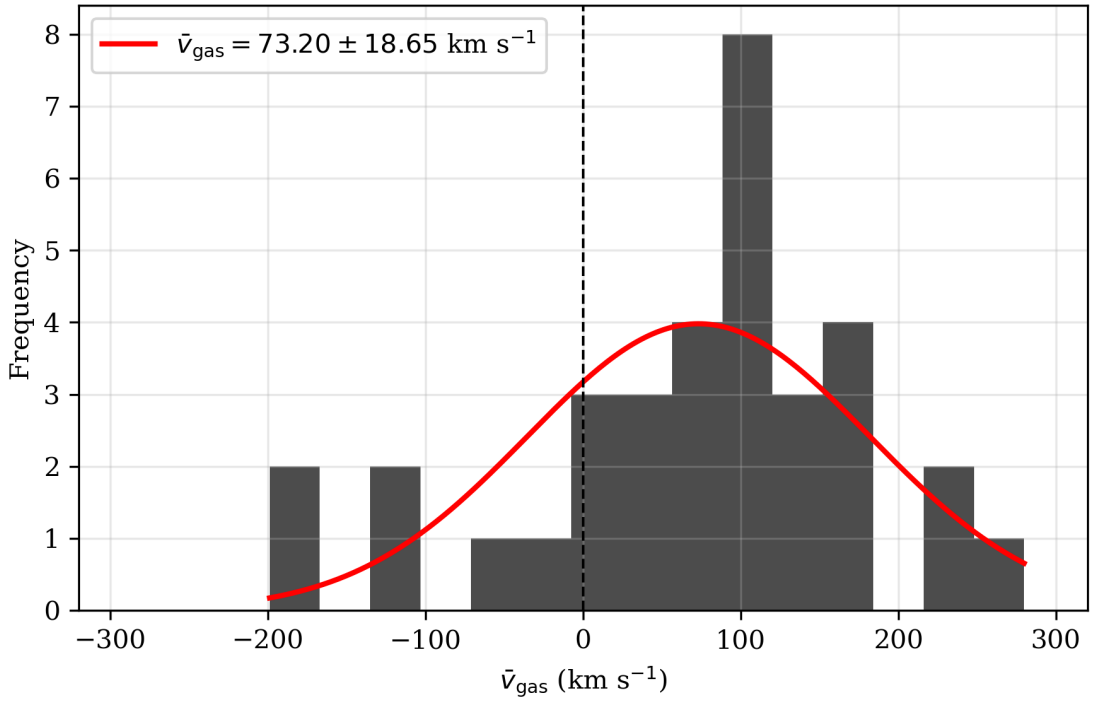

Figure 5.1: Mean gas velocity offset, averaged across all emitting pixels. The zero velocity is the mean stellar velocity averaged across a circle of 5kpc centred on the BCG.

tion: large column densities preferentially obscure the receding, far–side gas, so broad blueshifted components from the near side dominate the observed line profiles while the redshifted counterparts are attenuated [Soto et al., 2012]. In cluster cores, analogous line–of–sight asymmetries can also arise from flow geometry rather than dust: sloshing/cooling–flow models predict stagnation zones or contact discontinuities downstream of the BCG, where inflowing gas is disrupted and becomes less luminous or coherent along the line of sight [Inoue, 2021]. The sloshing of the ICM within the cluster's gravitational potential can kinematically decouple the collisional gas from the collisionless stellar component of the central BCG. This process can produce velocity offsets, though it should be of either sign with equal preference, and contribute to the observed scatter [Markevitch and Vikhlinin, 2007, Ubertosi et al., 2023]. Moreover, sloshing has been shown to displace not only the hot ICM but also the cooler multiphase gas surrounding BCGs, leading to observable asymmetries between gas and galactic components [Hamer et al., 2016].

Outflows driven by active galactic nucleus (AGN) feedback are also prevalent in

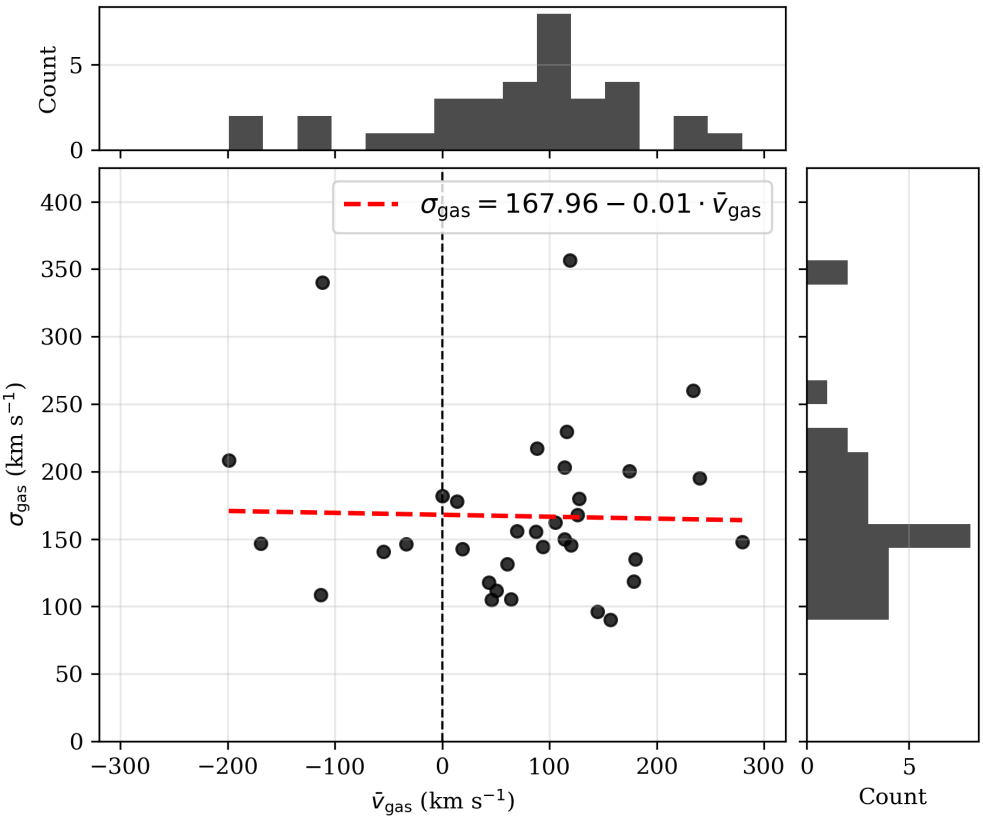

Figure 5.2: Scatter of the mean gas velocity offset, $\bar{v}_{\rm gas}$, relative to the stellar systemic velocity versus the characteristic gas velocity dispersion, $\sigma_{\rm gas}$. We see no correlation between the two properties.

BCGs, as evidenced by anisotropic, metal-rich outflows aligned with radio jet axes in cluster cores [Kirkpatrick et al., 2011]. Jets and winds launched by the central supermassive black hole typically generate net blueshifts, as emission from the approaching, unobscured side dominates. The presence of a net redshift in the sample therefore implies that outflows are not the dominant large-scale motion. Their role is instead to increase the velocity dispersion through kinematic disturbance and to populate the blueshifted tail of the distribution.

The positive centroid of the Gaussian fit is consistent with a scenario in which inflow constitutes a significant component of the large-scale gas motions in this sam-

ple [1] , potentially tracing accretion from the ICM and/or from gas stripped from satellite galaxies [e.g. Gaspari et al., 2018, Tremblay et al., 2018]. However, the underlying physical drivers remain uncertain, and the observed offset could also arise from a combination of inflow, outflow, and bulk motions induced by cluster-scale dynamical processes. The substantial width of the velocity-offset distribution likely reflects a mixture of factors, including variations in inflow geometry and rate, the impact of AGN-driven outflows [Kirkpatrick et al., 2011, McNamara and Nulsen, 2007], and differences in the dynamical state of the host clusters, which span from relaxed cool-core systems to more disturbed, environments [Markevitch and Vikhlinin, 2007]. We can explore the relevant parameter values required to achieve an observed mean velocity offset of ~ 100 km s^{-1} in the context of a simplified, symmetric geometry.

5.1.1 Toy Model

We can construct a very simple toy model to explain the $\langle v_{\rm gas} \rangle \approx +100\,{\rm km/s}$, and estimate the values for the parameters which may cause it. We adopt a simple population of cold-gas clouds moving radially, and explore how geometry and obscuration bias the luminosity-weighted mean line-of-sight velocity. The four simplified geometric scenarios and the resultant velocity shift are listed in § 5.1.1

Location of Gas	**Physical Process**	**Velocity Shift**
Near Side	Inflow (Towards Centre)	Redshift
Near Side	Outflow (Away from Centre)	Blueshift
Far Side	Inflow (Towards Centre)	Blueshift
Far Side	Outflow (Away from Centre)	Redshift

Table 5.1: The four geometric scenarios for gas flow and their resulting spectral shift.

Assuming each cloud moves at fixed radial speed $v_{\rm inf}$ we can define the following parameters:

[1] If the observed velocity offset were produced primarily by outflowing gas, it would require the impossible scenario of the near-side component to be more heavily obscured than the far side.

- Polar angle θ measured from the line of sight toward the near side (so $\theta = 0$ is the near side, $\theta = \pi$ the far side).
- Line-of-sight velocity (positive = redshift):

$$v_{\rm los}(\theta) = v_{\rm inf} \cos\theta. \tag{5.1}$$

- Angular distribution $f(\theta)$ normalised so $\int f \, d\Omega = 1$.
- Visibility weight $w(\theta)$ (e.g. from dust).

Then the luminosity-weighted mean velocity is

$$\langle v_{\rm obs} \rangle = \frac{\displaystyle\int_{4\pi} v_{\rm los}(\theta)\, w(\theta)\, f(\theta)\, d\Omega}{\displaystyle\int_{4\pi} w(\theta)\, f(\theta)\, d\Omega}. \tag{5.2}$$

We can explore this equation for different parameter values.

Model A: Spherical Infall + Mid-Plane Dust

- $f(\theta) = 1/(4\pi)$ (uniform).
- Dust screen at mid-plane:

$$w(\theta) = \begin{cases} 1, & 0 \le \theta < \pi/2 \quad \text{(near side, redshifted)}, \\ e^{-\tau}, & \pi/2 < \theta \le \pi \quad \text{(far side, blueshifted)}. \end{cases}$$

One finds

$$\langle v_{\rm obs} \rangle = v_{\rm inf} \, \frac{1 - e^{-\tau}}{1 + e^{-\tau}} > 0 \quad \text{(net redshift)}. \tag{5.3}$$

Model B: Localised Near-Side Conical Infall (No Dust)

All clouds lie within a cone of half-angle α around the *near* side, with no obscuration:

$$f(\theta) = \begin{cases} \dfrac{1}{2\pi\,(1-\cos\alpha)}, & 0 \le \theta \le \alpha, \\ 0, & \text{otherwise}, \end{cases}$$

$$w(\theta) \equiv 1.$$

Then

$$\langle v_{\rm obs} \rangle = \frac{\displaystyle\int_0^{\alpha} v_{\rm inf} \cos\theta \, \sin\theta \, d\theta}{\displaystyle\int_0^{\alpha} \sin\theta \, d\theta} = \frac{v_{\rm inf}}{2}\,(1+\cos\alpha). \tag{5.4}$$

To achieve $\langle v_{\rm obs} \rangle = +100\,\mathrm{km/s}$:

$$\alpha = 2\arccos\!\big(2 \times 100/v_{\rm inf} - 1\big). \tag{5.5}$$

Example values:

Table 5.2: Cone half-angles for various infall speeds

$v_{\rm inf}$ (km/s)	α (deg)
150	40
200	60
300	77
400	83

Model C: Mixed Spherical + Conical Infall

Let a fraction $f_{\rm cone}$ of clouds lie in the near-side cone (Model B) and the rest be spherical with dust (Model A). Denote

$$v_{\rm cone} = \tfrac{v_{\rm inf}}{2}(1+\cos\alpha),$$
$$v_{\rm sph} = v_{\rm inf}\,\frac{1-e^{-\tau}}{1+e^{-\tau}}.$$

Then

$$\langle v_{\rm obs} \rangle = f_{\rm cone}\, v_{\rm cone} + (1 - f_{\rm cone})\, v_{\rm sph}. \tag{5.6}$$

By tuning $f_{\rm cone}$, $v_{\rm inf}$, α, and τ, it is possible, in principle, to reproduce $\sim +100\,\mathrm{km/s}$,

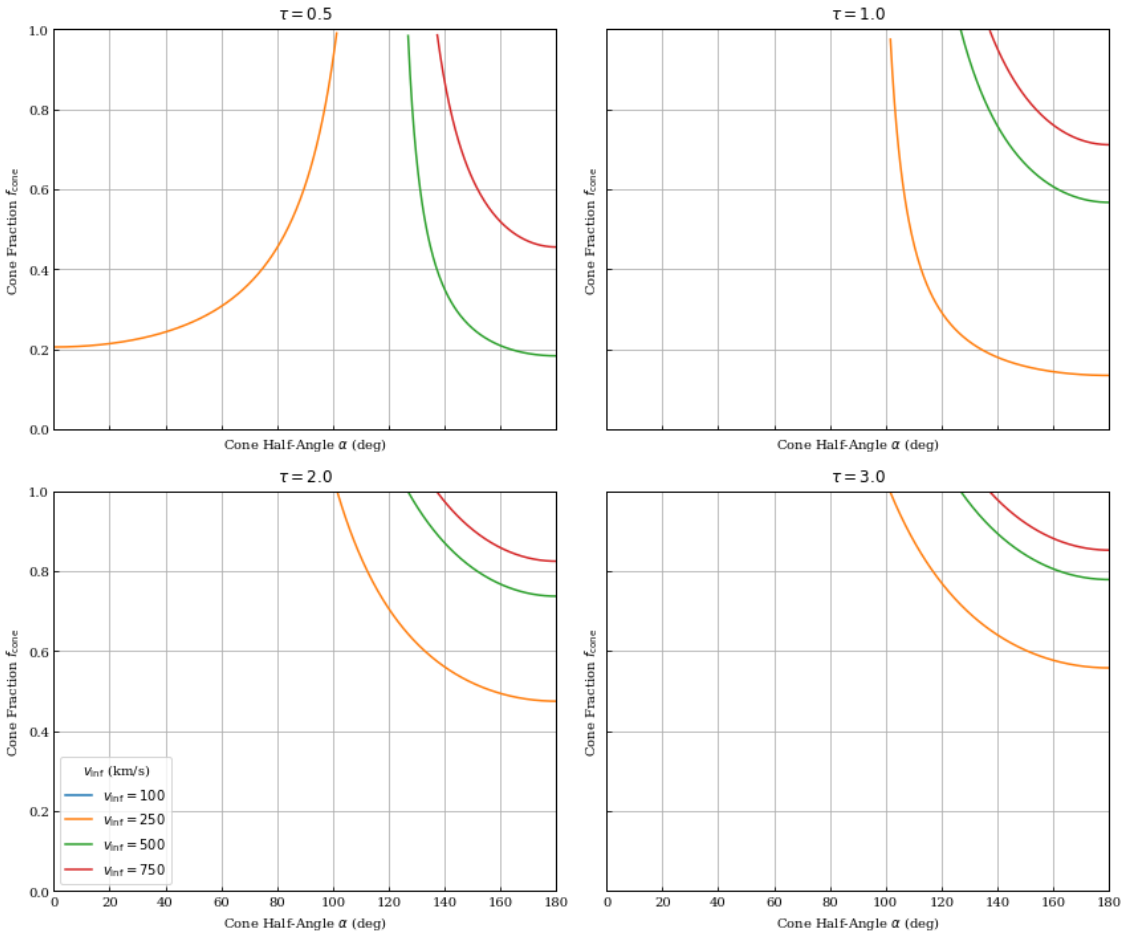

Figure 5.3: The combination of input parameters to yield an average line of sight velocity of $\sim +100\,\mathrm{km/s}$ in eq. (5.6). The value of 100km/s, while included as a physically plausible infall velocity, lies outside the parameter range depicted in the plots.

as shown in Fig. 5.3. However to do so typically requires parameter values that are physically extreme relative to expectations from observations and simulations.

For the spherical infall with mid-plane dust configuration (Model A), reproducing the observed offset requires large optical depths, $\tau \gtrsim 2$–3, even at high inflow speeds ($v_{\rm inf} \sim 500$–$750\,{\rm km\,s^{-1}}$). Although comparable values have been reported in some cluster cores [e.g., Laine et al., 2003], the optical depths we infer from the reddening of the Balmer decrement are typically much smaller (§ 7.4). This suggests that the level of obscuration required to suppress far-side emission in this scenario would be atypically large, and even if present in a minority of systems, it cannot account for the nearly universal velocity offset that we observe. Similarly, for purely geometric near-side cones (Model B), the half-opening angles required to produce the offset are implausibly small unless the inflow velocities are low. At $v_{\rm inf} \gtrsim 500\,{\rm km\,s^{-1}}$, the model requires $\alpha \lesssim 80°$, corresponding to a strongly anisotropic and collimated inflow, inconsistent with the more chaotic, filamentary accretion patterns seen in simulations of cluster cores [e.g. Gaspari and Sądowski, 2017, Tremblay et al., 2018].

The mixed spherical+conical case (Model C) can formally reproduce the offset with more moderate values of τ or α, but only by fine-tuning the cone fraction $f_{\rm cone}$ in a narrow range. This level of tuning is unlikely in a heterogeneous sample of BCGs, where inflow geometry and obscuration are expected to vary substantially from system to system.

While these simple models are capable of producing a net positive gas–star velocity offset through a combination of anisotropic inflow and obscuration, the parameter space consistent with the observed $\langle v_{\rm gas} \rangle$ appears to require optical depths, inflow collimations, or geometric fine-tuning that are beyond current physical expectations for BCGs. This suggests that additional processes—such as kinematic asymmetries induced by mergers, large-scale sloshing, or complex multi-phase feedback cycles—likely contribute to the observed signal [e.g. McDonald et al., 2012a, Olivares et al., 2022].

The parameter exploration summarised in Fig. 5.3 demonstrates that achieving an average line-of-sight velocity offset of $\sim$ 100 km s^{-1} via simplified geometric and obscuration effects is possible only within a restricted and seemingly physically

implausible region of parameter space. This would imply that while anisotropic inflow and dust obscuration may contribute to the observed positive velocity offset, they are unlikely to be the sole drivers. More plausibly, the measured $\langle v_{\rm gas} \rangle$ reflects the interplay of multiple processes, including asymmetric inflow from the ICM, AGN-driven outflows, kinematic perturbations from cluster mergers, and ICM sloshing [e.g. Markevitch and Vikhlinin, 2007, McDonald et al., 2012a, Olivares et al., 2022].

Alternative physical origins of a $\sim$+100 km s^{-1} gas–star velocity offset

Beyond obscuration-biased inflow/outflow geometries, several dynamical and weighting effects can naturally yield a positive luminosity-weighted offset between the ionised gas and the stellar systemic velocity in BCGs.

If the warm gas resides in a rotating disc whose angular momentum axis is misaligned with the stellar body, projection effects and asymmetric illumination/attenuation can bias the luminosity–weighted mean velocity away from the stellar systemic value. Misaligned gas is common in early–type galaxies due to external accretion [e.g. Davis et al., 2011, 2013], and we see examples of both rotating discs and filamentary structures in BCGs [Hamer et al., 2016, Olivares et al., 2019]. In a simple axisymmetric disc with rotation curve $v_\phi(R)$, inclination i, and surface brightness $I(R, \phi)$, the integrated offset scales as $\langle v_{\rm gas} \rangle \propto \int I \, v_\phi(R) \sin i \cos \phi \, dA \, / \, \int I \, dA$, so any azimuthal asymmetry in I (from star formation, shocks, or dust) or partial spatial coverage will drive a non-zero mean even if the global velocity field is symmetric.

Additionally, cluster cores frequently undergo sloshing, generating cold fronts and coherent bulk motions of the hot atmosphere [Markevitch and Vikhlinin, 2007]. If multiphase filaments are partially entrained by these flows, the warm gas can acquire a net line–of–sight velocity relative to the collisionless stars of the BCG. Observations of line–of–sight sloshing in Abell 907 imply velocity shears of order several hundred km s^{-1} within the cool core [Ueda et al., 2019], easily sufficient for a $\sim$100 km s^{-1} luminosity–weighted offset if one side dominates the emission. Turbulent motions associated with gentle AGN heating [Zhuravleva et al., 2014b] likewise provide a stochastic but nonzero contribution to bulk gas velocities that need not average to zero over the limited, bright emission regions probed by IFU

data.

Buoyant radio bubbles and wide-angle outflows can lift low–entropy, multiphase gas off the nucleus, imparting ordered velocities of tens to a few hundred $\mathrm{km\,s^{-1}}$ along jet axes; if the near–side uplift dominates the line emission (due to compression, irradiation, or lower extinction), a persistent positive or negative offset results. ALMA and optical IFU studies reveal molecular and ionised gas trailing radio bubbles in several BCGs (e.g. Abell 1835, Phoenix, Abell 1795), with coherent kinematics and large displaced reservoirs [McNamara et al., 2014, Russell et al., 2016, 2017]. In such cases the integrated warm–gas velocity reflects the momentum imparted by jet/bubble coupling rather than purely gravitational streaming.

Gas–rich satellites captured on non–radial orbits can deposit cold gas with angular momentum and systemic velocities offset from the BCG stars, temporarily shifting the luminosity–weighted velocity of the ionised phase until dynamical friction and mixing act. Offsets between the BCG and the local cooling peak, extended plumes, and coherent velocity gradients are observed in several systems [e.g. Pasini et al., 2019], consistent with intermittent external fueling. Because the brightest spaxels are often located within the newly accreted structures, their kinematics can dominate the integrated mean.

Recombination line emissivity in the warm phase scales approximately with the emission measure ($\propto n_{\mathrm{e}}^2$ under Case B conditions), so dense clumps and shocked interfaces can dominate the line flux [Osterbrock and Ferland, 2006]. If these high–surface–brightness zones occupy a restricted range of velocities (e.g. only the receding side of a disc is unobscured; only the near–side uplift is bright), the spaxel–averaged velocity will be biased away from the mass–weighted mean of the full gas distribution. This physical weighting is further compounded by spatial masking (signal–to–noise cuts) that preferentially excludes low–surface–brightness regions with compensating velocities.

It is possible to concoct a combination of ingredients, geometry and physical effect to, in individual systems, generate a velocity offset of $\sim$100 $\mathrm{km\,s^{-1}}$ - a misaligned, externally (re)fuelled discs embedded in a gently sloshing, jet–disturbed atmosphere would work. However the degree of fine-tuning required makes scaling

the effect to even a modest sample size implausible. The strength of the Kaleidoscope sample is precisely that it enables us to move beyond anecdotal explanations for individual systems. If such an offset were detected in a number of galaxies studied in isolation (as it has been [Gingras et al., 2024]) it might reasonably be dismissed as a coincidental by-product of local conditions, not warranting further investigation. However, the fact that the same $\sim$100 $\mathrm{km\,s^{-1}}$ offset emerges systematically across a large, homogeneous sample immediately raises its significance. From the observational perspective, the uniform design, depth, and coverage of the Kaleidoscope survey ensure that this result is not an artifact of selection biases or small-number statistics, but a reproducible feature across diverse environments. From the theoretical perspective, the persistence of the offset across the population provides strong constraints on models of gas dynamics in cluster cores: any viable explanation must account for its near universality.

5.2 Chaotic Cold Accretion

Velocity offsets of this nature have been documented in several other systems (e.g., Gingras et al. [2024]). Within our analysis, this offset was first recognized as a systematic effect during the construction of diagnostic diagrams, which compare ratios of kinematic properties to investigate the origin of the gas. We now turn to a more detailed examination of these diagrams.

5.2.1 Kinematic Tracers of Multiphase Condensation in Cluster Cores

In cool-core galaxy clusters, the ICM develops a multiphase structure in which hot X-ray–emitting plasma ($T \sim 10^7$–$10^8\,\mathrm{K}$) coexists with warm ionised gas ($T \sim 10^4\,\mathrm{K}$; Hα nebulae) and cold molecular clouds ($T \lesssim 10^3\,\mathrm{K}$) [Crawford et al., 1999, Edge, 2001, Fabian, 1994]. A frequently proposed origin for this gas is that turbulence in the hot ICM seeds density fluctuations which cool non-linearly once the local cooling time, t_{cool}, becomes comparable to the characteristic eddy turnover time, t_{eddy} [e.g. Gaspari and Churazov, 2013a, Gaspari et al., 2018]. This regime is thought to trigger

a ‘top-down’ condensation cascade and chaotic cold accretion of cold clouds toward the central galaxy.

The eddy turnover time represents the characteristic timescale for turbulent motions to advect material across the size of the dominant energy-carrying eddies. It can be expressed as

$$t_{\rm eddy}(l) \;=\; \frac{l}{\sigma_v(l)}, \tag{5.7}$$

where l is the eddy scale (often taken to be comparable to the injection scale of turbulence, e.g. the size of buoyantly rising radio bubbles or sloshing fronts), and $\sigma_v(l)$ is the velocity dispersion at that scale [Gaspari et al., 2015, Hitomi Collaboration, 2016]. In the cluster core, l may range from $\sim$ 1–10 kpc, and σ_v from tens to a few hundred $\mathrm{km\,s^{-1}}$, giving $t_{\rm eddy}$ values of order $\sim 10^7$–10^8 yr.

A related dynamical timescale relevant to condensation models is the free-fall time, which quantifies the time for a test particle to fall to the cluster centre from radius r in the gravitational potential $\Phi(r)$. It is given by

$$t_{\rm ff}(r) \;=\; \sqrt{\frac{2\,r}{g(r)}} \;=\; \sqrt{\frac{2\,r^3}{G\,M(<r)}}, \tag{5.8}$$

where $g(r)$ is the gravitational acceleration and $M(<r)$ the enclosed mass [e.g. Sharma et al., 2012, Voit et al., 2015]. In cool-core BCGs, $t_{\rm ff}$ is typically of order 10^7 yr at radii of a few kpc, increasing with distance from the centre.

Thermal instability and precipitation models often invoke thresholds such as $t_{\rm cool}/t_{\rm ff} \lesssim 10$ [Sharma et al., 2012, Voit et al., 2015] or $t_{\rm cool} \approx t_{\rm eddy}$ [Gaspari et al., 2018] to delineate regions where cold gas condensation is expected to occur. In the CCA framework, when these timescales become comparable, turbulence both promotes density enhancements and mixes low-entropy gas to larger radii, enabling widespread, chaotic condensation across the core.

The kinematic signatures of the CCA theory can be explored across a range of spatial scales via different observational approaches. Ensemble measurements from a single, spatially–integrated spectrum over the entire warm/cold nebula (several kpc) blend many clouds. Its line width, $\sigma_{v,\rm LOS}$, tracks the turbulent velocity dispersion of the multiphase gas ensemble, and its centroid shift remains near, but not necessarily

at, systemic velocity [Gaspari et al., 2018]. Pencil-beam measurements[2] focus on a narrow sight-line, often searching for absorption against an AGN, and isolate one or several unresolved clouds. Lines are narrower due to lower internal dispersion but typically have larger bulk shifts ($|v_{\rm LOS}| \sim 10^2$–$10^3\,{\rm km\,s^{-1}}$) as clouds are inflowing or outflowing [Maccagni and De Blok, 2024, Tremblay et al., 2016a].

5.2.2 Turbulence as Traced by Cold Gas

High-resolution hydrodynamic simulations show that the ensemble LOS velocity dispersion of warm/cold gas closely matches the turbulent dispersion of the hot ICM, with nearly unity slope and ∼10–15% scatter [Gaspari et al., 2018]. Observationally, integrated Hα widths in 72 cluster/group cores yield $\sigma_{v,\rm warm} \sim 100$–$250\,{\rm km\,s^{-1}}$, consistent with subsonic ICM turbulence (Mach 0.1–0.3) and direct Hitomi X-ray measurements of $\sigma_{v,\rm hot} = 164 \pm 10\,{\rm km\,s^{-1}}$ in Perseus [Gaspari et al., 2018, Hitomi Collaboration, 2016]. Pencil-beam spectra commonly reveal dual kinematic components: a broad, low-shift component, which reflects the ensemble effect of many unresolved clouds moving at moderate velocities; and a narrow, high-shift component that typically arises from one or a few compact clouds—often infalling toward the central SMBH. These two-phase profiles provide insight into both the underlying turbulent medium and the discrete, high-velocity cloud motions superposed upon it [Struve and Conway, 2010]. Few clouds are at exactly zero velocity in pencil-beam data—most are in rapid motion, with $|v_{\rm LOS}|$ up to a few hundred ${\rm km\,s^{-1}}$ [Maccagni and De Blok, 2024, Salomé et al., 2006]. This further implies that multiphase gas in cluster cores is highly dynamic, continuously 'raining' in or being uplifted.

We can probe the potential origin for the ionised gas by observing the distribution of our sample in line shift-dispersion space, shown in Fig. 5.4. The x-axis represents the mean bulk velocity of the gas, $\log_{10}|v_{\rm bulk}|$, while the y-axis represents the mean gas velocity dispersion, $\log_{10}\sigma$. Bulk velocity traces coherent, large-scale

[2]In this context, a 'pencil beam' refers to an extremely narrow observational sight-line, typically set by the angular size of a bright background source such as the unresolved nucleus of an AGN or a compact radio continuum knot. Such a beam intercepts only a small cross-section of the multiphase medium, often sampling individual clouds or small groups of clouds along the line of sight, rather than the full nebula.

motions (inflow, outflow, sloshing), whereas velocity dispersion traces the magnitude of random, turbulent motions. This plot of velocity dispersion versus line shift therefore allows separation between the collective, chaotic motion of the entire gas system and the bulk motion of individual clouds, both of which are key predictions of the CCA model [Gaspari et al., 2018].

If cold, dense clouds condense out of the hot plasma, as predicted by CCA, we expect two distinct kinematic signatures. Firstly, a broadening of spectral lines. A large dispersion indicates a high degree of turbulence, as it captures the wide range of random velocities from many different clouds and filaments moving chaotically within the observed region. It is a measure of the system's overall turbulent kinetic energy [Gaspari et al., 2018]. Secondly we expect an offset of the spectral line's centre from the galaxy's systemic velocity, indicating the bulk motion of the gas along the line of sight (inflow/outflow)[Gaspari et al., 2018].

Ensemble measurements, the focus of this section, trace the light from many clouds whose individual high-speed bulk motions (large line shifts) occur in a variety of three-dimensional directions. These bulk velocities tend to cancel in projection, yielding a low net line shift. However, the superposition of their chaotic, multi-directional orbits produces significant turbulence, observed as a high velocity dispersion. In Gaspari et al. [2018], they also consider "pencil-beam" measurements, which can isolate just one or a few clouds along a narrow line of sight. Such measurements no longer average over the whole ensemble, but instead capture the motion of individual clouds. In this case, the spectrum often shows a large line shift, reflecting the high bulk velocity of a single cloud along its three-dimensional trajectory—frequently infalling toward the central galaxy—and a low velocity dispersion, because it only samples the comparatively small internal turbulence within that cloud.

5.2.3 Results

The Kaleidoscope survey represents a substantial improvement over the dataset previously used as the basis for this analysis, which was obtained primarily with the VIMOS instrument. The enhancements provided by MUSE (§ 2.1.1) are immediately

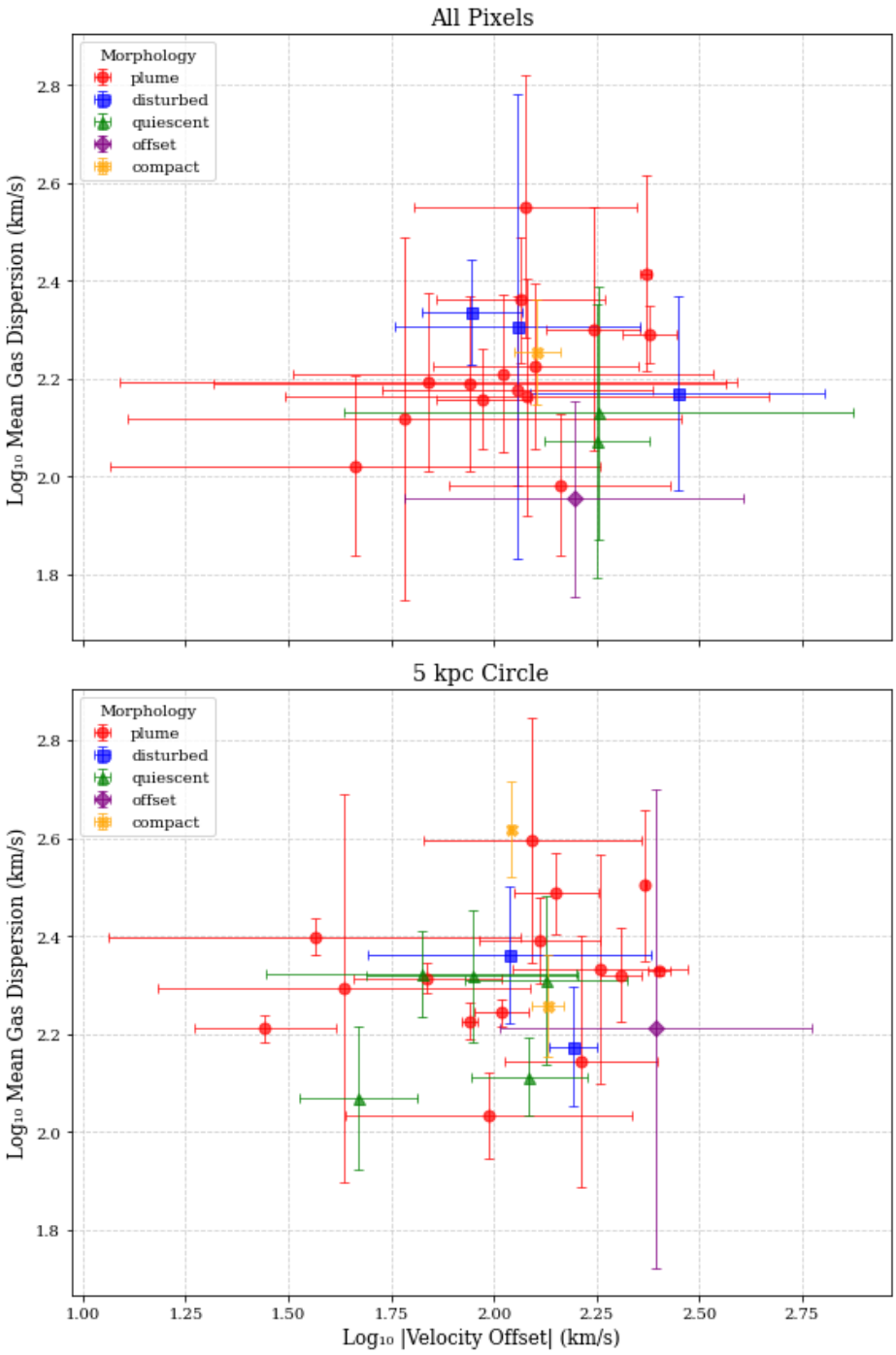

Figure 5.4: Mean LOS velocity (shift) vs. velocity dispersion (broadening) in log space for all emitting pixels (top) and for pixels within 5 kpc of the BCG (bottom). Different morphologies are colour-coded: plumes (red), disturbed (blue), quiescent (green), offset (purple), and compact (orange) as defined in § 4.3.1.

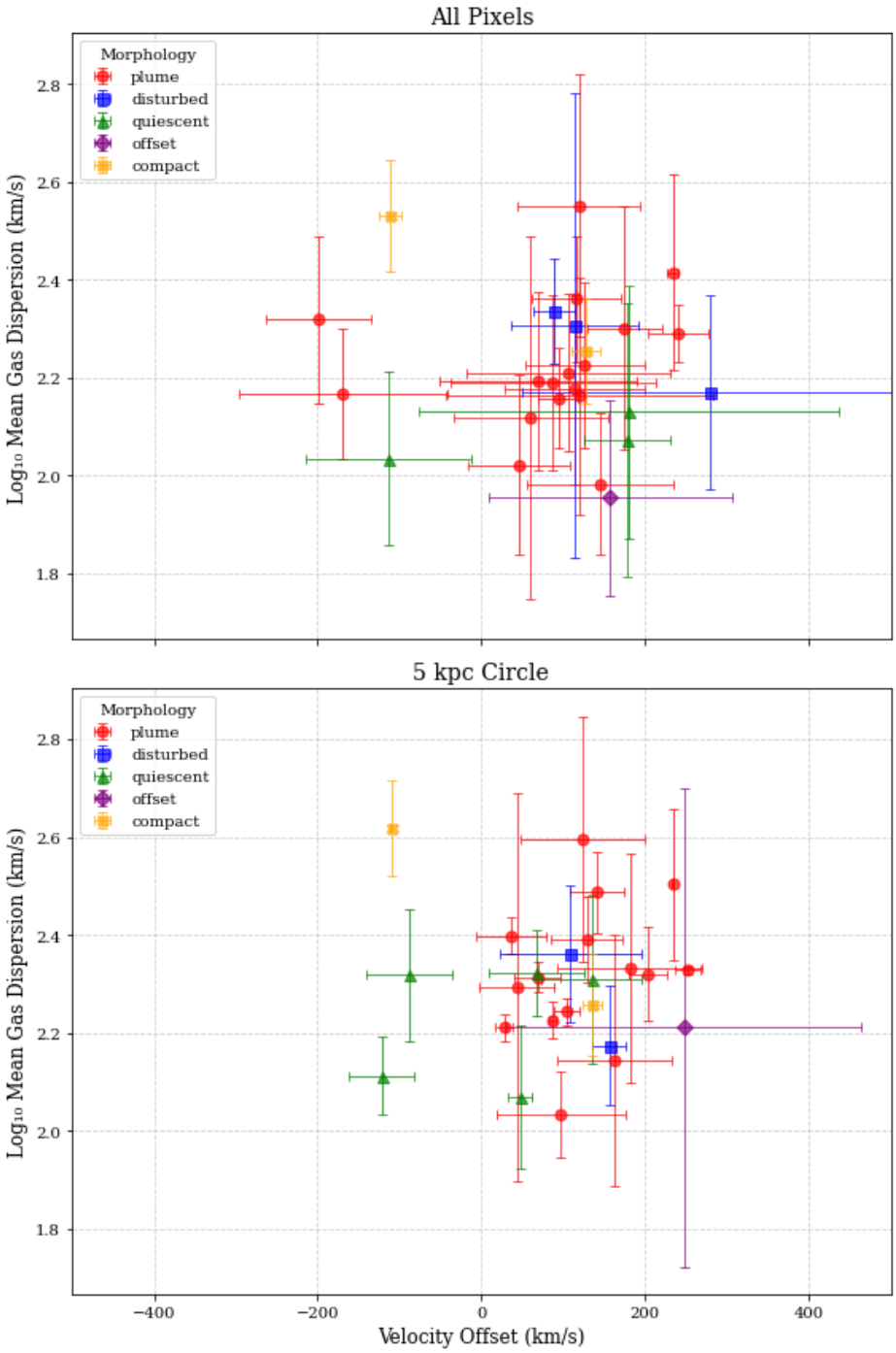

Figure 5.5: Mean gas velocity and mean gas dispersion for different morphological classes of galaxies using all emitting pixels (top) and for pixels within 5 kpc of the BCG (bottom). Different morphologies are colour-coded: plumes (red), disturbed (blue), quiescent (green), offset (purple), and compact (orange) as defined in § 4.3.1. Unlike Fig. 5.4, which shows the same relation using a logarithmic and modulus scaling of the x-axis (mean gas velocity), this figure displays the velocity on a linear axis, preserving the sign of the mean motion. The velocity offset, explored in § 5.1.1, is apparent.

apparent. The significantly larger field of view ($1' \times 1'$) enables the complete mapping of extended Hα nebulae—often tens of kiloparsecs in scale—in a single pointing, whereas VIMOS observations frequently required mosaicking or suffered from incomplete spatial coverage. This full spatial mapping ensures that the morphology, kinematics, and ionisation structure of the nebulae are captured without gaps, reducing uncertainties introduced by variable observing conditions across multiple pointings. Equally important is the contiguous spectral range of MUSE (4800–9300 Å), which, combined with its higher spectral resolution ($R \sim 3000$), allows multiple key diagnostic emission lines—Hα, [NII], [SII], and Hβ—as well as stellar absorption features to be observed simultaneously within the same dataset. By contrast, VIMOS covered only two disjoint spectral windows (HR_blue: 4150–6200 Å and HR_orange: 5250–7400 Å), requiring separate observations to capture the full suite of diagnostic lines. This simultaneity with MUSE eliminates the need to combine data from different instruments or wavelength settings, ensuring that relative fluxes and kinematics are measured under identical instrumental and atmospheric conditions. The result is a self-consistent determination of both gas and stellar kinematics, alongside more robust constraints on the ionisation mechanisms and physical state of the gas.

In Fig. 5.4 we reproduce a key diagnostic figure for CCA originally from Gaspari et al. [2018]. In the top panel the kinematics are averaged over the entire spatial extent of the detected gas. This provides a global view of the gas dynamics. In the lower panel the kinematics are averaged only within a central 5kpc radius centred on the BCG, probing the physical conditions in the galaxy's innermost core, where feedback effects are strongest. The scatter we observe reflects the diverse states of this multiphase structure: some systems may be dominated by infall, some by internal turbulence, and others by feedback-driven outflows.

There is excellent agreement with the observational data presented in the upper 'Ensemble' panel of Figure 4 by Gaspari et al. [2018]. Both datasets occupy the same region of the parameter space, which is characterised by substantial line broadening ($\sigma_{v,los} \approx 100 - 250\,\mathrm{km\,s^{-1}}$) and relatively low velocity shifts.

The physical implication is that an 'ensemble' measurement, which integrates the spectrum over the full extent of the cool gas nebula, provides a global, inte-

grated kinematic tracer for the turbulence in the hot, volume-filling plasma. The large-aperture measurement averages out the bulk motions of individual infalling or outflowing clouds, resulting in a low net line shift, while successfully capturing the global velocity dispersion driven by large-scale turbulence. This validated method allows the kinematics of the more accessible warm and cold gas phases to be used as a reliable proxy for the dynamics of the hot ICM.

The comparison with the version of this figure shown in Fig. 5.4, where the mean velocity is plotted on a log-modulus scale, highlights how the choice of axis representation shapes the physical interpretation. In the linear version presented here (Fig. 5.5), both blueshifted and redshifted motions are retained explicitly, enabling a direct identification of systems dominated by net inflow (negative mean velocities) versus those with outflow signatures (positive mean velocities). While the modulus representation has the advantage of compressing the dynamic range and emphasising turbulent velocity dispersions, the linear view makes clearer the asymmetries between inflowing and outflowing multiphase structures. Such asymmetries are well known from absorption-line studies, where redshifted H I [Morganti et al., 2007] and CO absorption [e.g. Rose et al., 2020, Tremblay et al., 2016b] have provided unambiguous evidence of cold gas inflows onto the brightest cluster galaxies. These observations demonstrate that the cold phase can participate directly in fuelling the central supermassive black hole, complementing the picture obtained from spatially resolved emission-line studies of the warm ionised phase. Together, the two views reinforce the emerging consensus that cluster cores host a dynamically complex multiphase medium, in which turbulence, condensation, and feedback-driven outflows coexist with channels of steady inflow.

In both panels of Fig. 5.5, there is a noticeable split in the velocity offsets based on morphology and it is particularly noteworthy for the 5 kpc circle (bottom panel). All plume morphologies show a positive velocity offset while the only objects to show a negative velocity are those which are compact and quiescent. While the inherent limitations of the morphology classification algorithm (§ 4.3) preclude definitive conclusions, this dichotomy suggests a possible physical link between the morphology of the ionised gas and it's velocity offsten relative to the stellar component.

CHAPTER 6

Velocity Structure Function

In the previous chapter we examined the systematic velocity offset between different components of the ionised gas, and argued that its ubiquity across the Kaleidoscope sample points to a genuine physical signature rather than an incidental feature of a few systems. While such offsets provide valuable constraints on bulk motions and global asymmetries, they do not fully capture the complexity of the velocity field within cluster cores. To move beyond global shifts and probe the scale-dependent nature of gas motions, we now turn to the velocity structure function (VSF).

The velocity structure function is a statistical measure of how velocity differences grow as a function of spatial separation. By quantifying correlations in the velocity field across scales, the VSF provides insight into the underlying dynamics of turbulence, inflows, and feedback-driven motions. Unlike simple global velocity offsets or dispersions, the VSF allows us to separate ordered flows from chaotic fluctuations, and to test whether observed gas kinematics follow expectations from turbulent cascades or are dominated by coherent large-scale streaming.

This chapter introduces the methodology we adopt for computing velocity structure functions in the Kaleidoscope sample, beginning with a brief overview of the theoretical background and its application in astrophysical systems. We then present

the practical steps used to derive the VSF from our data, and finally we discuss the implications of the measured scaling relations for the dynamics of cluster cores.

6.1 Background

The p-th order velocity structure function (VSF), $S_p(\ell)$, is defined as the p-th moment of the velocity difference between two points, $\mathbf{x}$ and $\mathbf{x} + \boldsymbol{\ell}$, separated by a lag vector $\boldsymbol{\ell}$.

$$S_p(\ell) = \langle |\mathbf{v}(\mathbf{x} + \boldsymbol{\ell}) - \mathbf{v}(\mathbf{x})|^p \rangle \tag{6.1}$$

where $\ell = |\boldsymbol{\ell}|$ is the separation scale and the brackets $\langle \cdot \rangle$ denote an average over all positions $\mathbf{x}$. We will focus on variations of the first-order VSF ($p = 1$), which is the mean absolute velocity difference:

$$S_1(\ell) = \langle |\delta v(\ell)| \rangle \tag{6.2}$$

In a turbulent medium within a self-similar inertial range we expect the VSF to exhibit a power-law relationship with the separation scale:

$$S_p(\ell) \propto \ell^{\zeta_p} \tag{6.3}$$

The scaling exponent, ζ_p, is the primary diagnostic tool derived from the VSF, as its value is predicted by theories of turbulence. This value quantifies the scale-dependent nature of turbulence and can reveal the presence of coherent structures, energy injection scales, and dissipation mechanisms.

6.2 Theory

Kolmogorov (1941) postulated that in the inertial range of a high-Reynolds-number, incompressible cascade, the only relevant driver is the energy dissipation rate per unit mass, ε. For an incompressible cascade eq. (6.1) can be reduced via dimensional

analysis to a second-order VSF dependent only on ε and the separation scale ℓ:

$$S_2(\ell) \propto (\varepsilon\,\ell)^{2/3} \quad \Longrightarrow \quad \zeta_2 = \tfrac{2}{3}\,. \tag{6.4}$$

Assuming a simple scaling relation between the moments, this implies $\zeta_1 = \zeta_2/2 = 1/3$ [Kolmogorov, 1941]. This has been used as a benchmark for subsonic, isotropic turbulence in the hot ICM around BCGs.

The energy dissipation rate, ε, arises directly from the viscous term in the Navier–Stokes equations. Writing the momentum equation for an incompressible fluid:

$$\frac{\partial \mathbf{v}}{\partial t} + (\mathbf{v}\cdot\nabla)\mathbf{v} = -\frac{1}{\rho}\nabla p + \nu\nabla^2\mathbf{v}\,, \tag{6.5}$$

one can form an equation for the evolution of kinetic energy, $E = \frac{1}{2}\langle|\mathbf{v}|^2\rangle$. Multiplying by $\mathbf{v}$ and averaging over a statistical ensemble yields:

$$\frac{\mathrm{d}E}{\mathrm{d}t} = -\underbrace{\nu\left\langle(\nabla\mathbf{v}) : (\nabla\mathbf{v})\right\rangle}_{\varepsilon} + (\text{injection terms})\,. \tag{6.6}$$

Thus, by definition, ε represents the rate at which turbulent kinetic energy is irreversibly converted into heat by molecular viscosity [Frisch, 1995, Kármán and Howarth, 1938]. In statistical steady state, energy injected at large scales cascades down to ever smaller eddies until it is dissipated at the Kolmogorov microscale.

By contrast, in the supersonic, shock-dominated regime—often idealized by the one-dimensional Burgers equation—the velocity field is not continuous but is instead characterized by sharp discontinuities (shocks). The velocity difference across a shock is roughly constant, but the probability of encountering a shock within a given separation distance ℓ is proportional to ℓ. Since the VSF is dominated by these strong velocity jumps, the second-order VSF scales linearly with this probability, leading to the prediction:

$$S_2(\ell) \propto \ell \quad \Longrightarrow \quad \zeta_2 = 1\,. \tag{6.7}$$

This linear scaling for the second-order VSF is a hallmark of Burgers-like turbulence

[Burgers, 1948].

To derive the first-order exponent, we again assume a simple scaling relationship where $\zeta_1 \approx \zeta_2/2$. Applying this to the Burgers result gives the well-known exponent for the first-order VSF in a shock-dominated medium:

$$\zeta_1 = \zeta_2/2 = 1/2\,. \tag{6.8}$$

Numerical studies have confirmed that highly compressible flows driven at high Mach numbers exhibit VSF slopes intermediate between the Kolmogorov ($\zeta_1 = 1/3$) and Burgers ($\zeta_1 = 1/2$) limits, depending on the driving mechanism and magnetic field strength [Federrath et al., 2008].

Observationally, the ICM in the cores of galaxy clusters has been shown to exhibit a dual regime. On scales of tens to hundreds of kiloparsecs—set by AGN-inflated bubbles and buoyant plumes—X-ray surface-brightness fluctuation analyses yield VSF gradients close to the Kolmogorov value, $\zeta_1 \approx 0.3$ [Gaspari and Churazov, 2013b, Zhuravleva et al., 2014a]. On smaller scales (a few kpc), where radiative cooling and AGN-driven shocks compress the gas, the measured VSF slopes steepen to $\zeta_1 \sim 0.5$–0.6, reflecting the growing importance of supersonic motions in the cold, multiphase filaments observed around BCGs [Lau et al., 2017].

6.3 Observational Status

BCGs display both organised bulk flows and chaotic turbulent motions as discussed in § 1.3.5. IFU spectroscopy, for example by [Hamer et al., 2016], has mapped complex velocity fields within Hα and [N II] emission around BCGs, indicating that VSFs computed from these data often show steep power-law slopes ($\sim \ell^{\gamma}$, with $\gamma > 2/3$)—significantly steeper than the classical Kolmogorov prediction of $\gamma = 2/3$. This steepness suggests turbulence dominated by feedback-driven structures—e.g. AGN bubbles or sloshing fronts—rather than a fully developed inertial cascade.

Similarly, [Gitti et al., 2012] and [Liu et al., 2021] used X-ray and optical line-width measurements to estimate turbulent velocities of several hundred km s^{-1} on kiloparsec scales. When converted into VSFs, these measurements imply that AGN

heating injects energy at scales of 5–20 kpc, balancing radiative cooling through turbulent dissipation. Their inferred VSF amplitudes are consistent with those measured in systems like Perseus and Abell 1795, reflecting a dynamic equilibrium between cooling losses and AGN-driven stirring.

These observational VSFs can be directly compared to predictions from high-resolution cluster simulations. For example, the XMAGNET simulations (Fournier et al., 2025) calculate both 3D and line-of-sight VSFs of cold ($T \leq 10^5$ K) and hot (10^6–10^8 K) gas in a cool-core cluster, finding that the slope and normalisation of VSFs vary both temporally and with viewing angle, highlighting how projection and instrumental smoothing can bias observed scalings Fournier et al. [2025]. These simulations predict steeper VSFs for the cold phase due to AGN-driven filaments and uplift, and show that observational effects (e.g., seeing, line-of-sight mixing) tend to further steepen measured slopes.

Idealised multiphase ICM simulations (Mohapatra et al., 2021) also compute second-order VSFs, finding that cold (10^4 K) and hot (10^7 K) phases share similar scale-dependence, but magnetic fields steepen the cold-phase VSF exclusively. Moreover, projection effects steepen the hot-phase VSF while flattening the cold-phase one Mohapatra et al. [2021]. These trends mirror observational inferences of steep VSFs in Hα around BCGs.

The most recent studies on AGN feedback modes have demonstrated that kinetic-mode feedback generate VSF slopes and amplitudes that match observations more closely than thermal-only models. Feedback precession and episodic jet activity inject turbulence at multiple scales, altering both the VSF slope and normalisation in the cold and hot components Wang et al. [2021].

6.4 Calculation

Cubes were reduced to a 100×100 pixel ($20 \times 20''$) spatial range centred on the BCG (continuum peak). This results in theoretical maximum values of ∼103 million pixel pairs and ∼57000 unique pixel separations. We reduce the pixels to those exhibiting line emission (the regions highlighted highlighted in Fig. 4.4).

For the VSF calculation, the projected separation, denoted by l, and the absolute velocity difference $|\delta v| = |v_i - v_j|$ are determined for all possible combinations of selected pixels within this line-emitting region. These pixel pairs are then grouped into distinct bins based on their separation l. Within each bin, the average of the velocity differences $\langle|\delta v|\rangle$ is computed to determine the VSF amplitude at that specific scale. We experimented with evenly grouping pairs across the scales of interest and confirmed that the VSF results remain consistent. Examples of the distribution in velocity difference for pixel pairs occupying a given separation bin are shown in the outer plots of Fig. 6.1 for the cluster A3017.

The measurements are taken only at scales exceeding the point-spread function (PSF) which for this purpose was approximated as the average Differential Image Motion Monitor (DIMM) seeing value for the observation. Bins with an insufficient number of pixel pairs can undermine the reliability of VSF measurements, especially at larger separations where the constraints of the image size become a limiting factor and we begin to see a morphology dependence in the profile obtained. Therefore bins where occupancy drops below 20% of the peak bin value are excluded. This follows the methodology of [Li et al., 2025]. The threshold ensures that sufficient pairs are included at each separation and we reduce the morphology dependence on the value (for example, low-occupancy, high separation bins typically correspond to filamentary structures). Such a threshold will also limit the 'window effect' where the finite field of view results in insufficient pixel pairs at large separations. The turnover scale refers to the point where the VSF amplitude reaches a local maximum. This scale may indicate the scale where energy is injected into the system and subsequently dissipates onto smaller scales, or it may be related to other factors such as bulk motions - both theories will be explored.

The velocity differences $|\delta v|$ exhibit a range of distributions within each bin. To distil this information into s simple the mean value does not adequately represent the $|\delta v|$ among all pairs. Therefore, to obtain a more comprehensive understanding, we analyse the $|\delta v|$ distribution at each measured scale. This approach maximises the information extracted from each observation and enhances our understanding of the characteristics of the resulting VSFs as well as the kinematics of gas within

the cluster cores. Pixel pairs are grouped into into 20 km s^{-1} bins, ranging between 0 and the maximum $|\delta v|$ for each object (a default value of 650km/s was defined in the fitting procedure). To allow for an efficient comparison analysis, each $|\delta v|$ bin count is normalised by the total number of pairs at that scale, ensuring value ranges between 0 and unity, allowing for comparison across scales.

The $|\delta v|$ distribution in each separation bin was fitted by a lognormal profile. Using the parameters from the best-fit model, the VSFs we calculated were based on the mean of the lognormal distribution. The lognormal distribution is a suitable model for the distribution of velocity differences, $|\delta v|$, for both mathematical and physical reasons. Mathematically, the data being fit is strictly positive and its probability distribution function (PDF) is typically right-skewed, featuring a sharp peak at low values and a long tail extending to higher velocities. Physically, the choice is motivated by the nature of turbulence itself. The turbulent energy cascade, where energy is transferred from large to small scales, is better described by hierarchical, multiplicative processes rather than additive ones. While the sum of many random variables tends towards a Gaussian distribution, the product of many random positive variables tends towards a lognormal distribution [Federrath et al., 2008]. To maintain consistency across objects and to allow comparisons with previous studies, such as [Li et al., 2025], we continue to use the lognormal averaging method for calculating the VSF.

We use a greedy algorithm to automatically identify linear regions in the VSF plot, which correspond to physical power-law regimes. The process starts at the smallest scales and fits a straight line to a small group of adjacent data points. It then calculates the quality of this fit using the R^2 coefficient of determination.

If the fit is good, in this case defined to be $R^2 > 0.97$, we extend the segment by one more data point and re-evaluate the fit. This continues until adding an additional point causes the fit quality to drop below the 0.97 threshold and the process stops. The longest successful segment is then recorded, and the algorithm resumes its search from where that segment ended, repeating the process until all data is analysed. The regions identified as linear by this process are highlighted in grey in the VSF figures, for example in Fig. 6.1.

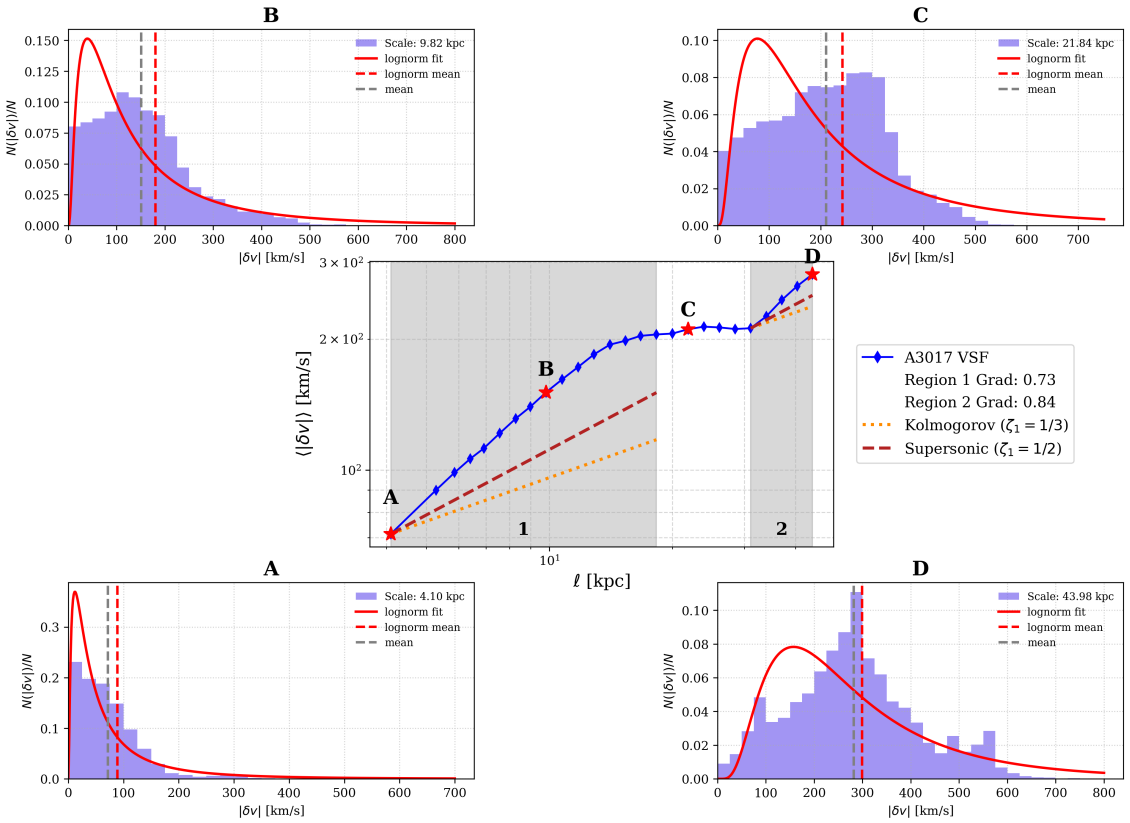

Figure 6.1: The central panel shows the VSF profile for A3017. The velocity value plotted is the lognormal mean of the distribution observed for each separation. This is illustrated for a subset of the separations by the plots in the corners of the figure. The grey regions highlight the linear regions identified by the greedy algorithm with the corresponding gradient shown in the legend. Kolmogorov and supersonic reference slops are plots in red and orange respectively in each of these regions.

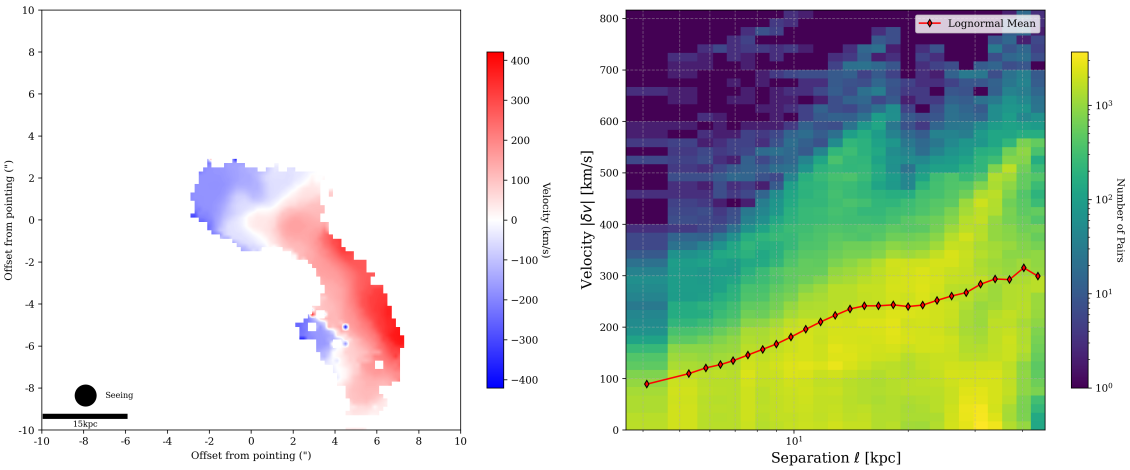

Figure 6.2: The left-hand panel shows the velocity map for the object A3017. The right-hand shows a 2D histogram of the velocity differences at each separation. The lognormal mean profile is overlaid.

The entire method is best understood with reference to this figure. The lognormal mean values of the velocity distribution are plotted for each separation bin in the central panel. The diversity of distributions at each separation are evident from the histograms surrounding the central figure where we explicitly plot the full distribution for four systematic separation. It is evident that reducing these values to a single number, however well-motivated the distribution, is to discard much of the information we have captured. To minimise this loss we produced a 2D heat-map shown in Fig. 6.2. Here the distribution of velocities at each separation is shown as a vertical heatmap which, when combined, enable the nature of the kinematic structure to be probed. These figures represent an extremely effective distillation of the LOS kinematic information, and I found it a fun distraction to play 'guess the structure' from these plots; it is often possible to predict the broad features of the LOSVD map. Extended regions of relatively quiescent gas appear as continuous streaks across the parameter space. Kinematically isolated pockets of gas appear as islands in the heatmap. This is demonstrated by the blue shifted pocket of gas in the southern half of the velocity map in Fig. 6.2.

The same plots are shown for three further objects which collectively highlight the four distinct VSF profiles observe. A3444, shown in Fig. 6.7 and Fig. 6.8 exhibits a negative quadratic shape with a peak in the VSF at $\sim$ 12kpc. We observe this shape in multiple objects, with the breakdown shown in Table 6.1. The VSF profile for A3112 is shown in Fig. 6.11 and Fig. 6.12. This shape, showing a decline with increasing separation is typically only found for the case of a embedded disc of rotating gas embedded in more quiescent gas. A linearly increasing VSF, as seen in Fig. 6.9 and Fig. 6.10, indicates a disc like rotating structure.

6.5 Analysis

There is, naturally, some information lost in translating a 2D LOS velocity map into plots of this form; even the most seasoned disciple of the VSF method would not be able draw a 2D velocity map given a VSF profile. He/she would get closer given the 2D heatmaps we have shown; though with some ambiguity remaining. What these

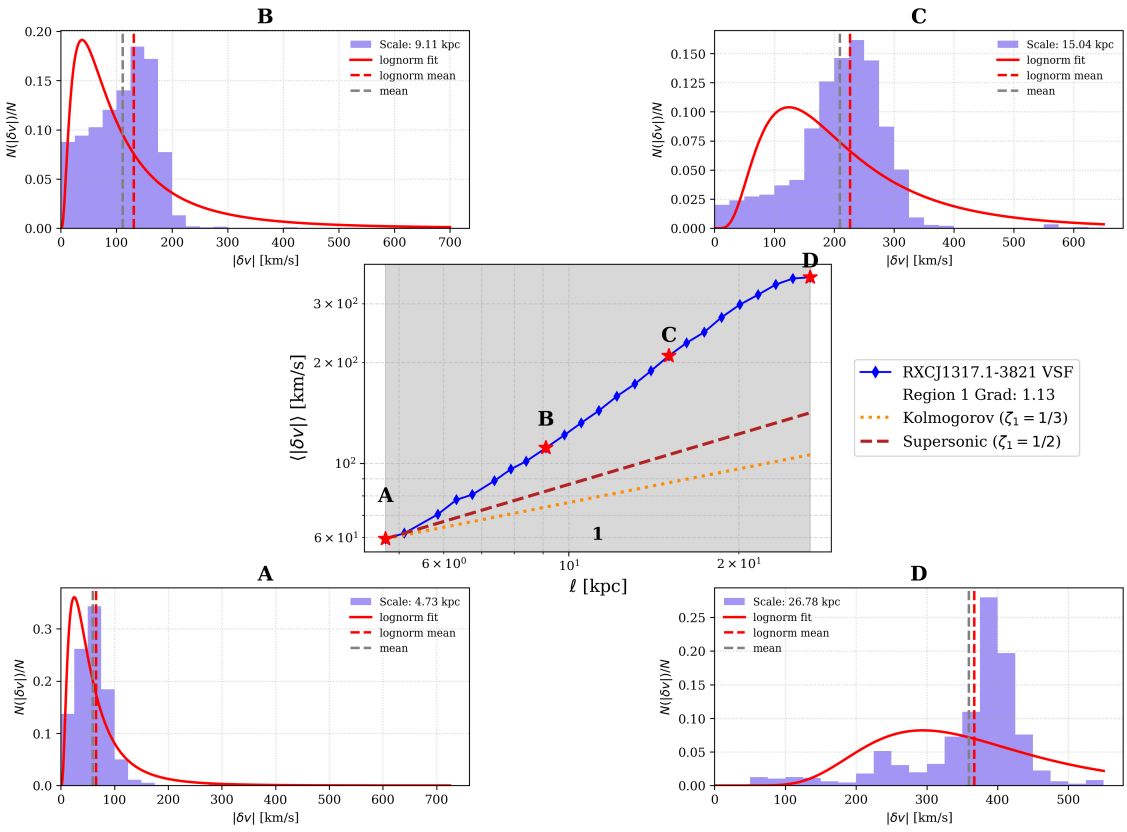

Figure 6.3: The simple power law VSF profile of RXCJ1317.1-3821

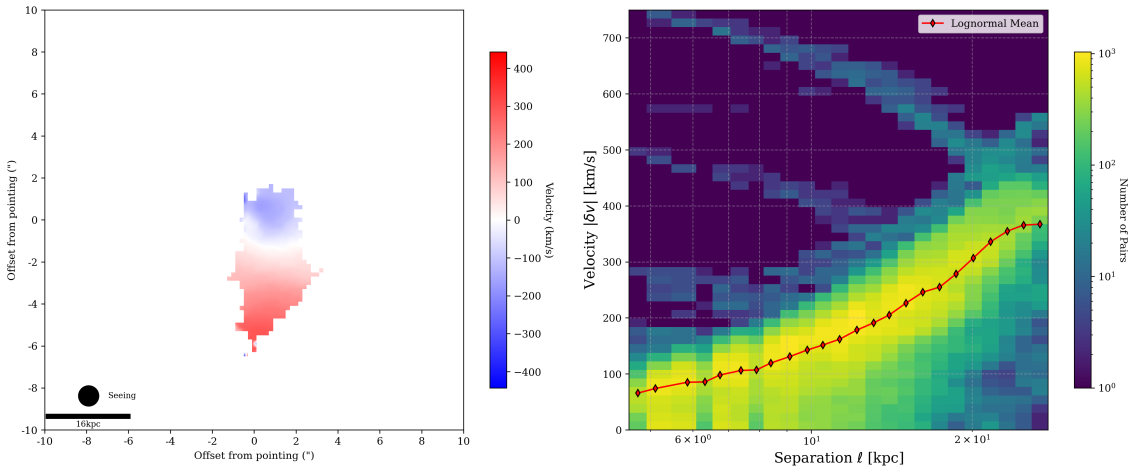

Figure 6.4: LOSVD and 2D VSF profile for RXCJ1317.1-3821.

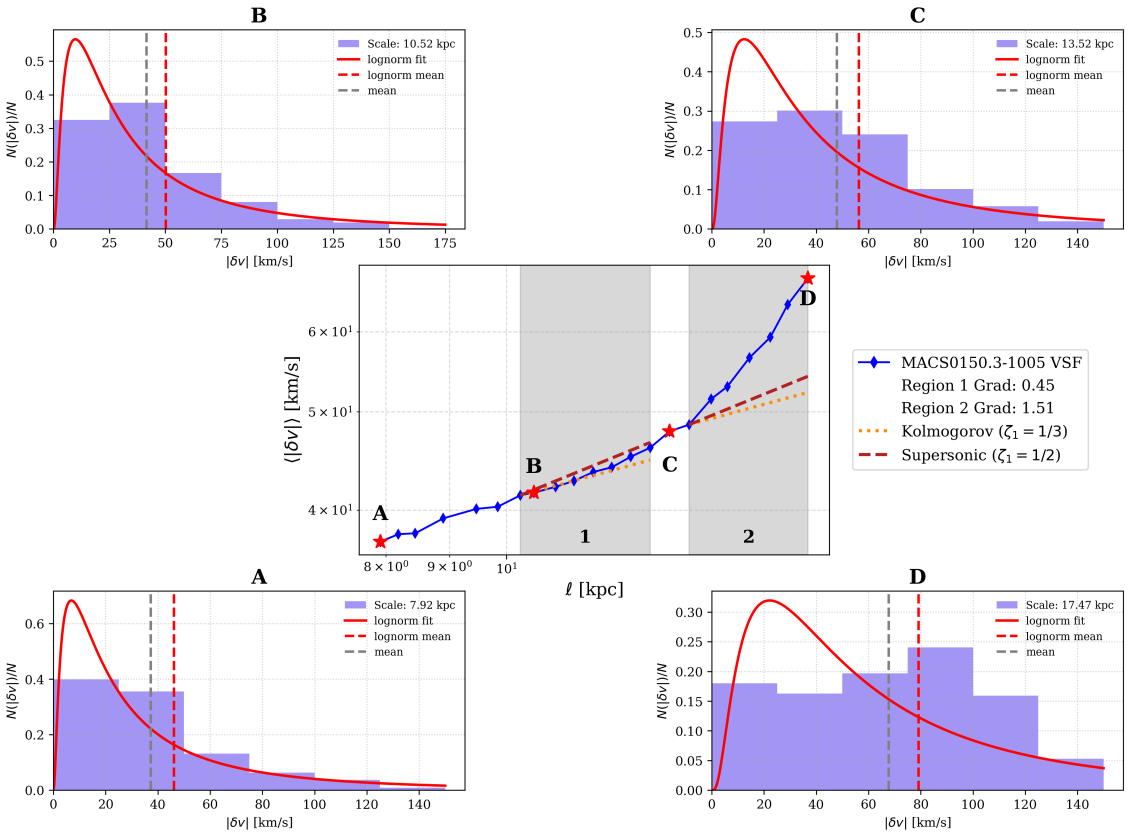

Figure 6.5: The broken power law VSF profile of MACS0150.3-1005.

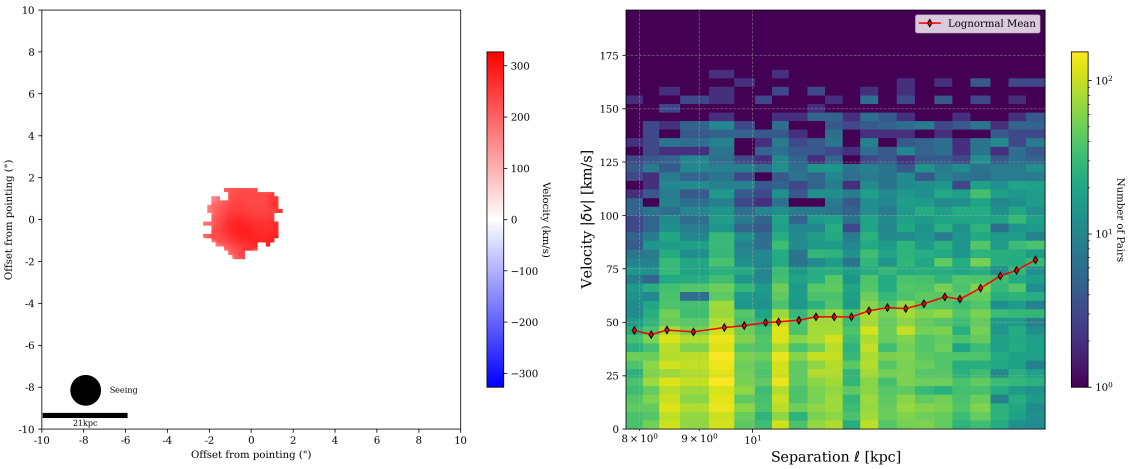

Figure 6.6: LOSVD and 2D VSF profile for MACS0150.3-1005.

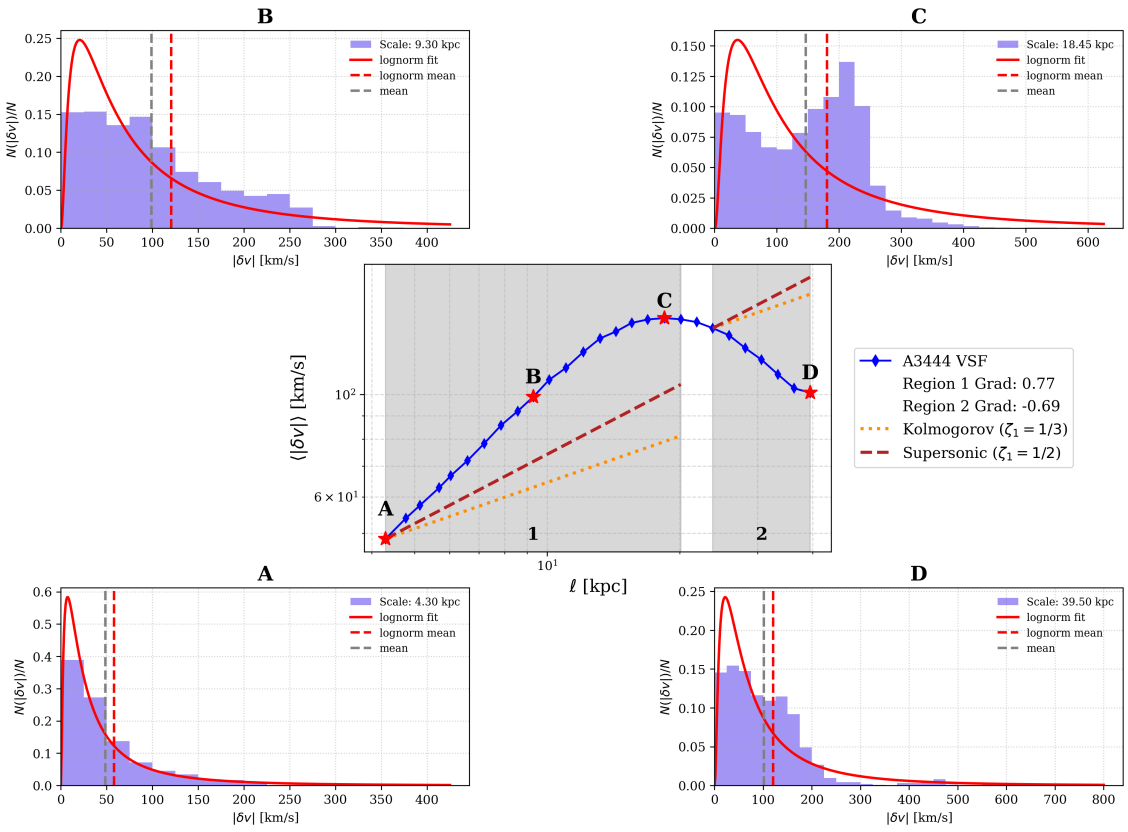

Figure 6.7: The inverse quadratic shaped VSF profile of A3444.

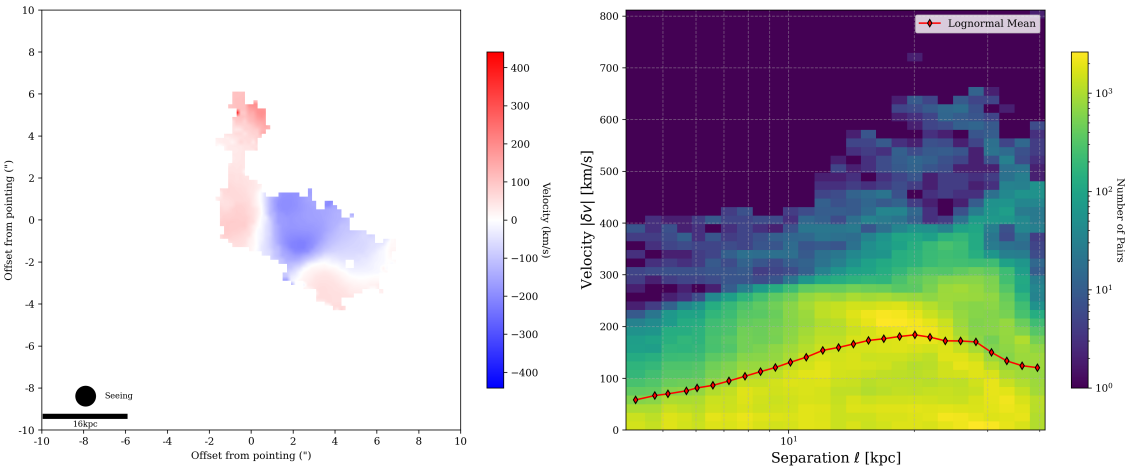

Figure 6.8: LOSVD and 2D VSF profile for A3444.

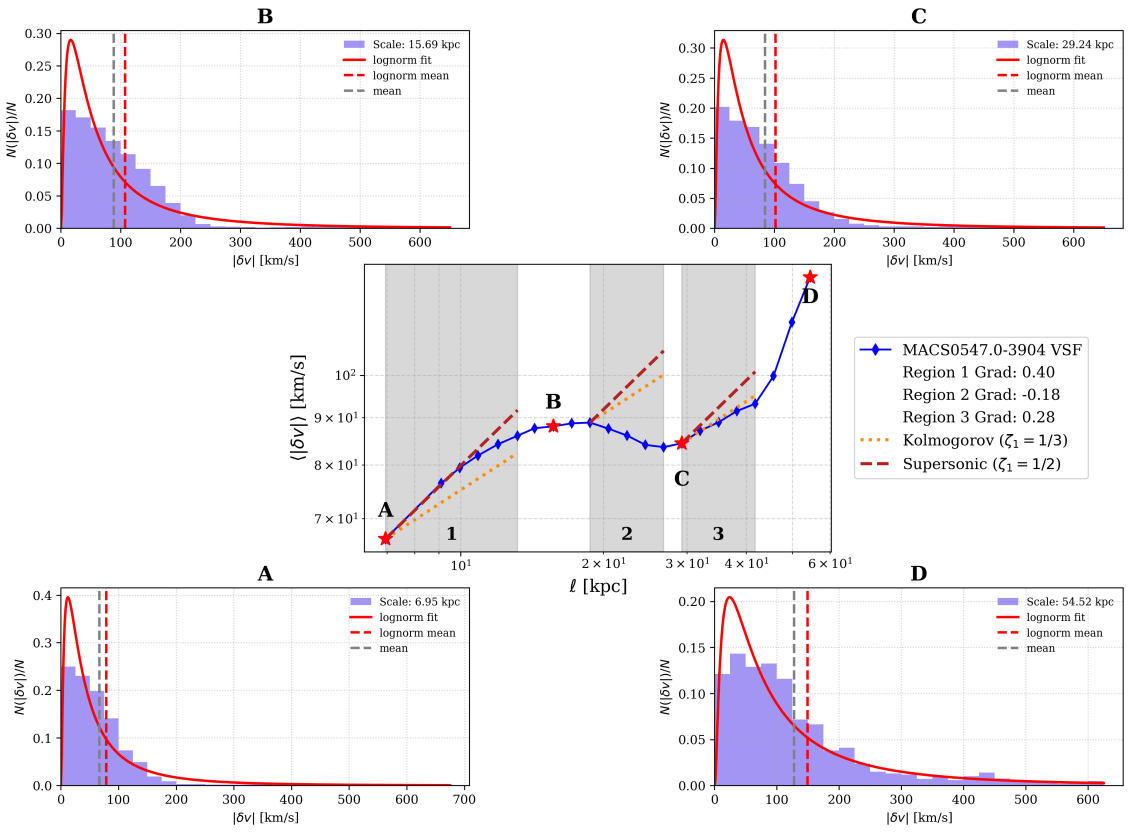

Figure 6.9: The 'cubic' VSF profile of MACS0547.0-3904

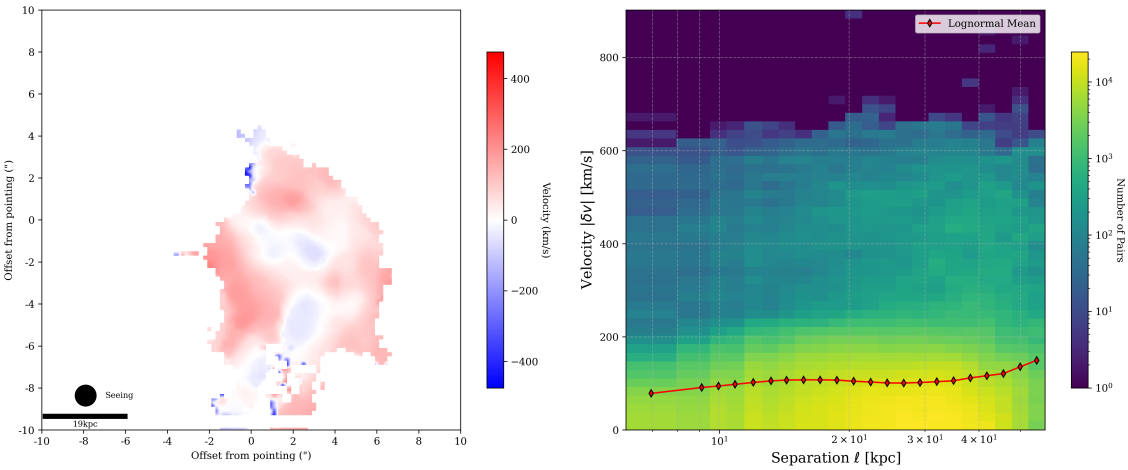

Figure 6.10: LOSVD and 2D VSF profile for MACS0547.0-3904.

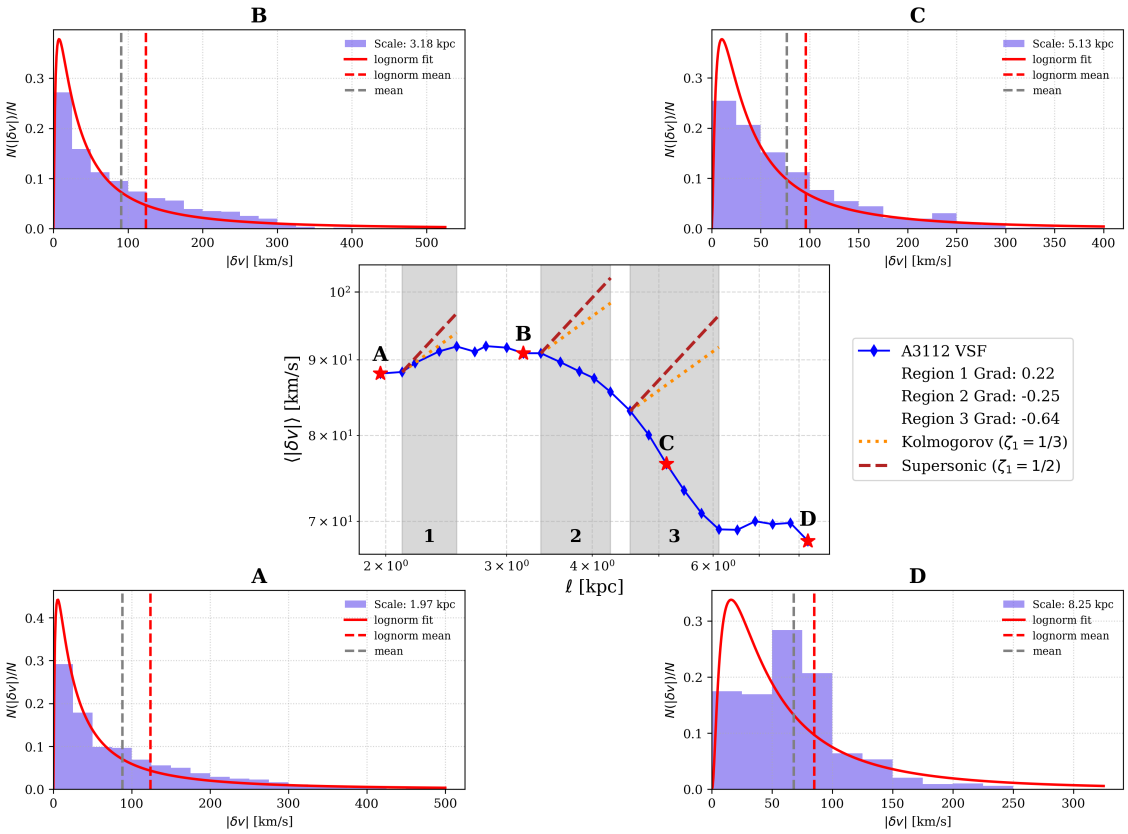

Figure 6.11: The decreasing VSF profile of A3112.

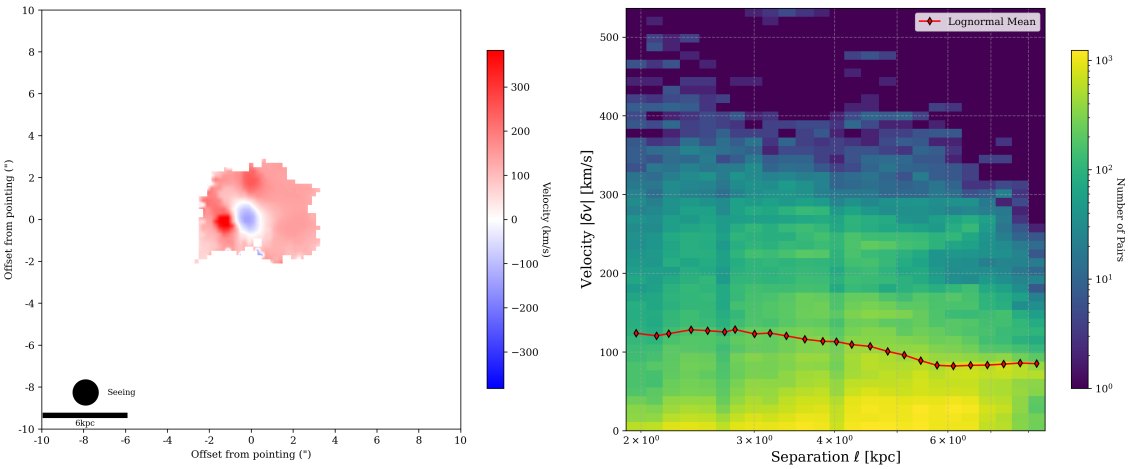

Figure 6.12: LOSVD and 2D VSF profile for A3112.

figures do allow is a point of comparison between the many objects which comprise the Kaleidoscope survey. We are able to extract VSF profiles for 36 objects in our sample. The obvious requirement that objects show line emission and the less obvious constraint that this emission be sufficiently extended to extract meaningful VSF profiles, discussed in § 6.4, reduces the full sample. We are able to further categorise this sub-sample based on the shape of the VSF profile. Archetypes of the five profile shapes - simple power law, broken power law, n-shape, 'cubic' and decreasing - are shown in Fig. 6.9 to Fig. 6.12. The decreasing profile we see for A3112 in Fig. 6.11 is a standalone case and not treated as a distinct profile category. The breakdown is shown in Table 6.1.

Table 6.1: Frequency of VSF Profile Types

VSF profile	Frequency
Power Law	17
Broken Power Law	5
Quadratic	9
Cubic	3

Fig. 6.13 shows the two–dimensional distribution of velocity differences, δv, as a function of projected separation, ℓ, combining all line emitting objects of sufficient spatial extent to extract the VSF in the Kaleidoscope sample. Each pixel represents the number of spatial pairs contributing to a given (ℓ, δv) bin, with colour indicating the logarithm of the counts. This plot provides a complementary view to the fitted gradients in Fig. 6.14, since it shows the raw pair statistics underlying the structure functions.

Several key features stand out. First, the distribution is strongly concentrated toward modest velocity differences ($\delta v \lesssim 200\,\mathrm{km\,s^{-1}}$), reflecting the prevalence of low–amplitude fluctuations in the gas velocity field across most separations. The ridge of high density that rises gently with ℓ traces the typical scaling of the VSF: on average, larger separations correspond to larger velocity increments. However, the distribution is also broad, extending to $\delta v \gtrsim 400$–$600\,\mathrm{km\,s^{-1}}$ at all radii, which indicates that extreme velocity differences are common and not confined to a particular spatial scale. This broad tail is consistent with our finding that many regions exhibit VSF exponents steeper than the classical Kolmogorov or Burgers expectations,

since both gravity–driven flows and intermittent AGN–driven structures can inject coherent velocity differences that dominate over random turbulence. The colour scaling highlights the growth in pixel pairs with separation ℓ (since more pixel pairs are separated by larger distances within each map), so the most statistically robust constraints come from intermediate to large separations. The persistence of broad δv distributions out to $\ell \sim 20$–$30\,\mathrm{kpc}$ demonstrates that coherent velocity differences are not a local phenomenon, but extend across the full radial range probed by our data. The heatmap underscores two important conclusions. The first is that the VSF slopes derived in the previous section genuinely reflect broad, underlying distributions rather than being dominated by a small number of outliers. The second is that the ubiquity of large velocity differences across scales supports a picture in which turbulence, gravitational inflow, and AGN feedback all contribute simultaneously to shaping the kinematics of the multiphase medium in BCGs. This multi–process interpretation is consistent with both numerical predictions [e.g., Gaspari and Sądowski, 2017, Mohapatra et al., 2023] and recent observational studies of individual systems [Tremblay et al., 2018].

A more selective distillation of the information is shown in Fig. 6.14. Here we plot all gradients we extract via the greedy algorithm (corresponding to the grey region in e.g. Fig. 6.11. The extent of the line represent the separation range over which the gradient was extracted. While a population of the measured scaling exponents (ζ_1) clusters between the Kolmogorov (1/3) and supersonic (1/2) values, a significant number of regions exhibit much steeper gradients, with $\zeta_1 > 0.5$. This suggests that the simple picture of turbulence driven solely by solenoidal or compressive forcing is insufficient to explain the data. The most probable explanation for scaling exponents steeper than the Burgers limit is the influence of gravity. In regions undergoing gravitational collapse or large-scale infall, the velocity field is not determined by a random turbulent cascade alone, but by a coherent, gravity-driven flow. The kernel–averaged radial profile in the lower panel of Fig. 6.14 shows no statistically significant trend of the mean VSF slope with separation ℓ across the scales we probe. Within the uncertainties, $\langle\zeta_1\rangle$ remains approximately constant and typically above the Kolmogorov and Burgers expectations. The absence of a clear

radial dependence argues against simple scenarios in which turbulence strength or driving mode varies monotonically with radius in cluster cores. Instead, it is consistent with a picture in which multiple processes inject and redistribute kinetic energy over a broad range of scales—AGN jets and buoyant bubbles, sloshing, and galaxy motions—yielding an approximately scale–free mixture of solenoidal and compressive fluctuations superposed with coherent inflow [e.g., Fabian, 2012, Gaspari and Sądowski, 2017, Gaspari et al., 2018, Hitomi Collaboration, 2016, Zhuravleva et al., 2014b]. In such a regime, the VSF measured at different radii reflects a quasi–steady balance between turbulent cascading and gravity–driven motions, rather than a radial stratification of a single driving mechanism. The flat profile therefore reinforces our conclusion from the object–by–object gradients that steep VSF slopes are a pervasive property of cool–core environments, not a feature confined to specific radii or to a narrow injection scale.

In a simple model of free-fall, the velocity scales with radius as $v \propto r^{1/2}$. For a region undergoing coherent collapse the velocity can scale linearly with distance, $v \propto r^{1}$. Since the first-order VSF scales as $S_1(\ell) \propto \ell^{\zeta_1}$, and is dominated by the underlying velocity-scale relation, these gravitational flows would produce steep exponents. Free-fall dominated regions, $\zeta_1 \approx 0.5$, would produce gradients that lie on or slightly above the Burgers limit. Coherent collapse / rotationally supported regions, $\zeta_1 \approx 1.0$, would explain the population of very steep gradients observed in the plot between $\zeta_1 \approx 0.8$ and 1.4. Many of the regions with the steepest gradients observed may not be in a state of simple, pressure-supported turbulence. Instead, their kinematics are dictated by ongoing gravitational contraction. This would match offset we discussed in § 5.1.

An alternative, perhaps complementary, explanation is intermittency. The VSF represents a spatial average; if this region contains highly energetic, coherent structures—such as powerful bipolar outflows then these localised features could dominate the statistics. Such outflows can inject momentum in a highly ordered manner, creating a steep velocity gradient across the structure that does not conform to standard turbulence theories. In this scenario, the measured ζ_1 would not represent a global turbulent cascade, but rather the specific properties of these isolated,

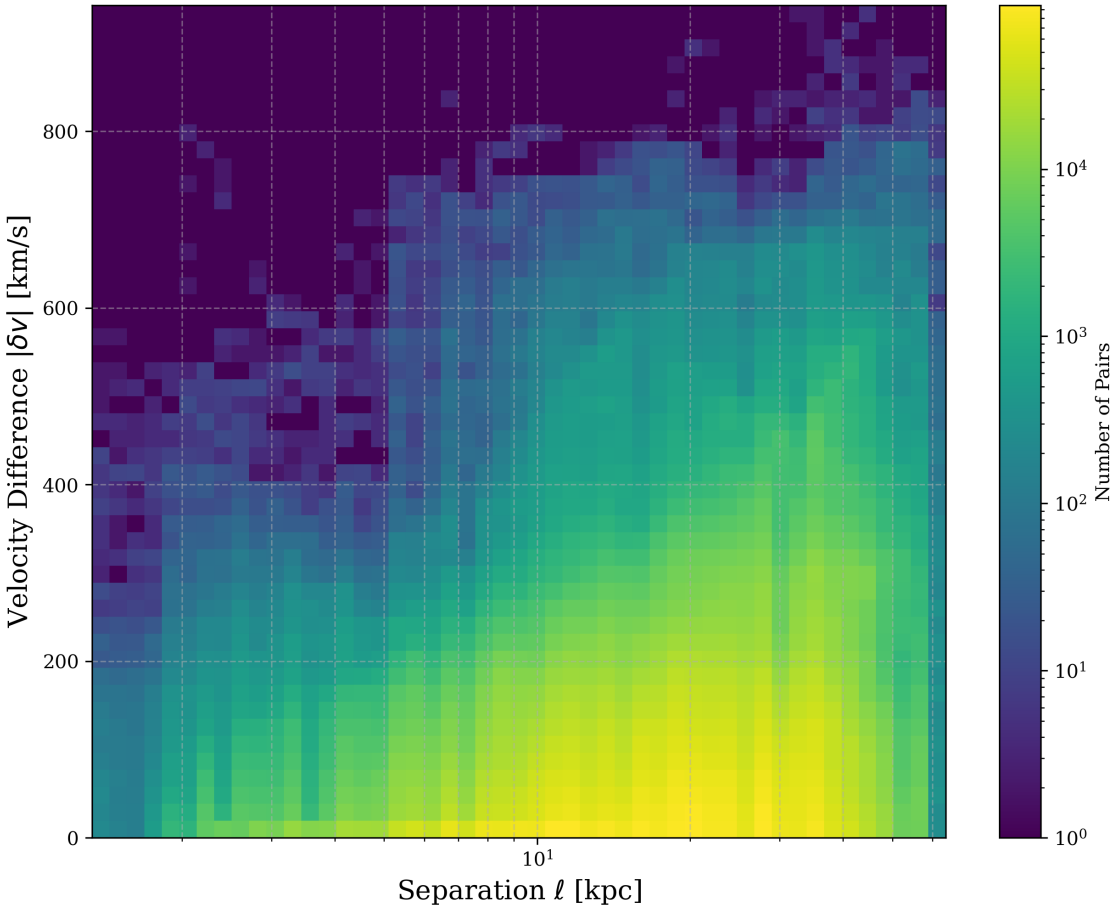

Figure 6.13: The combined 2D histogram of all 36 objects for which meaningful VSF profiles could be extracted.

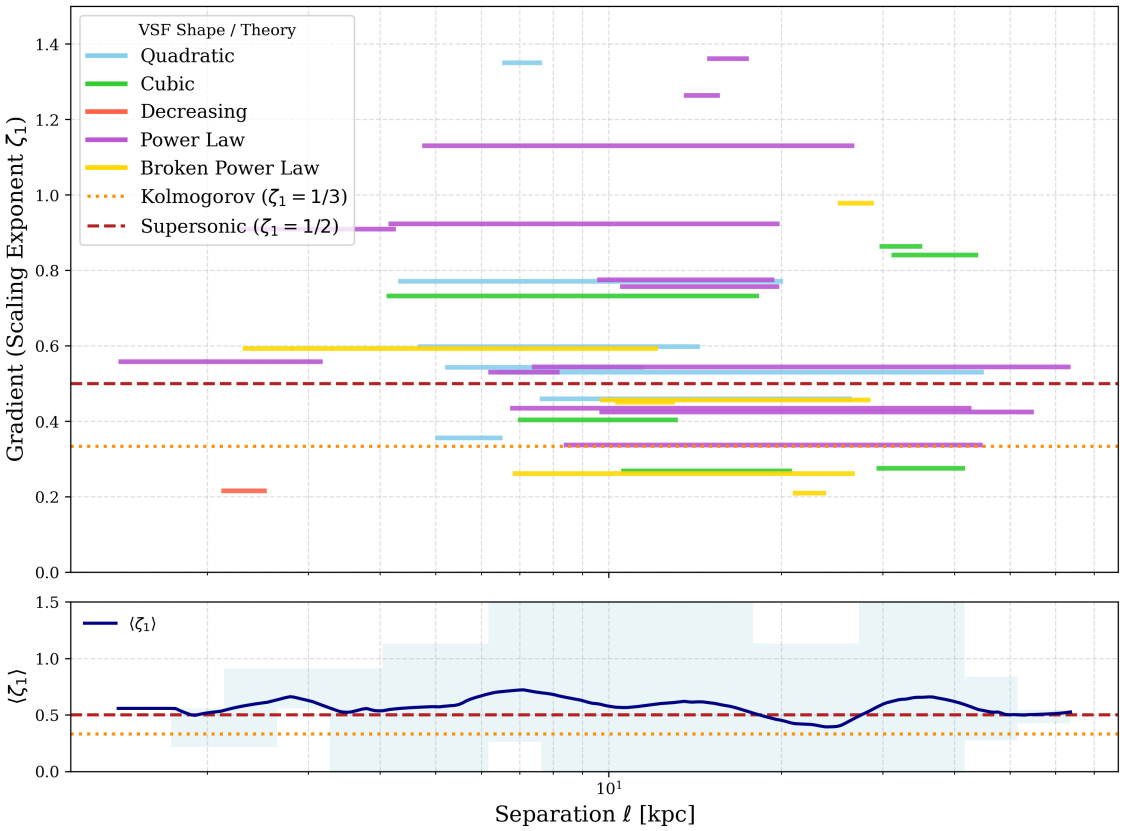

Figure 6.14: **Top panel:** Horizontal bars show the fitted scaling exponents ζ_1 for individual regions. The colour corresponds to the profile shape, the breakdown of which is shown in Table 6.1. Reference lines mark the Kolmogorov ($\zeta_1 = 1/3$; orange dotted) and supersonic ($\zeta_1 = 1/2$; red dashed) expectations. **Bottom panel:** Radial profile of the average gradient as a function of separation ℓ, obtained by overlap–weighted averaging in logarithmic bins.

energetic events.

6.6 Summary

Across the Kaleidoscope sample, the first–order VSF exponents, ζ_1, are systematically steep: most regions lie at or above the Burgers expectation ($\zeta_1 = 1/2$) and a large fraction reach $\zeta_1 \sim 0.8$–1.4, with no significant radial trend in the mean profile (Fig. 6.14). This behaviour argues against a picture in which the kinematics are governed solely by a steady, homogeneous cascade (Kolmogorov or Burgers). Instead, the data favour a superposition of (i) coherent, gravity–guided inflows and partial collapse that imprint large velocity gradients and naturally yield $\zeta_1 \gtrsim 0.5$–1, and (ii) intermittent AGN feedback (jets, bubbles, weak shocks) that injects momentum anisotropically and biases low–order VSFs toward steeper slopes. The lack of a clear radial dependence further suggests multi–scale, multi–channel driving (AGN, sloshing, galaxy motions) that redistributes kinetic energy across radii, producing an approximately scale–free mixture of solenoidal and compressive fluctuations superposed with ordered flows.

These population–level trends extend earlier VSF studies of BCGs. Study of three nearby cool–core clusters showed VSFs steeper than Kolmogorov, with features correlating with AGN bubble sizes, implying SMBH feedback as the primary driver of motions [Li et al., 2025]. Subsequent analyses expanded to $\sim$a dozen systems using MUSE and ALMA, again finding slopes steeper than Kolmogorov in most cases, occasional flattening toward Kolmogorov on the smallest resolvable scales, and inferred driving scales consistent with cavity sizes; those studies likewise concluded that the VSF often traces driver–imposed bulk motions more than a mature inertial cascade [Ganguly et al., 2023]. Case studies of individual BCGs that compute ionised and molecular–gas VSFs report $\zeta_1 \gtrsim 1/2$ for Hα and even $\sim$linear ($\zeta_1 \approx 1$) behaviour for molecular gas in regions dominated by laminar filaments or jet–ISM coupling, reinforcing the role of feedback and coherent flows [Tamhane et al., 2023]. Complementary constraints on the hot ICM using XMM–Newton show that VSFs (or closely related fluctuation diagnostics) are measurable in X–rays and are

consistent with AGN–stirred, low–Mach motions [Gatuzz et al., 2023]. On the theory side, VSF analyses of multiphase/MHD simulations demonstrate that magnetic fields, projection, compressive forcing, and intermittency can steepen VSF slopes beyond Kolmogorov and even Burgers, particularly for the cold phase and in the presence of driver–scale coherence [Mohapatra et al., 2023].

In this context, Kaleidoscope's homogeneous, object–by–object gradient census and ensemble radial profile add two key results: (1) the prevalence of $\zeta_1 > 0.5$ across many systems—not just a handful—indicates that steep VSFs are a generic property of cool–core environments, not an extreme property of a few sources; and (2) the flat mean profile with radius argues for persistent, multi–scale driving rather than a simple inside–out transition in turbulence regime. Together with the earlier VSF surveys, these results support a picture in which AGN feedback and gravity jointly regulate multiphase kinematics in BCGs: jets/bubbles set the injection scales and intermittency, while gravity channels and sustains coherent inflow, with the observed VSF slopes reflecting the relative local dominance of these processes.

CHAPTER 7

Excitation Mechanism

BCGs are often embedded in extended nebulae of warm ionised gas, visible as optical line emission. Unlike the hot ICM, observed primarily in X-rays, or the cold molecular component traced by CO and dust, this $T \sim 10^4\,\mathrm{K}$ phase is directly visible in the optical through its atomic transitions. The extended line emission serves as a powerful diagnostic, enabling us to probe the excitation, kinematics, and energetics of gas in regions where cooling, feedback, and star formation intersect. Each line arises from a well-defined radiative transition between energy levels in ions or atoms, governed by selection rules and collisional processes. The relative intensities of these lines encode the balance between excitation and de-excitation, which in turn depends on the local temperature, density, and ionisation conditions of the gas. For instance, collisionally excited forbidden lines such as [O II], [O III], and [N II] are strongly sensitive to electron density and temperature, while recombination lines like Hα and Hβ primarily trace the ionised fraction and therefore provide a measure of the ionising photon field. By mapping these diagnostics spatially, we can obtain not just the distribution of the warm gas but also its microphysical state, as dictated by the underlying atomic processes.

There are several standard diagnostic tools which form the basis of studies on the

extended emission of ionised gas. Line ratios such as [N II]/Hα or [O III]/Hβ provide a probe into the dominant ionisation mechanism—whether photoionisation by young stars, heating by AGN, shocks, or cosmic rays [e.g. Kewley et al., 2006]. Density diagnostics, such as the [S II]λ6716/λ6731 ratio, exploit the competition between collisional de-excitation and radiative decay, reflecting the fundamental balance of atomic level populations. Auroral transitions such as [O III]λ4363, though faint, provide temperature measurements by comparing high-lying states to their stronger counterparts.

MUSE enables mapping the fluxes, ratios, and kinematics of the emission lines across these structures, enabling spatial mapping of properties such as ionisation state, metallicity, and turbulence as a function of position. The extended line emission provides a link between the microscopic and macroscopic: the radiative signature of individual atoms and ions allow us to map the distribution, dynamics, and thermodynamic state of gas on galactic and cluster scales.

We summarised the basic line emission properties in the Kaleidoscope sample in Chapter 3 and defined the line-emitting sub-sample which will form the basis of this chapter. § 7.1 focusses on the metallicity variation. § 7.2, the main focus of the chapter, applies various diagnostic plots to probe the excitation mechanism driving the ionisation. We briefly discuss the illusive [OIII] λ4363 line and use it's frequent absence to constrain the electron temperature in § 7.3. 7.4 explores the dust properties of the sample.

7.1 Effects of Metallicity on Emission Line Ratios

The flux ratio of [NII] to Hα can probe the gas-phase metallicity of the observed galaxies. This ratio is a widely used empirical calibrator for metallicity in star-forming regions, as the abundance of nitrogen, a product of secondary nucleosynthesis, increases with the overall metal content of the gas. However, the ratio is also sensitive to the ionisation conditions (as explored in § 7.2), potentially creating a degeneracy.

Galaxies with low mean ratios implies gas that has a metallicity near or slightly

below solar values, typical of actively star-forming regions. In the absence of a hard ionisation field, this ratio points towards a conventional star-forming environment. A high mean ratio implies one of two physical scenarios. The gas may be highly enriched with metals (super-solar metallicity). This is possible in the central regions of massive BCGs, which have undergone extensive stellar processing. Alternatively, the high ratio may not be due to metallicity but rather to a hard ionisation field from an AGN or shock-heating of the gas. Both phenomena are common in the dynamic environments of galaxy clusters and can significantly boost the [NII]/Hα ratio irrespective of the underlying metallicity. Involving additional lines, as in 7.2, can eliminate the degeneracy and provide a more robust separatrix.

We show flux ratio maps for all objects exhibiting extended emission of both [NII] and Hα in Fig. 7.1. The sample of galaxies exhibits a very broad range of mean [NII]/Hα ratios, from approximately 0.35 to 3.24, suggesting a wide spread in the physical conditions of the gas across the sample.

7.1.1 Metallicity Estimation

The N2 index [Pettini and Pagel, 2004] is defined as:

$$\mathrm{N2} = \log_{10}\left(\frac{[\mathrm{NII}]_{6584}}{\mathrm{H}\alpha}\right) \tag{7.1}$$

This index can estimate oxygen abundance (O/H) as follows [Pettini and Pagel, 2004]:

$$12 + \log_{10}(\mathrm{O/H}) = 8.90 + 0.57 \times \mathrm{N2} \tag{7.2}$$

Calculating abundances for the extreme ratios we observe yields Table 7.1.

Cluster	**Mean [NII]/Hα**	$12 + \log_{10}$**(O/H)**
A2259	0.35	8.64
MACSJ1427.6-2521	3.24	9.19

Table 7.1: Calculated oxygen abundances for the extrema of observed [NII]/Hα ratios.

Pettini & Pagel Pettini and Pagel [2004] observed that oxygen abundances typ-

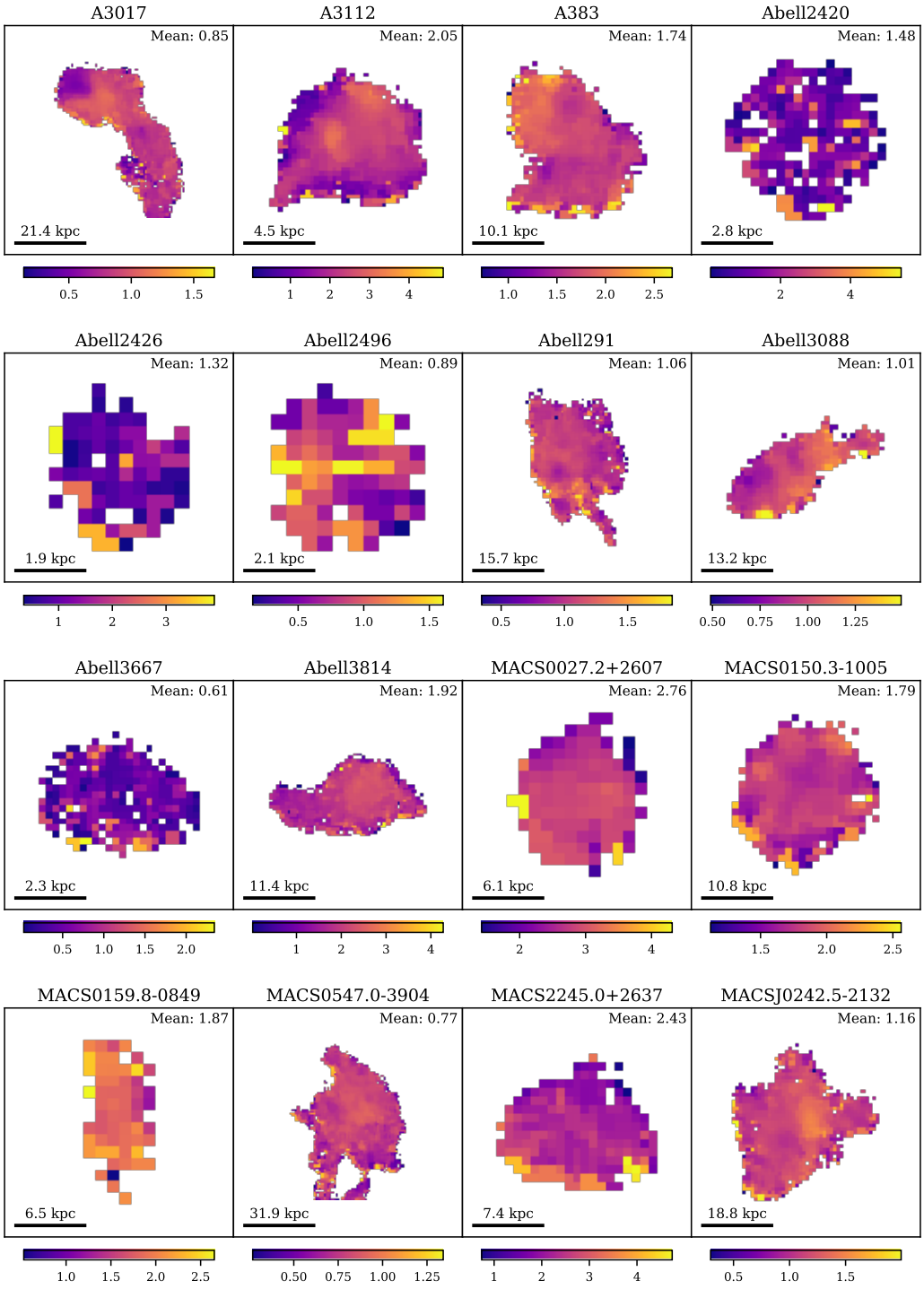

Figure 7.1: Spatially resolved maps of the [NII]/Hα flux ratio for the galaxy sample.

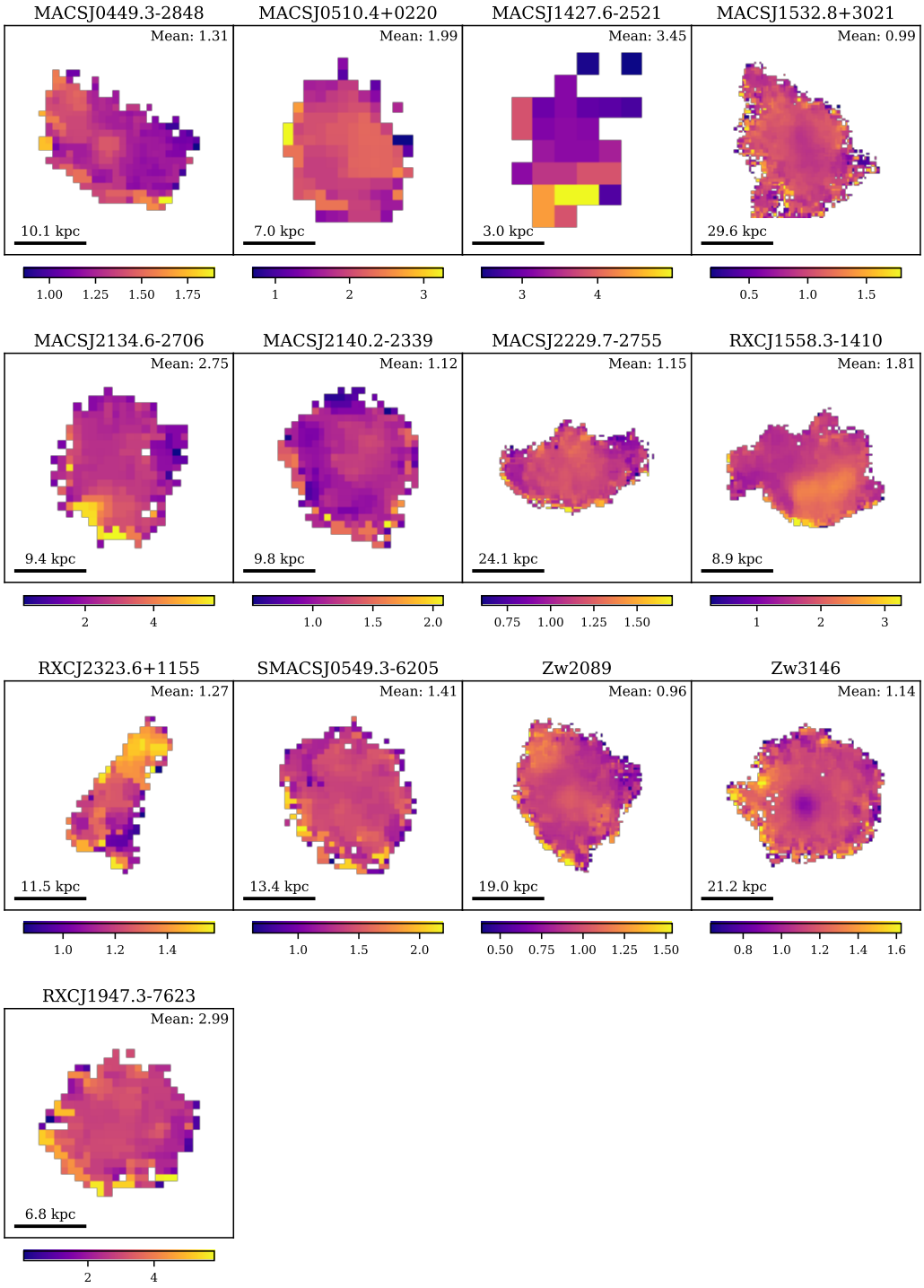
MACSJ0449.3-2848
Mean: 1.31
10.1 kpc
1.00 1.25 1.50 1.75
MACSJ0510.4+0220
Mean: 1.99
7.0 kpc
1 2 3
MACSJ1427.6-2521
Mean: 3.45
3.0 kpc
3 4
MACSJ1532.8+3021
Mean: 0.99
29.6 kpc
0.5 1.0 1.5
MACSJ2134.6-2706
Mean: 2.75
9.4 kpc
2 4
MACSJ2140.2-2339
Mean: 1.12
9.8 kpc
1.0 1.5 2.0
MACSJ2229.7-2755
Mean: 1.15
24.1 kpc
0.75 1.00 1.25 1.50
RXCJ1558.3-1410
Mean: 1.81
8.9 kpc
1 2 3
RXCJ2323.6+1155
Mean: 1.27
11.5 kpc
1.0 1.2 1.4
SMACSJ0549.3-6205
Mean: 1.41
13.4 kpc
1.0 1.5 2.0
Zw2089
Mean: 0.96
19.0 kpc
0.50 0.75 1.00 1.25 1.50
Zw3146
Mean: 1.14
21.2 kpc
0.8 1.0 1.2 1.4 1.6
RXCJ1947.3-7623
Mean: 2.99
6.8 kpc
2 4

Continued

ically lie within ±0.41 dex of the derived value. Our range is within this expected variation, supporting the assumption that metallicity differences across objects and spatially within each object are negligible.

Given the limited variation in the estimated metallicities, we conclude that metallicity has a negligible effect on the observed [NII]/Hα line ratios across this cluster sample. Variations observed in these line ratios are thus more likely influenced by other physical factors, such as ionisation conditions or shocks, rather than differences in metallicity.

7.2 BPT diagrams

The Baldwin–Phillips–Terlevich (BPT) diagram was introduced by [Baldwin et al., 1981] as a quantitative diagnostic to classify the dominant excitation source in emission-line galaxies. By plotting ratios of strong optical emission lines, BPT diagrams differentiate gas ionised by hot, young stars in HII regions from gas ionised by active galactic nuclei (AGN) or other energetic processes. The original BPT work showed that classical star-forming HII regions occupy a distinct locus, separated from AGN-ionised regions in certain line ratio spaces. It was shown that Seyfert nuclei and low-ionisation nuclear emission regions (LINERs) [Heckman, 1980] have much higher excitation line ratios than normal HII regions, allowing a clear separation between these ionisation sources.

Veilleux and Osterbrock [1987] expanded on the BPT concept by exploring multiple line-ratio diagrams as diagnostic tools. They formalised three classic optical diagnostic diagrams: (1) [O III]λ5007/Hβ vs. [NII]λ6584/Hα, (2) [OIII]λ5007/Hβ vs. [SII]$\lambda\lambda$6717, 6731/Hα, and (3) [OIII]λ5007/Hβ vs. [OI]λ6300/Hα. We will explore each of these in § 7.2.5.

7.2.1 Theory

These ratios involve emission lines that are close in wavelength (e.g. [OIII] 5007Å and Hβ 4861Å), making the line ratios relatively insensitive to dust extinction. By comparing different combinations of low- vs. high-ionisation lines, we can empirically

distinguish galaxies ionised by UV radiation from massive stars (which produce the spectra of HII regions) from those ionised by harder radiation fields characteristic of AGN or shock heating. Early applications of the BPT and Veilleux–Osterbrock diagrams demonstrated, for example, that Seyfert nuclei exhibit elevated [O III]/Hβ and [N II]/Hα ratios, while normal star-forming regions have much lower values of these ratios [Veilleux and Osterbrock, 1987]. LINERs were recognised to occupy a region intermediate to these, with relatively strong low-ionisation lines ([N II], [S II], [O I]) but lower excitation ([O III]/Hβ) compared to Seyferts. The most commonly used BPT diagram plots the logarithm of [O III]λ5007/Hβ (a measure of high-ionisation emission relative to recombination) on the vertical axis against the logarithm of [NII]λ6584/Hα (a measure of low-ionisation line strength relative to recombination) on the horizontal axis. Similar plots replace [NII]/Hα with either the sulfur doublet ratio [S II]$\lambda\lambda$6717, 6731/Hα or the neutral oxygen line [OI]λ6300/Hα depending on redshidt and line visibility. In each case, Hβ and Hα (Balmer recombination lines) serve as normalising fluxes, so the diagnostic ratios compare forbidden metal lines to the hydrogen emission. Physically, [OIII]/Hβ is sensitive to the ionisation parameter and the hardness of the ionising radiation field: AGN and shock-ionised regions tend to produce higher [O III]/Hβ because they generate a larger fraction of high-energy photons capable of doubly ionising oxygen. Meanwhile, line ratios like [N II]/Hα, [S II]/Hα, and [O I]/Hα gauge the relative strength of low-ionisation transitions. Star-forming regions powered by O-stars generally yield modest values of [N II]/Hα (on the order of $\sim$0.1 to 0.3 in ratio, $\log_{10}$[NII/Hα] ≈ -1 to -0.5) because the HII region radiation field is not hard enough to produce very strong forbidden low-ionisation lines. By contrast, an AGN with a power-law ionising continuum can excite a much larger partially ionised zone, boosting the strengths of [N II], [S II], and [O I] relative to Hα. For this reason, AGN (especially Seyfert 2 nuclei) typically show $\log_{10}$([N II]/Hα)$\sim$ 0 (i.e. [N II] comparable to Hα) or higher, along with elevated [O III]/Hβ [e.g., Kewley et al., 2006].

On the BPT diagram, pure star-forming galaxies form a tight sequence running from the lower-left (low [N II]/Hα, low [O III]/Hβ) toward the upper-left (higher [O III]/Hβ at still modest [N II]/Hα). This "star-forming locus" corresponds to HII

regions of increasing metallicity and decreasing ionisation parameter as one moves upward and to the right along the sequence since higher metallicity tends to lower [O III]/Hβ and raise [N II]/Hα;[see, e.g., Dopita et al., 2000, Kewley et al., 2019]. Galaxies hosting AGN (Seyfert 2s) populate the upper-right part of the [N II]–BPT plane, with line ratios of order [N II]/Hα $\sim$1 (log $\sim$0) and [O III]/Hβ $\gtrsim$ 3 (log $\gtrsim$ 0.5) being common for Seyfert nuclei [Kewley et al., 2006, Veilleux and Osterbrock, 1987]. LINERs, which are thought to be powered by either very low-luminosity AGN or other sources of ionisation, characteristically exhibit even stronger low-ionisation line ratios ([N II]/Hα and especially [O I]/Hα) but comparatively weak [O III]/Hβ. Thus, in the [O III]/Hβ vs. [N II]/Hα plane, LINERs fall to the right of the star-forming locus (high [N II]/Hα) but at lower vertical values than Seyferts. This is much easier visualised than described, the classic BPT diagram is shown in Fig. 7.3. The other two BPT diagrams using [S II] or [O I] in place of [N II] serve a similar purpose: both Seyferts and LINERs lie above the star-forming regions in [O III]/Hβ, but LINERs can be isolated by their relatively higher [S II]/Hα or [O I]/Hα ratios (since Seyfert nuclei typically have moderate [S II]/Hα and weak [O I]/Hα, whereas LINERs show strong forbidden-line emission in these low-ionisation species) [Veilleux and Osterbrock, 1987].

7.2.2 Application

With large spectroscopic surveys, the BPT diagram became a quantitative classification scheme. In particular, the Sloan Digital Sky Survey (SDSS) enabled statistical demarcation of different classes of emission-line objects in the BPT plane. [Kewley et al., 2001] used theoretical starburst photoionisation models to derive an upper limit for line ratios achievable by pure star formation. This resulted in the 'maximum starburst line' – a curve on the BPT diagram above which no purely star-forming model (even one with extreme metallicity or ionisation parameter) can lie. Galaxies above this theoretical line must have an additional source of ionisation (likely an AGN). In the [N II]/Hα vs. [O III]/Hβ plane, the [Kewley et al., 2001] boundary is often used to conservatively identify AGN: objects above this line are classified as AGN-dominated. An empirical refinement was later provided by [Kauffmann et al.,

2003], who examined ∼22,000 SDSS galaxy spectra and drew a slightly lower dividing curve that traces the observed upper envelope of the star-forming sequence. The Kauffmann et al. line sits below the Kewley et al. theoretical boundary, thereby encompassing a region between the two curves where galaxies show mixed properties. Objects that fall between the Kauffmann (2003) empirical line and the Kewley (2001) theoretical line are usually referred to as composite systems: their line ratios could be produced by a combination of star formation and AGN activity within the same galaxy. In practice, these 'composite' galaxies show evidence of both a young stellar population and a low-luminosity AGN or other harder ionising source [e.g., Stasinska et al., 2006]. Galaxies below the Kauffmann line (with even lower [O III]/Hβ at a given [N II]/Hα) are securely star-forming, dominated by HII-region-like spectra with no need for an AGN contribution. Finally, galaxies above the Kewley line are dominated by AGN (broadly defined, including both Seyfert and LINER-type objects), since star formation alone cannot explain their high-excitation line ratios [Kauffmann et al., 2003, Kewley et al., 2001]. This two-curve scheme has become the standard: for example, it was adopted in the MPA-JHU SDSS catalog to classify nuclear spectra into star-forming, composite, or AGN categories.

Distinguishing between Seyfert AGN and LINERs requires considering the low-ionisation line ratios in more detail. In the original BPT ([N II]-based) diagram, both Seyferts and LINERs often overlap in the AGN region. However, plotting [O I]/Hα or [S II]/Hα against [O III]/Hβ helps separate these sub-classes. Empirically, Seyfert 2 nuclei tend to have lower [S II]/Hα and [O I]/Hα (indicating a smaller partially-ionised zone, consistent with a higher ionisation parameter), whereas LINERs exhibit higher values of these ratios (indicative of a large partially-ionised region or collisional excitation in low-ionisation gas) [Heckman, 1980, Veilleux and Osterbrock, 1987]. [Kewley et al., 2006] analysed a large sample of SDSS AGN and formally derived dividing lines between Seyferts and LINERs on the [S II] and [O I] BPT diagrams. For example, one commonly used criterion is that LINERs have $\log_{10}([O\ \mathrm{I}]/H\alpha) > -1.3$ (at relatively modest [O III]/Hβ), or $\log_{10}([S\ \mathrm{II}]/H\alpha) > -0.5$, whereas Seyferts lie at lower [S II]/Hα (or [O I]/Hα) for a given $\log_{10}([O\ \mathrm{III}]/H\beta)$. In essence, LINERs occupy a branch of the BPT space

characterised by strong low-ionisation emission and weaker high-ionisation emission, reflecting a different ionisation continuum or gas condition than the Seyfert branch [Kewley et al., 2006, Schawinski et al., 2007]. Modern studies often apply these cuts: objects above the Kewley et al. (2001) line are tagged as AGN, and then sub-classified as Seyfert-like or LINER-like based on their position in the [S II] and [O I] diagnostic diagrams [e.g., Kewley et al., 2006]. It should be noted that 'LINER' can describe diverse phenomena (low accretion-rate AGN, or ionisation by evolved stars or shocks, as discussed later), so this spectroscopic classification does not reveal the energy source but labels a locus of the parameter space.

The BPT classification scheme, with its demarcation curves from [Kewley et al., 2001] and [Kauffmann et al., 2003] and its subdivision of AGN into Seyfert and LINER branches [Kewley et al., 2006], has been widely adopted in the literature. It provided a systematic way to analyse the nature of galaxies in large surveys: for example, using BPT diagnostics, [Kauffmann et al., 2003] were able to identify an abundant population of composite galaxies hosting both star formation and AGN.

7.2.3 Spatially Resolved BPT Diagnostics in the IFU Era

While the BPT diagram was originally applied to single, integrated spectra of galaxies or nuclei, modern integral field spectroscopic (IFS) surveys allow the power of BPT diagnostics to be extended into two dimensions [e.g., Belfiore et al., 2016, Sánchez and et al., 2012]. Instruments such as MUSE (and survey projects like CALIFA, MaNGA, and SAMI) provide a data cube of spectra, allowing us to compute BPT line ratios for each spaxel across the object with detectable line emission. The result is a spatially resolved BPT diagram.

7.2.4 Limitations, Ambiguities, and Recent Extensions of BPT Diagnostics

BPT diagrams, as with any technique in observational astronomy, come with limitations, caveats and interpretative ambiguities. One major challenge is that line ratio boundaries are empirical and do not perfectly correspond to a single physical

mechanism. The 'composite' region between the Kauffmann and Kewley curves, for example, likely contains a mix of different situations: some galaxies in this space host a genuine weak AGN plus star formation, while others might be star-forming galaxies with unusual H II region conditions (hard stellar spectra, high nebular N/O abundance, etc.) that cause elevated line ratios mimicking an AGN. Similarly, an object classified as a LINER from line ratios alone could either be an actual low-luminosity AGN or a "fake" AGN – a retired galaxy where old hot stars ionise the gas [Cid Fernandes et al., 2011]. The BPT classification alone can be ambiguous for galaxies with LINER-like emission, necessitating complementary diagnostics. The 'WHAN' diagram, which uses the $H\alpha$ equivalent width ($W_{H\alpha}$) and plots it against the [N II]/$H\alpha$ ratio [Cid Fernandes et al., 2011] has been explored as a solution. This diagram resolves the ambiguity by distinguishing between galaxies with strong $H\alpha$ emission, indicative of an active galactic nucleus (AGN), and those with very weak emission (EW($H\alpha$) < 3 Å). These weak-line systems are considered 'retired', as their ionisation is consistent with hot post-AGB stars from old stellar populations. Consequently, combining BPT analysis with this method reveals that a large fraction of galaxies in the LINER zone, particularly ellipticals, are powered by these old stars rather than by accreting supermassive black holes [Belfiore et al., 2016, Cid Fernandes et al., 2011].

Another ambiguity arises from shocks. Fast radiative shocks can produce line ratios overlapping the Seyfert or LINER regions of BPT space [e.g., Allen et al., 2008]. For instance, galactic wind shocks or interactions in merging galaxies may ionise gas such that on a BPT diagram those regions would be misidentified as LINER/AGN-like. Distinguishing shock-ionised gas from AGN-photoionised gas may require kinematic information (shocks often broaden lines) or specific shock-sensitive line ratios. Additional line ratios like [O I]/Hα and [S II]/Hα are used together with [N II]/Hα to better pin down shocks, or one may include ultraviolet lines when available.

7.2.5 BPT Results

The 'classic' BPT diagram requires four emission lines to be visible within the spectral range: $H\beta$, [OIII] 5007, $H\alpha$, and [NII] 6583. This is satisfied for any $z < 0.42$ with MUSE. The number of objects emitting in each of these lines is shown in Table 7.2.

Table 7.2: Emission line visibility in the Kaleidoscope Survey to diagnose excitation mechanism via the [O III]λ5007/Hβ - [NII]λ6584/Hα BPT diagram.

Line	Objects in Spectral Window	Objects with Line Emission
$H\beta$	127	39
[O III] λ5007	127	39
$H\alpha$	107	35
[N II] λ6583	106	35

The [N II]/$H\alpha$ ratios were previously shown in Fig. 7.1. [O III]/$H\beta$ maps, the other ratio required for a BPT diagnosis, are shown in Fig. 7.5. This ratio is a diagnostic of the gas ionisation state, serving as a proxy for the hardness of the ambient radiation field. A visual inspection of the maps reveals a clear and recurring morphological trend: a significant number of the galaxies exhibit centrally-concentrated, high-ratio regions. This can cause, if the gas is not extended, the mean ratio to be very high and again highlights the difficulty in disentangling morphology from other BCG properties. While some galaxies show more disturbed or patchy structure the centrally-peaked structure is the most prominent feature across the sample, as we would expect.

This strong central concentration of elevated [O III]/$H\beta$ ratios is a classic signature of an AGN. Producing doubly-ionised oxygen (O^{2+}), the species responsible for the [O III] line, requires high-energy photons (an energy of ¿35 eV). While massive star-forming regions can produce some [O III] emission, the very high ratios (¿1) seen in the centres of these galaxies necessitate a much harder ionising spectrum than can't be supplied by even the hottest young stars. This points to a non-stellar ionisation source. The accretion disk around the SMBH emits high-energy UV and X-ray photons, which create a highly-ionised region of gas in the nucleus. As this radiation propagates outwards, its flux becomes geometrically diluted, leading to a

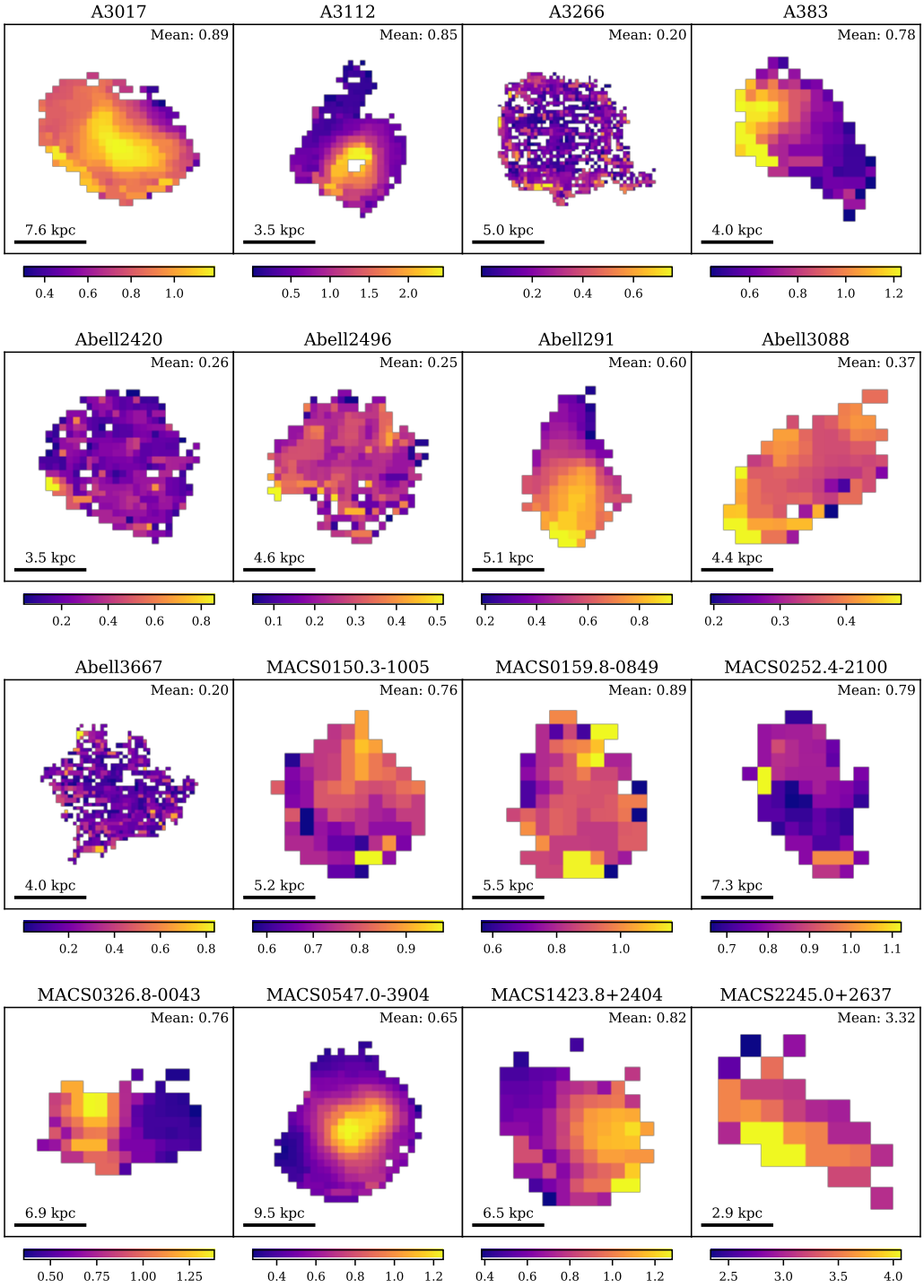

Figure 7.2: [OIII]/Hβ ratio maps for all objects defined as line emitting in [OIII] and Hβ

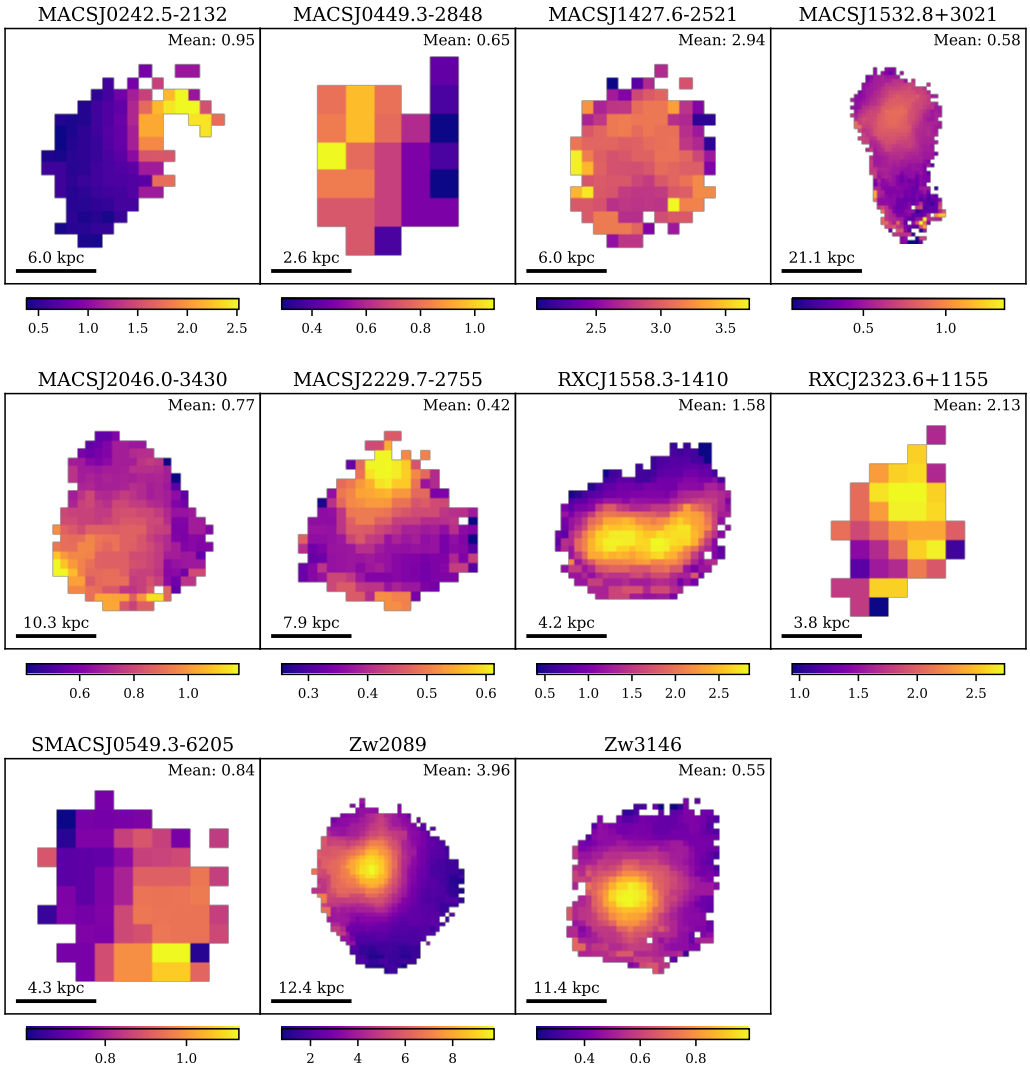
MACSJ0242.5-2132
Mean: 0.95
6.0 kpc
0.5 1.0 1.5 2.0 2.5
MACSJ0449.3-2848
Mean: 0.65
2.6 kpc
0.4 0.6 0.8 1.0
MACSJ1427.6-2521
Mean: 2.94
6.0 kpc
2.5 3.0 3.5
MACSJ1532.8+3021
Mean: 0.58
21.1 kpc
0.5 1.0
MACSJ2046.0-3430
Mean: 0.77
10.3 kpc
0.6 0.8 1.0
MACSJ2229.7-2755
Mean: 0.42
7.9 kpc
0.3 0.4 0.5 0.6
RXCJ1558.3-1410
Mean: 1.58
4.2 kpc
0.5 1.0 1.5 2.0 2.5
RXCJ2323.6+1155
Mean: 2.13
3.8 kpc
1.0 1.5 2.0 2.5
SMACSJ0549.3-6205
Mean: 0.84
4.3 kpc
0.8 1.0
Zw2089
Mean: 3.96
12.4 kpc
2 4 6 8
Zw3146
Mean: 0.55
11.4 kpc
0.4 0.6 0.8

Continued

lower ionisation state in the surrounding gas. This physical model naturally explains the observed morphology: a bright, high-ratio core coinciding with the location of the AGN, surrounded by gas with a progressively lower ratio at larger radii.

The ratio of the average values shown in Fig. 7.1 and Fig. 7.2 form the basic BPT diagram. This is plotted in Fig. 7.3. The solid black line of 'maximum-starburst' (discussed in § 7.2.2) divides our sample into two populations with 9 objects lying below this separatrix and 13 above. There is a notable absence of galaxies in both the pure HII (star-forming) and Seyfert regions.

It should be noted that the galaxy-wide average emission line ratios presented in this (and subsequent) BPT diagrams are plotted without individual uncertainty bars to maintain the legibility of the sample as a whole. While the formal measurement errors for the integrated fluxes are small, the significant spatial variation in the line ratios across each system leads to global values with correspondingly large characteristic error bars. Including these would produce an illegible plot for a sample of this size and diversity. These diagrams are provided primarily as a means of global comparison with similar studies, such as Hamer et al. [2016], who follow a comparable methodology in benchmarking the excitation properties of BCG samples. An exploration of the spatial variation in these ratios will be presented in Figures 7.7 to 7.12..

The lack of objects in the pure star-forming region implies that widespread, vigorous star formation is not the dominant source of ionising radiation. This is consistent with the standard (though sometimes lazy: Chapter 8) description of BCGs as massive, 'red and dead' elliptical galaxies with ancient stellar populations.

Much more surprising is the absence of objects in the Seyfert region. This is typically taken to mean the central SMBHs are not undergoing the radiatively efficient accretion characteristic of Seyfert nuclei. Instead of a standard thin accretion disk producing a hard UV continuum, the accretion in BCGs is believed to be radiatively inefficient. In this "jet-mode" feedback cycle, gas from the hot ICM accretes diffusely, and the bulk of the energy output is channelled into mechanical feedback via powerful radio jets, rather than a luminous, ionising spectrum. This explains the relative weakness of the high-ionisation [O III] dragging points away from the

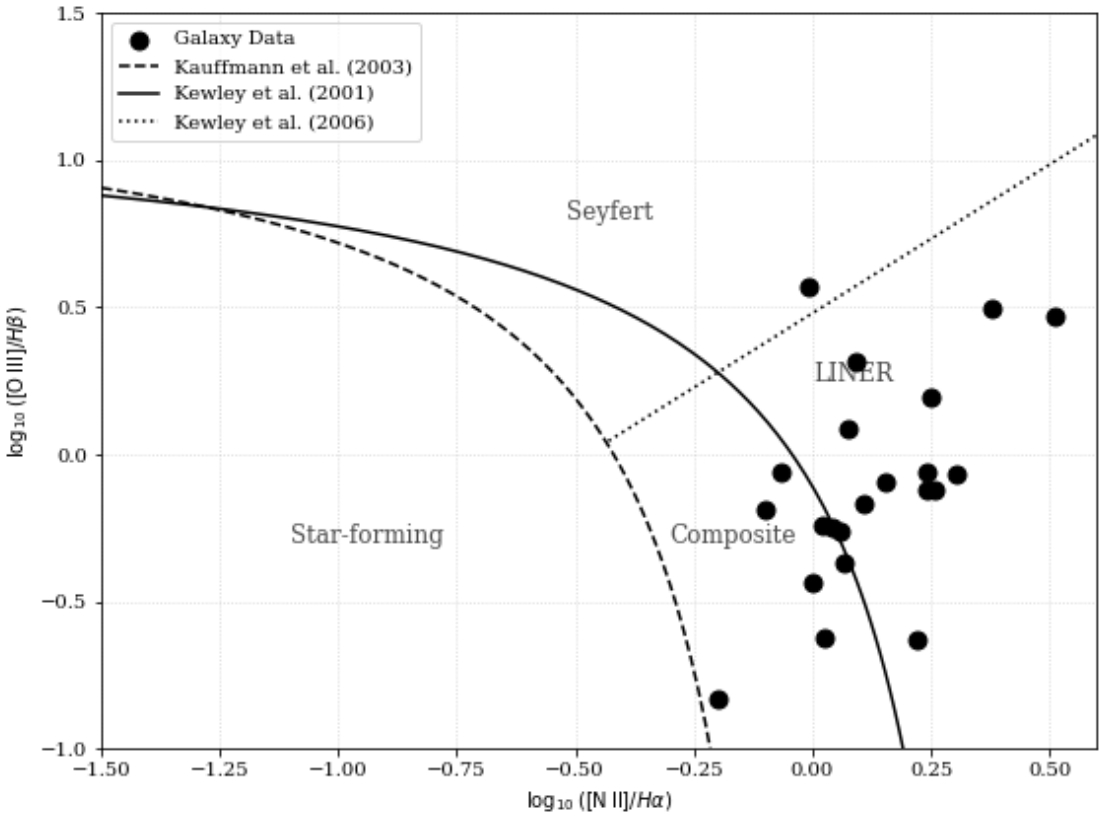

Figure 7.3: BPT diagnostic diagram for all Kaleidoscope galaxies with sufficient emission line detections to measure the relevant ratios. The demarcation curves from Kewley et al. [2001], Kauffmann et al. [2003], and Kewley et al. [2006] are shown, separating the loci of star–forming, composite, LINER, and Seyfert excitation. Most of the Kaleidoscope objects lie near the composite/LINER boundary, consistent with ionisation from a mixture of stellar and AGN-related processes. Only a single source, Zwicky 2089, falls clearly in the Seyfert region.

Seyfert locus in the diagram.

The dominance of the LINER and Composite regions points to an absence of high-energy ionisation souces. The LINER-like spectra can be attributed to several concurrent physical processes common in BCGs. The leading explanation is the presence of a Low-Luminosity AGN (LLAGN) possibly enhanced via radio jets driving shocks into the surrounding gas. A third potential contributor is photoionisation from the large population of old, hot post-AGB stars found in these massive galaxies. The spread of objects into the composite region suggests a mixture of these LINER-like mechanisms with a low level of residual star formation, perhaps fuelled by minor cooling flows that have not been fully offset by AGN feedback. This surprising diagnosis persists, with minor translation, in the other diagnostic plots discussed in § 7.2.2 and shown in Fig. 7.4 and Fig. 7.5.

Objects in all three diagrams populate approximately the same region implying an absence of highly ionising sources. The fact we do obtain a slightly different distribution for our sample in [SII]/Hα versus [NII]/Hβ compared to [OI]/Hα vs. [OIII]/Hβ and the traditional [NII]/Hα vs. [OIII]/Hβ diagrams does however hint at some additional complexity in the ionisation scenario. The [OI] emission arises predominantly from partially ionised regions, typically indicating shocks, turbulence, or diffuse ionised gas (DIG), rather than classical HII regions. Objects labelled as LINER in the [OI]/Hα diagram thus indicate significant contributions from shock excitation or ionisation from evolved stellar populations (e.g., post-AGB stars), which may not be clearly distinguished by the [SII] diagnostic alone Heckman [1980], Kewley et al. [2006]. Low-ionisation emission-line regions (LIERs) may be powered by older stellar populations, contributing to lower-ionisation emission lines like [NII] and [OI] more significantly. Thus, objects can appear star-forming when considering [SII], a line often sensitive to density rather than exclusively ionisation mechanism, but transition to LINER classification when using lines such as [OI], sensitive explicitly to partially ionised gas conditions [Belfiore et al., 2016, Yan and Blanton, 2012].

Elevated nitrogen abundances ([NII]) could push some galaxies towards the LINER regime on the traditional [NII]/Hα vs. [OIII]/Hβ diagram, while lower

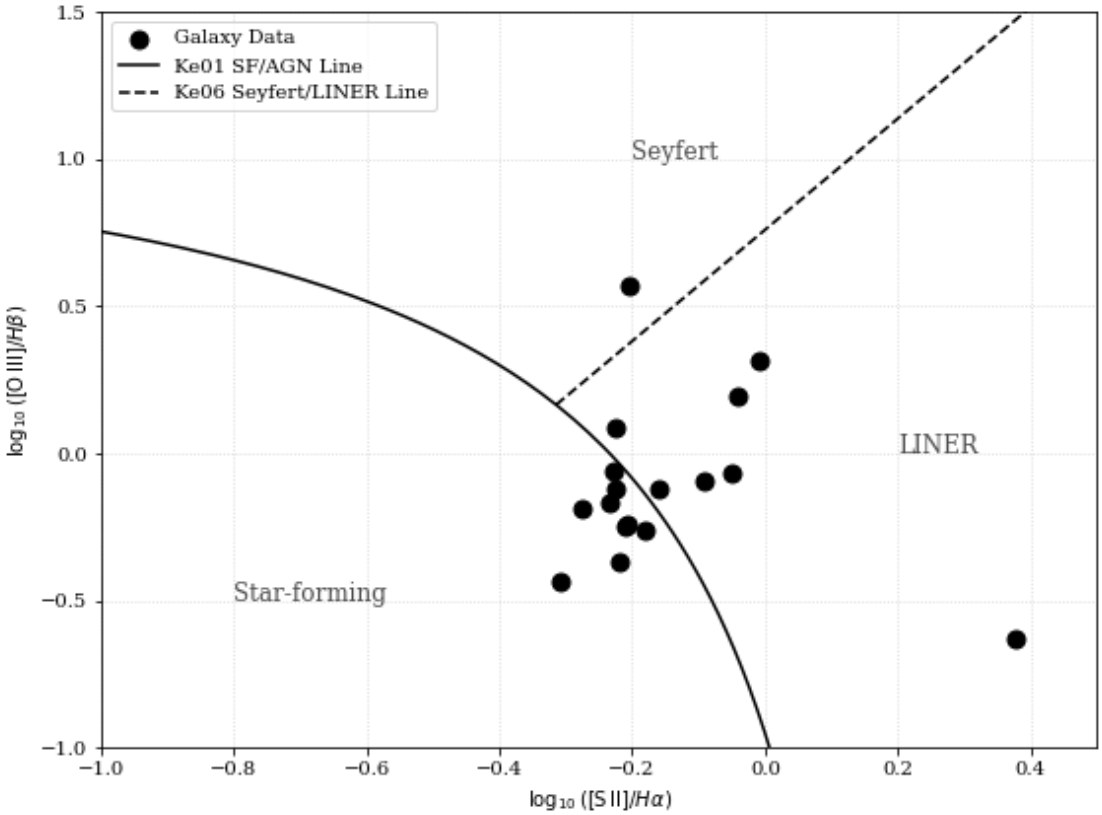

Figure 7.4: The [SII]/Hα versus [OIII]/Hβ diagnostic diagram. The data points represent the galaxy-wide average emission line ratios for the sample. The solid line denotes the maximum starburst line from Kewley et al. (2001), while the dashed line shows the empirical separation between Seyferts and LINERs from Kewley et al. (2006). The galaxies in the sample are distributed across the LINER and composite regions of the diagram.

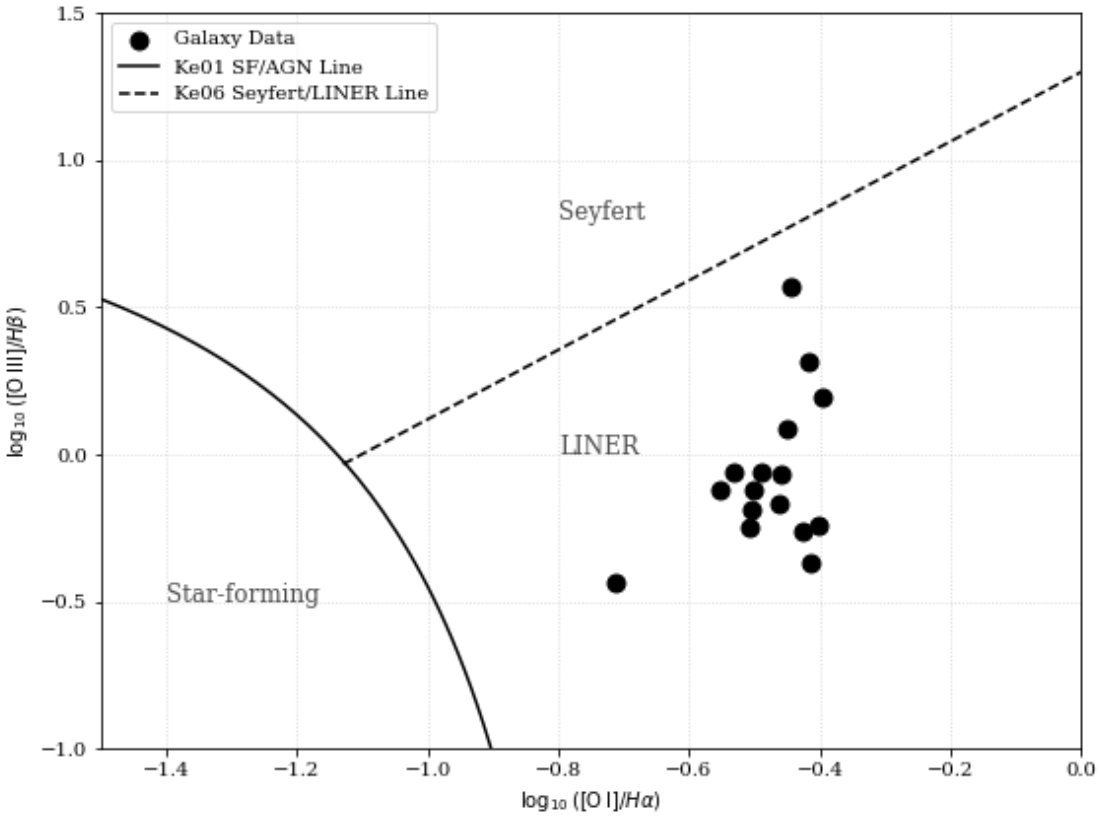

Figure 7.5: The [OI]/Hα versus [OIII]/Hβ diagnostic diagram for the galaxy sample. The black circles represent the galaxy-wide average emission line ratios. The solid black line is the theoretical "maximum starburst" line from Kewley et al. (2001) that separates star-forming galaxies from AGN. The dashed line is the empirical division from Kewley et al. (2006) that separates Seyfert galaxies from LINERs. There is little scatter in the plot and all galaxies in the sample are distributed across the LINER region of the diagram.

[SII] ratios remain consistent with star-forming regions due to reduced sensitivity to metallicity changes. Therefore metallicity, while unable to entirely explain the discrepancy, could be a partial case for the difference between these diagnostics [Kewley et al., 2019].

The complete absence of Seyfert classification typically implies a lack high ionisation sources. Seyfert galaxies exhibit strong high-ionisation lines (high [OIII]/Hβ ratios). The absence of Seyfert classifications suggests the sample lacks sufficiently energetic AGN or that the central black holes are inactive or obscured [Kauffmann et al., 2003]. Objects classified consistently as LINER rather than Seyfert may indicate low-luminosity AGN (LLAGN) or ionisation primarily from stellar sources, shocks, or diffuse gas, rather than from accretion-powered AGN [Ho et al., 1997, Kewley et al., 2006].

An alternative explanation is aperture dilution. An intense, high-excitation Seyfert nucleus, which produces very high [O III]/$H\beta$ ratios, is typically confined to the central few kiloparsecs. When this powerful central emission is averaged with the much larger area of a galaxy's disk—which may be dominated by low-excitation HII regions or older stellar populations—the resulting integrated ratio is effectively smeared out. The approach we have taken thus far, while still pervasive in the literature, fails to capture the the single most useful feature of an IFU, spatially resolved spectroscopy. We present pixel-by-pixel ionisation mechanism maps in Fig. 7.6.

These maps provide a direct visualisation of the dominant ionisation mechanism in different regions of each galaxy. Iterating through each region of the BPT diagram, shown as the different colours in the plots, reveals several key trends. A large fraction of the galaxies are classified almost entirely as LINERs across their full extent. This indicates that low-ionisation emission is the prevailing characteristic of the sample. Other galaxies present a complex mixture of Composite (green) and LINER regions. The spatial distribution of these zones is often irregular, without a single, simple pattern. Purely star-forming regions are rare, appearing only as small, isolated patches in a few objects. Finally, there are no pixels classified as Seyfert in any galaxy across the entire sample.

A surprising feature of these BPT maps is that they often lack the simple,

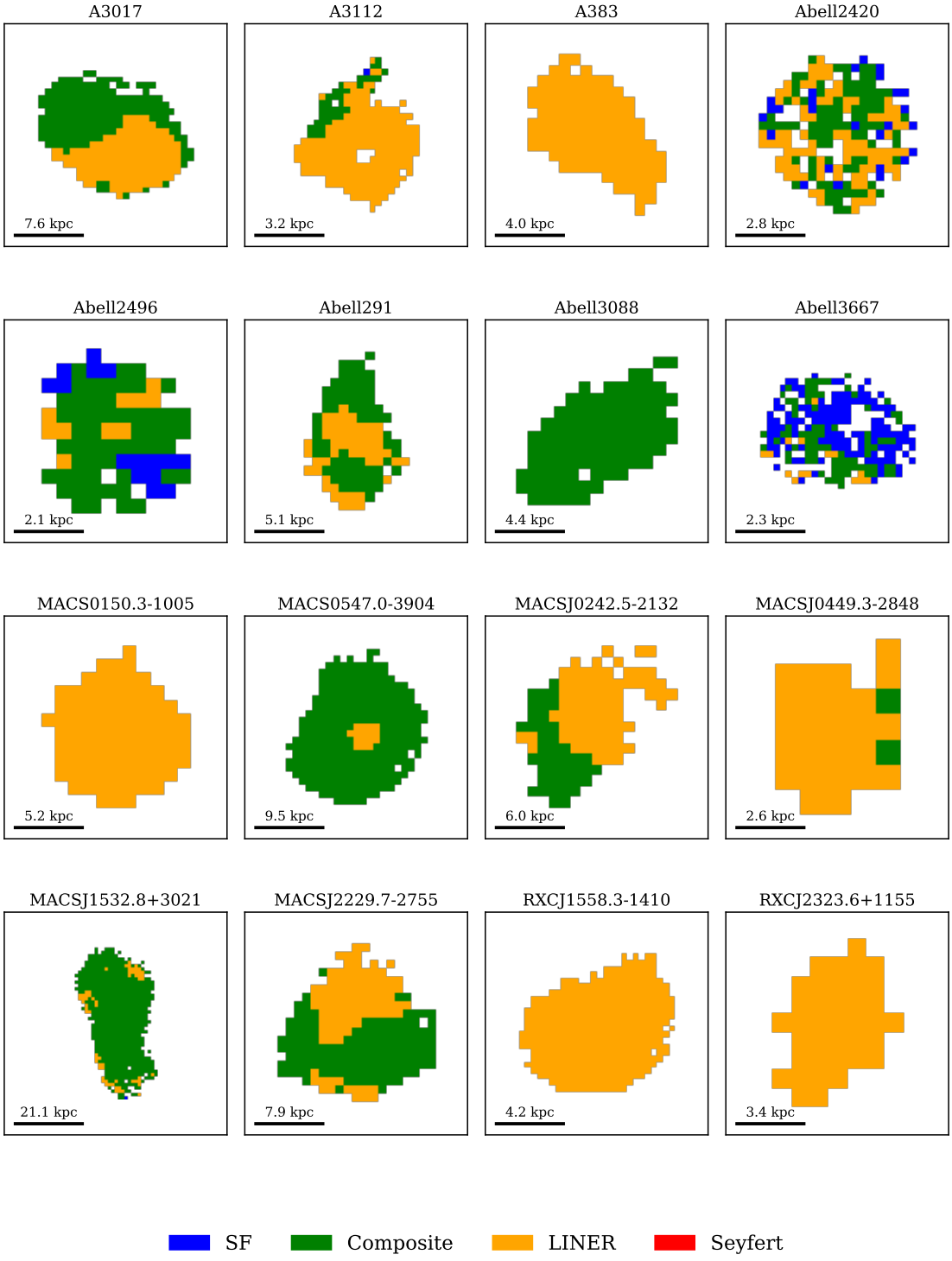

Figure 7.6: [OIII]/Hβ ratio maps for all objects defined as line emitting in [OIII] and Hβ

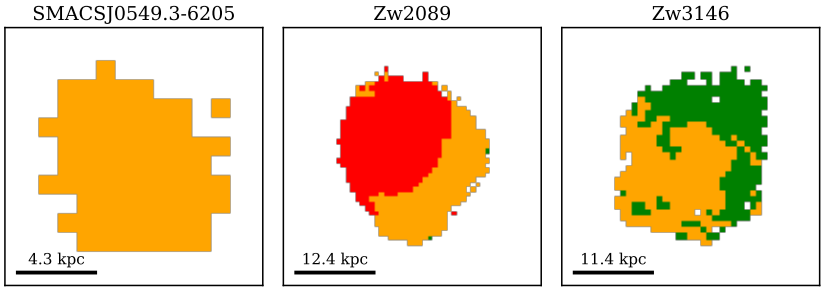
SMACSJ0549.3-6205
4.3 kpc
Zw2089
12.4 kpc
Zw3146
11.4 kpc


SF
Composite
LINER
Seyfert

Continued

centrally-peaked structure that was prominent in the [O III]/$H\beta$ single-ratio maps. The [O III]/$H\beta$ taken in isolation suggested a central engine whose ionising influence decreases radially outwards. In contrast, the BPT maps classify many of these same galaxies with a widespread LINER or Composite nature, obscuring a simple core-halo structure. This apparent difference arises because the BPT classification depends on *two* line ratios: [O III]/$H\beta$ (the y-axis) and '[N II]/$H\alpha$ (the x-axis). While the [O III]/$H\beta$ ratio traces the ionisation *state* (hardness) of the radiation field, the [N II]/$H\alpha$ ratio is also sensitive to other physical properties of the gas. The complex structure seen in the BPT maps, therefore, appear to be largely driven by the spatial distribution of the [N II]/$H\alpha$ ratio.

There are two physical processes that could elevate the [N II]/$H\alpha$ ratio on a galaxy-wide scale: metallicity and/or shocks. We can rule out metallicity based on § 7.1 which leaves shocks. The ionising source in these massive galaxies is not a simple, static AGN. It is often a "jet-mode" AGN driving powerful outflows. The resulting shock waves can propagate throughout the galaxy's interstellar medium. These shocks are highly efficient at heating gas and producing strong low-ionisation lines, which significantly increases the [N II]/$H\alpha$ ratio everywhere, not just at the centre. This would translate all regions of the galaxy horizontally to the right on the BPT diagram.

The diagnostic diagrams presented in Figures 7.7, 7.8 and 7.9 break down the ionisation source by radial distance from the centre of the BCG. Across all three diagrams—the [NII]/Hα, [SII]/Hα, and [OI]/Hα diagnostics—we observe no significant difference in either the average position or the scatter of data points representing the inner (< 5 kpc) and outer (≥ 5 kpc) regions of the galaxies - illustrated by the red star in both panels. The average line ratios, which trace the ionisation state of the gas, are remarkably consistent on scales extending beyond the central few kiloparsecs. Both the inner and outer regions of the BCGs are predominantly classified as LINERs, clustering in the same area of each diagram Kewley et al. [2006].

The lack of a strong radial gradient would typically imply the lack of a single, spatially concentrated ionisation source. If the observed line emission were powered primarily by a single, compact active galactic nucleus (AGN) at the galaxy's centre,

we would expect to see a clear ionisation gradient. The inner regions, being closer to the nucleus, would be exposed to a harder and more intense radiation field, placing them systematically higher in the diagrams (towards the Seyfert region) compared to the outer regions. The absence of such a trend strongly disfavours a radiatively-dominant central AGN as the primary source of ionisation for the extended gas we observe.

Instead, this result points towards an ionisation mechanism that is distributed on galaxy-wide scales. A leading candidate for powering such extended LINER-like emission in massive, passive galaxies is photoionisation from a diffuse population of hot, old, post-asymptotic giant branch (post-AGB) stars [Cid Fernandes et al., 2011]. These hot, evolved stars are distributed throughout the stellar body of the galaxy and their integrated hard UV radiation can produce the required ionisation state over large volumes, consistent with our observations of a uniform emission signature. Other potential distributed mechanisms include slow, large-scale shocks propagating through the interstellar medium, perhaps induced by interactions with the surrounding ICM [Ho et al., 1993], or heating via conduction from the hot X-ray halo [Fabian, 2012]. In any of these scenarios, our results suggest that the power source for the warm ionised gas in these BCGs is a galaxy-wide phenomenon, rather than being coupled to a central engine.

We can extend this approach to move beyond using a single, arbitrary fixed aperture and instead identifies a characteristic radius for each object where its properties on the BPT diagram change most significantly. We defines a grid of physical radii from 1.5 to 7.0 kpc. It then iterates through each potential separation radius, r, and partitions the galaxy's spatially resolved line ratio maps into an inner zone ($< r$) and an outer zone ($\geq r$), ensuring the outer zone contains at least 20% of the valid pixels for a robust comparison. The mean [N II]/$H\alpha$ and [O III]/$H\beta$ ratios are calculated for each zone, yielding two distinct points on the BPT diagram. The radius that maximises the Euclidean distance between these two points in the 2D diagnostic space is selected as the characteristic radius, r_i, for that galaxy.

These results are shown in Fig. 7.10, Fig. 7.11 and Fig. 7.12. Each galaxy is represented by two points: a circle for the mean line ratios of the inner region

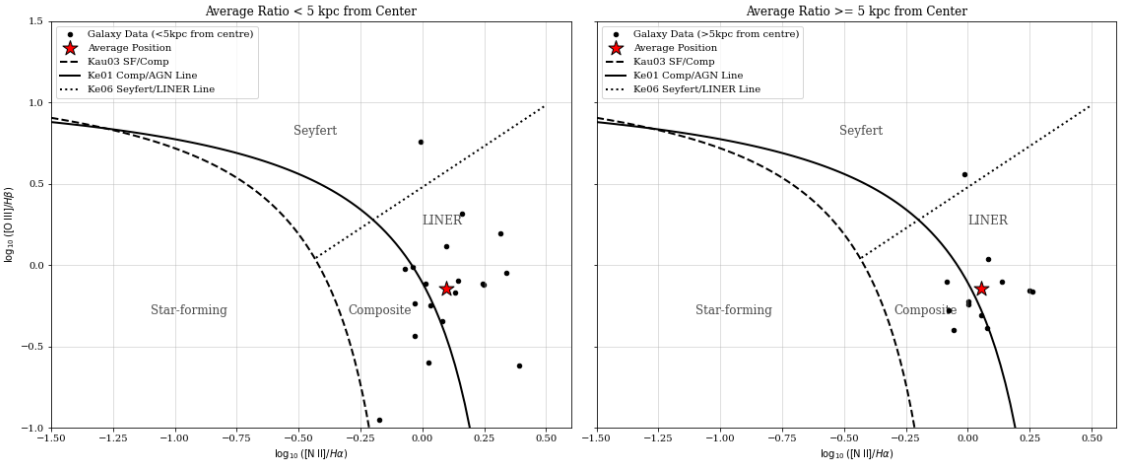

Figure 7.7: The [NII]/Hα versus [OIII]/Hβ (BPT) diagnostic diagram, comparing average emission-line ratios from different galactocentric distances. The left panel shows the average ratios for regions within 5 kpc of the galaxy center, while the right panel shows the average ratios for regions at or beyond 5 kpc. The diagnostic lines from Kauffmann et al. (2003) and Kewley et al. (2001, 2006) are shown, separating star-forming, composite, Seyfert, and LINER regions. The inner regions exhibit a greater spread into the composite and Seyfert classifications compared to the outer regions.

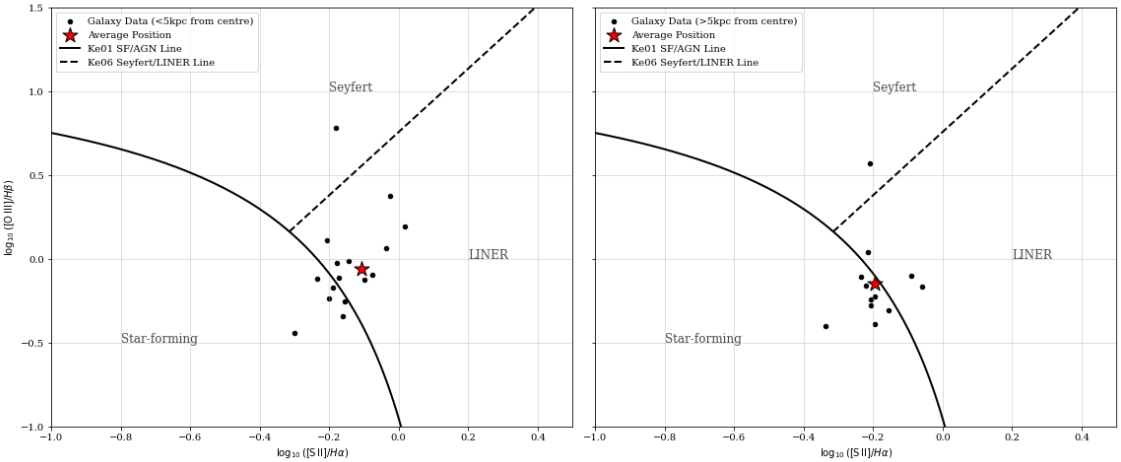

Figure 7.8: The [SII]/Hα versus [OIII]/Hβ diagnostic diagram. The plot compares the average line ratios for the inner regions (< 5 kpc, left panel) and outer regions (≥ 5 kpc, right panel) of the sample galaxies. The solid line from Kewley et al. (2001) separates star-forming galaxies from AGN, and the dashed line from Kewley et al. (2006) separates Seyferts from LINERs. In this diagnostic, both the inner and outer regions are predominantly classified as LINERs.

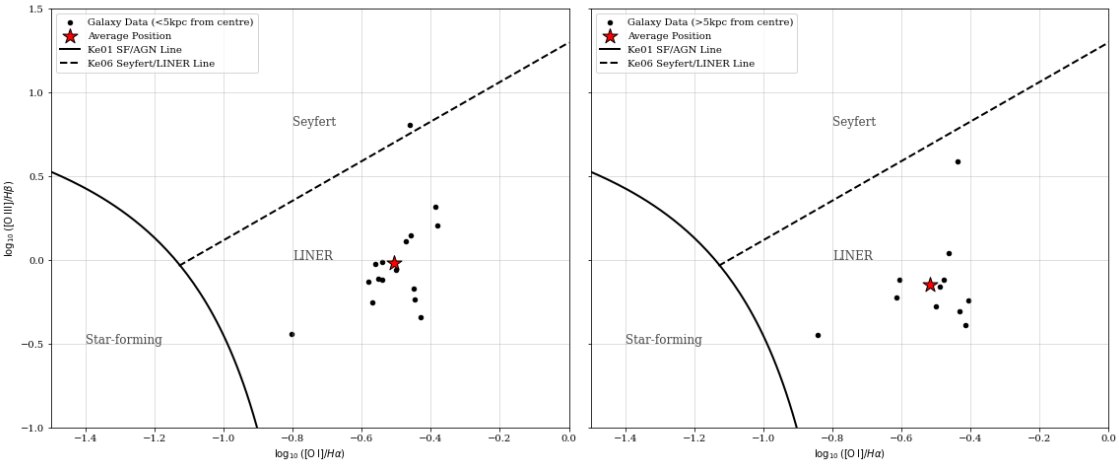

Figure 7.9: The [OI]/Hα versus [OIII]/Hβ diagnostic diagram. The average line ratios are plotted separately for regions within 5 kpc of the galactic center (left) and those at or beyond 5 kpc (right). The solid and dashed lines represent the AGN/star-forming and Seyfert/LINER separations from Kewley et al. (2001, 2006), respectively. Both the inner and outer regions of the sample galaxies are consistently classified as LINERs in this diagram.

($< r_i$), and a triangle for the outer region ($\geq r_i$), both evaluated at the optimal radius. The colour of both points corresponds to the physical value of this optimal radius in kpc, as indicated by the colour bar.

Across all three diagrams, the data points for both the inner (circles) and outer (triangles) regions lie almost exclusively above and to the right of the star-forming demarcation lines. The [O I] and [S II] plots, which are particularly effective at separating star formation from harder ionisation sources, show in the star-forming region. The data points are clustered, irrespective of radius, around the LINER regions where complete absence of galaxies in the upper portions of the Seyfert region suggests the sample is not composed of classical, radiatively efficient Seyferts.

The "maximum separation" method is designed to highlight internal variations, while the mean inner region for all plots occupies a high ionisation position in the given parameter space the translation is amazingly small. The colour-coding of the points, which represents the optimal separation radius, appears to provide a justification for the adaptive approach. The optimal radii span a wide range of physical scales, from as small as $\sim$ 2 kpc to 6 kpc (blue/purple points). This demonstrates that there is no single physical scale that characterises the transition

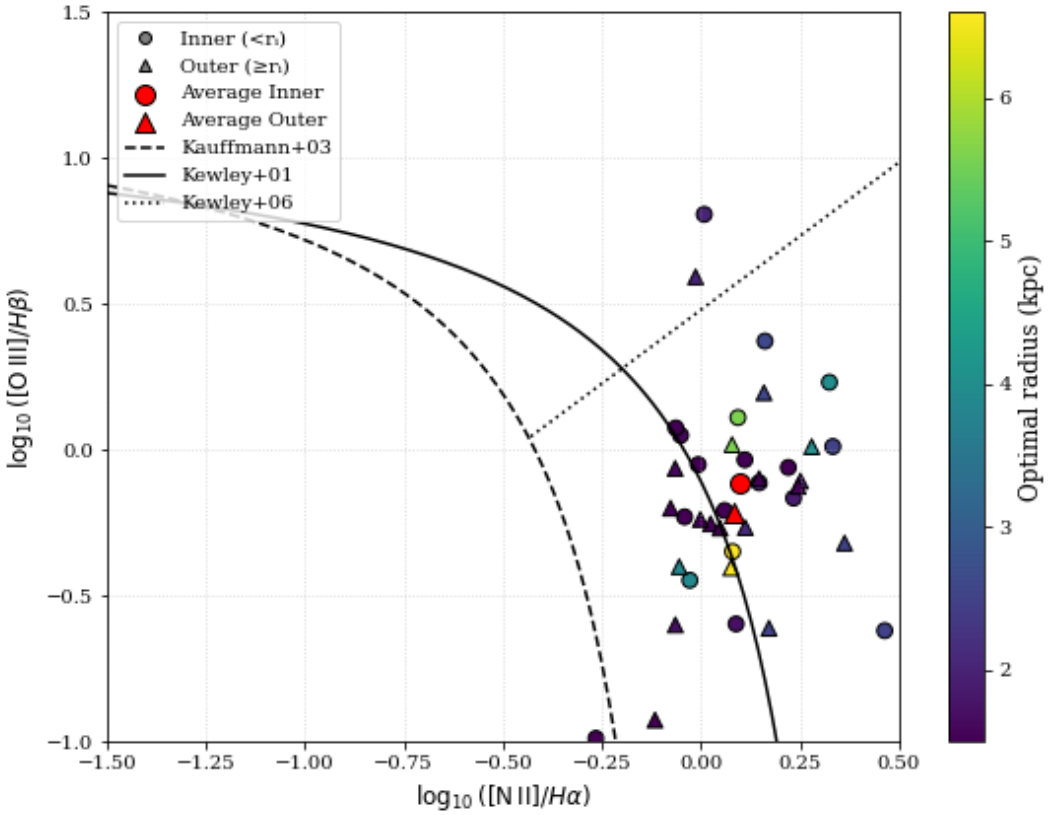

Figure 7.10: The BPT diagnostic diagram, plotting $\log_{10}([\mathrm{O\,III}]/H\beta)$ against $\log_{10}([\mathrm{N\,II}]/H\alpha)$. For each galaxy, we plot the average line ratios for the inner region ($< r_i$, circles) and outer region ($\geq r_i$, triangles). The separation radius r_i is individually chosen for each galaxy to maximise the distance between its two points in this diagnostic space. The colour of the points indicates the value of this optimal radius in kpc. Overplotted are the theoretical "maximum starburst" line from Kewley et al. (2001) (solid), the empirical star-forming classification line from Kauffmann et al. (2003) (dashed), and the Seyfert-LINER separation from Kewley et al. (2006) (dotted).

in ionisation for all galaxies in the sample. This is unsurprising given the diversity in morphology, kinematics and redshift in the underlying sample.

7.3 Temperature

The electron temperature (T_e) of ionised gas is a fundamental diagnostic of its physical state. In typical HII regions photoionised by young, massive stars, T_e is remarkably constant, hovering around a value of 10^4 K Osterbrock and Ferland [2006]. This consistency arises from a thermostatic balance between heating from photoion-

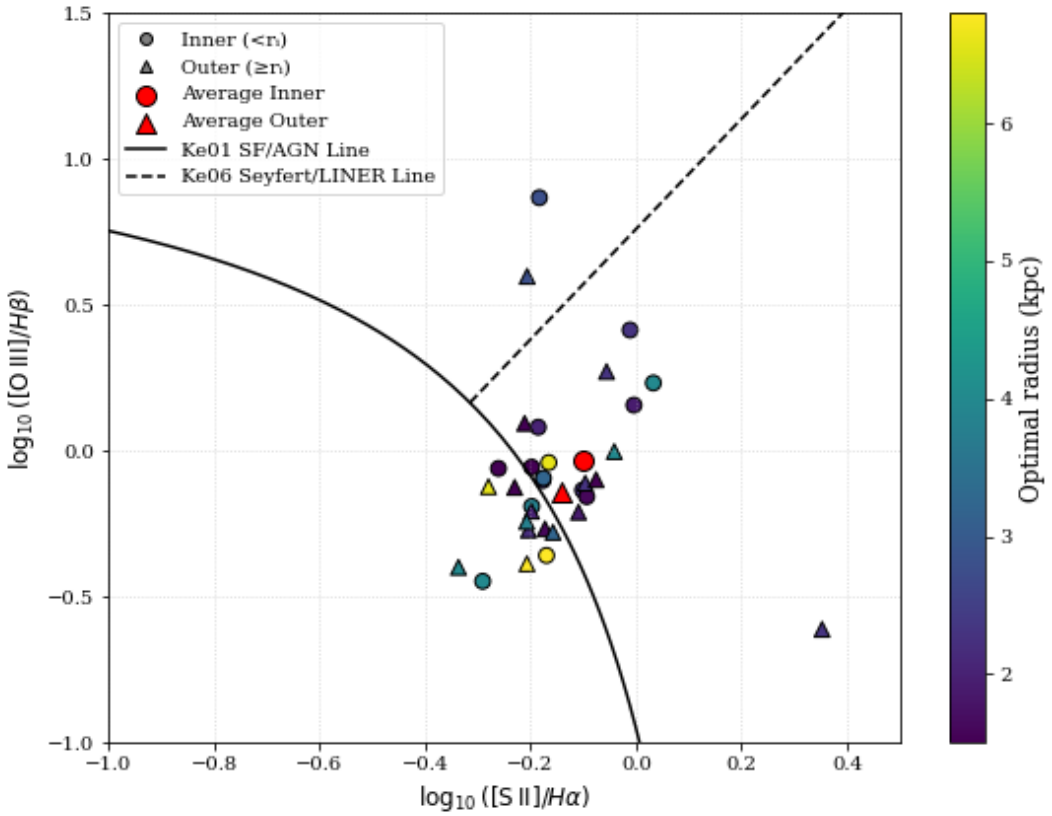

Figure 7.11: The [O I] diagnostic diagram, plotting $\log_{10}([\mathrm{O\,III}]/H\beta)$ against $\log_{10}([\mathrm{O\,I}]/H\alpha)$. Each galaxy is represented by its inner ($< r_i$, circles) and outer ($\geq r_i$, triangles) regions, where the separation radius r_i is individually optimised for each galaxy on this diagram to maximise the separation between the points. Point colours correspond to the value of the optimal radius in kpc. The solid line shows the star-forming/AGN separation from Kewley et al. (2001), while the dashed line separates Seyfert and LINER-like excitation (Kewley et al. 2006).

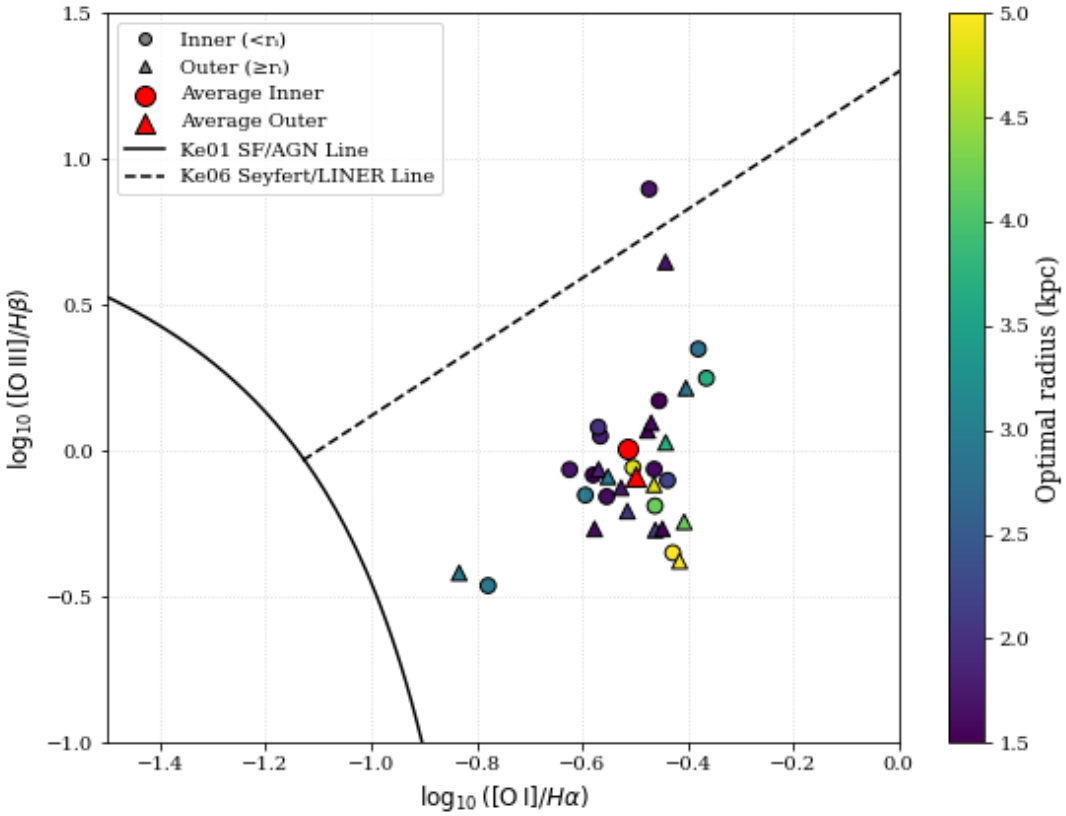

Figure 7.12: The [S II] diagnostic diagram, plotting $\log_{10}([\mathrm{O\,III}]/H\beta)$ against $\log_{10}([\mathrm{S\,II}]/H\alpha)$. We plot the average line ratios for the inner ($< r_i$, circles) and outer ($\geq r_i$, triangles) regions of each galaxy. The separation radius r_i is individually determined to maximise the distance between the two points on this diagram, and the colour of each point corresponds to this radius in kpc. The solid line from Kewley et al. (2001) separates star-forming galaxies from AGN, and the dashed line from Kewley et al. (2006) divides Seyferts and LINERs.

isation and highly efficient cooling from collisionally excited forbidden lines of heavy elements. While this is a robust estimate for star-forming regions, other mechanisms, such as shocks or AGN, can heat gas to substantially higher temperatures Kewley et al. [2006].

Table 7.3: Upper Limits on Electron Temperature

Object Name	T_e Upper Limit (K)
A3017	$<$ 20,868
A3378	$<$ 100,000
A3444	$<$ 43,102
A383	$<$ 100,000
Abell S780	$<$ 100,000
Abell291	$<$ 100,000
Abell3088	$<$ 100,000
MACS0252.4-2100	$<$ 30,588
MACS0326.8-0043	$<$ 100,000
MACS0547.0-3904	$<$ 19,198
MACSJ0449.3-2848	$<$ 100,000
MACSJ1115.8+0129	$<$ 100,000
MACSJ1447.4+0828	$<$ 35,346
MACSJ1532.8+3021	$<$ 34,620
MACSJ2046.0-3430	$<$ 26,957
MACSJ2229.7-2755	$<$ 47,854
RXCJ1317.1-3821	$<$ 100,000
RXCJ2323.6+1155	$<$ 100,000
SMACSJ0234.7-5831	$<$ 49,169
MACS0027.2+2607	$<$ 83,016
Abell2496	$<$ 100,000
Abell3814	$<$ 69,161
A3866	$<$ 130,159
MACS0150.3-1005	$<$ 100,000
MACS0159.8-0849	$<$ 100,000
MACSJ0510.4+0220	$<$ 100,000
SMACSJ0549.3-6205	$<$ 100,000
MACS1423.8+2404	$<$ 61,913
MACSJ1427.6-2521	$<$ 100,000
MACSJ2134.6-2706	$<$ 100,000

The method we employ relies on the flux ratio of the faint auroral line [OIII] λ4363 to the strong nebular lines [OIII] $\lambda\lambda 4959, 5007$. The upper energy level of the λ4363 transition requires higher-energy electron collisions to become populated, making the line ratio exceptionally sensitive to T_e. In the low-density limit, this physical

relationship is well-described by the equation:

$$\frac{I(\lambda 4959) + I(\lambda 5007)}{I(\lambda 4363)} \approx 7.90 \exp\left(\frac{3.29 \times 10^4}{T_e}\right) \tag{7.3}$$

where $I(\lambda)$ is the flux of the emission line and T_e is the electron temperature in Kelvin Osterbrock and Ferland [2006]. To determine the temperature from our observations, this equation is rearranged to solve for T_e. By defining the observed line ratio as R, we calculate the temperature directly:

$$T_e \approx \frac{32,900}{\ln(R/7.90)} \tag{7.4}$$

Since the λ4363 line is rarely in our spectra, we use an upper limit on its flux, derived from the local spectral noise. Using this flux limit to calculate the ratio R allows us to place a robust upper limit on the electron temperature of the gas. We show the upper limits in Table 7.3. The upper limit is capped at 100,000K. The upper limits on the electron temperature calculated for our sample, presented in Table 7.3, are in many cases quite high (often $T_e > 100,000$ K). Here we begin to see the limitations of the relatively short exposures of the Kaleidoscope Survey where the flux upper limit is determined by the local noise in the spectrum rather than a direct line detection. Shorter exposures result in a higher noise floor and therefore a larger, less constraining, upper limit on the λ4363 flux.

This directly impacts the temperature calculation. As the flux limit for $I(\lambda 4363)$ increases, the resulting ratio R in Equation (1) decreases. From Equation (2), a smaller value of R leads to an exponentially larger value for the derived temperature. Consequently, the upper limits we calculate are not powerful enough to robustly distinguish between different gas heating mechanisms. For example, a limit of $T_e < 150,000$ K cannot differentiate between photoionisation, which typically produces gas at $\sim 10,000 - 20,000$ K, and heating by fast shocks, which can produce temperatures well in excess of 30,000 K. Deeper observations would be required to lower the detection limits and place more scientifically constraining limits on the temperature of the ionised gas in these BCGs.

7.4 Dust

BCGs often host significant reservoirs of dust. Historically, massive early-type systems such as BCGs were thought to be largely devoid of cold gas and dust, owing to the combined effects of ram-pressure stripping, sputtering in the hot ICM, and energetic feedback from active galactic nuclei (AGN) [Fabian, 1994, Voit, 2005, Voit and Donahue, 2015]. In such environments, dust grains are expected to be destroyed on short timescales ($\lesssim 10^7$ yr) through thermal sputtering [Draine and Salpeter, 1979], implying that any observed dust must be recently accreted or continuously replenished. However, multi-wavelength observations—particularly in the infrared and sub-millimetre—have revealed that dust in BCGs is more prevalent than previously assumed [de Messières et al., 2009, Edge et al., 1999, Rawle et al., 2012].

Dust plays a fundamental role in regulating the thermodynamic and chemical evolution of BCGs. By efficiently absorbing ultraviolet (UV) and optical photons and re-emitting this energy in the infrared (IR), dust alters the galaxy's spectral energy distribution (SED) and can obscure or reveal key phases of star formation [Calzetti, 2001, Casey et al., 2014]. In dusty star-forming regions, this reprocessing modifies the emergent radiation field, influencing both observational diagnostics and the local gas dynamics. Dust grains also act as catalytic sites for the formation of molecular hydrogen (H_2) and other molecules [Draine, 2011, Watson and Salpeter, 1972], enabling efficient radiative cooling in the interstellar medium (ISM) and facilitating the collapse of dense gas clouds into stars.

The persistence of dust in BCGs embedded in hot ($T \gtrsim 10^7$ K) cluster cores is thus both surprising and informative. It suggests that dust replenishment mechanisms are active, these include: stellar mass loss from evolved stars in the BCG [Clemens et al., 2010], accretion of dust-rich material via mergers or tidal stripping of satellite galaxies [Goudfrooij et al., 1994] and in-situ dust formation associated with residual star formation sustained by cooling flows [Donahue et al., 2007, Edge, 2001, Voigt and Fabian, 2004].

Morphological dust features—such as lanes, shells, and extended filaments—often trace recent dynamical interactions in cluster cores [Martel et al., 2004, Rafferty et al., 2008]. These structures can arise from the tidal disruption of infalling galax-

ies or from the uplift of dust and cold gas by AGN-driven outflows [McNamara et al., 2004]. Their distribution and kinematics offer valuable constraints on the assembly history of the BCG and the ongoing baryon cycle within the cluster environment.

7.4.1 Tracing Dust via the Ca II 7291 Å Emission Line.

In [Donahue and Voit, 1993], the authors argue that significant depletion of calcium onto dust grains makes the Ca II 7291 Å emission (and absorption) line a powerful diagnostic of dust in massive early-type galaxies. First, calcium is readily removed from the gas phase when dust forms, leading to a measurable deficit in Ca II line strength if dust is present. Second, dust can scatter and absorb radiation, altering the observed line profile and creating characteristic asymmetries or reduced intensities compared to lines that are less affected by dust. Third, the presence of calcium in the ISM is tied to overall metallicity—a higher metal content often correlates with more dust formation, since dust requires a reservoir of heavy elements. Examining changes in the Ca II 7291 Å feature provides indirect evidence for dust content and distribution, especially when its behaviour is contrasted with infrared (IR) dust emission or other optical indicators.

Across our sample, the Ca II λ7291 emission line is undetected at all confidence levels. This is consistent with the findings of Donahue and Voit [1993], who report that Ca is highly depleted from the gas phase due to condensation onto dust grains. The absence of this line, even in systems with minimal Balmer-derived extinction, suggests that dust is present but not always spatially co-located with the Balmer-emitting gas. This reinforces the interpretation that dust in BCGs can be patchy or confined to cold, dense clouds rather than uniformly mixed with the warm ionised medium.

7.4.2 Tracing Dust via the Balmer Decrement

The Balmer decrement provides a well-established diagnostic for dust extinction in ionised gas regions. Under *Case B* recombination, the intrinsic line ratios of the Balmer series are largely insensitive to density and temperature variations for

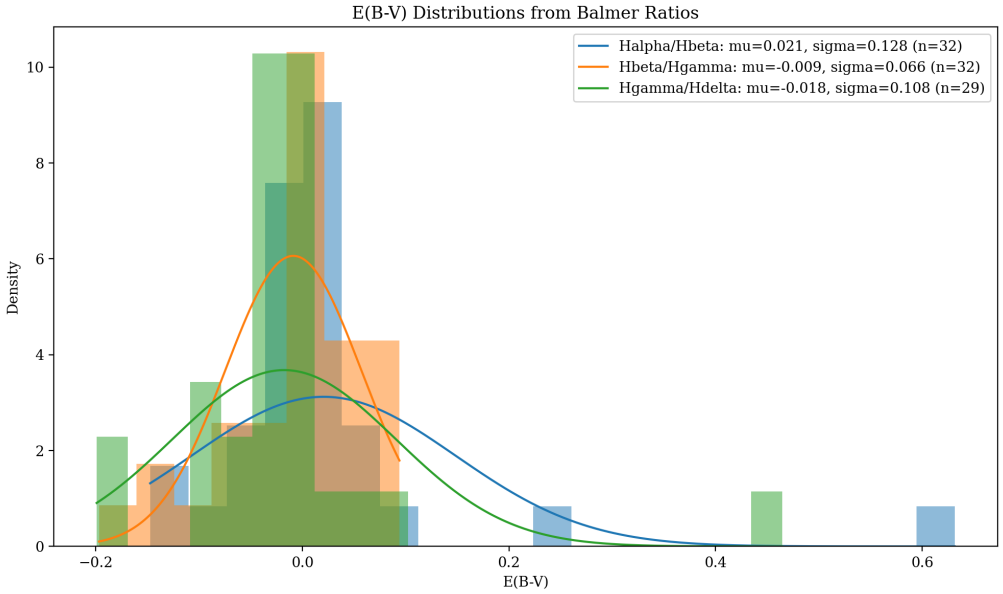

Figure 7.13: Distributions of $E(B-V)$ values derived from different Balmer line ratios for the sample of line-emitting BCGs. The histograms show the extinction values obtained from Hα/Hβ (blue), Hβ/Hγ (orange), and Hγ/Hδ (green). The solid lines represent Gaussian kernel density estimates, with the legend reporting the mean (μ), standard deviation (σ), and number of objects (n) for each distribution. All three indicators are consistent with negligible reddening, in line with previous studies of BCG emission-line nebulae.

typical H II region conditions ($T_e \sim 10^4$ K, $n_e \lesssim 10^4$ cm^{-3}). Any deviation from the theoretical ratios is attributed to wavelength-dependent dust attenuation, which preferentially dims the bluer lines [Osterbrock and Ferland, 2006].

For this work, we retain only the relevant theoretical Case B ratios (at $T = 10^4$ K) for extinction measurements:

Table 7.4: Intrinsic Balmer Line Ratios (Case B, $T = 10^4$ K)

Ratio	Value
$H\alpha/H\beta$	2.87
$H\gamma/H\beta$	0.466
$H\delta/H\beta$	0.256

Observed E(B–V) Distributions

The distributions of $E(B-V)$ derived from Balmer decrements for our sample of line-emitting brightest cluster galaxies (BCGs) are shown in Fig. 7.13. We compute extinction values using three different Balmer ratios: Hα/Hβ, Hβ/Hγ, and Hγ/Hδ.

The resulting distributions are all centered close to zero reddening, with modest dispersions. Specifically, the Hα/Hβ ratio yields a mean of $\mu \approx 0.021$ with $\sigma \approx 0.128$ ($n = 32$), while the higher-order ratios Hβ/Hγ and Hγ/Hδ give slightly negative means ($\mu \approx -0.009$ and $\mu \approx -0.018$, respectively) with comparable scatter ($\sigma \approx 0.066$ and $\sigma \approx 0.108$). The overlap between the three distributions is substantial, indicating broadly consistent results.

In the context of Case B recombination at $T \sim 10^4$ K and $n_e \sim 10^2$–10^4 cm^{-3}, the expected intrinsic Balmer line ratios are Hα/H$\beta \approx 2.86$, Hβ/H$\gamma \approx 0.468$, and Hγ/H$\delta \approx 0.259$ [Osterbrock and Ferland, 2006]. Departures from these intrinsic values are interpreted as dust reddening. The near-zero $E(B-V)$ values we derive therefore suggest that the nebular emission in BCGs is subject to very little internal extinction. The small positive offset seen in Hα/Hβ is consistent with a mild amount of dust, whereas the slightly negative means for the higher-order ratios are non-physical and most likely arise from observational uncertainties, including low signal-to-noise in weak lines, contamination from sky features, and imperfect subtraction of underlying stellar absorption.

Our findings are in good agreement with previous work. Optical spectroscopy of BCGs has shown that their emission-line regions generally exhibit very low reddening, with $E(B-V) \lesssim 0.2$ in the majority of systems [Crawford et al., 1999, Salomé et al., 2011]. Similarly, Donahue et al. [2010b] reported negligible internal extinction in a sample of line-emitting BCGs, reinforcing the view that these environments are unusually dust-poor compared to other star-forming galaxies. This stands in contrast to typical starburst galaxies, where values of $E(B-V) \approx 0.3$–0.5 are often observed [Calzetti, 2001]. The relatively dust-free nature of BCG nebular emission may reflect either a genuine paucity of dust in the cluster cores or a clumpy geometry in which much of the dust does not intercept the line-emitting regions.

The $E(B-V)$ distributions derived here confirm that extinction toward the ionised gas in BCGs is minimal, and consistent with prior observational studies. While higher-order Balmer ratios are more susceptible to systematic uncertainties, all three indicators converge on the same conclusion: reddening is negligible for the majority of line-emitting BCGs.

7.5 Summary

In this chapter we have examined the excitation mechanisms operating in the line-emitting Kaleidoscope sample. Using Baldwin–Phillips–Terlevich (BPT) diagnostic diagrams, we classified the dominant ionisation sources in those systems exhibiting the requisite line emission. The majority of galaxies occupy the composite/LINER regime, indicating that their line ratios are consistent with a mixture of stellar and non-stellar excitation processes, while only a single object, Zwicky 2089, is unambiguously classified as a Seyfert. Beyond line-ratio diagnostics, we explored the thermal state of the warm ionised gas, constraining characteristic temperatures from the emission spectra, and mapped the distribution of metallicity across the sample. Together, these analyses provide a consistent picture in which ionisation in brightest cluster galaxies is neither purely star-formation driven nor entirely AGN-dominated, but instead reflects the complex interplay between stellar populations, AGN feedback, and the intracluster medium.

In the next chapter we analyse their stellar content, exploring ages, star formation histories, and stellar metallicities, in order to place the gas properties discussed here into the wider context of galaxy evolution in cluster cores.

CHAPTER 8

BCGs - Red and Dead?

The preceding chapters have concentrated on the characteristics of the ionised gas, which is detected in approximately 35% of the BCGs in our sample. Having established its prevalence and properties, we now switch to analysing the stellar populations and return to the full extent of the Kaleidoscope sample.

BCGs, residing at the luminous tip of the galaxy red sequence, have long been considered the archetypal "red and dead" systems in the Universe — massive ellipticals dominated by ancient stellar populations, exhibiting limited reservoirs of cold gas or active star formation [Fabian, 1994]. This view was largely supported by observations in the local Universe showing the majority of BCGs are quiescent, with typical star formation rates (SFRs) well below $10\,M_{\odot}\,\mathrm{yr}^{-1}$ [O'Dea et al., 2008]. However there were some studies which hinted at deviations from passive evolution. Detailed stellar population analysis of BCG cores, revealing a diversity in age and metallicity gradients, indicating episodes of more recent star formation or merger-driven assembly Loubser et al. [2009] . In denser, low-entropy cluster environments, some BCGs exhibit UV and blue optical cores indicative of young stellar populations, often correlated with ICM cooling phenomena [Cavagnolo et al., 2008, Green, 2017, Pipino et al., 2009].

Surveys across cosmic time further challenge the 'dead' label. Infrared studies spanning $0 < z \lesssim 1.8$ uncover substantial SFRs—tens to hundreds of solar masses per year—in a significant fraction of BCGs, implying that active, dust-obscured star formation persists to relatively low redshifts [Bonaventura et al., 2017]. Similarly, HST and spectroscopy of CLASH cluster BCGs reveal strong UV and Hα star-forming knots and filaments, with SFRs ranging from modest to well over $100\,M_\odot\,\mathrm{yr}^{-1}$, often co-located with low-entropy gas cores [Fogarty et al., 2015].

BCG stellar populations are shaped by both in situ star formation, often fuelled by residual cooling flows or AGN-regulated precipitation, and by hierarchical growth via mergers. At high redshift ($z \gtrsim 1$), rapid in situ formation and early assembly dominate, while at later times, minor mergers and residual star formation contribute to mass growth, though typically at lower levels [Castignani et al., 2022, Dunne et al., 2021].

8.1 Estimating Stellar Ages with pPXF

pPXF estimates stellar ages by fitting observed galaxy spectra with a linear combination of single stellar population (SSP) templates drawn from stellar population synthesis (SPS) models [Cappellari, 2017, Cappellari and Emsellem, 2004]. The method simultaneously recovers the stellar kinematics and star formation history (SFH) by minimising the residuals between the observed spectrum and a model spectrum constructed from the chosen templates, with an optional regularisation term to enforce smoothness in the SFH. From the best-fitting SFH, both light- and mass-weighted stellar ages are derived.

This method has been extensively validated in the literature and has been shown to achieve competitive or superior performance compared to alternative spectral fitting techniques. In particular, Woo et al. [2024] benchmarked pPXF against other popular full-spectrum fitting codes and deep learning approaches, finding that it recovers stellar population parameters with high accuracy and robustness across a wide range of signal-to-noise ratios and galaxy types. These results, combined with the flexibility in accommodating different SPS template libraries, make it a

well-suited choice for our stellar population analysis.

To ensure that our stellar age estimates are not significantly affected by the choice of stellar template library, we ran the full pPXF pipeline separately with four SPS template sets. These are: (i) the FSPS v3.2 models [Conroy et al., 2009, 2010], (ii) the GALAXEV v2020 models [Bruzual and Charlot, 2003], (iii) the E-MILES models [Vazdekis et al., 2016], and (iv) the X-Shooter Spectral Library (XSL) models [Gonneau et al., 2020]. This approach allowed us to test for library dependence in the recovered stellar ages.

The FSPS and GALAXEV models cover a wide range of stellar ages, making them suitable for both quiescent and star-forming systems. The E-MILES and XSL libraries, on the other hand, only include models with ages older than 63 Myr and 50 Myr, respectively, and are therefore less suited for galaxies with significant recent star formation. Nevertheless, including all four in our analysis ensures robustness in our derived ages and highlights any systematic offsets introduced by template selection. Across the sample, we find that the inferred stellar ages are consistent within the statistical uncertainties, indicating minimal dependence on the choice of SPS library. The FSPS models were used for all results shown in this chapter.

8.2 Distribution of Stellar Ages in the Kaleidoscope Survey

Fig. 8.1 demonstrates the variation in stellar age range within the Kaleidoscope survey where two features are immediately apparent. Firstly, the majority of BCGs exhibit narrow age distributions: both the global and $R \leq 5$kpc histograms peak at $\Delta \log_{10}(\text{age}) \lesssim 0.3\,\text{dex}$. A minority have very broad global age widths, which sharply diminish in the inner ≤ 5kpc: the dotted line marks an empirical complexity threshold at $1.5\,\text{dex}$ (a factor ~ 30 in age). Above this, we count global $N(>1.50) = 27$ objects but only ≤ 5kpc $N(>1.50) = 3$ - the large spread is almost entirely suppressed when restricting to the central region.

Nearby BCGs are well known to host predominantly old, α-enhanced, metal-rich stellar populations in their centres, with stellar-population gradients (in age

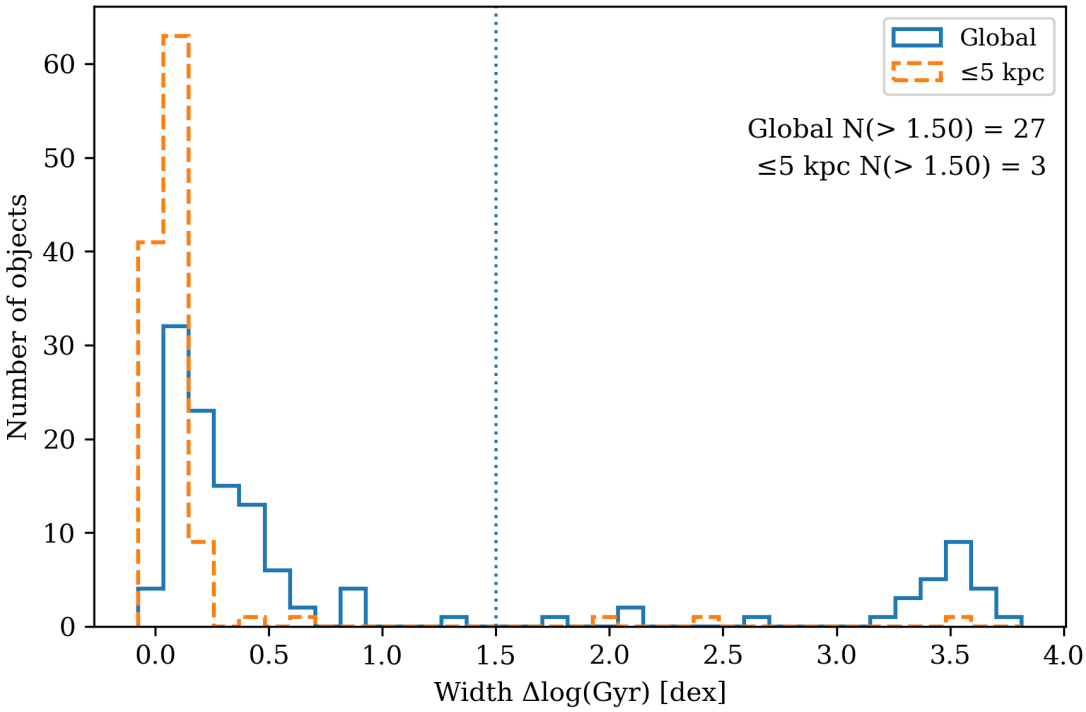

Figure 8.1: Histogram of the logarithmic age width, $\Delta \log_{10}(\mathrm{age/Gyr})$, for the BCG sample. The blue solid curve shows measurements from spectra integrated over a FOV of $(20'' \times 20'')$, whereas the orange dashed curve shows measurements from a central aperture of radius $\leq 5\,\mathrm{kpc}$. Here, the width is defined as the 16th–84th percentile range of $\log_{10}(\mathrm{age/Gyr})$ returned by the stellar–population fit to each object; small values indicate well–constrained, single–age–like solutions, while large values reflect broad/degenerate posteriors or complex/extended star-formation histories. The vertical dotted line marks $\Delta \log_{10}(\mathrm{age}) = 1.5\,\mathrm{dex}$ (a factor of ~ 30 in age) which we will use as a separatrix to form a sub-sample of potential starburst-hosting BCGs. Both distributions are strongly peaked at small widths ($\lesssim 0.3\,\mathrm{dex}$); the central $\leq$5 kpc apertures are systematically narrower than the global measurements—consistent with higher S/N and/or more uniform stellar populations in the cores—while a minority of globally integrated spectra show very broad widths (including a tail at $\gtrsim 3\,\mathrm{dex}$).

and [α/Fe]) that are on average shallow compared to ordinary ellipticals of similar mass [Loubser and Sánchez-Blázquez, 2012, Loubser et al., 2009]. In SSP-equivalent terms, the central light is commonly dominated by stars formed at $z \gtrsim 2$ and then passively evolved, yielding intrinsically narrow posterior age distributions when fit with standard index- or full-spectrum methods. This is exactly what the sharp peak at $\Delta \log_{10}(\mathrm{age}) \lesssim 0.3\,\mathrm{dex}$ reflects for both apertures.

The appearance of a sub-sample with greater width in age when expanding to the full extent of the galaxy follows logically from the discussion in § 1.3. BCGs assemble a large fraction of their stellar mass ex-situ via dry/minor mergers and tidal stripping at late times. The associated ICL and extended envelopes mix stars of different ages/metallicities at radii $\gtrsim$ a few to tens of kpc. Two additional effects further broaden global age posteriors. Firstly, in clusters with low central entropy, star formation often occurs in filamentary structures extending $\sim$ 10–50kpc from the BCG [e.g. Bildfell et al., 2008, Fogarty et al., 2015]. These young components (sometimes accompanied by nebular emission and dust) are down-weighted in small nuclear apertures but contribute non-negligibly when integrating over large radii, naturally producing a multi-age mixture and a broad posterior in the global fits. Secondly, BCG age and [α/Fe] gradients are typically shallow inside $\sim R_{\mathrm{e}}$, but metallicity declines outward and the outer envelope can include stars accreted from satellites with more extended SFHs [Loubser and Sánchez-Blázquez, 2012]. Such spatially varying mixtures inflate the global $\Delta \log_{10}(\mathrm{age})$ relative to the nuclear value.

The dramatic reduction from $N(>1.5\ \mathrm{dex}) = 27$ (global) to 3 ($\leq$ 5kpc) therefore implies that most of the complexity resides outside the central few kiloparsecs. In physical terms, BCG cores are typically uniform and old, whereas their extended envelopes encode signatures of more recent accretion and/or low-level star formation tied to intracluster medium (ICM) cooling. It is important to note, however, in all the above analysis that as the radial distance from the BCG increases, the likelihood of contamination also rises, either from other cluster members projected along the line of sight or from foreground stars. The enhanced scatter we observe at larger radii may therefore be explained—either in part or in full—by such effects, rather than by

intrinsic stellar population variations. Distinguishing which would require a more individualised asking strategy, capable of identifying and excluding contaminating sources on a case-by-case basis.

The literature links star-forming BCGs to thermodynamically unstable, low-entropy cores, with empirical thresholds around $K_0 \lesssim 30$ keV cm^2 or $t_{\rm cool}/t_{\rm ff} \lesssim 10$–$20$, where cold precipitation and AGN feedback self-regulate the cooling cycle [Fogarty et al., 2015, Rafferty et al., 2008, Voit et al., 2008]. Our finding that broad global age widths largely disappear in the nucleus is consistent with this picture: the youngest stars and line emission often reside in filaments and knots at $R \gtrsim 5$–20kpc rather than exclusively in the inner $\sim$ 5kpc, as clearly resolved in CLASH BCGs [Fogarty et al., 2015]. Where blue cores are present, they still tend to be geometrically compact (typical sizes $\sim$ 20kpc or less) and associated with cool-core clusters [Bildfell et al., 2008, Green, 2017, Loubser et al., 2009, O'Dea et al., 2008]. Central BCG spectra generally indicate old SSP-equivalent ages, super-solar metallicities, and elevated [α/Fe], with only a minority showing young/intermediate ages; gradients inside $\sim R_{\rm e}$ are modest [Loubser and Sánchez-Blázquez, 2012, Loubser et al., 2009]. This matches our narrow nuclear age-width distribution.

UV/optical line diagnostics show that $\sim$half of the CLASH sample of BCGs host on-going SF with clumpy, filamentary morphology on $\sim$ 10–50kpc scales; SFRs span 0.1–$\sim 300 M_\odot\, yr^{-1}$ in the most extreme systems [Fogarty et al., 2015]. Such extended young components (plus ex-situ envelopes) naturally broaden global SFHs, explaining the long global tail to $\Delta \log_{10}(\text{age}) \gtrsim 1.5$ dex while leaving the inner $\leq$ 5kpc comparatively simple.

The contrast between narrow nuclear and broader global age distributions supports a scenario in which compact, old cores form early, while extended stellar envelopes assemble later via accretion/stripping, sometimes augmented by ICM-fed star formation in cool cores [Edwards et al., 2019].

Fig. 8.5 compares the inner–5 kpc stellar age distributions for line–emitting (green) and non–emitting (red) BCGs. The curves are PDFs, so their areas are unity and the heights can be compared directly. Both classes peak at old ages, as expected for massive quenched galaxies, but the line–emitting subset is shifted

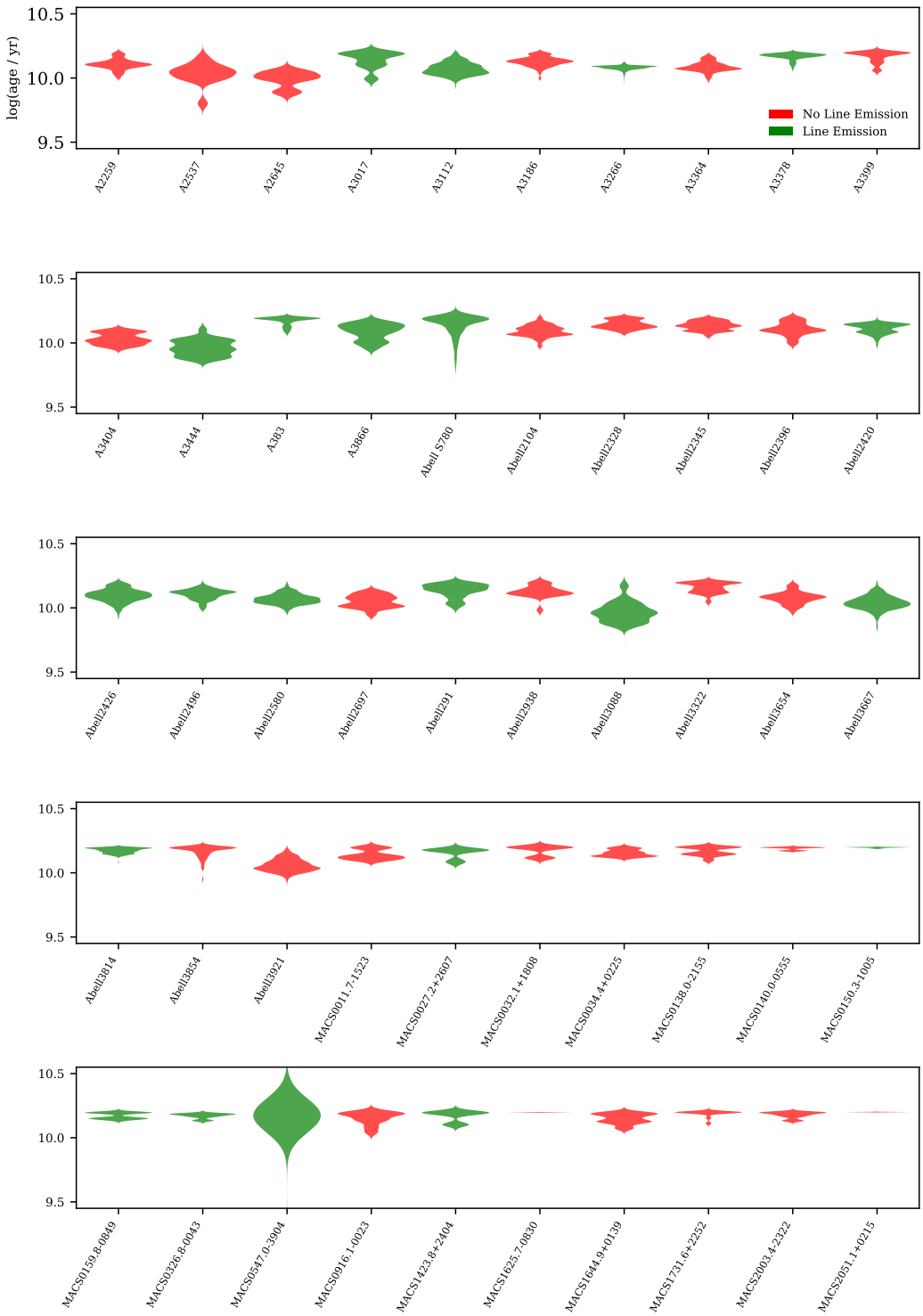

Figure 8.2: Violin plots showing the distribution of luminosity-weighted stellar population ages for the BCG sample. The horizontal width of each violin indicates the relative probability density at a given log(age/yr).

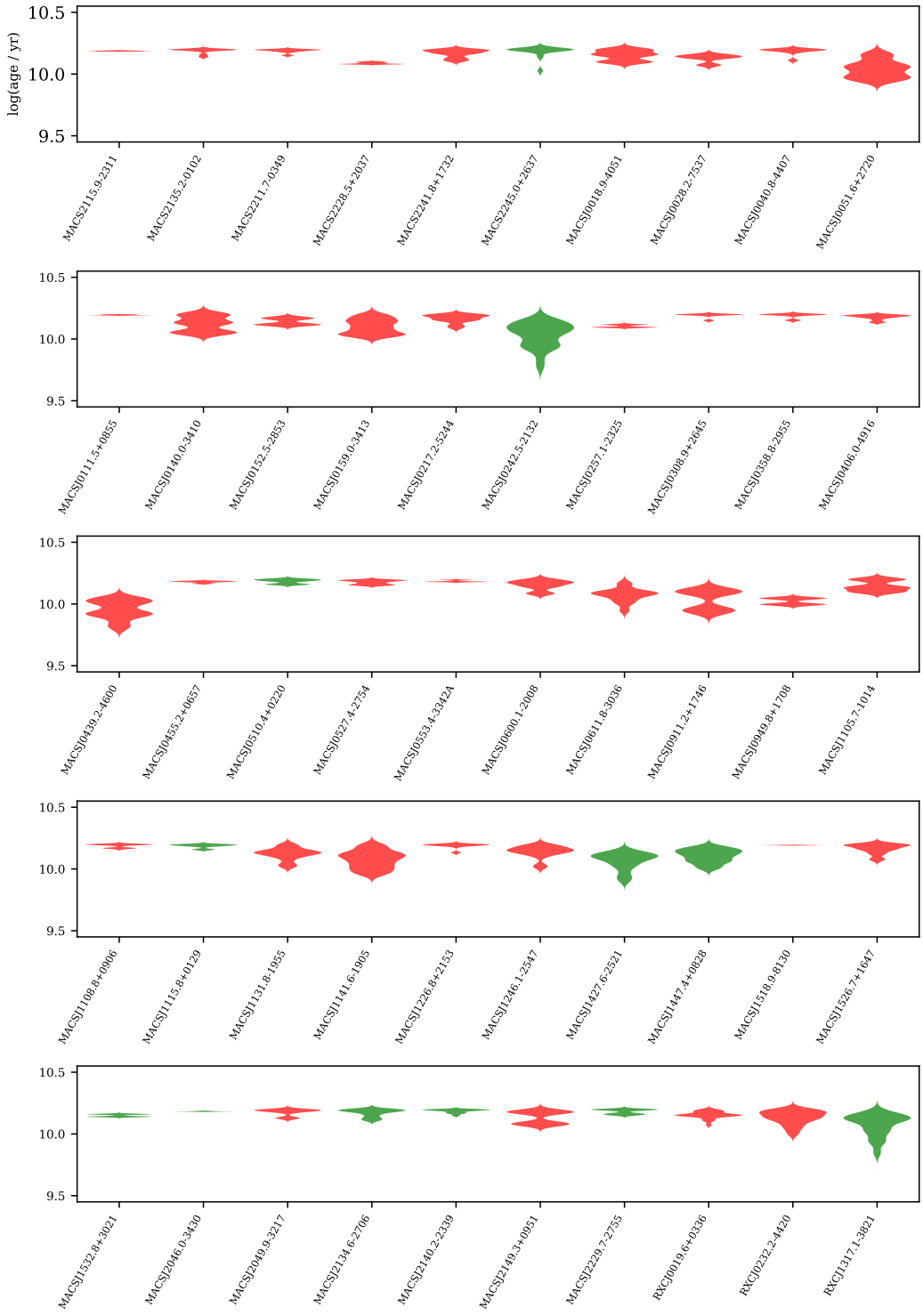

Figure 8.3: Continued

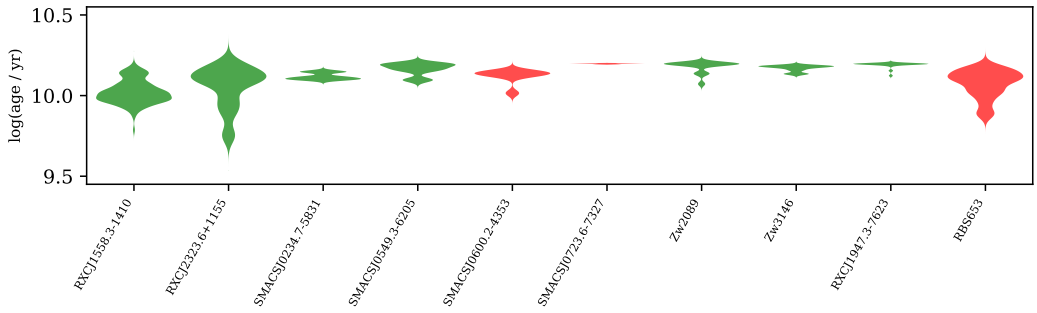

Figure 8.4: Continued

slightly toward younger ages and is a bit narrower. The Gaussian fits quantify this: the emitters have $\mu \simeq 10.079$ and $\sigma \simeq 0.049$, while the non–emitters have $\mu \simeq 10.095$ and $\sigma \simeq 0.053$.

Interpreted in linear age, the fitted means correspond to $\sim$ 12.0 Gyr for the emitters and $\sim$ 12.4 Gyr for the non–emitters - a modest $\sim$ 0.4–0.5 Gyr offset. The widths of $\sim$ 0.05 dex imply $\approx$10–12% scatter in linear age for both classes (assuming approximately log–normal errors/mixtures), with the non–emitters exhibiting a slightly broader high–age tail. Taken together, the distributions indicate that BCG cores are dominated by ancient stellar populations, with line emission possibly associated with a small ($\sim$few per cent in age) rejuvenation or population mix difference but certainly no strong, global shift to young ages.

8.3 Summary

The analysis presented in this chapter demonstrates that, while BCGs have historically been regarded as archetypal 'red and dead' systems, the reality is more nuanced. For the majority of the *Kaleidoscope* sample, the stellar populations within the central ≤ 5 kpc are indeed dominated by old ($\gtrsim 11$ Gyr), metal-rich populations with narrow age distributions. This confirms that the cores of BCGs formed early and have experienced little subsequent star formation, consistent with the picture of rapid assembly at $z \gtrsim 2$ followed by largely passive evolution.

At the same time, the comparison between global and nuclear measurements reveals evidence of more complex stellar population mixes at larger radii. Broad posterior age distributions in the global fits point to the influence of extended stellar envelopes assembled through minor mergers and the accretion of satellites, often bringing in stars of more diverse ages and metallicities. In some systems, particularly those with line emission and signatures of multiphase gas, the broadening also reflects young stellar components associated with cooling-driven star formation in extended filaments. Observations with HST have shown that this star formation often occurs in compact knots embedded within filaments, with typical sizes of $\lesssim 1$ kpc [e.g. Donahue et al., 2015]. The dramatic reduction in age-width complexity when

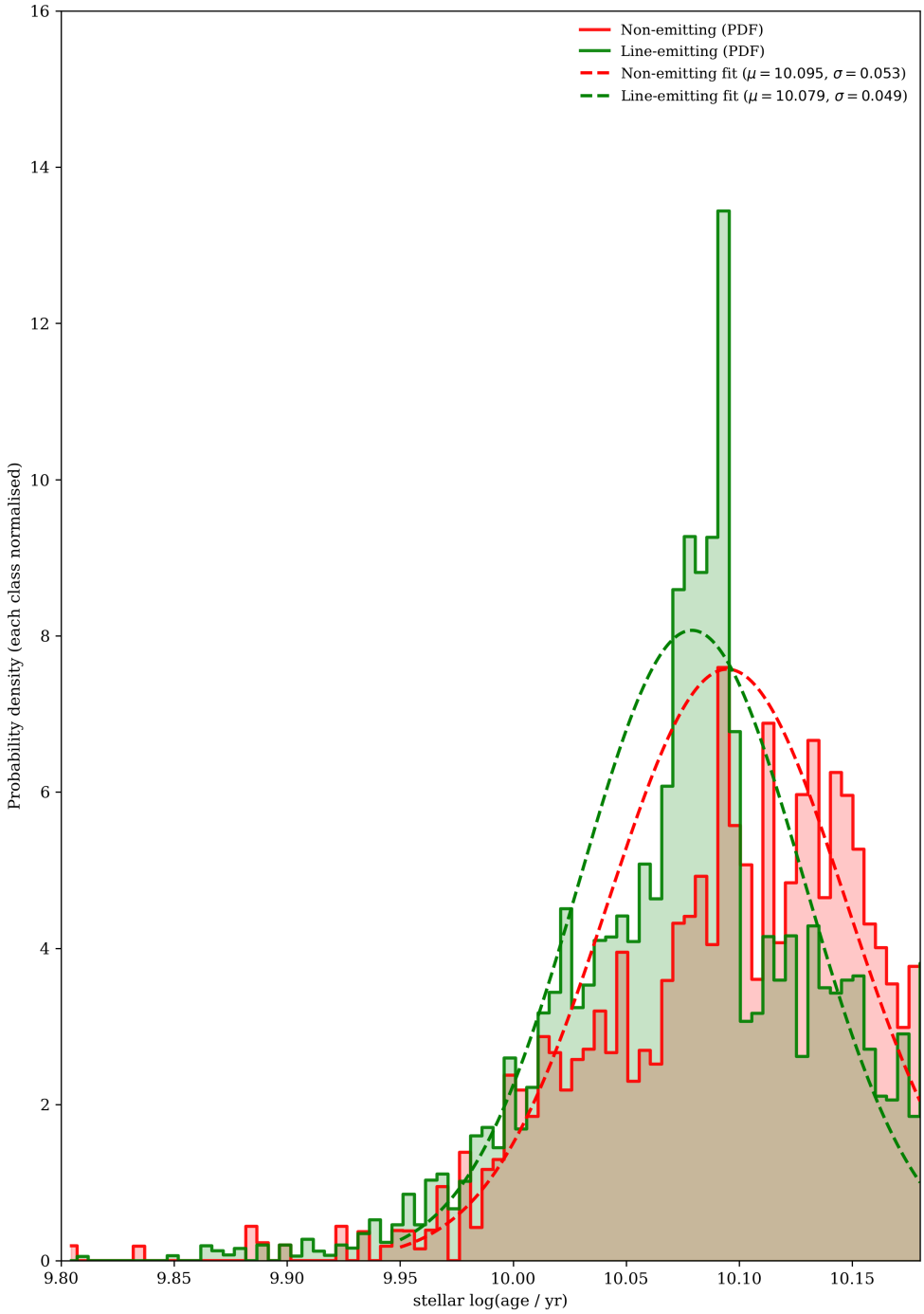

Figure 8.5: Continuum–weighted, per–class normalised age distributions for Voronoi bins within 5 kpc across the BCG sample. Red shows non–line–emitting systems; green shows line–emitting systems. Each class is normalised to unit area. Dashed curves are Gaussian fits performed only over $9.95 \leq \log_{10}(\text{age/yr}) \leq 10.18$ to mitigate edge effects from the upper age limit of the stellar template library; the legend reports the fitted μ and σ.

restricting to the central ≤ 5 kpc supports this picture: the cores remain uniform and old, while the envelopes encode late-time growth and intermittent rejuvenation.

The contrast between line-emitting and non-emitting systems provides further nuance. Both subsets are dominated by old stellar populations, but line-emitters are marginally shifted toward younger mean ages, with slightly narrower nuclear distributions. This suggests that even where ionised gas is present, its impact on the integrated stellar light is modest. The rejuvenation episodes are likely minor in mass fraction, affecting only a few per cent of the stellar population, but they nonetheless signal that residual star formation persists in a subset of BCGs under the right thermodynamic conditions. It is also worth noting that our Voronoi bins, chosen to achieve the S/N required for robust stellar continuum fits, can span areas an order of magnitude larger than the intrinsic scales of star-forming knots. Any spectral signatures of young stars are therefore diluted by the surrounding, older stellar populations, and future higher-resolution or deeper spectroscopic data will be required to resolve and isolate these compact starburst regions.

CHAPTER 9

Conclusions and Future Work

This thesis has presented the first comprehensive analysis of the BCG properties within the Kaleidoscope survey, representing the largest homogeneous sample of X-ray-selected BCGs observed with MUSE. By leveraging the high spatial and spectral resolution, this work has moved beyond simple morphological classification to provide a multi-scale view of the feeding and feedback cycle that governs the evolution of these massive systems.

Having defined the line-emitting subset of the sample, the focus shifted to characterising the chemical and physical state of the multiphase gas. The wide spectral coverage of MUSE enabled the simultaneous measurement of the Balmer decrement ($H\alpha/H\beta$) alongside gas kinematics, allowing us to eliminate one of the major uncertainties—extrinsic reddening—that often plagues this type of analysis.

The observation that Balmer ratios in the vast majority of these systems are remarkably consistent with the theoretical values predicted for Case B recombination provides a physical anchor for the subsequent kinematic results. The absence of significant dust removes a primary source of potential bias, providing a more robust foundation for the interpretation of the VSFs. In the presence of variable dust, uneven line-of-sight obscuration can create artificial velocity gradients or shift line

centroids, effectively mimicking turbulent motion.

By demonstrating that these systems are relatively dust-free, we break the degeneracy between dust-induced reddening and true gas motion. This allows the observed velocity fluctuations to be interpreted as a clean measurement of the gas's turbulent kinetic energy, enabling us to more confidently link the flattening of the VSF at specific spatial scales to physical energy injection from AGN feedback.

In the following sections, I summarise the main results from each chapter, highlighting how these interconnected findings regarding gas physics, stellar populations, and kinematics provide a unified picture of cluster physics while outlining future avenues of investigation.

Chapter 3: Incidence of Optical Line Emission

We established that $32-36\%$ of X-ray–selected BCGs in the Kaleidoscope survey exhibit extended optical line emission. This fraction is consistent with previous smaller studies, but our sample size provides the most statistically robust measurement to date for a purely X-Ray selected sample. This result constrains the prevalence of multiphase condensation and residual cooling in cluster cores.

Combining MUSE data with deep X-ray observations (e.g., Chandra and Athena) will allow stronger correlations between thermodynamic state and line-emission incidence. This will help determine whether feedback is universally effective or if its efficiency varies with environment.

Chapter 4: Morphology of the Ionised Gas

We constructed a new morphology catalogue for the ionised gas, revealing a diverse set of structures from extended filaments to compact clumps. Crucially, we examined the spatial correspondence between Hα emission, X-ray peaks, and stellar continuum centroids, probing the dynamical coupling between cold, hot, and stellar phases. The results suggest that while many systems show alignment, there are spatial offsets greater than the seeing, pointing to the role of sloshing, AGN feedback, or mergers

in displacing the gas.

A key finding is that 59% of line-emitting BCGs in our sample are classified as hosting extended plumes of ionised gas. This fraction is markedly higher than the 14% reported in the VIMOS-based study of Hamer et al. [2016]. The difference highlights both the improved sensitivity and spatial coverage of MUSE and the importance of uniform, high-quality datasets for morphological classification. Moreover, the true incidence of plumes is arguably even higher than our observed fraction, since orientation effects will inevitably cause some extended structures to be projected along the line of sight and therefore appear more compact. This result strongly suggests that extended, filamentary ionised gas is a far more common feature of BCGs than previously recognised, and that earlier surveys, often limited by field of view and/or resolution, significantly underestimated their prevalence.

Deeper observations will better trace low-surface-brightness emission, testing whether apparently compact systems also host faint extended filaments. Cross-comparison with ALMA observations of molecular gas will probe whether ionised and molecular phases share morphologies. Further algorithmic development could enable automated classification schemes applicable to next-generation surveys.

Chapter 5: Gas–Stellar Kinematic Coupling

We uncovered a persistent systematic velocity offset of $\sim 100\,\mathrm{km\,s^{-1}}$ between the mean ionised gas velocity and the systemic stellar velocity. There was no significant correlation with any other properties of the BCG. Possible explanations, including projection effects, obscuration by dust, or genuine physical decoupling driven by processes such as AGN feedback or the accretion of external gas reservoirs, require a level of fine-tuning incompatible with the consistency of the offset across our sample.

As an aside, this discovery further highlights the power of MUSE compared to previous instruments such as VIMOS. The large, contiguous spectral window provided by MUSE enables the simultaneous fitting of the stellar continuum and multiple emission lines across the same dataset. This capability removes the need to rely on heterogeneous measurements of stars and gas from different spectral se-

tups, which often introduced systematic uncertainties. With MUSE, we are able to determine both the systemic stellar velocity and the ionised gas kinematics in a self-consistent framework, greatly increasing the robustness of our comparison. There are, however, limitations of the Kaleidoscope dataset. The programme was proposed as a 'filler' survey and therefore often executed under sub-optimal seeing conditions with relatively short exposure times. While this does not at all undermine the existence of the velocity offset itself, it does have implications for the spatial resolution at which the stellar continuum could be reliably fitted. To achieve the required signal-to-noise ratio for the stellar absorption features, Voronoi binning was applied, and the resulting bins were generally too large to provide high-resolution, spatially resolved maps of the gas-to-stellar velocity offset. With higher-quality data, it would be possible to probe more accurately the spatial region driving the offset - for example at specific radial distances or along morphological features such as filaments.

Future work should therefore combine higher-resolution stellar kinematics from integral-field units such as KCWI with molecular gas kinematics from ALMA to test whether offsets persist across multiple gas phases and to determine whether they vary systematically with radius or local environment. Such observations would place stringent constraints on whether the observed decoupling arises from external accretion, feedback-driven motions, or more subtle dynamical effects within the cluster core.

Chapter 6: Velocity Structure Functions

We applied velocity structure functions (VSFs) to the ionised gas, quantifying the scale dependence of turbulent motions and probing energy injection scales. The observed VSF slopes and amplitudes are consistent with turbulence regulated by both cooling and feedback, although system-to-system variation suggests a range of driving mechanisms.

We focussed on two-dimensional VSF heatmaps, rather than relying on one-dimensional radial profiles alone. By retaining the full spatial information, the

heatmaps capture local variations in turbulence and highlight anisotropies that would be averaged out in a simple profile. Furthermore, the creation of a combined heatmap covering the full Kaleidoscope sample provides an unbiased reference distribution of kinematic structures. This global reference framework enables individual systems to be placed in context, allowing the 'extremeness' of their turbulence properties to be assessed relative to the population baseline. In this way, extreme outliers can be identified in a statistically rigorous manner, ensuring that theoretical interpretations are grounded in the behaviour of the full sample.

Expanding this analysis to broader wavelengths would provide a more complete characterisation of turbulence properties in BCGs. Direct comparisons of VSF heatmaps across ionised, molecular, and X-ray–emitting phases will test whether turbulence cascades coherently through the multiphase medium or is damped at particular transitions. Linking these observed VSFs to high-resolution cosmological simulations will clarify whether turbulence is seeded primarily by AGN jets, cluster mergers, or sloshing motions.

Chapter 7: Excitation Mechanisms and Dust

Using BPT diagrams and related diagnostics, we found that the majority of BCGs occupy the LINER/Composite boundary, indicating a complex mix of excitation processes. While AGN photoionisation plays a role, shocks and star formation contribute in varying proportions depending on local conditions. Measurements of Balmer decrements provided estimates of reddening, with most systems showing $E(B-V) \approx 0$, indicating little to no dust extinction in the ionised gas. This suggests that, although dust is present in some BCGs, particularly those with strong extended line emission, the majority of the sample is characterised by relatively unobscured line-emitting regions. Nevertheless, a subset of systems exhibited significant dust attenuation, pointing to the coexistence of substantial cold-gas reservoirs in those cluster cores. Future deep spectroscopic observations across multiple wavelengths (UV to IR) will allow more precise decomposition of ionisation sources. JWST spectroscopy offers a powerful opportunity to measure mid-IR line ratios sensitive

to star formation and shocks. Multi-wavelength dust tracers (e.g., with ALMA and *Herschel* archives) could constrain the total dust mass and its spatial distribution, clarifying whether dust preferentially coexists with star-forming regions or extends more diffusely through the intracluster medium. Combining such data with extinction measurements will help determine the role of dust in shielding, cooling, and regulating the ionised gas.

Chapter 8: Stellar Populations

Although BCGs have traditionally been regarded as archetypal 'red and dead' galaxies, our analysis shows a more nuanced picture. In the Kaleidoscope sample, the central ≤ 5 kpc are overwhelmingly dominated by old ($\gtrsim 11$ Gyr), metal-rich populations, confirming that their cores formed early and have remained largely quiescent since $z \gtrsim 2$. However, broader age distributions at larger radii reveal the imprint of extended stellar envelopes built through minor mergers and, in some cases, young stellar components linked to cooling-driven star formation in filaments. The distinction between line-emitting and non-emitting systems is subtle, with both dominated by old stars but the former showing slightly younger mean ages, consistent with modest rejuvenation affecting only a few per cent of the stellar mass. Future work combining deeper IFU spectroscopy with UV–IR and millimetre observations would disentangle these small but significant rejuvenation episodes from the dominant old stellar populations, and to establish how widespread such low-level star formation remains across cosmic time.

Final Remarks

Taken together, the results of this thesis emphasise that BCGs and their environments cannot be understood solely through the lens of individual, extreme systems. Population-level studies such as the Kaleidoscope survey are essential for establishing the baseline properties and statistical distributions upon which theoretical models must be built.

A guiding principle of the survey has been the emphasis on population-level conclusions. Frequently much of the literature has been driven by individual, often extreme systems, however our approach has been to anchor theories of cooling, feedback, and gas dynamics in the ensemble properties of a representative sample. Only through such a statistical baseline can we distinguish between processes that are typical of cluster cores and those that are exceptional. Nevertheless, the survey has also uncovered a number of particularly striking systems whose complexity warrants dedicated follow-up. Both aspects—global statistical trends and targeted case studies—are essential for advancing our understanding.

Future progress will therefore depend on combining two complementary approaches. On the one hand, expanding statistical surveys is essential for establishing robust ensemble properties across redshift and mass scales; it is only through the distributions of global populations that theoretical frameworks can be properly constrained. On the other hand, detailed multi-wavelength studies of individual outliers remain indispensable. These extreme cases serve two critical roles: first, to verify that such systems genuinely occupy the loci implied by the global distributions, ensuring that our population-level understanding is not biased by measurement or selection effects; and second, to act as laboratories where the most pronounced manifestations of physical processes can be observed in isolation. In this sense, insights from the extremes may provide a form of 'trickle-down' theory, guiding us to physical mechanisms that operate universally but are only visible in a more subtle form in the broader population. This work has been centred on the first of these approaches—establishing global statistics—yet the dataset also contains a number of intriguing systems that merit dedicated follow-up.

There are also impending hardware advancements that will greatly expand the scope and depth of future investigations into BCGs and their environments. Wide-field spectroscopy with DESI and 4MOST will provide homogeneously selected cluster and group samples with precise redshifts and dynamics, anchoring population statistics and environmental trends. Time-domain imaging from the Rubin Observatory LSST will trace variability and transients in BCGs and cluster cores (e.g. AGN duty cycles, tidal events). High-resolution, multi-band imaging and spectroscopy

with JWST is already underway and will continue to provide transformative maps of dust, molecular gas, and warm ionised phases in BCGs at cosmic noon, directly probing cold accretion and star-formation efficiency. Spatially resolved optical diagnostics from BlueMUSE will expand the spectral window in which we can probe ionisation, kinematics, and mixing layers via blue/UV lines across extended nebulae. All-sky low-resolution spectra from SPHEREx will deliver uniform SEDs and emission-line constraints for large samples, enabling cross-survey calibration and robust energy-budget estimates. At radio wavelengths, LOFAR and the SKA will reveal aged and low-surface-brightness synchrotron plasma, jet energetics, and fossil bubbles, tying feedback work to duty cycles and ICM coupling. In X-rays, XRISM will measure line broadening and shifts to quantify turbulence, bulk flows, and metal transport in the ICM, providing the missing dynamical link between AGN energy injection and thermal regulation. Together, these facilities transform both halves of the programme outlined here: they scale population studies to the precision and volume needed to constrain theory, and they enable incisive, multi-wavelength follow-up of exceptional systems that illuminate the physical mechanisms governing BCGs and their environments.

Taken together, these strategies offer a pathway to a more complete understanding of how BCGs regulate the baryon cycle at the centres of galaxy clusters, and ultimately how feedback shapes the evolution of the most massive galaxies in the Universe.

Bibliography

N. Aghanim, Y. Akrami, M. Ashdown, J. Aumont, C. Baccigalupi, M. Ballardini, A. J. Banday, R. B. Barreiro, N. Bartolo, S. Basak, et al. Planck 2018 results. VI. Cosmological parameters. *Astron. Astrophys.*, 641:A6, 2020. doi: 10.1051/0004-6361/201833910. 1.1.1

Shadab Alam, Metin Ata, Stephen Bailey, Florian Beutler, Dmitry Bizyaev, Jonathan A. Blazek, Adam S. Bolton, Joel R. Brownstein, Angela Burden, Chia-Hsun Chuang, et al. The clustering of galaxies in the completed SDSS-III Baryon Oscillation Spectroscopic Survey: cosmological analysis of the DR12 galaxy sample. *Mon. Not. Roy. Astron. Soc.*, 470(3):2617–2652, 2017. doi: 10.1093/mnras/stx721. 1.1.1

M. G. Allen, B. A. Groves, M. A. Dopita, R. S. Sutherland, and L. J. Kewley. The mappings iii library of fast radiative shock models. *The Astrophysical Journal Supplement Series*, 178(1):20–55, 2008. doi: 10.1086/589652. 1.4.3, 7.2.4

S. W. Allen, A. E. Evrard, and A. B. Mantz. Cosmological parameters from observations of galaxy clusters. *Annual Review of Astronomy and Astrophysics*, 49:409–470, 2011. 1.1.4

R. Bacon, Y. Copin, G. Monnet, B. W. Miller, J. R. Allington-Smith, M. Bureau, C. M. Carollo, R. L. Davies, E. Emsellem, H. Kuntschner, R. F. Peletier, E. K.

Verolme, and P. T. de Zeeuw. The sauron project - i. the panoramic integral-field spectrograph. *Monthly Notices of the Royal Astronomical Society*, 326(1):23–35, 2001. doi: 10.1111/j.1365-8711.2001.04612.x. 2.3.2

R. Bacon et al. The muse second-generation vlt instrument. *Proc. SPIE*, 7735: 773508, 2010. doi: 10.1117/12.856027. 1.4.1

R. Bacon et al. The muse instrument. *The Messenger*, 157:13–19, 2014. 1.4.1

Roland Bacon, Laure Piqueras, Simon Conseil, Johan Richard, and Martin Shepherd. MPDAF: MUSE Python Data Analysis Framework. Astrophysics Source Code Library, record ascl:1611.003, November 2016. 2.1.1

J. A. Baldwin, M. M. Phillips, and R. Terlevich. Classification parameters for the emission-line spectra of extragalactic objects. *PASP*, 93:5, 1981. 1.4.3, 7.2

Michael L. Balogh, Frazer R. Pearce, Richard G. Bower, and Scott T. Kay. Revisiting the cosmic cooling crisis. *Monthly Notices of the Royal Astronomical Society*, 326(4):1228–1234, October 2001. ISSN 1365-2966. doi: 10.1111/j.1365-2966.2001.04667.x. URL `http://dx.doi.org/10.1111/j.1365-2966.2001.04667.x`. 1.1.6

M. C. Begelman and A. C. Fabian. Turbulent mixing layers in the interstellar medium. *Monthly Notices of the Royal Astronomical Society*, 244:26P–29P, 1990. 4, 1.4.3

F. Belfiore, R. Maiolino, C. Maraston, and et al. Sdss iv manga - spatially resolved diagnostic diagrams: a proof that many galaxies are liers. *MNRAS*, 461:3111, 2016. 7.2.3, 7.2.4, 7.2.5

Eric F. Bell, Thorsten Naab, Daniel H. McIntosh, Rachel S. Somerville, John A. R. Caldwell, Marco Barden, Christian Wolf, Hans-Walter Rix, Steven V. Beckwith, Andrea Borch, Boris Haussler, Catherine Heymans, Knud Jahnke, Shardha Jogee, Sergey Koposov, Klaus Meisenheimer, Chien Y. Peng, Sebastian F. Sanchez, and Lutz Wisotzki. Dry mergers in gems: The dynamical evolution of massive early-type galaxies. *The Astrophysical Journal*, 640(1):241–251, March 2006. ISSN 1538-4357. doi: 10.1086/499931. URL `http://dx.doi.org/10.1086/499931`. 1.2.3

Andrew J. Benson. Galaxy formation theory. *Physics Reports*, 495(2–3):33–86, October 2010. ISSN 0370-1573. doi: 10.1016/j.physrep.2010.06.001. URL http://dx.doi.org/10.1016/j.physrep.2010.06.001. 1.1.6

Mariangela Bernardi. Evolution in the structural properties of early-type brightest cluster galaxies at small lookback time and dependence on the environment. *Monthly Notices of the Royal Astronomical Society*, 395(3):1491–1506, May 2009. ISSN 1365-2966. doi: 10.1111/j.1365-2966.2009.14601.x. URL http://dx.doi.org/10.1111/j.1365-2966.2009.14601.x. 1.2.3

Mariangela Bernardi, Ravi K. Sheth, James Annis, Scott Burles, Daniel J. Eisenstein, Douglas P. Finkbeiner, David W. Hogg, Robert H. Lupton, David J. Schlegel, Mark SubbaRao, Neta A. Bahcall, John P. Blakeslee, J. Brinkmann, Francisco J. Castander, Andrew J. Connolly, István Csabai, Mamoru Doi, Masataka Fukugita, Joshua Frieman, Timothy Heckman, Gregory S. Hennessy, Željko Ivezić, G. R. Knapp, Don Q. Lamb, Timothy McKay, Jeffrey A. Munn, Robert Nichol, Sadanori Okamura, Donald P. Schneider, Aniruddha R. Thakar, and Donald G. York. Early-Type Galaxies in the Sloan Digital Sky Survey. III. The Fundamental Plane. , 125 (4):1866–1881, April 2003. doi: 10.1086/367794. 1.2.2

C. Bildfell, H. Hoekstra, A. Babul, and A. Mahdavi. Resurrecting the red from the dead: Optical properties of brightest cluster galaxies in x-ray luminous clusters. *Monthly Notices of the Royal Astronomical Society*, 389:1637–1654, 2008. doi: 10.1111/j.1365-2966.2008.13684.x. URL https://arxiv.org/abs/0802.2712. 8.2

L. Bîrzan, D. A. Rafferty, B. R. McNamara, M. W. Wise, and P. E. J. Nulsen. A Systematic Study of Radio-Induced X-Ray Cavities in Groups and Clusters of Galaxies. *The Astrophysical Journal*, 607(2):800–809, June 2004. doi: 10.1086/383519. 4.1

E. L. Blanton, S. W. Randall, T. E. Clarke, C. L. Sarazin, et al. A very deep chandra observation of the galaxy cluster a2052: Bubbles, shocks, and sloshing. *The Astrophysical Journal*, 737(2):99, 2011. doi: 10.1088/0004-637X/737/2/99. 1.3.2, 1.4.4

G. R. Blumenthal, S. M. Faber, J. R. Primack, and M. J. Rees. Formation of galaxies and large-scale structure with cold dark matter. *Nature*, 311:517–525, 1984. doi: 10.1038/311517a0. 1.2.1

N. R. Bonaventura, T. M. A. Webb, A. Muzzin, A. Noble, C. Lidman, G. Wilson, H. K. C. Yee, J. Geach, Y. Hezaveh, D. Shupe, and J. Surace. Red but not dead: unveiling the star-forming far-infrared spectral energy distribution of SpARCS brightest cluster galaxies at 0 ¡ z ¡ 1.8. , 469(2):1259–1281, August 2017. doi: 10.1093/mnras/stx722. 8

H. Bondi. On spherically symmetrical accretion. *Monthly Notices of the Royal Astronomical Society*, 112:195–204, 1952. doi: 10.1093/mnras/112.2.195. 7

S. Borgani, G. Murante, V. Springel, A. Diaferio, K. Dolag, L. Moscardini, G. Tormen, L. Tornatore, and P. Tozzi. X-ray properties of galaxy clusters and groups from a cosmological hydrodynamical simulation. *Monthly Notices of the Royal Astronomical Society*, 348(3):1078–1096, March 2004. ISSN 1365-2966. doi: 10.1111/j.1365-2966.2004.07431.x. URL `http://dx.doi.org/10.1111/j.1365-2966.2004.07431.x`. 1.1.6

A. Boselli and G. Gavazzi. Environmental effects on late-type galaxies in nearby clusters. *Publications of the Astronomical Society of the Pacific*, 118(840):517–559, 2006. doi: 10.1086/500691. 1.2.3, 5.1

Michael Boylan-Kolchin, Chung-Pei Ma, and Eliot Quataert. Dynamical friction and galaxy merging time-scales. *Monthly Notices of the Royal Astronomical Society*, 383(1):93–101, 2008. doi: 10.1111/j.1365-2966.2007.12530.x. 1.2.2

M. Brüggen and E. Scannapieco. AGN-driven Turbulence in Galaxy Clusters. 44: 63–68, January 2010. doi: 10.1051/eas/1044011. 1.3.3

G. Bruzual and S. Charlot. Stellar population synthesis at the resolution of 2003. *MNRAS*, 344(4):1000–1028, 2003. doi: 10.1046/j.1365-8711.2003.06897.x. 8.1

K. Bundy, M. A. Bershady, D. R. Law, R. Yan, N. Drory, N. MacDonald, D. A. Wake, B. Cherinka, J. R. Sánchez-Gallego, A.-M. Weijmans, D. Thomas,

C. Tremonti, K. Masters, L. Coccato, A. M. Diamond-Stanic, A. Aragón-Salamanca, V. Avila-Reese, C. Badenes, J. Falcón-Barroso, F. Belfiore, D. Bizyaev, G. A. Blanc, J. Bland-Hawthorn, M. R. Blanton, J. R. Brownstein, N. Byler, M. Cappellari, C. Conroy, A. A. Dutton, E. Emsellem, J. Etherington, P. M. Frinchaboy, H. Fu, J. E. Gunn, P. Harding, E. J. Johnston, G. Kauffmann, M. A. Klaene, J. H. Knapen, A. Leauthaud, C. Li, L. Lin, R. Maiolino, E. Malanushenko, V. Malanushenko, S. Mao, C. Maraston, R. M. McDermid, M. R. Merrifield, R. C. Nichol, D. Oravetz, K. Pan, J. K. Parejko, S. F. Sanchez, D. J. Schlegel, A. Simmons, O. Steele, M. Steinmetz, K. Thanjavur, B. Thompson, J. L. Tinker, R. C. E. van den Bosch, K. B. Westfall, D. Wilkinson, S. Wright, T. Xiao, K. Zhang, Z. Zheng, G. Zhu, and H. Zou. Overview of the sdss-iv manga survey: Mapping nearby galaxies at apache point observatory. *Astrophysical Journal*, 798(1):7, 2015. doi: 10.1088/0004-637X/798/1/7. 2.3.2

J. M. Burgers. A mathematical model illustrating the theory of turbulence. *Advances in Applied Mechanics*, 1:171–199, 1948. 6.2

Claire Burke and Chris A. Collins. Growth of brightest cluster galaxies via mergers since z=1. *Monthly Notices of the Royal Astronomical Society*, 434(4):2856–2865, August 2013. ISSN 1365-2966. doi: 10.1093/mnras/stt1192. URL `http://dx.doi.org/10.1093/mnras/stt1192`. 1.2.5

Claire Burke, Matt Hilton, and Chris Collins. Coevolution of brightest cluster galaxies and intracluster light using clash. *Monthly Notices of the Royal Astronomical Society*, 449(3):2353–2367, 03 2015. ISSN 0035-8711. doi: 10.1093/mnras/stv450. URL `https://doi.org/10.1093/mnras/stv450`. 1.1.5, 1.2.4

D. Calzetti. The dust content and opacity of actively star-forming galaxies. *Publications of the Astronomical Society of the Pacific*, 113:1449–1485, 2001. doi: 10.1086/324269. 7.4, 7.4.2

R. E. A. Canning, H. R. Russell, N. A. Hatch, A. C. Fabian, A. I. Zabludoff, C. S. Crawford, L. J. King, B. R. McNamara, S. Okamoto, and S. I. Raimundo. Riding the wake of a merging galaxy cluster: Abell 2146 bcg. *Monthly Notices*

of the Royal Astronomical Society, 420(4):2956–2968, February 2012. ISSN 0035-8711. doi: 10.1111/j.1365-2966.2011.20116.x. URL `http://dx.doi.org/10.1111/j.1365-2966.2011.20116.x`. 1.3.4

R. E. A. Canning et al. A multi-wavelength view of cooling vs. AGN heating in the X-ray luminous cool-core of Abell 3581. *Mon. Not. Roy. Astron. Soc.*, 435:1108, 2013. doi: 10.1093/mnras/stt1345. 1.3

M. Cappellari, E. Emsellem, D. Krajnović, R. M. McDermid, N. Scott, G. A. Verdoes Kleijn, L. M. Young, K. Alatalo, R. Bacon, L. Blitz, M. Bois, F. Bournaud, M. Bureau, R. L. Davies, T. A. Davis, P. T. de Zeeuw, P.-A. Duc, S. Khochfar, H. Kuntschner, P.-Y. Lablanche, R. Morganti, T. Naab, T. Oosterloo, M. Sarzi, P. Serra, and A.-M. Weijmans. The atlas^{3D} project - i. a volume-limited sample of 260 nearby early-type galaxies: science goals and selection criteria. *Monthly Notices of the Royal Astronomical Society*, 413(2):813–836, 2011. doi: 10.1111/j.1365-2966.2010.18174.x. 2.3.2

Michele Cappellari. Improving the full spectral fitting method: accurate convolution, stellar population moments, and nested sampling. , 466(1):798–811, April 2017. doi: 10.1093/mnras/stw3020. 1.4.1, 2.3.2, 2.3.2, 8.1

Michele Cappellari and Eric Emsellem. Parametric Recovery of Line-of-Sight Velocity Distributions from Absorption-Line Spectra of Galaxies via Penalized Likelihood. , 116(816):138–147, February 2004. doi: 10.1086/381875. 2.3.2, 2.3.2, 8.1

C. L. Carilli and G. B. Taylor. Cluster magnetic fields. *ARA&A*, 40:319, 2002. 1.3.3

C. M. Casey, D. Narayanan, and A. Cooray. Dusty star-forming galaxies at high redshift. *Physics Reports*, 541:45–161, 2014. doi: 10.1016/j.physrep.2014.02.009. 7.4

G. Castignani et al. Star-forming and gas-rich brightest cluster galaxies at $z \sim$?. *Astronomy Astrophysics*, 2022. 8

K. W. Cavagnolo, M. Donahue, G. M. Voit, and M. Sun. Entropy profiles in the cores of cooling flow clusters. *Astrophysical Journal*, 682:821–838, 2008. 1.3.1, 1.3.7, 1.4.5, 3.2, 8

K. W. Cavagnolo, M. Donahue, G. M. Voit, and M. Sun. Intracluster medium entropy profiles for a chandra archival sample of galaxy clusters. *The Astrophysical Journal Supplement Series*, 182:12, 2009. doi: 10.1088/0067-0049/182/1/12. 1.3.1, 2.4.1, 3

Gilles Chabrier. Galactic stellar and substellar initial mass function. *Publications of the Astronomical Society of the Pacific*, 115:763–795, 2003. doi: 10.1086/376392. 2.3.2

S. Chandrasekhar. Dynamical friction. i. general considerations: the coefficient of dynamical friction. *The Astrophysical Journal*, 97:255, 1943. doi: 10.1086/144517. 1.2.2

A. Chu, F. Pacaud, N. Clerc, et al. Physical properties of brightest cluster galaxies up to $z = 1.8$. *Astronomy & Astrophysics*, 649:A36, 2021. doi: 10.1051/0004-6361/202040245. 1.2.5

A. Chu, F. Pacaud, N. Clerc, et al. Physical properties of more than one thousand brightest cluster galaxies: early formation and slow growth. *Astronomy & Astrophysics*, 665:A98, 2022. doi: 10.1051/0004-6361/202243504. 1.2.5

E. Churazov, M. Bruggen, C. R. Kaiser, H. Bohringer, and W. Forman. Evolution of buoyant bubbles in m87. *The Astrophysical Journal*, 554(1):261–273, June 2001. ISSN 1538-4357. doi: 10.1086/321357. URL `http://dx.doi.org/10.1086/321357`. 1.3.3

R. Cid Fernandes, G. Stasińska, A. Mateus, and N. Vale Asari. Past and present star formation in agn hosts: the whan diagram revisited. *MNRAS*, 413:1687, 2011. 7.2.4, 7.2.5

M. S. Clemens, A. P. Jones, A. Bressan, et al. The origin of dust in early-type galaxies. *Astronomy & Astrophysics*, 518:L50, 2010. doi: 10.1051/0004-6361/201014600. 7.4

Alison L. Coil. *The Large-Scale Structure of the Universe*, page 387–421. Springer Netherlands, 2013. ISBN 9789400756090. doi: 10.1007/978-94-007-5609-0_8. URL http://dx.doi.org/10.1007/978-94-007-5609-0_8. 1.1.3

Chris A. Collins, John P. Stott, Matt Hilton, Scott T. Kay, S. Adam Stanford, Michael Davidson, Mark Hosmer, Ben Hoyle, Andrew Liddle, Ed Lloyd-Davies, Robert G. Mann, Nicola Mehrtens, Christopher J. Miller, Robert C. Nichol, A. Kathy Romer, Martin Sahlén, Pedro T. P. Viana, and Michael J. West. Early assembly of the most massive galaxies. *Nature*, 458(7238):603–606, April 2009. ISSN 1476-4687. doi: 10.1038/nature07865. URL http://dx.doi.org/10.1038/nature07865. 1.2.5

C. Conroy, J. E. Gunn, and M. White. The propagation of uncertainties in stellar population synthesis modeling. i. the relevance of uncertain aspects of stellar evolution and the initial mass function to the derived physical properties of galaxies. *ApJ*, 699:486–506, 2009. doi: 10.1088/0004-637X/699/1/486. 8.1

C. Conroy, M. White, and J. E. Gunn. The propagation of uncertainties in stellar population synthesis modeling. ii. the challenge of comparing galaxy evolution models to observations. *ApJ*, 708:58–89, 2010. doi: 10.1088/0004-637X/708/1/58. 8.1

E. Contini. On the origin and evolution of the intra-cluster light. *Galaxies*, 9(3): 60, 2021. doi: 10.3390/galaxies9030060. 1.2.4

A. Contreras-Santos, F. Pearce, W. Cui, et al. Characterising the intra-cluster light in the three hundred galaxy clusters. *Astronomy & Astrophysics*, 684:A92, 2024. doi: 10.1051/0004-6361/202348474. 1.2.4, 1.2.7

C. S. Crawford, S. W. Allen, H. Ebeling, A. C. Edge, and A. C. Fabian. The rosat brightest cluster sample (bcs): Iii. optical spectra of the central cluster galaxies.

Monthly Notices of the Royal Astronomical Society, 306(4):857–896, 1999. doi: 10.1046/j.1365-8711.1999.02583.x. 3, 3.2, 5.2.1, 7.4.2

C. S. Crawford, N. A. Hatch, A. C. Fabian, and J. S. Sanders. The extended h-emitting filaments surrounding ngc 4696, the central galaxy of the centaurus cluster. *Monthly Notices of the Royal Astronomical Society*, 363(1):216–222, 10 2005. ISSN 0035-8711. doi: 10.1111/j.1365-2966.2005.09463.x. URL `https://doi.org/10.1111/j.1365-2966.2005.09463.x`. 1.3.3

Roohi Dalal, Michael A. Strauss, Tomomi Sunayama, Masamune Oguri, Yen-Ting Lin, Song Huang, Youngsoo Park, and Masahiro Takada. Brightest cluster galaxies are statistically special from z = 0.3 to z = 1. , 507(3):4016–4029, November 2021. doi: 10.1093/mnras/stab2363. 1.2.5

R. Davies, N. M. Förster Schreiber, G. Cresci, R. Genzel, N. Bouché, A. Burkert, P. Buschkamp, S. Genel, E. Hicks, J. Kurk, D. Lutz, S. Newman, K. Shapiro, A. Sternberg, L. J. Tacconi, and S. Wuyts. How well can we measure the intrinsic velocity dispersion of distant disk galaxies? *The Astrophysical Journal*, 741(2):69, October 2011. ISSN 1538-4357. doi: 10.1088/0004-637x/741/2/69. URL `http://dx.doi.org/10.1088/0004-637X/741/2/69`. 1.4.2

Timothy A. Davis, Katherine Alatalo, Marc Sarzi, Martin Bureau, Lisa M. Young, Leo Blitz, Alison Crocker, Estelle Bayet, Maxime Bois, Frédéric Bournaud, Michele Cappellari, Roger L. Davies, P. T. de Zeeuw, Pierre-Alain Duc, Eric Emsellem, Jesús Falcón-Barroso, Sadegh Khochfar, Davor Krajnović, Harald Kuntschner, Pierre-Yves Lablanche, Richard M. McDermid, Raffaella Morganti, Thorsten Naab, Tom Oosterloo, Nicholas Scott, Paolo Serra, Anne-Marie Weijmans, and Glenn van de Ven. The atlas3d project - iii. a census of the molecular gas in early-type galaxies. *MNRAS*, 417:882–899, 2011. doi: 10.1111/j.1365-2966.2011.19379.x. 5.1.1

Timothy A. Davis, Katherine Alatalo, Martin Bureau, Michele Cappellari, Marc Sarzi, Lisa M. Young, Leo Blitz, Alison F. Crocker, Estelle Bayet, P. Tim de Zeeuw, Eric Emsellem, Sadegh Khochfar, Davor Krajnović, Harald Kuntschner, Richard M. McDermid, Raffaella Morganti, Thorsten Naab, Tom Oosterloo,

Nicholas Scott, Paolo Serra, and Anne-Marie Weijmans. Molecular gas and stellar kinematics in early-type galaxies: misalignments, masses and morphologies. *Monthly Notices of the Royal Astronomical Society*, 429(1):534–555, 2013. doi: 10.1093/mnras/sts353. 5.1.1

Gabriella De Lucia and Jérôme Blaizot. The hierarchical formation of the brightest cluster galaxies. *Monthly Notices of the Royal Astronomical Society*, 375(1):2–14, 2007. doi: 10.1111/j.1365-2966.2006.11287.x. 1.2.1, 1.2.6

G. E. de Messières, R. W. O'Connell, B. R. McNamara, M. Donahue, P. E. J. Nulsen, G. M. Voit, and M. W. Wise. Spitzer mid-infrared spectra of cool-core galaxy clusters. 2009. URL `https://arxiv.org/abs/0908.3445`. 7.4

Tahlia DeMaio, Anthony H. Gonzalez, Ann Zabludoff, Dennis Zaritsky, and Maruša Bradač. On the origin of the intracluster light in massive galaxy clusters. *Monthly Notices of the Royal Astronomical Society*, 448(2):1162–1177, February 2015. ISSN 0035-8711. doi: 10.1093/mnras/stv033. URL `http://dx.doi.org/10.1093/mnras/stv033`. 1.2.4

Tahlia DeMaio, Anthony H Gonzalez, Ann Zabludoff, Dennis Zaritsky, Thomas Connor, Megan Donahue, and John S Mulchaey. Lost but not forgotten: intracluster light in galaxy groups and clusters. *Monthly Notices of the Royal Astronomical Society*, 474(3):3009–3031, 11 2017. ISSN 0035-8711. doi: 10.1093/mnras/stx2946. URL `https://doi.org/10.1093/mnras/stx2946`. 1.2.4

Theresa DeMaio, Megan Donahue, Maruša Bradač, et al. The growth of brightest cluster galaxies and intracluster light over the past 10 billion years. *Monthly Notices of the Royal Astronomical Society*, 491(3):3751–3768, 2020. doi: 10.1093/mnras/stz3236. 1.2.4, 1.2.7

Roberto De Propris, Michael J West, Felipe Andrade-Santos, Cinthia Ragone-Figueroa, Elena Rasia, William Forman, Christine Jones, Rain Kipper, Stefano Borgani, Diego García Lambas, Elena A Romashkova, and Kishore C Patra. Brightest cluster galaxies: the centre can(not?) hold. *Monthly Notices of the Royal Astronomical Society*, 500(1):310–318, October 2020. ISSN 1365-2966. doi:

10.1093/mnras/staa3286. URL http://dx.doi.org/10.1093/mnras/staa3286. 1.2.5

M. Donahue, T. Connor, K. Fogarty, A. Hoffer, A. M. Koekemoer, N. Prasad, G. M. Voit, R. E. Williams, G. Bartosch Caminha, C. Grillo, A. Zitrin, and et al. Ultraviolet morphologies and star formation rates of clash brightest cluster galaxies. *Astrophysical Journal*, 805(2):177, 2015. doi: 10.1088/0004-637X/805/2/177. 8.3

Megan Donahue and G. M. Voit. Calcium Depletion in Cooling-Flow Nebulae and the Origin of the Line-emitting Gas. , 414:L17, September 1993. doi: 10.1086/186985. 7.4.1

Megan Donahue, Andres Jordan, Stefi A. Baum, Patrick Cote, Laura Ferrarese, Paul Goudfrooij, Duccio Macchetto, Sangeeta Malhotra, Christopher P. O'Dea, James E. Pringle, James E. Rhoads, William B. Sparks, and G. Mark Voit. Infrared emission from the nearby cool core cluster abell 2597. *The Astrophysical Journal*, 670(1):231–236, November 2007. ISSN 1538-4357. doi: 10.1086/522575. URL http://dx.doi.org/10.1086/522575. 7.4

Megan Donahue, Seth Bruch, Emily Wang, G. Mark Voit, Amalia K. Hicks, Deborah B. Haarsma, Judith H. Croston, Gabriel W. Pratt, Daniele Pierini, Robert W. O'Connell, and Hans Böhringer. Star formation and UV colors of the brightest cluster galaxies in the REXCESS survey. *The Astrophysical Journal*, 715(2):881–896, 2010a. doi: 10.1088/0004-637X/715/2/881. 3.2

Megan Donahue, Seth Bruch, Emily Wang, G. Mark Voit, Amalia K. Hicks, Deborah B. Haarsma, Judith H. Croston, Gabriel W. Pratt, Daniele Pierini, Robert W. O'Connell, and Hans Böhringer. Star formation and uv colors of the brightest cluster galaxies in the representativexmm-newtoncluster structure survey. *The Astrophysical Journal*, 715(2):881–896, May 2010b. ISSN 1538-4357. doi: 10.1088/0004-637x/715/2/881. URL http://dx.doi.org/10.1088/0004-637X/715/2/881. 7.4.2

M. A. Dopita and R. S. Sutherland. Spectral signatures of fast shocks. ii. optical diagnostic diagrams. *The Astrophysical Journal Supplement Series*, 102:161–+, 1996. doi: 10.1086/192255. 3, 1.4.3

M. A. Dopita, L. J. Kewley, C. A. Heisler, and R. S. Sutherland. A theoretical reassessment of the h ii region abundance sequence. *ApJ*, 542:224, 2000. 7.2.1

B. T. Draine. *Physics of the Interstellar and Intergalactic Medium*. Princeton University Press, 2011. 7.4

B. T. Draine and E. E. Salpeter. Destruction mechanisms for interstellar dust. *The Astrophysical Journal*, 231:77–94, 1979. doi: 10.1086/157165. 7.4

John Dubinski. The Effect of Dissipation on the Shapes of Dark Halos. , 431:617, August 1994. doi: 10.1086/174512. 1.2.1

Delaney A. Dunne, Tracy M. A. Webb, Allison Noble, Christopher Lidman, Heath Shipley, Adam Muzzin, Gillian Wilson, and H. K. C. Yee. A co survey of sparcs star-forming brightest cluster galaxies: Evidence for uniformity in bcg molecular gas processing across cosmic time. *The Astrophysical Journal Letters*, 909(2):L29, March 2021. ISSN 2041-8213. doi: 10.3847/2041-8213/abeb6f. URL `http://dx.doi.org/10.3847/2041-8213/abeb6f`. 8

H. Ebeling, A. C. Edge, and J. P. Henry. MACS: A Quest for the Most Massive Galaxy Clusters in the Universe. , 553(2):668–676, June 2001. doi: 10.1086/320958. 2.2.1

A. C. Edge. The detection of molecular gas in the central galaxies of cooling-flow clusters. *Monthly Notices of the Royal Astronomical Society*, 328:762–782, 2001. doi: 10.1046/j.1365-8711.2001.04802.x. 1.3.1, 1.3.3, 1.3.5, 1.4, 1.4.4, 5.2.1, 7.4

A. C. Edge, R. J. Ivison, Ian Smail, A. W. Blain, and J.-P. Kneib. The detection of dust in the central galaxies of distant cooling-flow clusters. *Monthly Notices of the Royal Astronomical Society*, 306(3):599–606, 07 1999. ISSN 0035-8711. doi: 10.1046/j.1365-8711.1999.02539.x. URL `https://doi.org/10.1046/j.1365-8711.1999.02539.x`. 7.4

A. C. Edge, J. B. R. Oonk, R. Mittal, S. W. Allen, S. A. Baum, H. Böhringer, J. N. Bregman, M. N. Bremer, F. Combes, C. S. Crawford, M. Donahue, E. Egami, A. C. Fabian, G. J. Ferland, S. L. Hamer, N. A. Hatch, W. Jaffe, R. M. Johnstone, B. R. McNamara, C. P. O'Dea, P. Popesso, A. C. Quillen, P. Salomé, C. L. Sarazin, G. M. Voit, R. J. Wilman, and M. W. Wise. Herschel photometry of brightest cluster galaxies in cooling flow clusters. , 518:L47, July 2010. doi: 10.1051/0004-6361/201014572. 1.4

L. O. V. Edwards, Michael J. Hudson, Michael L. Balogh, and Russell J. Smith. Line emission in the brightest cluster galaxies of the NOAO fundamental plane and SDSS surveys. *Monthly Notices of the Royal Astronomical Society*, 379:100–110, 2007. doi: 10.1111/j.1365-2966.2007.11910.x. 3, 3.2

Louise O. V. Edwards and David R. Patton. Close companions to brightest cluster galaxies: support for minor mergers and downsizing: Close companions to brightest cluster galaxies. *Monthly Notices of the Royal Astronomical Society*, 425(1): 287–295, July 2012. ISSN 0035-8711. doi: 10.1111/j.1365-2966.2012.21457.x. URL `http://dx.doi.org/10.1111/j.1365-2966.2012.21457.x`. 1.2.5

Louise O V Edwards, Matthew Salinas, Steffanie Stanley, Priscilla E Holguin West, Isabella Trierweiler, Hannah Alpert, Paula Coelho, Saisneha Koppaka, Grant R Tremblay, Hugo Martel, and Yuan Li. Clocking the formation of today's largest galaxies: wide field integral spectroscopy of brightest cluster galaxies and their surroundings. *Monthly Notices of the Royal Astronomical Society*, 491(2):2617–2638, 09 2019. ISSN 0035-8711. doi: 10.1093/mnras/stz2706. URL `https://doi.org/10.1093/mnras/stz2706`. 1.1.5, 8.2

A. C. Fabian. Cooling flows in clusters of galaxies. *Annual Review of Astronomy and Astrophysics*, 32:277–318, 1994. doi: 10.1146/annurev.aa.32.090194.001425. 1.1.4, 1.3, 1.3.1, 4.2, 5.2.1, 7.4, 8

A. C. Fabian. Observational evidence of active galactic nuclei feedback. *Annual Review of Astronomy and Astrophysics*, 50:455–489, 2012. doi: 10.1146/annurev-astro-081811-125521. 1.1.5, 1.1.6, 1.3.2, 1.3.3, 1.4, 1.4.4, 4.1, 6.5, 7.2.5

A. C. Fabian, J. S. Sanders, S. Ettori, G. B. Taylor, S. W. Allen, C. S. Crawford, K. Iwasawa, and R. M. Johnstone. Chandra imaging of the x-ray core of abell 1795. *Monthly Notices of the Royal Astronomical Society*, 321(2):L33–L36, February 2001. ISSN 1365-2966. doi: 10.1046/j.1365-8711.2001.04243.x. URL http://dx.doi.org/10.1046/j.1365-8711.2001.04243.x. 1.3.3

A. C. Fabian, J. S. Sanders, S. W. Allen, C. S. Crawford, K. Iwasawa, R. M. Johnstone, and R. W. Schmidt. A deep chandra observation of the perseus cluster: shocks, ripples and conduction. *MNRAS*, 344:L43, 2003. 1.3.3, 1.3.4, 1.4, 1.4.5

A. C. Fabian, J. S. Sanders, G. B. Taylor, and et al. A very deep chandra observation of the core of the perseus cluster: shocks, ripples and conduction. *Nature*, 454:968, 2008. 1.3.3

Christoph Federrath, Ralf S. Klessen, and Wolfram Schmidt. The Density Probability Distribution in Compressible Isothermal Turbulence: Solenoidal versus Compressive Forcing. , 688(2):L79, December 2008. doi: 10.1086/595280. 6.2, 6.4

G. J. Ferland, A. C. Fabian, N. A. Hatch, R. M. Johnstone, R. L. Porter, P. A. M. van Hoof, and R. J. R. Williams. Collisional heating as the origin of filament emission in galaxy clusters. *Monthly Notices of the Royal Astronomical Society*, 392(4): 1475–1502, February 2009. ISSN 1365-2966. doi: 10.1111/j.1365-2966.2008.14153.x. URL http://dx.doi.org/10.1111/j.1365-2966.2008.14153.x. 4, 1.4.3

Laura Ferrarese and David Merritt. A fundamental relation between supermassive black holes and their host galaxies. *The Astrophysical Journal*, 539(1):L9–L12, August 2000. ISSN 0004-637X. doi: 10.1086/312838. URL http://dx.doi.org/10.1086/312838. 1.1.6

K. Fogarty, M. Postman, T. Connor, M. Donahue, and J. Moustakas. Star formation activity in clash brightest cluster galaxies. *Astrophysical Journal*, 813:117, 2015. 8, 8.2

W. Forman, C. Jones, E. Churazov, M. Markevitch, P. Nulsen, A. Vikhlinin, M. Begelman, H. Böhringer, J. Eilek, S. Heinz, R. Kraft, F. Owen, and M. Pahre.

Filaments, Bubbles, and Weak Shocks in the Gaseous Atmosphere of M87. , 665 (2):1057–1066, August 2007. doi: 10.1086/519480. 1.3.2, 1.4.4

M. Fournier, P. Grete, M. Brüggen, B. W. O'Shea, D. Prasad, B. D. Wibking, F. W. Glines, and R. Mohapatra. XMAGNET: Velocity structure functions of AGN-driven turbulence in the multiphase intracluster medium. *Astronomy Astrophysics*, 698:A121, June 2025. doi: 10.1051/0004-6361/202451031. Includes 3D and LOS VSFs for cold ($T \leq 10^5$K) and hot (10^6–10^8K) phases, shows projection and smoothing effects steepen cold-phase VSFs :contentReference[oaicite:1]index=1. 6.3

Uriel Frisch. *Turbulence: The Legacy of A. N. Kolmogorov*. Cambridge University Press, 1995. 6.2

A. Fruscione, J. C. McDowell, G. E. Allen, N. S. Brickhouse, D. J. Burke, J. E. Davis, N. Durham, M. Elvis, E. C. Galle, D. E. Harris, D. P. Huenemoerder, J. C. Houck, B. Ishibashi, M. Karovska, F. Nicastro, M. S. Noble, M. A. Nowak, F. A. Primini, A. Siemiginowska, R. K. Smith, and M. Wise. Ciao: Chandra's data analysis system. In *Society of Photo-Optical Instrumentation Engineers (SPIE) Conference Series*, volume 6270, page 62701V, 2006. doi: 10.1117/12.671760. 2.1.2

V. Gaibler, S. Khochfar, M. Krause, and J. Silk. Jet-induced star formation in gas-rich galaxies. *Monthly Notices of the Royal Astronomical Society*, 425(1):438–449, 09 2012. ISSN 0035-8711. doi: 10.1111/j.1365-2966.2012.21479.x. URL `https://doi.org/10.1111/j.1365-2966.2012.21479.x`. 1.1.6

Shalini Ganguly, Yuan Li, Valeria Olivares, Yuanyuan Su, Francoise Combes, Sampadaa Prakash, Stephen Hamer, Pierre Guillard, and Trung Ha. The nature of the motions of multiphase filaments in the centers of galaxy clusters. 2023. URL `https://arxiv.org/abs/2304.09879`. 6.6

G. P. Garmire, M. W. Bautz, P. G. Ford, J. A. Nousek, and G. R. Ricker. Advanced ccd imaging spectrometer (acis) instrument on the chandra x-ray observatory. *Proceedings of SPIE*, 4851:28–44, 2003. doi: 10.1117/12.461599. 2.1.2

M. Gaspari and E. Churazov. Constraining turbulence and conduction in the hot icm through density perturbations. *Astronomy amp; Astrophysics*, 559:A78, November 2013a. ISSN 1432-0746. doi: 10.1051/0004-6361/201322295. URL http://dx.doi.org/10.1051/0004-6361/201322295. 1.3, 1.3.4, 5.2.1

M. Gaspari and E. Churazov. Causal connection between turbulence and agn feedback in the hot gas of galaxy clusters. *Astronomy & Astrophysics*, 559, 2013b. doi: 10.1051/0004-6361/201322001. 6.2

M. Gaspari and A. Sądowski. Unifying the micro and macro properties of agn feeding and feedback. *The Astrophysical Journal*, 837(2):149, 2017. doi: 10.3847/1538-4357/aa61a3. 1.3.4, 5.1.1, 6.5

M. Gaspari, F. Brighenti, and P. Temi. Chaotic cold accretion on to black holes. *Astronomy & Astrophysics*, 579:A62, 2015. doi: 10.1051/0004-6361/201425535. 1.3.4, 1.3.7, 5.2.1

M. Gaspari, M. McDonald, S. L. Hamer, F. Brighenti, P. Temi, M.-L. Gendron-Marsolais, J. Hlavacek-Larrondo, A. C. Edge, N. Werner, P. Tozzi, et al. Shaken Snow Globes: Kinematic Tracers of the Multiphase Condensation Cascade in Massive Galaxies, Groups, and Clusters. *The Astrophysical Journal*, 854:167, 2018. doi: 10.3847/1538-4357/aaaa1b. 5.2.2, 5.2.3

M. Gaspari, M. McDonald, S. L. Hamer, et al. Shaken snow globes: Kinematics of cool gas in cluster cores support chaotic cold accretion. *The Astrophysical Journal*, 854(2):167, 2018. doi: 10.3847/1538-4357/aaa54d. 1.3, 1.3.4, 1.4.2, 5.1, 5.2.1, 5.2.1, 5.2.2, 5.2.3, 6.5

Massimo Gaspari, Francesco Tombesi, and Massimo Cappi. Linking macro-, meso- and microscales in multiphase agn feeding and feedback. *Nature Astronomy*, 4 (1):10–13, January 2020. ISSN 2397-3366. doi: 10.1038/s41550-019-0970-1. URL http://dx.doi.org/10.1038/s41550-019-0970-1. (document), 1.1

Efrain Gatuzz, R. Mohapatra, C. Federrath, J. S. Sanders, A. Liu, S. A. Walker, and C. Pinto. Measuring the hot icm velocity structure function using xmm-

newton observations. *Monthly Notices of the Royal Astronomical Society*, 524(2): 2945–2953, 2023. doi: 10.1093/mnras/stad2039. 6.6

Karl Gebhardt, Ralf Bender, Gary Bower, Alan Dressler, S. M. Faber, Alexei V. Filippenko, Richard Green, Carl Grillmair, Luis C. Ho, John Kormendy, Tod R. Lauer, John Magorrian, Jason Pinkney, Douglas Richstone, and Scott Tremaine. A relationship between nuclear black hole mass and galaxy velocity dispersion. *The Astrophysical Journal*, 539(1):L13–L16, August 2000. ISSN 0004-637X. doi: 10.1086/312840. URL `http://dx.doi.org/10.1086/312840`. 1.1.6

Marie-Joëlle Gingras, Alison L. Coil, B. R. McNamara, Serena Perrotta, Fabrizio Brighenti, H. R. Russell, Muzi Li, S. Peng Oh, and Wenmeng Ning. Complex velocity structure of nebular gas in active galaxies centred in cooling x-ray atmospheres, 2024. URL `https://arxiv.org/abs/2404.02212`. 5.1.1, 5.2

Myriam Gitti, Fabrizio Brighenti, and Brian R. McNamara. Evidence for agn feedback in galaxy clusters and groups. *Advances in Astronomy*, 2012:1–24, 2012. ISSN 1687-7977. doi: 10.1155/2012/950641. URL `http://dx.doi.org/10.1155/2012/950641`. 6.3

Jesse B. Golden-Marx, Y. Zhang, R. L. C. Ogando, S. Allam, D. L. Tucker, C. J. Miller, M. Hilton, B. Mutlu-Pakdil, T. M. C. Abbott, M. Aguena, O. Alves, F. Andrade-Oliveira, J. Annis, D. Bacon, E. Bertin, S. Bocquet, D. Brooks, D. L. Burke, A. Carnero Rosell, M. Carrasco Kind, F. J. Castander, C. Conselice, M. Costanzi, L. N. da Costa, M. E. S. Pereira, J. De Vicente, S. Desai, P. Doel, S. Everett, I. Ferrero, B. Flaugher, J. Frieman, J. García-Bellido, D. W. Gerdes, D. Gruen, R. A. Gruendl, G. Gutierrez, S. R. Hinton, D. L. Hollowood, K. Honscheid, D. J. James, K. Kuehn, N. Kuropatkin, O. Lahav, J. L. Marshall, P. Melchior, J. Mena-Fernández, R. Miquel, J. J. Mohr, A. Palmese, F. Paz-Chinchón, A. Pieres, A. A. Plazas Malagón, J. Prat, M. Raveri, M. Rodriguez-Monroy, A. K. Romer, E. Sanchez, V. Scarpine, I. Sevilla-Noarbe, C. Sifón, M. Smith, E. Suchyta, M. E. C. Swanson, G. Tarle, M. Vincenzi, N. Weaverdyck, B. Yanny, and DES Collaboration. Characterizing the intracluster light over the redshift

range 0.2 ¡ z ¡ 0.8 in the DES-ACT overlap. , 521(1):478–496, May 2023. doi: 10.1093/mnras/stad469. 1.2.4, 1.2.7

A. Gonneau, M. Lyubenova, A. Lançon, S. C. Trager, R. F. Peletier, A. Arentsen, Y.-P. Chen, P. R. T. Coelho, M. Dries, J. Falcón-Barroso, P. Prugniel, P. Sánchez-Blázquez, A. Vazdekis, and K. Verro. The x-shooter spectral library (xsl): Data release 2. *Astronomy amp; Astrophysics*, 634:A133, February 2020. ISSN 1432-0746. doi: 10.1051/0004-6361/201936825. URL `http://dx.doi.org/10.1051/0004-6361/201936825`. 8.1

Anthony H. Gonzalez, Ann I. Zabludoff, and Dennis Zaritsky. Intracluster Light in Nearby Galaxy Clusters: Relationship to the Halos of Brightest Cluster Galaxies. , 618(1):195–213, January 2005. doi: 10.1086/425896. 1.2.4

P. Goudfrooij, L. Hansen, H. E. Jorgensen, and H. U. Norgaard-Nielsen. The origin of dust and ionized gas in elliptical galaxies. *Astronomy and Astrophysics Supplement Series*, 105:341–366, 1994. 7.4

F. Govoni, M. Markevitch, A. Vikhlinin, and et al. Magnetic fields in clusters of galaxies. *ApJ*, 605:695, 2004. 1.3.3

Timothy Stephen Green. *A Study of Brightest Cluster Galaxies Over the Last Five Billion Years*. Phd thesis, Durham University, 2017. Available at Durham E-Theses Online: `http://etheses.dur.ac.uk/12338`. 8, 8.2

J. E. Gunn and J. R. Gott. On the infall of matter into clusters of galaxies and some effects on their evolution. *The Astrophysical Journal*, 176:1–19, 1972. doi: 10.1086/151605. 1.2.3

Q. Guo, S. White, M. Boylan-Kolchin, G. De Lucia, G. Kauffmann, G. Lemson, C. Li, V. Springel, and S. Weinmann. From dwarf spheroidals to cd galaxies: Simulating the galaxy population in a λcdm cosmology. *Monthly Notices of the Royal Astronomical Society*, 413(1):101–131, 2011. doi: 10.1111/j.1365-2966.2010.18114.x. 1.2.1

S. L. Hamer, A. C. Edge, A. M. Swinbank, R. J. Wilman, H. R. Russell, A. C. Fabian, J. S. Sanders, and P. Salomé. The relation between line emission and brightest cluster galaxies in three exceptional clusters: evidence for gas cooling from the intracluster medium. *Monthly Notices of the Royal Astronomical Society*, 421 (4):3409–3417, 04 2012. ISSN 0035-8711. doi: 10.1111/j.1365-2966.2012.20566.x. URL `https://doi.org/10.1111/j.1365-2966.2012.20566.x`. 3.2, 4.2

S. L. Hamer, A. C. Edge, A. M. Swinbank, R. J. Wilman, F. Combes, P. Salomé, A. C. Fabian, C. S. Crawford, H. R. Russell, J. Hlavacek-Larrondo, B. R. McNamara, and M. N. Bremer. Optical emission line nebulae in galaxy cluster cores 1: the morphological, kinematic and spectral properties of the sample. *Monthly Notices of the Royal Astronomical Society*, 460(2):1758–1789, May 2016. ISSN 1365-2966. doi: 10.1093/mnras/stw1054. URL `http://dx.doi.org/10.1093/mnras/stw1054`. (document), 1.3.4, 1.3.5, 1.3.6, 1.4, 1.4.2, 1.4.3, 2.1.1, 2.3.2, 4.3.1, 4.3.1, 4.1, 5.1, 5.1.1, 6.3, 7.2.5, 9

N. A. Hatch, C. S. Crawford, and R. M. Johnstone. The origin of emission-line nebulae in brightest cluster galaxies. *Monthly Notices of the Royal Astronomical Society*, 367:433–444, 2006. 1.3.5, 2, 1.4.3, 4.5

T. M. Heckman. An Optical and Radio Survey of the Nuclei of Bright Galaxies - Activity in the Normal Galactic Nuclei. , 87:152, July 1980. 1.3.6, 7.2, 7.2.2, 7.2.5

Timothy M Heckman and Philip N Best. The coevolution of galaxies and supermassive black holes: A local perspective. *Annual Review of Astronomy and Astrophysics*, 52:589–660, 2014. doi: 10.1146/annurev-astro-081913-035722. 1.1.6

Edmund Christian Herenz, Tanya Urrutia, Lutz Wisotzki, Josephine Kerutt, Rikke Saust, Maria Werhahn, Kasper Borello Schmidt, Joseph Caruana, Catrina Diener, Roland Bacon, Jarle Brinchmann, Joop Schaye, Michael Maseda, and Peter M. Weilbacher. The muse-wide survey: A first catalogue of 831 emission line galaxies. *Astronomy amp; Astrophysics*, 606:A12, September 2017. ISSN 1432-0746. doi: 10.1051/0004-6361/201731055. URL `http://dx.doi.org/10.1051/0004-6361/201731055`. 2.1.1

Lars Hernquist and P. J. Quinn. Formation of Shell Galaxies. I. Spherical Potentials. , 331:682, August 1988. doi: 10.1086/166592. 1.1.5

William Herschel. Catalogue of one thousand new nebulae and clusters of stars; with remarks on the construction of the heavens. *Philosophical Transactions of the Royal Society of London*, 76:457–517, 1786. 1.1.2

G. Hinshaw, D. Larson, E. Komatsu, D. N. Spergel, C. L. Bennett, J. Dunkley, M. R. Nolta, M. Halpern, R. S. Hill, N. Odegard, et al. Nine-Year Wilkinson Microwave Anisotropy Probe (WMAP) Observations: Cosmological Parameter Results. *Astrophys. J. Suppl.*, 208(2):19, 2013. doi: 10.1088/0067-0049/208/2/19. 1.1.1

Hitomi Collaboration. The Quiescent Intracluster Medium in the Core of the Perseus Cluster. *Nature*, 535:117–121, 2016. doi: 10.1038/nature18627. 5.2.1, 5.2.2, 6.5

Luis C. Ho, Alexei V. Filippenko, and Wallace L. W. Sargent. A Reevaluation of the Excitation Mechanism of LINERs. , 417:63, November 1993. doi: 10.1086/173291. 7.2.5

Luis C. Ho, Alexei V. Filippenko, and Wallace L. W. Sargent. A Search for "Dwarf" Seyfert Nuclei. V. Demographics of Nuclear Activity in Nearby Galaxies. , 487(2): 568–578, October 1997. doi: 10.1086/304638. 7.2.5

M. T. Hogan, A. C. Edge, J. Hlavacek-Larrondo, K. J. B. Grainge, S. L. Hamer, E. K. Mahony, H. R. Russell, A. C. Fabian, B. R. McNamara, and R. J. Wilman. A comprehensive study of the radio properties of brightest cluster galaxies. *Monthly Notices of the Royal Astronomical Society*, 453(2):1201–1222, 08 2015. ISSN 0035-8711. doi: 10.1093/mnras/stv1517. URL `https://doi.org/10.1093/mnras/stv1517`. 4.2

Edwin Hubble. A relation between distance and radial velocity among extragalactic nebulae. *Proceedings of the National Academy of Sciences*, 9(3):199–203, 1923. 1.1.2

Hajime Inoue. Origin of cool cores, cold fronts, and spiral structures in cool core clusters of galaxies. *Publications of the Astronomical Society of Japan*, 74 (1):152–160, December 2021. ISSN 2053-051X. doi: 10.1093/pasj/psab114. URL http://dx.doi.org/10.1093/pasj/psab114. 5.1

Lilian Jiang, Shaun Cole, Till Sawala, and Carlos S. Frenk. Orbital parameters of infalling satellite haloes in the hierarchical ΛCDM model. , 448(2):1674–1686, April 2015. doi: 10.1093/mnras/stv053. 1.2.2

Immanuel Kant. *Allgemeine Naturgeschichte und Theorie des Himmels*. Johann Friedrich Hartknoch, Königsberg, 1755. 1.1.2

Theodore von Kármán and Leslie Howarth. On the statistical theory of isotropic turbulence. *Proceedings of the Royal Society A*, 164:192–215, 1938. 6.2

G. Kauffmann, T. M. Heckman, C. Tremonti, J. Brinchmann, S. Charlot, S. D. M. White, S. E. Ridgway, J. Brinkmann, M. Fukugita, P. B. Hall, et al. The host galaxies of active galactic nuclei. *Monthly Notices of the Royal Astronomical Society*, 346:1055–1077, 2003. doi: 10.1111/j.1365-2966.2003.07154.x. (document), 1.4.3, 7.2.2, 7.3, 7.2.5

R. C. Kennicutt and N. J. Evans. Star formation in the milky way and nearby galaxies. *Annual Review of Astronomy and Astrophysics*, 50:531–608, 2012. doi: 10.1146/annurev-astro-081811-125610. 1.4.4

L. J. Kewley, M. A. Dopita, R. S. Sutherland, C. A. Heisler, and J. Trevena. Theoretical modeling of starburst galaxies. *ApJ*, 556:121, 2001. (document), 1.4.3, 7.2.2, 7.3

L. J. Kewley, B. Groves, G. Kauffmann, and T. Heckman. The host galaxies and classification of active galactic nuclei. *Monthly Notices of the Royal Astronomical Society*, 372(3):961—-976, November 2006. ISSN 1365-2966. doi: 10.1111/j.1365-2966.2006.10859.x. URL http://dx.doi.org/10.1111/j.1365-2966.2006.10859.x. (document), 1.4.3, 7, 7.2.1, 7.2.2, 7.3, 7.2.5, 7.2.5, 7.3

L. J. Kewley, D. C. Nicholls, and R. S. Sutherland. Understanding galaxy evolution through emission lines. *Annual Review of Astronomy and Astrophysics*, 57:511–570, 2019. doi: 10.1146/annurev-astro-081817-051832. 7.2.1, 7.2.5

Carl C. Kirkpatrick, B. R. McNamara, and K. W. Cavagnolo. Anisotropic metal-enriched outflows driven by agn in clusters of galaxies. *The Astrophysical Journal*, 731(2):L23, 2011. doi: 10.1088/2041-8205/731/2/L23. Observational evidence of metal-rich gas being transported from BCGs into the ICM along large-scale radio jet axes. 5.1, 5.1

Andrey Nikolaevich Kolmogorov. The local structure of turbulence in incompressible viscous fluid for very large reynolds numbers. *Doklady Akademii Nauk SSSR*, 30:301–305, 1941. 6.2

John Kormendy and Luis C. Ho. Coevolution (Or Not) of Supermassive Black Holes and Host Galaxies. , 51(1):511–653, August 2013. doi: 10.1146/annurev-astro-082708-101811. 1.1.6

D. Krajnović, M. Cappellari, P. T. de Zeeuw, and Y. Copin. Kinemetry: a generalization of photometry to the higher moments of the line-of-sight velocity distribution. *Monthly Notices of the Royal Astronomical Society*, 366(3):787–802, 2006. doi: 10.1111/j.1365-2966.2005.09902.x. 1.4.2

Andrey V. Kravtsov and Stefano Borgani. Formation of Galaxy Clusters. *Annual Review of Astronomy and Astrophysics*, 50:353–409, 2012. doi: 10.1146/annurev-astro-081811-125502. 1.1.3

Arieh Königl. Theory of bipolar outflows from high-mass young stellar objects. *New Astronomy Reviews*, 43(1):67–77, May 1999. ISSN 1387-6473. doi: 10.1016/s1387-6473(99)00003-2. URL `http://dx.doi.org/10.1016/S1387-6473(99)00003-2`. 1.1.6

David J Lagattuta, Johan Richard, Franz Erik Bauer, Catherine Cerny, Adélaïde Claeyssens, Lucia Guaita, Mathilde Jauzac, Alexandre Jeanneau, Anton M Koekemoer, Guillaume Mahler, Gonzalo Prieto Lyon, Ana Acebron, Massimo

Meneghetti, Anna Niemiec, Adi Zitrin, Matteo Bianconi, Thomas Connor, Renyue Cen, Alastair Edge, Andreas L Faisst, Marceau Limousin, Richard Massey, Mauro Sereno, Keren Sharon, and John R Weaver. Pilot-wings: An extended muse view of the structure of abell 370. *Monthly Notices of the Royal Astronomical Society*, 514(1):497–517, June 2022. ISSN 1365-2966. doi: 10.1093/mnras/stac418. URL http://dx.doi.org/10.1093/mnras/stac418. 2.3.1

Seppo Laine, Roeland P. van der Marel, Tod R. Lauer, Marc Postman, Christopher P. O'Dea, and Frazer N. Owen. [ital]hubble space telescope[/ital] imaging of brightest cluster galaxies. *The Astronomical Journal*, 125(2):478–505, February 2003. ISSN 1538-3881. doi: 10.1086/345823. URL http://dx.doi.org/10.1086/345823. 5.1.1

Chervin F. P. Laporte, Simon D. M. White, Thorsten Naab, and Liang Gao. The growth in size and mass of cluster galaxies since z = 2. *Monthly Notices of the Royal Astronomical Society*, 435(2):901–909, September 2013. ISSN 0035-8711. doi: 10.1093/mnras/stt912. URL http://dx.doi.org/10.1093/mnras/stt912. 1.2.2, 1.2.3

Erwin T. Lau, Massimo Gaspari, Daisuke Nagai, and Paolo Coppi. Physical origins of gas motions in galaxy cluster cores: Interpreting hitomi observations of the perseus cluster. *The Astrophysical Journal*, 849(1):54, October 2017. ISSN 1538-4357. doi: 10.3847/1538-4357/aa8c00. URL http://dx.doi.org/10.3847/1538-4357/aa8c00. 6.2

Tod R. Lauer, S. M. Faber, Douglas Richstone, Karl Gebhardt, Scott Tremaine, Marc Postman, Alan Dressler, M. C. Aller, Alexei V. Filippenko, Richard Green, Luis C. Ho, John Kormendy, John Magorrian, and Jason Pinkney. The Masses of Nuclear Black Holes in Luminous Elliptical Galaxies and Implications for the Space Density of the Most Massive Black Holes. , 662(2):808–834, June 2007. doi: 10.1086/518223. 1.1.5

Tod R. Lauer, Marc Postman, Michael A. Strauss, Genevieve J. Graves, and Nora E. Chisari. Brightest Cluster Galaxies at the Present Epoch. , 797(2):82, December 2014. doi: 10.1088/0004-637X/797/2/82. 4.2

O. Le Fèvre, M. Saisse, D. Mancini, S. Brau-Nogue, O. Caputi, L. Castinel, S. D'Odorico, B. Garilli, M. Kissler-Patig, C. Lucuix, D. Mancini, A. Pauget, G. Sciarretta, M. Scodeggio, L. Tresse, G. Vettolani, and G. Zamorani. Commissioning and performances of the vimos multi-object spectrograph at the eso very large telescope. *The Messenger*, 111:18–24, 2003. 2.1.1

Muzi Li, B.R. McNamara, Alison L. Coil, Marie-Joëlle Gingras, Fabrizio Brighenti, H.R. Russell, Prathamesh D. Tamhaneh, S. Peng Oh, and Serena Perrotta. Velocity structure correlations between the nebular, molecular, and atmospheric gases in the cores of four cool core clusters. *The Astrophysical Journal*, 984(1):22, apr 2025. doi: 10.3847/1538-4357/adc102. URL `https://dx.doi.org/10.3847/1538-4357/adc102`. 6.4, 6.6

Yuan Li and Greg L. Bryan. Modeling active galactic nucleus feedback in cool-core clusters: The balance between heating and cooling. *The Astrophysical Journal*, 789(1):54, June 2014. ISSN 1538-4357. doi: 10.1088/0004-637x/789/1/54. URL `http://dx.doi.org/10.1088/0004-637X/789/1/54`. 1.3.2

C. Lidman, J. Suherli, A. Muzzin, G. Wilson, R. Demarco, S. Brough, A. Rettura, J. Cox, A. DeGroot, H. K. C. Yee, D. Gilbank, H. Hoekstra, M. Balogh, E. Ellingson, A. Hicks, J. Nantais, A. Noble, M. Lacy, J. Surace, and T. Webb. Evidence for significant growth in the stellar mass of brightest cluster galaxies over the past 10 billion years: Brightest cluster galaxies. *Monthly Notices of the Royal Astronomical Society*, 427(1):550–568, November 2012. ISSN 1365-2966. doi: 10.1111/j.1365-2966.2012.21984.x. URL `http://dx.doi.org/10.1111/j.1365-2966.2012.21984.x`. 1.1.5, 1.2.5

C. Lidman, G. Iacobuta, A. E. Bauer, L. F. Barrientos, P. Cerulo, W. J. Couch, L. Delaye, R. Demarco, E. Ellingson, A. J. Faloon, D. Gilbank, M. Huertas-Company, S. Mei, J. Meyers, A. Muzzin, A. Noble, J. Nantais, A. Rettura,

P. Rosati, R. Sánchez-Janssen, V. Strazzullo, T. M. A. Webb, G. Wilson, R. Yan, and H. K. C. Yee. The importance of major mergers in the build up of stellar mass in brightest cluster galaxies at z = 1. *Monthly Notices of the Royal Astronomical Society*, 433(1):825–837, June 2013. ISSN 1365-2966. doi: 10.1093/mnras/stt777. URL http://dx.doi.org/10.1093/mnras/stt777. 1.2.5

Yen-Ting Lin, Kai-Feng Chen, Tsung-Chi Chen, Chen-Yu Chuang, and Masamune Oguri. Evolution of massive red galaxies in clusters from z=1.0 to z=0.3. 2025. URL https://arxiv.org/abs/2503.13592. 1.2.5

F. S. Liu, Shude Mao, Z. G. Deng, X. Y. Xia, and Z. L. Wen. Major dry mergers in early-type brightest cluster galaxies. *Monthly Notices of the Royal Astronomical Society*, 396(4):2003–2010, July 2009. ISSN 1365-2966. doi: 10.1111/j.1365-2966.2009.14907.x. URL http://dx.doi.org/10.1111/j.1365-2966.2009.14907.x. 1.2.3

F. S. Liu, F. J. Lei, X. M. Meng, and D. F. Jiang. Ongoing growth of the brightest cluster galaxies via major dry mergers in the last ∼6 Gyr. , 447(2):1491–1497, February 2015. doi: 10.1093/mnras/stu2543. 1.2.5

Haonan Liu, Andrew C Fabian, Ciro Pinto, Helen R Russell, Jeremy S Sanders, and Brian R McNamara. Suppressed cooling and turbulent heating in the core of x-ray luminous clusters rxcj1504.1-0248 and abell 1664. *Monthly Notices of the Royal Astronomical Society*, 505(2):1589–1599, 05 2021. ISSN 0035-8711. doi: 10.1093/mnras/stab1372. URL https://doi.org/10.1093/mnras/stab1372. 6.3

S. I. Loubser and P. Sánchez-Blázquez. Stellar population gradients in brightest cluster galaxies. *Monthly Notices of the Royal Astronomical Society*, 425:841–860, 2012. doi: 10.1111/j.1365-2966.2012.21079.x. URL https://academic.oup.com/mnras/article/425/2/841/1199539. 8.2

S. I. Loubser, P. Sánchez-Blázquez, A. E. Sansom, and I. K. Soechting. Stellar populations in the centres of brightest cluster galaxies. *Monthly Notices of the Royal Astronomical Society*, 398:133–156, 2009. doi: 10.1111/j.1365-2966.2009.15122.x. URL https://academic.oup.com/mnras/article/398/1/133/1093355. 8, 8.2

S I Loubser, A Babul, H Hoekstra, Y M Bahé, E O'Sullivan, and M Donahue. Dynamical masses of brightest cluster galaxies i: stellar velocity anisotropy and mass-to-light ratios. *Monthly Notices of the Royal Astronomical Society*, 496(2): 1857–1880, 06 2020. ISSN 0035-8711. doi: 10.1093/mnras/staa1682. URL `https://doi.org/10.1093/mnras/staa1682`. 1.1.5

Filippo Marcello Maccagni and W.J.G. De Blok. "neutral atomic hydrogen surveys: past, present and future ". In *Proceedings of the 4th URSI Atlantic RadioScience Conference – AT-RASC 2024*, URSI AT-RASC 2024. URSI – International Union of Radio Science, 2024. doi: 10.46620/ursiatrasc24/uxqp4342. URL `http://dx.doi.org/10.46620/URSIATRASC24/UXQP4342`. 5.2.1, 5.2.2

John Magorrian, Scott Tremaine, Douglas Richstone, Ralf Bender, Gary Bower, Alan Dressler, S. M. Faber, Karl Gebhardt, Richard Green, Carl Grillmair, John Kormendy, and Tod Lauer. The demography of massive dark objects in galaxy centers. *The Astronomical Journal*, 115(6):2285–2305, June 1998. ISSN 0004-6256. doi: 10.1086/300353. URL `http://dx.doi.org/10.1086/300353`. 1.1.6, 1.2.7

R Maiolino, HR Russell, AC Fabian, S Carniani, G Cresci, C Cicone, S Cristiani, V D'Odorico, A Ferrara, F Fiore, et al. Star formation inside a galactic outflow. *Nature*, 544(7649):202–206, 2017. doi: 10.1038/nature21677. 1.1.6

Maxim Markevitch and Alexey Vikhlinin. Shocks and cold fronts in galaxy clusters. *Physics Reports*, 443(1):1–53, May 2007. ISSN 0370-1573. doi: 10.1016/j.physrep.2007.01.001. URL `http://dx.doi.org/10.1016/j.physrep.2007.01.001`. 5.1, 5.1, 5.1.1, 5.1.1

A. R. Martel, H. C. Ford, L. D. Bradley, H. D. Tran, F. Menanteau, Z. I. Tsvetanov, G. D. Illingworth, G. F. Hartig, and M. Clampin. Dust and ionized gas in nine nearby early-type galaxies imaged with thehubble space telescopeadvanced camera for surveys. *The Astronomical Journal*, 128(6):2758–2771, December 2004. ISSN 1538-3881. doi: 10.1086/425628. URL `http://dx.doi.org/10.1086/425628`. 7.4

David Martínez-Delgado, R Jay Gabany, Ken Crawford, Stefano Zibetti, Steven R Majewski, Hans-Walter Rix, Jürgen Fliri, Julio A Carballo-Bello, Daniella C

Bardalez-Gagliuffi, Jorge Peñarrubia, et al. Stellar tidal streams in spiral galaxies of the local volume: A pilot survey with modest aperture telescopes. *The Astronomical Journal*, 140(4):962, 2010. doi: 10.1088/0004-6256/140/4/962. 1.1.5

Davide Martizzi, Romain Teyssier, and Ben Moore. The formation of the brightest cluster galaxies in cosmological simulations: the case for active galactic nucleus feedback. , 420(4):2859–2873, March 2012. doi: 10.1111/j.1365-2966.2011.19950.x. 1.2.1, 1.2.2, 1.2.6

William G. Mathews and Fabrizio Brighenti. Energetics of x-ray cavities and radio lobes in galaxy clusters. *The Astrophysical Journal*, 685(1):128–137, September 2008. ISSN 1538-4357. doi: 10.1086/590402. URL `http://dx.doi.org/10.1086/590402`. 1.3.3

Thomas A Matthews, William Wilson Morgan, and Maarten Schmidt. A discussion of galaxies identified with radio sources. *The Astrophysical Journal*, 140:35, 1964. doi: 10.1086/147890. 1.1.5

Michael McCourt, Prateek Sharma, Eliot Quataert, and Ian J. Parrish. Thermal instability in gravitationally stratified plasmas: implications for multiphase structure in clusters and galaxy haloes. , 419(4):3319–3337, February 2012. doi: 10.1111/j.1365-2966.2011.19972.x. 1.3.2

M. McDonald, M. Bayliss, B. A. Benson, R. J. Foley, J. Ruel, P. Sullivan, S. Veilleux, K. A. Aird, M. L. N. Ashby, M. Bautz, G. Bazin, L. E. Bleem, M. Brodwin, J. E. Carlstrom, C. L. Chang, H. M. Cho, A. Clocchiatti, T. M. Crawford, A. T. Crites, T. de Haan, S. Desai, M. A. Dobbs, J. P. Dudley, E. Egami, W. R. Forman, G. P. Garmire, E. M. George, M. D. Gladders, A. H. Gonzalez, N. W. Halverson, N. L. Harrington, F. W. High, G. P. Holder, W. L. Holzapfel, S. Hoover, J. D. Hrubes, C. Jones, M. Joy, R. Keisler, L. Knox, A. T. Lee, E. M. Leitch, J. Liu, M. Lueker, D. Luong-Van, A. Mantz, D. P. Marrone, J. J. McMahon, J. Mehl, S. S. Meyer, E. D. Miller, L. Mocanu, J. J. Mohr, T. E. Montroy, S. S. Murray, T. Natoli, S. Padin, T. Plagge, C. Pryke, T. D. Rawle, C. L. Reichardt, A. Rest, M. Rex, J. E. Ruhl, B. R. Saliwanchik, A. Saro, J. T. Sayre, K. K. Schaffer, L. Shaw,

E. Shirokoff, R. Simcoe, J. Song, H. G. Spieler, B. Stalder, Z. Staniszewski, A. A. Stark, K. Story, C. W. Stubbs, R. Šuhada, A. van Engelen, K. Vanderlinde, J. D. Vieira, A. Vikhlinin, R. Williamson, O. Zahn, and A. Zenteno. A massive, cooling-flow-induced starburst in the core of a luminous cluster of galaxies. *Nature*, 488 (7411):349–352, August 2012a. ISSN 1476-4687. doi: 10.1038/nature11379. URL http://dx.doi.org/10.1038/nature11379. 1.3.1, 1, 1.4.3, 5.1.1

M. McDonald, S. W. Allen, J. Hlavacek-Larrondo, A. B. Mantz, M. Bayliss, B. A. Benson, M. Brodwin, E. Bulbul, R. E. A. Canning, I. Chiu, W. R. Forman, G. P. Garmire, N. Gupta, G. Khullar, J. J. Mohr, C. L. Reichardt, and T. Schrabback. A detailed study of the most relaxed spt-selected galaxy clusters: Properties of the cool core and central galaxy. *The Astrophysical Journal*, 870(2):85, January 2019. ISSN 1538-4357. doi: 10.3847/1538-4357/aaf394. URL http://dx.doi.org/10.3847/1538-4357/aaf394. 1.3.1, 1.4.5

Michael McDonald. Optical line emission in brightest cluster galaxies at 0 lt; z lt; 0.6: Evidence for a lack of strong cool cores 3.5 gyr ago? *The Astrophysical Journal*, 742(2):L35, November 2011. ISSN 2041-8213. doi: 10.1088/2041-8205/742/2/l35. URL http://dx.doi.org/10.1088/2041-8205/742/2/L35. 3.2

Michael McDonald, Sylvain Veilleux, and David S. N. Rupke. Optical spectroscopy of h filaments in cool core clusters: Kinematics, reddening, and sources of ionization. *The Astrophysical Journal*, 746(2):153, February 2012b. ISSN 1538-4357. doi: 10.1088/0004-637x/746/2/153. URL http://dx.doi.org/10.1088/0004-637X/746/2/153. 1.3.5, 1.3.6, 2, 3, 1.3.6, 1.3.7, 1.4.2, 1.4.3, 1.4.5, 4.5

B. R. McNamara and P. E. J. Nulsen. Mechanical feedback from active galactic nuclei in galaxies, groups, and clusters. *Annual Review of Astronomy and Astrophysics*, 45:117–175, 2007. 1.3, 1.3.2, 1.3.3, 1.4, 4.1, 4.2, 5.1

B. R. McNamara, P. E. J. Nulsen, M. W. Wise, D. A. Rafferty, C. Carilli, C. L. Sarazin, and E. L. Blanton. Heating a distant galaxy cluster by giant x-ray cavities and large-scale shock fronts. 2004. URL https://arxiv.org/abs/astro-ph/0411553. 1.3.2, 1.3.3, 1.3.7, 1.4.4, 7.4

B. R. McNamara, H. R. Russell, P. E. J. Nulsen, A. N. Vantyghem, B. Ménard, N. Murray, and M. W. Wise. A ten billion solar mass molecular gas outflow in the abell 1835 brightest cluster galaxy. *The Astrophysical Journal*, 785(1):44, 2014. doi: 10.1088/0004-637X/785/1/44. 1.3.2, 1.3.4, 5.1.1

Charles Messier. *Catalogue des Nébuleuses et des Amas d'Étoiles*. Imprimerie Royale, Paris, 1781. 1.1.2

Rajsekhar Mohapatra, Mrinal Jetti, Prateek Sharma, and Christoph Federrath. Velocity structure functions in multiphase turbulence: interpreting kinematics of h filaments in cool-core clusters. *Monthly Notices of the Royal Astronomical Society*, 510(2):2327–2343, 11 2021. ISSN 0035-8711. doi: 10.1093/mnras/stab3429. URL `https://doi.org/10.1093/mnras/stab3429`. 6.3

Rajsekhar Mohapatra, Prateek Sharma, Christoph Federrath, and Eliot Quataert. Multiphase condensation in cluster haloes: interplay of cooling, buoyancy, and mixing. *Monthly Notices of the Royal Astronomical Society*, 525(3):3831–3848, August 2023. ISSN 1365-2966. doi: 10.1093/mnras/stad2574. URL `http://dx.doi.org/10.1093/mnras/stad2574`. 6.5, 6.6

Mireia Montes. The intracluster light and its role in galaxy evolution in clusters. 2019. URL `https://arxiv.org/abs/1912.01616`. 1.1.5

R. Morganti, C. Tadhunter, T. Oosterloo, J. Holt, and B. Emonts. Fast Neutral Outflows in Nearby Radio Galaxies: A Major Source of Feedback. 373:343, October 2007. doi: 10.48550/arXiv.astro-ph/0701440. 5.2.3

Patrick Morrissey, Matuesz Matuszewski, D. Christopher Martin, James D. Neill, Harland Epps, Jason Fucik, Bob Weber, Behnam Darvish, Sean Adkins, Steve Allen, Randy Bartos, Justin Belicki, Jerry Cabak, Shawn Callahan, Dave Cowley, Marty Crabill, Willian Deich, Alex Delecroix, Greg Doppman, David Hilyard, Ean James, Steve Kaye, Michael Kokorowski, Shui Kwok, Kyle Lanclos, Steve Milner, Anna Moore, Donal O'Sullivan, Prachi Parihar, Sam Park, Andrew Phillips, Luca Rizzi, Constance Rockosi, Hector Rodriguez, Yves Salaun, Kirk Seaman, David Sheikh, Jason Weiss, and Ray Zarzaca. The keck cosmic web imager integral

field spectrograph. *The Astrophysical Journal*, 864(1):93, September 2018. ISSN 1538-4357. doi: 10.3847/1538-4357/aad597. URL http://dx.doi.org/10.3847/1538-4357/aad597. 1.4.1

Thorsten Naab, Peter H. Johansson, and Jeremiah P. Ostriker. Minor mergers and the size evolution of elliptical galaxies. *The Astrophysical Journal*, 699(2): L178–L182, June 2009. ISSN 1538-4357. doi: 10.1088/0004-637x/699/2/l178. URL http://dx.doi.org/10.1088/0004-637X/699/2/L178. 1.2.1

Julio F. Navarro, Carlos S. Frenk, and Simon D. M. White. A universal density profile from hierarchical clustering. *The Astrophysical Journal*, 490(2):493–508, December 1997. ISSN 1538-4357. doi: 10.1086/304888. URL http://dx.doi.org/10.1086/304888. 1.1.1

James W Nightingale, Russell J Smith, Qiuhan He, Conor M O'Riordan, Jori Liesenborgs, Simon Dye, David Harvey, Richard J Massey, Aristeidis Amvrosiadis, Ardavanh Angthong, et al. Abell 1201: detection of an ultramassive black hole in a strong gravitational lens. *Monthly Notices of the Royal Astronomical Society*, 521(3):3298–3322, 2023. doi: 10.1093/mnras/stad587. 1.1.6

Carlo Nipoti and James Binney. Cold filaments in galaxy clusters: effects of heat conduction. *Monthly Notices of the Royal Astronomical Society*, 349(4):1509–1515, 04 2004. ISSN 0035-8711. doi: 10.1111/j.1365-2966.2004.07628.x. URL https://doi.org/10.1111/j.1365-2966.2004.07628.x. 1.3.3

Christopher P. O'Dea, Stefi A. Baum, George Privon, Jacob Noel-Storr, Alice C. Quillen, Nicholas Zufelt, Jaehong Park, Alastair Edge, Helen Russell, Andrew C. Fabian, Megan Donahue, Craig L. Sarazin, Brian McNamara, Joel N. Bregman, and Eiichi Egami. An Infrared Survey of Brightest Cluster Galaxies. II. Why are Some Brightest Cluster Galaxies Forming Stars? , 681(2):1035–1045, July 2008. doi: 10.1086/588212. 1.3.1, 1.3.3, 1, 1.4, 1.4.3, 1.4.4, 8, 8.2

V. Olivares, P. Salome, F. Combes, S. Hamer, P. Guillard, M. D. Lehnert, F. L. Polles, R. S. Beckmann, Y. Dubois, M. Donahue, A. Edge, A. C. Fabian, B. McNamara, T. Rose, H. R. Russell, G. Tremblay, A. Vantyghem, R. E. A. Canning,

G. Ferland, B. Godard, S. Peirani, and G. Pineau des Forets. Ubiquitous cold and massive filaments in cool core clusters. *Astronomy amp; Astrophysics*, 631: A22, October 2019. ISSN 1432-0746. doi: 10.1051/0004-6361/201935350. URL http://dx.doi.org/10.1051/0004-6361/201935350. 1.3.5, 1.4.2, 1.4.4, 5.1.1

V. Olivares, P. Lagos, M. J. Hardcastle, et al. Gas condensation in brightest group galaxies unveiled with muse. *A&A*, 666:A132, 2022. 1.4, 5.1.1

Ludwig Oser, Jeremiah P. Ostriker, Thorsten Naab, Peter H. Johansson, and Andreas Burkert. The two phases of galaxy formation. *The Astrophysical Journal*, 725(2):2312–2323, December 2010. ISSN 1538-4357. doi: 10.1088/0004-637x/725/2/2312. URL http://dx.doi.org/10.1088/0004-637X/725/2/2312. 1.2, 1.2.1

Donald E. Osterbrock and Gary J. Ferland. *Astrophysics of gaseous nebulae and active galactic nuclei*. University Science Books, 2006. 2.3.2, 5.1.1, 7.3, 7.3, 7.4.2, 7.4.2

Matt S. Owers, Warrick J. Couch, Paul E. J. Nulsen, and Scott W. Randall. Shocking tails in the major merger abell 2744. *The Astrophysical Journal*, 750 (1):L23, April 2012. ISSN 2041-8213. doi: 10.1088/2041-8205/750/1/l23. URL http://dx.doi.org/10.1088/2041-8205/750/1/L23. 1.2.3

T. Pasini, M. Gitti, F. Brighenti, P. Temi, A. Amblard, S. L. Hamer, S. Ettori, E. O'Sullivan, and F. Gastaldello. A bcg with offset cooling: Is the agn feedback cycle broken in a2495? *The Astrophysical Journal*, 885(2):111, November 2019. ISSN 1538-4357. doi: 10.3847/1538-4357/ab4808. URL http://dx.doi.org/10.3847/1538-4357/ab4808. 5.1.1

J. R. Peterson and A. C. Fabian. X-ray spectroscopy of cooling clusters. *Physics Reports*, 427(1):1–39, 2006. doi: 10.1016/j.physrep.2005.12.007. 1.1.4, 1.3.1

M. Pettini and B. E. J. Pagel. [NII]/Hα as an abundance indicator. *Monthly Notices of the Royal Astronomical Society*, 348(3):L59–L63, 2004. doi: 10.1111/j.1365-2966.2004.07591.x. 7.1.1, 7.1.1, 7.1.1

A. Pillepich, D. Nelson, V. Springel, R. Pakmor, et al. First results from the illustristng simulations: the stellar mass content of groups and clusters of galaxies. *Monthly Notices of the Royal Astronomical Society*, 475(1):648–675, 2018. doi: 10.1093/mnras/stx3112. 1.2.4

A. Pipino, S. Kaviraj, C. Bildfell, A. Babul, H. Hoekstra, and J. Silk. Evidence for recent star formation in bcgs: a correspondence between blue cores and uv excess. *Monthly Notices of the Royal Astronomical Society*, 395(1):462–471, 04 2009. ISSN 0035-8711. doi: 10.1111/j.1365-2966.2009.14534.x. URL `https://doi.org/10.1111/j.1365-2966.2009.14534.x`. 8

Bianca M. Poggianti, Yara L. Jaffé, Alessia Moretti, Marco Gullieuszik, Mario Radovich, Stephanie Tonnesen, Jacopo Fritz, Daniela Bettoni, Benedetta Vulcani, Giovanni Fasano, et al. Gasp. i. gas stripping phenomena in galaxies with muse. *The Astrophysical Journal*, 844(1):48, 2017. doi: 10.3847/1538-4357/aa78ed. 1.2.3

Francesco L. Polles, Patrick Salomé, Pierre Guillard, Andrew C. Fabian, Nicolas Werner, Alastair C. Edge, Filippo Macchetto, Rupal Mittal, and Helen R. Russell. Excitation mechanisms in the intracluster filaments surrounding brightest cluster galaxies. *Astronomy & Astrophysics*, 2021. submitted; arXiv:2103.09842. 4, 1.4.3

Ewald Puchwein, Volker Springel, Debora Sijacki, and Klaus Dolag. Intracluster stars in simulations with active galactic nucleus feedback. , 406(2):936–951, August 2010. doi: 10.1111/j.1365-2966.2010.16786.x. 1.2.6

D. A. Rafferty, B. R. McNamara, and P. E. J. Nulsen. The regulation of cooling and star formation in luminous galaxies and cluster cores. *The Astrophysical Journal*, 687:899–918, 2008. doi: 10.1086/591242. URL `https://ui.adsabs.harvard.edu/abs/2008ApJ...687..899R/abstract`. 7.4, 8.2

D.A. Rafferty, B.R. McNamara, P.E.J. Nulsen, and M.W. Wise. The feedback-regulated growth of black holes and bulges through gas accretion and starbursts in cluster central dominant galaxies. *Astrophysical Journal*, 652:216–231, 2006. doi: 10.1086/507672. 1.3.1

A. Ragagnin, E. Rasia, A. Biviano, et al. Galaxies in the central regions of simulated galaxy clusters. *Astronomy & Astrophysics*, 665:A163, 2022. doi: 10.1051/0004-6361/202243651. 1.2.1, 1.2.6

Cinthia Ragone-Figueroa, Gian Luigi Granato, Giuseppe Murante, Stefano Borgani, and Weiguang Cui. Brightest cluster galaxies in cosmological simulations: achievements and limitations of active galactic nuclei feedback models. *Monthly Notices of the Royal Astronomical Society*, 436(2):1750–1764, October 2013. ISSN 0035-8711. doi: 10.1093/mnras/stt1693. URL `http://dx.doi.org/10.1093/mnras/stt1693`. 1.2.1, 1.2.6

T. D. Rawle, A. C. Edge, E. Egami, M. Rex, G. P. Smith, B. Altieri, A. Fiedler, C. P. Haines, M. J. Pereira, P. G. Pérez-González, J. Portouw, I. Valtchanov, G. Walth, P. P. van der Werf, and M. Zemcov. The relation between cool cluster cores andherschel-detected star formation in brightest cluster galaxies. *The Astrophysical Journal*, 747(1):29, February 2012. ISSN 1538-4357. doi: 10.1088/0004-637x/747/1/29. URL `http://dx.doi.org/10.1088/0004-637X/747/1/29`. 1.4, 7.4

Y. Revaz, F. Combes, and P. Salomé. Formation of cold filaments in cooling flow clusters. *Astronomy amp; Astrophysics*, 477(3):L33–L36, December 2007. ISSN 1432-0746. doi: 10.1051/0004-6361:20078915. URL `http://dx.doi.org/10.1051/0004-6361:20078915`. 1.3.3

Adam G. Riess, Alexei V. Filippenko, Peter Challis, Alejandro Clocchiatti, Alan Diercks, Peter M. Garnavich, Ron L. Gilliland, Craig J. Hogan, Saurabh Jha, Robert P. Kirshner, et al. Observational evidence from supernovae for an accelerating universe and a cosmological constant. *Astron. J.*, 116:1009–1038, 1998. doi: 10.1086/300499. 1.1.1

Tom Rose, A C Edge, F Combes, M Gaspari, S Hamer, N Nesvadba, H Russell, G R Tremblay, S A Baum, C O'Dea, A B Peck, C Sarazin, A Vantyghem, M Bremer, M Donahue, A C Fabian, G Ferland, B R McNamara, R Mittal, J B R Oonk, P Salomé, A M Swinbank, and M Voit. Deep and narrow co absorption revealing

molecular clouds in the hydra-a brightest cluster galaxy. *Monthly Notices of the Royal Astronomical Society*, 485(1):229–238, February 2019. ISSN 1365-2966. doi: 10.1093/mnras/stz406. URL http://dx.doi.org/10.1093/mnras/stz406. 1.3.2, 1.3.4

Tom Rose, A C Edge, F Combes, S Hamer, B R McNamara, H Russell, M Gaspari, P Salomé, C Sarazin, G R Tremblay, S A Baum, M N Bremer, M Donahue, A C Fabian, G Ferland, N Nesvadba, C O'Dea, J B R Oonk, and A B Peck. A molecular absorption line survey towards the agn of hydra-a. *Monthly Notices of the Royal Astronomical Society*, 496(1):364–380, May 2020. ISSN 1365-2966. doi: 10.1093/mnras/staa1474. URL http://dx.doi.org/10.1093/mnras/staa1474. 5.2.3

M. Rossetti, F. Gastaldello, G. Ferioli, M. Bersanelli, S. De Grandi, D. Eckert, S. Ghizzardi, D. Maino, and S. Molendi. Measuring the dynamical state ofplancksz-selected clusters: X-ray peak – bcg offset. *Monthly Notices of the Royal Astronomical Society*, 457(4):4515–4524, February 2016. ISSN 1365-2966. doi: 10.1093/mnras/stw265. URL http://dx.doi.org/10.1093/mnras/stw265. 4.2

Vera C. Rubin and Jr. Ford, W. Kent. Rotation of the Andromeda Nebula from a Spectroscopic Survey of Emission Regions. *Astrophys. J.*, 159:379, 1970. doi: 10.1086/150317. 1.1.1

C.S. Rudick, J.C. Mihos, and C. McBride. Simulating diffuse light in galaxy clusters. page 227–231, 2007. ISSN 1611-6143. doi: 10.1007/978-3-540-71173-5_37. URL http://dx.doi.org/10.1007/978-3-540-71173-5_37. 1.1.5

H. R. Russell, B. R. McNamara, A. C. Fabian, P. E. J. Nulsen, A. C. Edge, F. Combes, N. W. Murray, I. J. Parrish, P. Salomé, J. S. Sanders, S. A. Baum, M. Donahue, R. A. Main, R. W. O'Connell, C. P. O'Dea, J. B. R. Oonk, G. Tremblay, A. N. Vantyghem, and G. M. Voit. Alma observations of cold molecular gas filaments trailing rising radio bubbles in pks 0745191. *Monthly Notices of the Royal Astronomical Society*, 458(3):3134–3149, February 2016. ISSN 1365-2966. doi: 10.1093/mnras/stw409. URL http://dx.doi.org/10.1093/mnras/stw409. 5.1.1

H. R. Russell, B. R. McNamara, A. C. Fabian, P. E. J. Nulsen, F. Combes, A. C. Edge, M. T. Hogan, M. McDonald, P. Salomé, G. Tremblay, and A. N. Vantyghem. Close entrainment of massive molecular gas flows by radio bubbles in the central galaxy of abell 1795. *Monthly Notices of the Royal Astronomical Society*, 472(4): 4024–4037, September 2017. ISSN 1365-2966. doi: 10.1093/mnras/stx2255. URL http://dx.doi.org/10.1093/mnras/stx2255. 5.1.1

H R Russell, B R McNamara, A C Fabian, P E J Nulsen, F Combes, A C Edge, M Madar, V Olivares, P Salomé, and A N Vantyghem. Driving massive molecular gas flows in central cluster galaxies with agn feedback. *Monthly Notices of the Royal Astronomical Society*, 490(3):3025–3045, September 2019. ISSN 1365-2966. doi: 10.1093/mnras/stz2719. URL http://dx.doi.org/10.1093/mnras/stz2719. 1.3.2, 1.3.3, 1.3.4, 1.3.5, 1.4.2, 1.4.4, 1.4.5, 4.1

M. Ruszkowski, M. Brüggen, and M. C. Begelman. Heating, conduction, and minimum temperatures in cooling flow clusters. *ApJ*, 665:1049, 2007. 1.3.3

P. Salomé and F. Combes. Cold molecular gas in cooling flow clusters of galaxies. , 412:657–667, December 2003. doi: 10.1051/0004-6361:20031438. 1.3.1, 1.3.5, 1.4, 1.4.4

P. Salomé, F. Combes, A. C. Edge, C. Crawford, M. Erlund, A. C. Fabian, N. A. Hatch, R. M. Johnstone, J. S. Sanders, and R. J. Wilman. Cold molecular gas in the perseus cluster core: Association with x-ray cavity, h filaments and cooling flow. *Astronomy amp; Astrophysics*, 454(2):437–445, July 2006. ISSN 1432-0746. doi: 10.1051/0004-6361:20054745. URL http://dx.doi.org/10.1051/0004-6361:20054745. 5.2.2

P. Salomé, F. Combes, Y. Revaz, D. Downes, A. C. Edge, and A. C. Fabian. A very extended molecular web around ngc 1275. *Astronomy amp; Astrophysics*, 531:A85, June 2011. ISSN 1432-0746. doi: 10.1051/0004-6361/200811333. URL http://dx.doi.org/10.1051/0004-6361/200811333. 7.4.2

Sánchez and et al. Califa, the calar alto legacy integral field area survey. i. survey presentation. *A&A*, 538:A8, 2012. 7.2.3

S. F. Sánchez, R. García-Benito, S. Zibetti, C. J. Walcher, B. Husemann, M. A. Mendoza, R. M. González Delgado, L. Galbany, J. Falcón-Barroso, D. Mast, J. Aceituno, A. L. de Amorim, J. Bland-Hawthorn, M. Cano-Díaz, R. Cid Fernandes, C. Cortijo-Ferrero, H. Dannerbauer, M. Demleitner, E. Florido, A. Gil de Paz, J. Iglesias-Páramo, B. Jungwiert, R. López-Fernández, R. A. Marino, E. Mármol-Queraltó, J. Mendez-Abreu, M. Mollá, A. Monreal-Ibero, A. del Olmo, P. Papaderos, E. Pérez, A. Quirrenbach, F. F. Rosales-Ortega, T. Ruiz-Lara, P. Sánchez-Blázquez, K. Spekkens, V. Stanishev, S. Trager, J. M. Vilchez, L. Wisotzki, and B. Ziegler. Califa, the calar alto legacy integral field area survey. iii. second public data release. *Astronomy & Astrophysics*, 594:A36, 2016. doi: 10.1051/0004-6361/201628661. 2.3.2

Alastair J. R. Sanderson and Trevor J. Ponman. X-ray modelling of galaxy cluster gas and mass profiles. *Monthly Notices of the Royal Astronomical Society*, 402(1): 65–84, 2010. doi: 10.1111/j.1365-2966.2009.15888.x. URL `https://arxiv.org/abs/0910.3212`. 4.2

C. L. Sarazin. X-ray emission from clusters of galaxies. *Reviews of Modern Physics*, 58(1):1–115, 1986. 1.1.4

Kevin Schawinski, Daniel Thomas, Marc Sarzi, Claudia Maraston, Sugata Kaviraj, Seok-Joo Joo, Sukyoung K. Yi, and Joseph Silk. Observational evidence for AGN feedback in early-type galaxies. , 382(4):1415–1431, December 2007. doi: 10.1111/j.1365-2966.2007.12487.x. 7.2.2

Harlow Shapley and Heber D. Curtis. The scale of the universe. *Bulletin of the National Research Council*, 2:171–217, 1921. 1.1.2

P. Sharma, M. McCourt, E. Quataert, and I. J. Parrish. Thermal instability and the feedback regulation of hot halos in clusters, groups, and galaxies. *Monthly Notices of the Royal Astronomical Society*, 420:3174–3194, 2012. doi: 10.1111/j.1365-2966.2011.19970.x. 1.3.2, 5.2.1

Jonathan D. Slavin, J. M. Shull, and Mitchell C. Begelman. Turbulent Mixing Layers in the Interstellar Medium of Galaxies. , 407:83, April 1993. doi: 10.1086/172494. 4, 1.4.3

Rachel S Somerville and Romeel Davé. Physical models of galaxy formation in a cosmological context. *Annual Review of Astronomy and Astrophysics*, 53:51–93, 2015. doi: 10.1146/annurev-astro-082812-140951. 1.1.6

Kurt T. Soto, Crystal L. Martin, Moire K. M. Prescott, and Lee Armus. The emission-line spectra of major mergers: Evidence for shocked outflows. *Monthly Notices of the Royal Astronomical Society*, 2012. Finds broad, shock-excited blueshifted emission components dominating in ULIRG mergers, with redshifted components suppressed/or obscured. 5.1

W. B. Sparks, J. E. Pringle, M. Donahue, et al. Hα filaments and the direction of motion of the bcg in abell 1795. *The Astrophysical Journal*, 704(1):L20–L24, 2009. doi: 10.1088/0004-637X/704/1/L20. 5, 1.4.3

G. Stasinska, R. C. Fernandes, A. Mateus, L. Sodre, and N. V. Asari. Semi-empirical analysis of sloan digital sky survey galaxies - iii. how to distinguish agn hosts. *Monthly Notices of the Royal Astronomical Society*, 371(2):972–982, September 2006. ISSN 1365-2966. doi: 10.1111/j.1365-2966.2006.10732.x. URL `http://dx.doi.org/10.1111/j.1365-2966.2006.10732.x`. 7.2.2

P. J. Storey and C. J. Zeippen. Theoretical values for the [o iii] 5007/4959 line-intensity ratio and homologous cases. *Monthly Notices of the Royal Astronomical Society*, 312(4):813–816, 03 2000. ISSN 0035-8711. doi: 10.1046/j.1365-8711.2000.03184.x. URL `https://doi.org/10.1046/j.1365-8711.2000.03184.x`. 2.3.2

C. Struve and J. E. Conway. An hi absorbing circumnuclear disk in cygnus a. *Astronomy and Astrophysics*, 513:A10, April 2010. ISSN 1432-0746. doi: 10.1051/0004-6361/200913572. URL `http://dx.doi.org/10.1051/0004-6361/200913572`. 5.2.2

P. D. Tamhane, B. R. McNamara, H. R. Russell, et al. Radio jet–ism interaction and positive radio-mechanical feedback in abell 1795. *Monthly Notices of the Royal Astronomical Society*, 519(3):3338–3350, 2023. doi: 10.1093/mnras/stac3803. 6.6

G. R. Tremblay, J. B. R. Oonk, F. Combes, et al. Cold, clumpy accretion onto an active supermassive black hole. *Nature*, 534:218–221, 2016a. doi: 10.1038/nature17969. 1.3.4, 1.3.5, 1.4.2, 5.2.1

G. R. Tremblay, F. Combes, J. B. R. Oonk, H. R. Russell, M. A. McDonald, M. Gaspari, B. Husemann, P. E. J. Nulsen, B. R. McNamara, S. L. Hamer, C. P. O'Dea, S. A. Baum, T. A. Davis, M. Donahue, G. M. Voit, A. C. Edge, E. L. Blanton, M. N. Bremer, E. Bulbul, T. E. Clarke, L. P. David, L. O. V. Edwards, D. Eggerman, A. C. Fabian, W. Forman, C. Jones, N. Kerman, R. P. Kraft, Y. Li, M. Powell, S. W. Randall, P. Salomé, A. Simionescu, Y. Su, M. Sun, C. M. Urry, A. N. Vantyghem, B. J. Wilkes, and J. A. ZuHone. A galaxy-scale fountain of cold molecular gas pumped by a black hole. *The Astrophysical Journal*, 865(1): 13, September 2018. ISSN 1538-4357. doi: 10.3847/1538-4357/aad6dd. URL `http://dx.doi.org/10.3847/1538-4357/aad6dd`. 1.3.3, 2.3.2, 4.1, 4.5, 5.1, 5.1.1, 6.5

Grant R. Tremblay, J. B. Raymond Oonk, Françoise Combes, Philippe Salomé, Christopher P. O'Dea, Stefi A. Baum, G. Mark Voit, Megan Donahue, Brian R. McNamara, Timothy A. Davis, Michael A. McDonald, Alastair C. Edge, Tracy E. Clarke, Roberto Galván-Madrid, Malcolm N. Bremer, Louise O. V. Edwards, Andrew C. Fabian, Stephen Hamer, Yuan Li, Anaëlle Maury, Helen R. Russell, Alice C. Quillen, C. Megan Urry, Jeremy S. Sanders, and Michael W. Wise. Cold, clumpy accretion onto an active supermassive black hole. *Nature*, 534 (7606):218–221, June 2016b. ISSN 1476-4687. doi: 10.1038/nature17969. URL `http://dx.doi.org/10.1038/nature17969`. 5.2.3

F. Ubertosi, M. Gitti, and F. Brighenti. Chasing ICM cooling and AGN feedback from the macro to the meso scales in the galaxy cluster ZwCl 235. , 670:A23, February 2023. doi: 10.1051/0004-6361/202244023. 5.1

Shutaro Ueda, Yuto Ichinohe, Tetsu Kitayama, and Keiichi Umetsu. Line-of-sight gas sloshing in the cool core of abell 907. *The Astrophysical Journal*, 871(2):207, February 2019. ISSN 1538-4357. doi: 10.3847/1538-4357/aafa19. URL http://dx.doi.org/10.3847/1538-4357/aafa19. 5.1.1

P. G. van Dokkum, K. E. Whitaker, G. Brammer, M. Franx, M. Kriek, et al. The growth of massive galaxies since $z = 2$. *The Astrophysical Journal*, 709(2): 1018–1041, 2010. doi: 10.1088/0004-637X/709/2/1018. 1.2.3

A. Vazdekis, M. Koleva, E. Ricciardelli, B. Röck, and J. Falcón-Barroso. Evolutionary stellar population synthesis with miles - ii. scaled-solar and α-enhanced models. *MNRAS*, 463(3):3409–3436, 2016. doi: 10.1093/mnras/stw2231. 2.3.2, 8.1

S. Veilleux and D. E. Osterbrock. Spectral classification of emission-line galaxies. *ApJS*, 63:295, 1987. 7.2, 7.2.1, 7.2.2

Wolfgang Voges, Bernd Aschenbach, Thomas Boller, Heinrich Braeuninger, Ulrich Briel, Wolfgang Burkert, Konrad Dennerl, Jakob Englhauser, Rainer Gruber, Frank Haberl, Gisela Hartner, Guenther Hasinger, Elmar Pfeffermann, Wolfgang Pietsch, Peter Predehl, Cristina Rosso, Juergen H. M. M. Schmitt, Joachim Truemper, and Hans-Ulrich Zimmermann. The rosat all-sky survey bright source catalogue, 1999. URL https://arxiv.org/abs/astro-ph/9909315. 2.2.1

L. M. Voigt and A. C. Fabian. Thermal conduction and reduced cooling flows in galaxy clusters. *Monthly Notices of the Royal Astronomical Society*, 347(4): 1130–1149, February 2004. ISSN 1365-2966. doi: 10.1111/j.1365-2966.2004.07285.x. URL http://dx.doi.org/10.1111/j.1365-2966.2004.07285.x. 7.4

G. M. Voit. Tracing cosmic evolution with clusters of galaxies. *Reviews of Modern Physics*, 77(1):207–258, 2005. 1.1.4, 7.4

G. M. Voit, K. W. Cavagnolo, M. Donahue, D. A. Rafferty, B. R. McNamara, and P. E. J. Nulsen. Conduction and the star formation threshold in brightest cluster galaxies. *The Astrophysical Journal*, 681(1):L5–L8, June 2008. ISSN 1538-4357. doi: 10.1086/590344. URL http://dx.doi.org/10.1086/590344. 8.2

G. M. Voit, M. Donahue, G. L. Bryan, and B. W. O'Shea. Regulation of star formation in giant galaxies by precipitation, feedback and conduction. *Nature*, 519:203–206, 2015. doi: 10.1038/nature14156. 1.3, 1.3.1, 1.3.2, 5, 1.3.7, 1.4.3, 5.2.1

G. Mark Voit. A Role for Turbulence in Circumgalactic Precipitation. , 868(2): 102, December 2018. doi: 10.3847/1538-4357/aae8e2. 1.3.2

G. Mark Voit and Megan Donahue. Cooling time, freefall time, and precipitation in the cores of accept galaxy clusters. *The Astrophysical Journal*, 799(1):L1, January 2015. ISSN 2041-8213. doi: 10.1088/2041-8205/799/1/l1. URL `http://dx.doi.org/10.1088/2041-8205/799/1/L1`. 7.4

C Wang, M Ruszkowski, C Pfrommer, S Peng Oh, and H-Y K Yang. Non-kolmogorov turbulence in multiphase intracluster medium driven by cold gas precipitation and agn jets. *Monthly Notices of the Royal Astronomical Society*, 504 (1):898–909, April 2021. ISSN 1365-2966. doi: 10.1093/mnras/stab966. URL `http://dx.doi.org/10.1093/mnras/stab966`. 6.3

W. D. Watson and E. E. Salpeter. Molecule Formation on Interstellar Grains. , 174:321, June 1972. doi: 10.1086/151492. 7.4

M. C. Weisskopf, B. Brinkman, C. Canizares, G. Garmire, S. Murray, and L. P. Van Speybroeck. An overview of the performance and scientific results from the chandra x-ray observatory. *Publications of the Astronomical Society of the Pacific*, 114(791):1–24, 2002. doi: 10.1086/338108. 2.1.2

N. Werner, J. B. R. Oonk, M. Sun, P. E. J. Nulsen, S. W. Allen, R. E. A. Canning, A. Simionescu, A. Hoffer, T. Connor, M. Donahue, A. C. Edge, A. C. Fabian, A. Van de Linden, C. S. Reynolds, and M. Ruszkowski. The origin of cold gas in giant elliptical galaxies and its role in fueling radio-mode agn feedback. *Monthly Notices of the Royal Astronomical Society*, 439(3):2291–2306, 2014. doi: 10.1093/mnras/stu006. 1.3.2, 1.3.4, 1.3.6, 1.3.7, 1.4, 1.4.2, 1.4.3

I. M. Whiley, A. Aragón-Salamanca, G. De Lucia, A. von der Linden, S. P. Bamford, P. Best, M. N. Bremer, P. Jablonka, O. Johnson, B. Milvang-Jensen, S. Noll,

B. M. Poggianti, G. Rudnick, R. Saglia, S. White, and D. Zaritsky. The evolution of the brightest cluster galaxies since $z \sim 1$ from the eso distant cluster survey (ediscs). *Monthly Notices of the Royal Astronomical Society*, 387(3):1253–1263, 2008. doi: 10.1111/j.1365-2966.2008.13324.x. 1.2.5

S. D. M. White and M. J. Rees. Core condensation in heavy halos: a two-stage theory for galaxy formation and clustering. *Monthly Notices of the Royal Astronomical Society*, 183:341–358, 1978. doi: 10.1093/mnras/183.3.341. 1.2.1

H. Wolter. Spiegelsysteme streifenden einfalls als abbildende optiken für röntgenstrahlen. *Annalen der Physik*, 445(1-2):94–114, 1952. doi: 10.1002/andp.19524450108. 2.1.2

Joanna Woo, Dan Walters, Finn Archinuk, S M Faber, Sara L Ellison, Hossen Teimoorinia, and Kartheik Iyer. Stellar populations with optical spectra: deep learning versus popular spectrum fitting codes. *Monthly Notices of the Royal Astronomical Society*, 530(4):4260–4276, April 2024. ISSN 1365-2966. doi: 10.1093/mnras/stae1114. URL `http://dx.doi.org/10.1093/mnras/stae1114`. 8.1

Thomas Wright. *An Original Theory or New Hypothesis of the Universe, founded upon the Laws of Nature, and solving by Mathematical Principles the general Phænomena of the visible Creation; and particularly the Via Lactea.* Printed for the Author; sold by H. Chapelle, London, 1750. Contains engravings (32 plates) and presents the first disc-like model of the Milky Way and speculation on faint nebulae as external stellar systems ("island universes"). 1.1.2

R. Yan and M. R. Blanton. The nature of liner-like emission in red galaxies. *The Astrophysical Journal*, 747:61, 2012. doi: 10.1088/0004-637X/747/1/61. 7.2.5

I. Zhuravleva, E. Churazov, P. Arévalo, S. W. Allen, W. R. Forman, N. Werner, A. Simionescu, and H. Böhringer. Turbulent heating in galaxy clusters brightest in x-rays. *Nature*, 515:85–87, 2014a. doi: 10.1038/nature13830. 6.2

Irina Zhuravleva, Eugene Churazov, Alexander A. Schekochihin, Steven W. Allen, Pablo Arévalo, Andrew C. Fabian, William R. Forman, J. Sanders, Aurora

Simionescu, Rashid Sunyaev, Alexey Vikhlinin, and Norbert Werner. Turbulent heating in galaxy clusters brightest in x-rays. *Nature*, 515(7525):85–87, 2014b. doi: 10.1038/nature13830. URL `https://doi.org/10.1038/nature13830`. 5.1.1, 6.5

Stefano Zibetti, Simon D. M. White, Donald P. Schneider, and Jon Brinkmann. Intergalactic stars in z~0.25 galaxy clusters: systematic properties from stacking of Sloan Digital Sky Survey imaging data. , 358(3):949–967, April 2005. doi: 10.1111/j.1365-2966.2005.08817.x. 1.1.5

F. Zwicky. On the Masses of Nebulae and of Clusters of Nebulae. *Astrophys. J.*, 86:217, 1937. doi: 10.1086/143864. 1.1.1

APPENDIX A

Appendix

Kaleidoscope Survey Table

Table A.1: Properties of the Kaleidoscope Sample. We show redshift (z), the presence of spatially extended emission lines, the central stellar velocity dispersion ($\sigma_\star$) and the extent of emission ($R_{\rm maj}$)

Name	z	Em. Lines	$\sigma_\star$ (km s^{-1})	$R_{\rm maj}$ (kpc)
Abell 141	0.21367	✓	395.1	-
Abell 267	0.27420	✗	213.3	-
Abell 291	0.19590	✓	247.3	36.23
Abell 383	0.18440	✓	397.9	26.35
Abell 2104	0.15790	✗	256.2	-
Abell 2259	0.17040	✗	288.3	-
Abell 2328	0.15960	✗	327.8	-
Abell 2345	0.17770	✗	314.3	-
Abell 2355	0.12590	✗	590.8	5.44
Abell 2396	0.19100	✗	412.7	4.42
Abell 2420	0.08800	✓	289.5	7.65
Abell 2426	0.09830	✓	268.1	5.01
Abell 2496	0.12570	✓	330.0	5.73

continued on next page

Name	z	Extended Em. Lines	$\sigma_\star$ (km s^{-1})	$R_{\rm maj}$ (kpc)
Abell 2537	0.29800	✗	342.7	-
Abell 2580	0.11440	✓	637.7	7.04
Abell 2588	0.16630	✗	650.0	-
Abell 2631	0.16630	✗	253.8	-
Abell 2645	0.25240	✗	164.8	-
Abell 2697	0.23020	✗	265.9	-
Abell 2811	0.10892	✓	348.9	-
Abell 2813	0.29320	✗	276.6	-
Abell 2830	0.21030	✗	650.0	-
Abell 2938	0.27990	✗	329.5	-
Abell 3017	0.21935	✓	252.0	57.34
Abell 3088	0.25330	✓	251.5	33.79
Abell 3112	0.07581	✓	314.8	11.18
Abell 3186	0.13190	✗	253.7	-
Abell 3230	0.07860	✗	184.4	-
Abell 3266	0.05740	✓	318.3	-
Abell 3322	0.19330	✗	252.5	-
Abell 3364	0.14940	✗	289.2	-
Abell 3378	0.14095	✓	365.8	22.33
Abell 3399	0.21260	✗	227.7	-
Abell 3404	0.16740	✗	315.0	-
Abell 3444	0.25210	✓	289.3	43.39
Abell 3654	0.17460	✗	276.2	-
Abell 3667	0.05640	✓	275.8	6.06
Abell 3739	0.19190	✗	650.0	2.78
Abell 3814	0.13050	✓	366.3	24.55
Abell 3854	0.14200	✗	339.8	-
Abell 3866	0.15380	✓	262.7	23.93
Abell 3888	0.18125	✗	303.4	-
Abell 3921	0.09230	✗	304.4	4.07
Abell 3984	0.07440	✗	548.0	-
Abell S520	0.29721	✗	496.8	-
Abell S780	0.23950	✓	346.8	55.97
MACS0011.7-1523	0.38140	✗	319.0	-

continued on next page

Name	z	Extended Em. Lines	$\sigma_\star$ (km s^{-1})	$R_{\rm maj}$ (kpc)
MACS0027.2+2607	0.36670	✓	296.1	13.63
MACS0032.1+1808	0.39030	✗	650.0	-
MACS0034.4+0225	0.38660	✗	387.1	17.98
MACS0035.4-2015	0.34630	✗	363.3	-
MACS0138.0-2155	0.35990	✗	650.0	21.47
MACS0140.0-0555	0.45220	✗	310.2	-
MACS0150.3-1005	0.36280	✓	468.9	25.03
MACS0159.8-0849	0.40570	✓	342.2	32.22
MACS0252.4-2100	0.70140	✓	333.3	60.99
MACS0326.8-0043	0.44720	✓	326.0	86.94
MACS0547.0-3904	0.31860	✓	156.1	68.54
MACS0916.1-0023	0.33620	✗	306.6	-
MACS1423.8+2404	0.54060	✓	458.5	47.55
MACS1625.7-0830	0.47730	✗	650.0	50.70
MACS1644.9+0139	0.33870	✗	306.0	-
MACS1731.6+2252	0.39110	✗	624.6	-
MACS2003.4-2322	0.31240	✗	329.9	-
MACS2051.1+0215	0.33430	✗	650.0	-
MACS2115.9-2311	0.31160	✗	430.0	-
MACS2135.2-0102	0.33190	✗	534.1	-
MACS2211.7-0349	0.39890	✗	427.2	-
MACS2228.5+2037	0.41080	✗	282.8	-
MACS2241.8+1732	0.32990	✗	378.6	-
MACS2243.3-0935	0.43350	✗	650.0	-
MACS2245.0+2637	0.29730	✓	361.1	20.25
MACS2311.3-0946	0.29450	✗	650.0	-
MACSJ0018.5+1626	0.54900	✗	303.5	-
MACSJ0018.9-4051	0.48490	✗	311.8	-
MACSJ0025.4-1222	0.58380	✗	129.9	-
MACSJ0028.2-7537	0.38930	✗	283.4	-
MACSJ0040.8-4407	0.37630	✗	650.0	-
MACSJ0051.6+2720	0.37350	✗	307.4	-
MACSJ0111.5+0855	0.48500	✗	341.4	-
MACSJ0140.0-3410	0.39770	✗	293.6	-

continued on next page

Name	z	Extended Em. Lines	$\sigma_\star$ (km s^{-1})	$R_{\rm maj}$ (kpc)
MACSJ0152.5-2853	0.42140	✗	290.4	-
MACSJ0159.0-3413	0.40370	✗	295.7	-
MACSJ0217.2-5244	0.34650	✗	361.3	-
MACSJ0242.5-2132	0.31520	✓	291.7	39.83
MACSJ0257.1-2325	0.50370	✗	330.4	-
MACSJ0257.6-2209	0.32120	✓	359.1	5.19
MACSJ0308.9+2645	0.34640	✗	370.1	-
MACSJ0358.8-2955	0.44730	✗	480.2	-
MACSJ0404.6+1109	0.34920	✗	417.8	-
MACSJ0406.0-4916	0.27660	✗	650.0	-
MACSJ0439.2-4600	0.31700	✗	273.0	-
MACSJ0449.3-2848	0.32640	✓	461.9	26.30
MACSJ0455.2+0657	0.45090	✗	315.9	-
MACSJ0510.4+0220	0.40120	✓	303.0	18.49
MACSJ0527.4-2754	0.31460	✗	257.3	16.95
MACSJ0529.7-3145	0.34290	✗	436.2	-
MACSJ0553.4-3342A	0.43500	✗	316.9	-
MACSJ0600.1-2008	0.42700	✗	297.6	-
MACSJ0611.8-3036	0.31480	✗	307.4	-
MACSJ0911.2+1746	0.50770	✗	326.5	9.87
MACSJ0949.8+1708	0.38620	✗	302.3	-
MACSJ1105.7-1014	0.41740	✗	250.2	-
MACSJ1108.8+0906	0.47990	✗	347.0	-
MACSJ1115.8+0129	0.35920	✓	295.6	61.73
MACSJ1131.8-1955	0.30470	✗	266.8	-
MACSJ1141.6-1905	0.30270	✗	205.0	-
MACSJ1226.8+2153	0.43670	✗	358.1	-
MACSJ1246.1-2547	0.30610	✗	438.9	-
MACSJ1427.6-2521	0.31770	✓	355.5	-
MACSJ1447.4+0828	0.37520	✓	391.0	50.05
MACSJ1518.9-8130	0.48220	✗	409.8	-
MACSJ1526.7+1647	0.32780	✗	276.9	-
MACSJ1532.8+3021	0.36390	✓	342.0	72.19
MACSJ1551.9-0207	0.30170	✗	347.3	15.69

continued on next page

Name	z	Extended Em. Lines	$\sigma_\star$ (km s^{-1})	$R_{\rm maj}$ (kpc)
MACSJ2046.0-3430	0.42060	✓	376.3	60.82
MACSJ2049.9-3217	0.32220	✗	294.8	-
MACSJ2134.6-2706	0.36370	✓	355.3	24.33
MACSJ2140.2-2339	0.31160	✓	383.4	24.23
MACSJ2149.3+0951	0.38830	✗	650.0	-
MACSJ2229.7-2755	0.32710	✓	354.6	55.31
MACSJ2311.5+0338	0.30060	✗	318.5	-
RBS653	0.29151	✓	293.5	23.06
RXCJ0019.6+0336	0.26170	✗	313.5	-
RXCJ0218.3-3141	0.27240	✗	247.3	-
RXCJ0232.2-4420	0.27040	✗	344.8	-
RXCJ1317.1-3821	0.25490	✓	285.1	38.79
RXCJ1546.0-1408	0.25033	✗	431.6	-
RXCJ1558.3-1410	0.09800	✓	257.7	21.12
RXCJ1617.5-0715	0.25746	✗	416.9	-
RXCJ1636.4+0308	0.27011	✗	326.7	-
RXCJ1936.1-4518	0.27337	✗	290.8	-
RXCJ1947.3-7623	0.21638	✓	361.2	15.65
RXCJ2023.3-5535	0.22549	✗	306.8	-
RXCJ2323.6+1155	0.31300	✓	334.7	34.30
SMACSJ0234.7-5831	0.40420	✓	260.5	21.70
SMACSJ0549.3-6205	0.37320	✓	315.1	34.11
SMACSJ0600.2-4353	0.29540	✗	650.0	-
SMACSJ0723.6-7327	0.38890	✗	252.3	-
Zw2089	0.23421	✓	242.1	49.15
Zw3146	0.29479	✓	559.9	49.72